LIGHT-NANOMATERIAL INTERACTIONS FOR ENERGY EFFICIENT NANOPHOTONIC DEVICES

EDITED BY: Han Lin, Keng-Te Lin and Zhongquan Nie
PUBLISHED IN: Frontiers in Materials and Frontiers in Physics

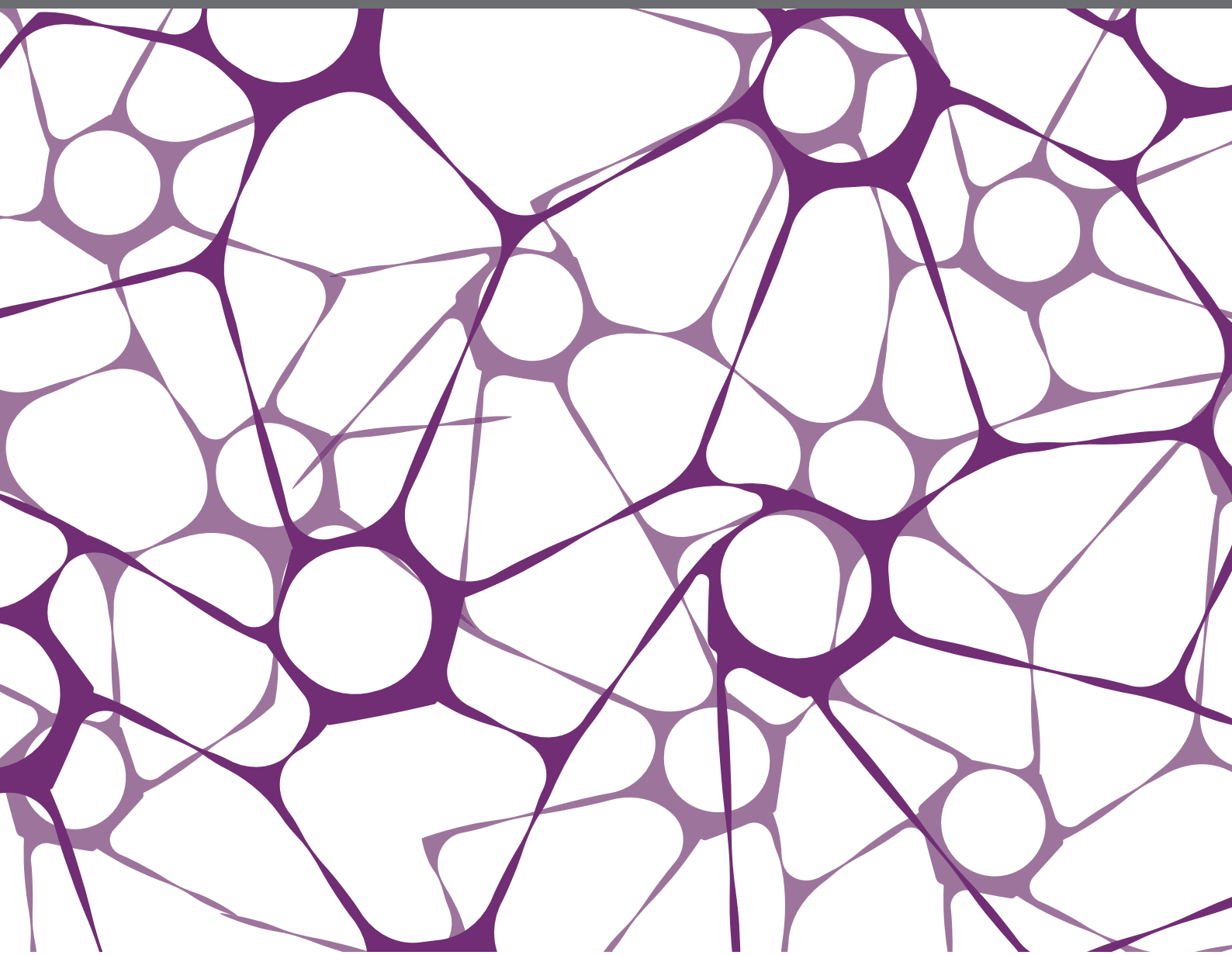

frontiers Research Topics

ISSN 1664-8714
ISBN 978-2-88976-030-5
DOI 10.3389/978-2-88976-030-5

About Frontiers

Frontiers is more than just an open-access publisher of scholarly articles: it is a pioneering approach to the world of academia, radically improving the way scholarly research is managed. The grand vision of Frontiers is a world where all people have an equal opportunity to seek, share and generate knowledge. Frontiers provides immediate and permanent online open access to all its publications, but this alone is not enough to realize our grand goals.

Frontiers Journal Series

The Frontiers Journal Series is a multi-tier and interdisciplinary set of open-access, online journals, promising a paradigm shift from the current review, selection and dissemination processes in academic publishing. All Frontiers journals are driven by researchers for researchers; therefore, they constitute a service to the scholarly community. At the same time, the Frontiers Journal Series operates on a revolutionary invention, the tiered publishing system, initially addressing specific communities of scholars, and gradually climbing up to broader public understanding, thus serving the interests of the lay society, too.

Dedication to Quality

Each Frontiers article is a landmark of the highest quality, thanks to genuinely collaborative interactions between authors and review editors, who include some of the world's best academicians. Research must be certified by peers before entering a stream of knowledge that may eventually reach the public - and shape society; therefore, Frontiers only applies the most rigorous and unbiased reviews.
Frontiers revolutionizes research publishing by freely delivering the most outstanding research, evaluated with no bias from both the academic and social point of view. By applying the most advanced information technologies, Frontiers is catapulting scholarly publishing into a new generation.

What are Frontiers Research Topics?

Frontiers Research Topics are very popular trademarks of the Frontiers Journals Series: they are collections of at least ten articles, all centered on a particular subject. With their unique mix of varied contributions from Original Research to Review Articles, Frontiers Research Topics unify the most influential researchers, the latest key findings and historical advances in a hot research area! Find out more on how to host your own Frontiers Research Topic or contribute to one as an author by contacting the Frontiers Editorial Office: frontiersin.org/about/contact

LIGHT-NANOMATERIAL INTERACTIONS FOR ENERGY EFFICIENT NANOPHOTONIC DEVICES

Topic Editors:
Han Lin, Swinburne University of Technology, Australia
Keng-Te Lin, Swinburne University of Technology, Australia
Zhongquan Nie, Taiyuan University of Technology, China

Citation: Lin, H., Lin, K.-T., Nie, Z., eds. (2022). Light-Nanomaterial Interactions for Energy Efficient Nanophotonic Devices. Lausanne: Frontiers Media SA.
doi: 10.3389/978-2-88976-030-5

Table of Contents

frontiers | Frontiers in Materials

EDITORIAL
published: 06 April 2022
doi: 10.3389/fmats.2022.865312

Editorial: Light-Nanomaterial Interactions for Energy Efficient Nanophotonic Devices

Han Lin[1]*, *Zhongquan Nie*[2] *and Keng-Te Lin*[1]

[1]Centre of Translational Atomaterials (CTAM), Faculty of Science, Engineering and Technology, Swinburne University of Technology, Hawthorn, VIC, Australia, [2]Key Lab of Advanced Transducers and Intelligent Control System, Ministry of Education and Shanxi Province, College of Physics and Optoelectronics, Taiyuan University of Technology, Taiyuan, China

Keywords: nanophotonic, 2D material, light-matter interaction, nanomaterial, laser nano fabrication, non-linearity

Editorial on the Research Topic

Light-Nanomaterial Interactions for Energy Efficient Nanophotonic Devices

Light-matter interaction is the fundamental principle of optical/photonic devices, which includes absorption, transmission, and reflection at the fundamental level and can be further used to control emission, detection and amplification, as well as optical magnetization. Therefore, controlling the light-matter interaction holds the key in designing advanced functional optical/photonic devices. In the last few decades, the advancement in development of nanomaterials and nanofabrication techniques allows achieving light-matter interaction at nanoscale beyond the diffraction limit, which enable advanced manipulation of electromagnetic waves. Recent advancement in developing two-dimensional (2D) materials, such as graphene (Lin et al., 2019; Yang et al., 2019; Lin et al., 2020a; Lin et al., 2021), transition-metal dichalcogenides (TMDCs) (Lin et al., 2020b), perovskites (Wen et al., 2018; Wang et al., 2020) and hexagonal boron nitride (hBN) Wu et al., further pushed the light-matter interaction down to deep subwavelength scale, even to a single atomic layer, which is fascinating and extraordinary due to the 2D confinement of electrons. Therefore, light-nanomaterial interaction offers a broad range of applications in various areas including sensing, imaging, renewable energy harvesting, optical data storage, and optical communication, which is the technology revolution in the 21st century affecting our lives in medical, health, energy consumption, and communication.

This research topic has 9 research papers, focusing on the cutting-edge advances in research of light-matter interaction with different types of nanostructures and nanomaterials, including dielectric materials (silicon, Sb_2Se_3, β-Ga_2O_3 and diamond), 2D materials (graphene and MoS_2) and magnetic nanomaterials ($Ca_2Nb_2O_7$ PLD Film), covering different interactions, such as linear and non-linear optical responses, and magnetic response. In addition, there are several applications based on the fundamental light-matter interaction are demonstrated, such as silicon ring waveguides, hologram, nano-thermometers.

Optical non-linearity (Tan et al., 2017; Yang et al., 2018; Yang et al., 2020) is an important characteristic of materials for the applications of optical modulators, switches, high harmonic generation. There are four studies on the optical non-linearity of different nanomaterials in this research topic. Sun et al. experimentally demonstrated tuning the optical non-linearity of graphene/MoS_2/Ag thin films by controlling the DC power of magnetron sputtering power, which manipulate the local surface plasmon resonance effect of the Ag thin films. Such an enhanced surface plasmon resonance effect can enhance the non-linearity of the entire system. It is an interesting tuning method, with which the non-linearity is enhanced by the unique surface plasmonic effect. the magnetron sputtering technology has also been applied to tune the doping level of the Co-doped

Edited and reviewed by:
Vincent G. Harris, Northeastern University, United States

***Correspondence:**
Han Lin
hanlin@swin.edu.au

Specialty section:
This article was submitted to Quantum Materials, a section of the journal Frontiers in Materials

Received: *29 January 2022*
Accepted: *18 March 2022*
Published: *06 April 2022*

Citation:
Lin H, Nie Z and Lin K-T (2022) Editorial: Light-Nanomaterial Interactions for Energy Efficient Nanophotonic Devices. Front. Mater. 9:865312. doi: 10.3389/fmats.2022.865312

Sb2Se3, which exhibits ultrafast carrier absorption (<1 ps) and a stronger transient absorption intensity of ΔOD >6.3, thus, it may find applications in broadband non-linear photonic devices. Meanwhile, Xiao et al. found that with the introduction of nitrogen defects, the diamond can have the non-linear absorption in addition to the intrinsic non-linear refraction. In this way, the fundamental light-matter interaction in diamonds has been significantly modified, which can open up more applications of diamond materials. Sun et al. investigated the different non-linear optical mechanisms and defect-related carrier dynamics in Sn-doped β-Ga2O3 crystal and found that by choosing a proper probe wavelength that matches the defect state to the valence band, the non-linear absorption and refraction of the carriers can be greatly enhanced. This method provides an important reference for the design of gallium oxide-based waveguide materials and all-optical switching materials in the future.

In addition to fundamental optical property studies, there are three applications of light-matter interaction published in this topic. Liu et al. propose a holographic near-eye 3D display method based on large-size computer-generated holograms (CGHs), which are generated and they record the information of the 3D object from different angles. The unique feature of this method is the large viewing angle, which currently is one of the limiting factors. Wang et al. theoretically demonstrated a silicon ring waveguide, in order to tune the frequency of the phonon field of stimulated Brillouin scattering (SBS) laser based on the silicon substrate of the ring cavity. This silicon waveguide based on ring cavity provides a new technical scheme for designing tunable SBS lasers by tuning the ring widths. Li et al. investigated the up-conversion luminescence and optical temperature sensing properties of $Ho^{3+}/Tm^{3+}/Yb^{3+}$-co-doped $NaLuF_4$ phosphors, which could be potentially applied in far infrared temperature sensing in biological tissue for their high sensing sensitivity.

Finally, as the emerging field, magnetic property of materials has attracted broad applications, which enables unique interaction between light and nanomaterials, by introducing non-unity permeability of materials to modulate the magnetic part of the electromagnetic waves. Here Wu et al. study the introduction of magnetism in ferroelectric $Ca_2Nb_2O_7$ by the intrinsic complex vacancy of V_{Nb+O}. This method might be applicable to other $A_2Nb_2O_7$-type niobate ferroelectric films as well.

In addition to the collected papers, the light-matter interaction can also be applied to modify material to directly fabricate functional photonic devices, such as light reduction of graphene oxide materials (Zheng et al., 2015; Zheng et al., 2017), laser introduced phase change (Cho et al., 2015; Tan et al., 2018; Chaste et al., 2020), laser ablation (Cao et al., 2019; Li et al., 2020a; Wei et al., 2021), laser introduction of defects (Li et al., 2020b), laser introduced doping (Guo et al., 2014), and opto-magnetization (Nie et al., 2017). By using tightly focused laser beam, those light-matter interaction can be localized to achieve nanoscale modification to produce nanostructure. In turn those fabricated nanostructures with well-designed spatial distribution can further enhance the light-matter interaction to achieve advanced functionality. Furthermore, the laser fabrication technique can generally achieve high flexibility, low-cost and large area fabrication. As a result, by considering both material modulation of light and light modification of material, it is possible to not only improve the energy efficiency of the functional optical/photonic devices, but also the energy efficiency of the fabrication process. In this way, highly energy efficient nanophotonic devices can be achieved.

AUTHOR CONTRIBUTIONS

All authors listed have made a substantial, direct, and intellectual contribution to the work and approved it for publication.

REFERENCES

Cao, G., Lin, H., Fraser, S., Zheng, X., Del Rosal, B., Gan, Z., et al. (2019). Resilient Graphene Ultrathin Flat Lens in Aerospace, Chemical, and Biological Harsh Environments. *ACS Appl. Mater. Inter.* 11 (22), 20298–20303. doi:10.1021/acsami.9b05109

Chaste, J., Hnid, I., Khalil, L., Si, C., Durnez, A., Lafosse, X., et al. (2020). Phase Transition in a Memristive Suspended MoS2 Monolayer Probed by Opto- and Electro-Mechanics. *ACS nano* 14 (10), 13611–13618. doi:10.1021/acsnano.0c05721

Cho, S., Kim, S., Kim, J. H., Zhao, J., Seok, J., Keum, D. H., et al. (2015). Phase Patterning for Ohmic Homojunction Contact in MoTe 2. *Science* 349 (6248), 625–628. doi:10.1126/science.aab3175

Guo, L., Zhang, Y.-L., Han, D.-D., Jiang, H.-B., Wang, D., Li, X.-B., et al. (2014). Laser-Mediated Programmable N Doping and Simultaneous Reduction of Graphene Oxides. *Adv. Opt. Mater.* 2 (2), 120–125. doi:10.1002/adom.201300401

Li, J., Yang, X., Liu, Y., Huang, B., Wu, R., Zhang, Z., et al. (2020). General synthesis of two-dimensional van der Waals heterostructure arrays. *Nature* 579 (7799), 368–374. doi:10.1038/s41586-020-2098-y

Li, X., Wei, S., Cao, G., Lin, H., Zhao, Y., and Jia, B. (2020). Graphene Metalens for Particle Nanotracking. *Photon. Res.* 8 (8), 1316–1322. doi:10.1364/prj.397262

Lin, H., Xu, Z. Q., Cao, G., Zhang, Y., Zhou, J., Wang, Z., et al. (2020). Diffraction-limited Imaging with Monolayer 2D Material-Based Ultrathin Flat Lenses. *Light Sci. Appl.* 9 (1), 137. doi:10.1038/s41377-020-00374-9

Lin, H., Lin, K. T., Yang, T., and Jia, B. (2021). Graphene Multilayer Photonic Metamaterials: Fundamentals and Applications. *Adv. Mater. Technol.* 6 (5), 2000963. doi:10.1002/admt.202000963

Lin, H., Sturmberg, B. C. P., Lin, K.-T., Yang, Y., Zheng, X., Chong, T. K., et al. (2019). A 90-Nm-Thick Graphene Metamaterial for strong and Extremely Broadband Absorption of Unpolarized Light. *Nat. Photon.* 13 (4), 270–276. doi:10.1038/s41566-019-0389-3

Lin, K. T., Lin, H., Yang, T., and Jia, B. (2020). Structured Graphene Metamaterial Selective Absorbers for High Efficiency and Omnidirectional Solar thermal Energy Conversion. *Nat. Commun.* 11 (1), 1389. doi:10.1038/s41467-020-15116-z

Nie, Z.-Q., Lin, H., Liu, X.-F., Zhai, A.-P., Tian, Y.-T., Wang, W.-J., et al. (2017). Three-dimensional Super-resolution Longitudinal Magnetization Spot Arrays. *Light Sci. Appl.* 6 (8), e17032. doi:10.1038/lsa.2017.32

Tan, S. J. R., Abdelwahab, I., Ding, Z., Zhao, X., Yang, T., Loke, G. Z. J., et al. (2017). Chemical Stabilization of 1T′ Phase Transition Metal Dichalcogenides with Giant Optical Kerr Nonlinearity. *J. Am. Chem. Soc.* 139 (6), 2504–2511. doi:10.1021/jacs.6b13238

Tan, Y., Luo, F., Zhu, M., Xu, X., Ye, Y., Li, B., et al. (2018). Controllable 2H-To-1t′ Phase Transition in Few-Layer MoTe2. *Nanoscale* 10 (42), 19964–19971. doi:10.1039/c8nr06115g

Wang, Z., Yang, T., Zhang, Y., Ou, Q., Lin, H., Zhang, Q., et al. (2020). Flat Lenses Based on 2D Perovskite Nanosheets. *Adv. Mater.* 32 (30), 2001388. doi:10.1002/adma.202001388

Wei, S., Cao, G., Lin, H., Yuan, X., Somekh, M., and Jia, B. (2021). A Varifocal Graphene Metalens for Broadband Zoom Imaging Covering the Entire Visible Region. *ACS Nano* 15 (3), 4769–4776. doi:10.1021/acsnano.0c09395

Wen, X., Chen, W., Yang, J., Ou, Q., Yang, T., Zhou, C., et al. (2018). Role of Surface Recombination in Halide Perovskite Nanoplatelets. *ACS Appl. Mater. Inter.* 10 (37), 31586–31593. doi:10.1021/acsami.8b06931

Yang, T., Abdelwahab, I., Lin, H., Bao, Y., Rong Tan, S. J., Fraser, S., et al. (2018). Anisotropic Third-Order Nonlinearity in Pristine and Lithium Hydride Intercalated Black Phosphorus. *ACS Photon.* 5 (12), 4969–4977. doi:10.1021/acsphotonics.8b01200

Yang, T., Lin, H., and Jia, B. (2020). Ultrafast Direct Laser Writing of 2D Materials for Multifunctional Photonics Devices [Invited]. 中国光学快报 18 (2), 023601. doi:10.3788/col202018.023601

Yang, Y., Lin, H., Zhang, B. Y., Zhang, Y., Zheng, X., Yu, A., et al. (2019). Graphene-Based Multilayered Metamaterials with Phototunable Architecture for On-Chip Photonic Devices. *ACS Photon.* 6 (4), 1033–1040. doi:10.1021/acsphotonics.9b00060

Zheng, X., Jia, B., Lin, H., Qiu, L., Li, D., and Gu, M. (2015). Highly Efficient and Ultra-broadband Graphene Oxide Ultrathin Lenses with Three-Dimensional Subwavelength Focusing. *Nat. Commun.* 6 (1), 8433. doi:10.1038/ncomms9433

Zheng, X., Lin, H., Yang, T., and Jia, B. (2017). Laser Trimming of Graphene Oxide for Functional Photonic Applications. *J. Phys. D: Appl. Phys.* 50 (7), 074003. doi:10.1088/1361-6463/aa54e9

Conflict of Interest: The authors declare that the research was conducted in the absence of any commercial or financial relationships that could be construed as a potential conflict of interest.

Publisher's Note: All claims expressed in this article are solely those of the authors and do not necessarily represent those of their affiliated organizations, or those of the publisher, the editors and the reviewers. Any product that may be evaluated in this article, or claim that may be made by its manufacturer, is not guaranteed or endorsed by the publisher.

frontiers in Materials

ORIGINAL RESEARCH
published: 05 August 2021
doi: 10.3389/fmats.2021.736011

Intrinsic Complex Vacancy-Induced d^0 Magnetism in $Ca_2Nb_2O_7$ PLD Film

Linjie Wu[1], *Yongjia Zhang*[1], *Zhongquan Nie*[2] *and Ensi Cao*[1]*

[1]College of Physics and Optoelectronics, Taiyuan University of Technology, Taiyuan, China, [2]Key Lab of Advanced Transducers and Intelligent Control System, Ministry of Education, Taiyuan University of Technology, Taiyuan, China

Introducing magnetism into the ferroelectric $Ca_2Nb_2O_7$ with high Curie temperature can make it a potential multiferroic material at room temperature. Stoichiometric $Ca_2Nb_2O_7$, nonstoichiometric $Ca_{1.9}Nb_2O_{7-\delta}$ and $Ca_2Nb_{1.9}O_{7-\delta}$ single phase films were deposited on STO (110) substrate by pulsed laser deposition under appropriate conditions. The films were characterized by XRD, FE-SEM, Element mapping and XPS. Both stoichiometric $Ca_2Nb_2O_7$ and $Ca_{1.9}Nb_2O_{7-\delta}$ films were diamagnetic in the magnetic measurement and *ab initio* calculations, while the $Ca_2Nb_{1.9}O_{7-\delta}$ film with the complex vacancy of V_{Nb+O} exhibited ferromagnetic behavior at room temperature, with the saturated magnetization of 3.6 emu/cm^3. Calculations on the $Ca_2Nb_2O_7$ (010) surface indicate that the V_{Nb+O} can induce spin polarization on the residual O atoms around the Nb vacancies, and the system was most stable when the Nb and O vacancies were the 4th nearest-neighbored, with FM coupling energetically more stable than the AFM coupling. Our work verified experimentally and theoretically the feasibility of introducing ferromagnetism into $Ca_2Nb_2O_7$ film by the intrinsic complex vacancy of V_{Nb+O}.

Keywords: PLD, ab initio calculation, complex vacancy, Ca2Nb2O7, d0 magnetism

OPEN ACCESS

Edited by:
Han Lin,
Swinburne University of Technology, Australia

Reviewed by:
Tongshuai Xu,
Anyang Normal University, China
Feng Jiang,
Dalian University of Technology, China

****Correspondence:***
Ensi Cao
ECao@163.com

Specialty section:
This article was submitted to Quantum Materials, a section of the journal Frontiers in Materials

Received: *04 July 2021*
Accepted: *22 July 2021*
Published: *05 August 2021*

Citation:
Wu L, Zhang Y, Nie Z and Cao E (2021) Intrinsic Complex Vacancy-Induced d^0 Magnetism in $Ca_2Nb_2O_7$ PLD Film. Front. Mater. 8:736011. doi: 10.3389/fmats.2021.736011

INTRODUCTION

Multiferroic materials with the co-existance of ferroelectricity (FE) and ferromagnetism (FM) have received considerable attention in recent years due to the unique physical mechanism of magnetoelectric coupling and potential applications in the fields of information storage, processing and sensing (Fiebig, 2005; Chun et al., 2012). However, the natural conflict between FM and FE leads to the rarity of multiferroic material at room temperature (RT) (Hill, 2000). $Ca_2Nb_2O_7$ is a member of the $A_nNb_nO_{3n+2}$ family with n = 4, which has layered perovskite structure and high ferroelectric Curie temperature (above 1850°C) (Lichtenberg et al., 2001). The introduction of FM into ferroelectric $Ca_2Nb_2O_7$ could make it a potential multiferroic material at RT.

In order to achieve FM in ferroelectric materials, doping magnetic elements was the most frequently adopted method. So far, RTFM has been experimentally observed in the Fe-doped $BaTiO_3$ films (Ramana et al., 2013; Chand Verma et al., 2014), Fe-doped $LiTaO_3$ ceramics (Song et al., 2014) and Fe-doped $K_{0.45}Na_{0.49}Li_{0.06}NbO_3$ ceramics (Liu et al., 2015), the origin of which can be theoretically well explained by the F-center model for diluted magnetic semiconductors. Besides, nonmagnetic element doping induced d^0 magnetism has been observed in $BaTiO_3$ film/ceramics, Nb-doped $BaTiO_3$ film and $LiNbO_3$ nanocrystallites, the origin of which was ascribed to the oxygen vacancy (Mangalam et al., 2009; Yang et al., 2010; Díaz-Moreno et al., 2014). However, the observed FM in Eu-doped $CdNb_2O_6$ powders was elucidated with the intrinsic exchange interactions between the magnetic moments associated with the unpaired 4*f* electrons in Eu^{3+} ions (Topkaya et al., 2017). The RTFM in $K_{0.5}Na_{0.5}NbO_3$ PLD film was related to the cationic K and Na vacancies (Cao et al.,

2011a), while the RTFM observed in $BaNb_2O_6$ film was contributed mainly by the oxygen vacancy, with certain contribution by the Nb vacancy (Cao et al., 2012). In the aspect of theoretical study, both Ti and O vacancies were found to be able to induce FM in $BaTiO_3$ bulk material and (001) surface (Cao et al., 2009; Cao et al., 2011b) and in $PbTiO_3$ (Shimada et al., 2012). However, O vacancy was found to be able to induce FM in $LiNbO_3$ but cannot induce FM in $LiTaO_3$ and Sr_2AlNbO_6 (Cao et al., 2013; Li et al., 2014).

Therefore, the origin of FM in undoped ferroelectric material is still controversial in both experimental and theoretical results. Meanwhile, most of the analyses on the vacancy-induced d^0 magnetism in ferroelectric oxide films just considered various cation vacancies or oxygen vacancy alone, the synergistic effect of cation and oxygen vacancies, i.e., the effect of complex vacancy, was seldom studied. Herein, the advantage of the identical composition between the film and ceramic target in pulsed laser deposition (PLD) was utilized to prepare stoichiometric $Ca_2Nb_2O_7$ single phase film and those with the complex vacancy of V_{Ca+O} or V_{Nb+O} by varying the composition of $Ca_2Nb_2O_7$ ceramic targets. The probability of achieving d^0 magnetism in the nonstoichiometric $Ca_2Nb_2O_7$ single phase film by complex vacancy was comprehensively examined by magnetic measurement and ab initio calculations.

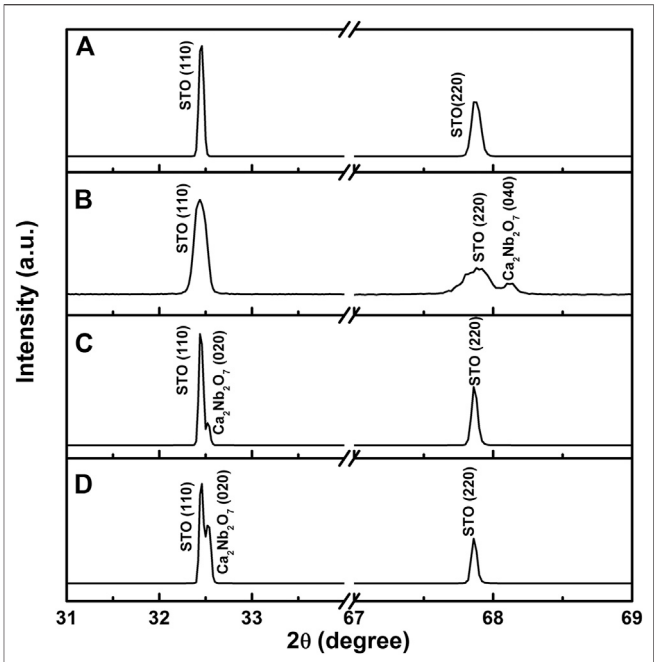

FIGURE 1 | XRD patterns of the STO substrate **(A)**, the as-deposited films using stoichiometric $Ca_2Nb_2O_7$ target **(B)**, nonstoichiometric $Ca_2Nb_2O_7$ target with 5% Ca deficiency **(C)** and Nb deficiency **(D)**.

MATERIALS AND METHODS

$CaCO_3$ and Nb_2O_5 were used as raw material and weighted according to the atomic ratio of Ca/Nb as 0.95/1, 1/1, and 1/0.95, respectively. Stoichiometric and nonstoichiometric $Ca_2Nb_2O_7$ ceramic targets with intrinsic cation vacancies were then obtained by the conventional solid state reaction. Ablation of the targets were achieved using a KrF excimer laser source (λ = 248 nm, pulse duration = 20 ns, energy of pulse = 200 mJ, frequency of pulse = 3 Hz). $SrTiO_3$ (110) substrate in the size of 5 mm × 5 mm was chosen due to its smaller lattice mismatch with the $Ca_2Nb_2O_7$ lattice. The deposition duration was 0.5 h, the distance between the target and substrate was 60 mm, the substrate temperature (T_S) was 650°C, and the oxygen pressure (P_O) was 1 mTorr for all depositions.

The crystal structure was examined by High Resolution X-ray Diffractometer (D8 discover, Bruker AXS GmbH, German) using Cu Kα radiation. The SEM and element mapping on the surface were performed by Scanning Electron Microscope (SU8010, Hitachi, Japan). X-ray photoelectron spectra were obtained by X-ray Photoelectron Spectrometer with monochromated Al Kα radiation (Escalab 250, Thermo Electron Corporation, United States). Magnetic properties were measured by Magnetic Property Measurement System (MPMS-5XL, Quantum design, United States) with magnetic field parallel to the surface of film. The film thickness was checked by Stylus Surface Profiler (Dektak 150, Veeco Metrology, France).

RESULTS AND DISCUSSION

Structural and Surface Characterizations

Figure 1 shows the XRD patterns of the STO substrate and the as-deposited films. Aside from the (110) and (220) diffraction peaks from the substrate (see **Figure 1A**), the only appearance of (040) diffraction peaks from orthorhombic $Ca_2Nb_2O_7$ (PDF#70-2006) in **Figure 1B** means that single phase of stoichiometric $Ca_2Nb_2O_7$ was obtained under the current deposition conditions without impurity phase. The $Ca_2Nb_2O_7$ (020) diffraction peaks in **Figures 1C,D** indicated that the single phase of $Ca_2Nb_2O_7$ was maintained using the targets with 5% Ca or Nb deficiency. To maintain the charge neutrality, the Ca or Nb vacancy would lead to the concomitant appearance of oxygen vacancy in the $Ca_2Nb_2O_7$ lattice, therefore, the nonstoichiometric $Ca_2Nb_2O_7$ films were denoted as $Ca_{1.9}Nb_2O_{7-\delta}$ and $Ca_2Nb_{1.9}O_{7-\delta}$, respectively. The film thickness of the three samples was close and approximated to be 100 nm. The SEM images for the $Ca_2Nb_2O_7$, $Ca_{1.9}Nb_2O_{7-\delta}$ and $Ca_2Nb_{1.9}O_{7-\delta}$ surfaces are displayed in the **Supplementary Figure S1**. Smooth and even surface could be observed for the $Ca_2Nb_2O_7$ film, while bumps and hollows were present on the surface of nonstoichiometric films, with the highest degree of roughness obtained by the $Ca_2Nb_{1.9}O_{7-\delta}$ surface. The corresponding element mapping images show that the elements Ca and Nb from the $Ca_2Nb_2O_7$ films were uniformly distributed on the surface of STO substrate for all samples, while the element O exhibited higher degree of density due to the simultaneous contribution from the film and substrate.

Figure 2 shows the core level XPS for the $Ca_2Nb_2O_7$, $Ca_{1.9}Nb_2O_{7-\delta}$ and $Ca_2Nb_{1.9}O_{7-\delta}$ films. All spectra were charge

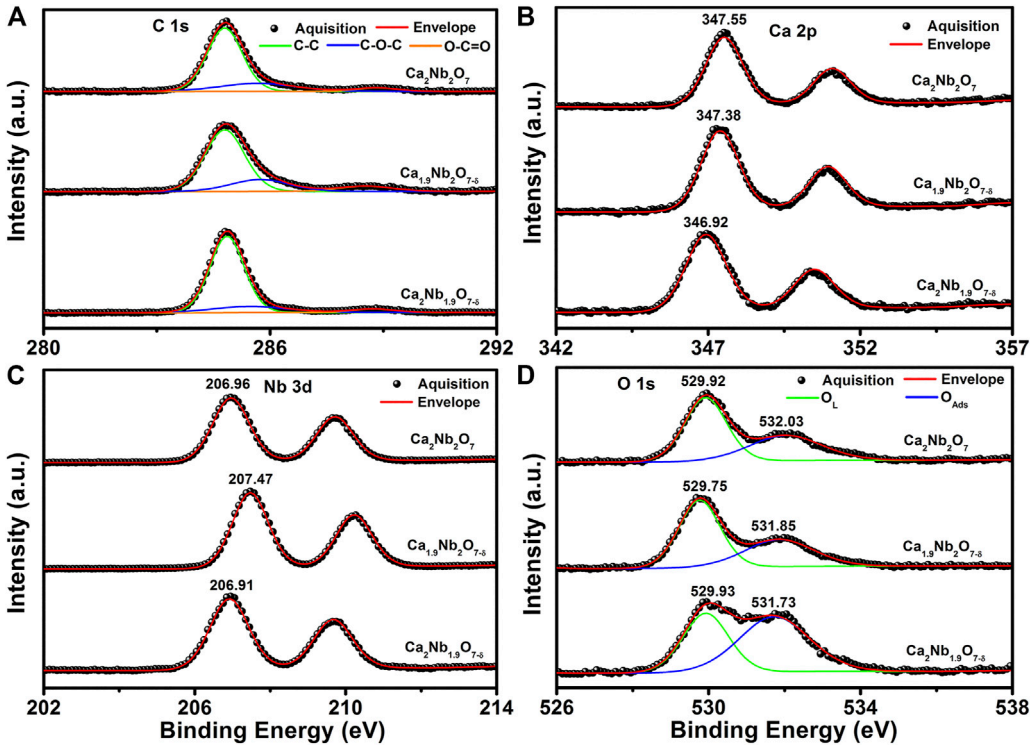

FIGURE 2 | C 1s **(A)**, Ca 2p **(B)**, Nb 3d **(C)** and O 1s **(D)** core level XPS for the $Ca_2Nb_2O_7$, $Ca_{1.9}Nb_2O_{7-\delta}$ and $Ca_2Nb_{1.9}O_{7-\delta}$ films.

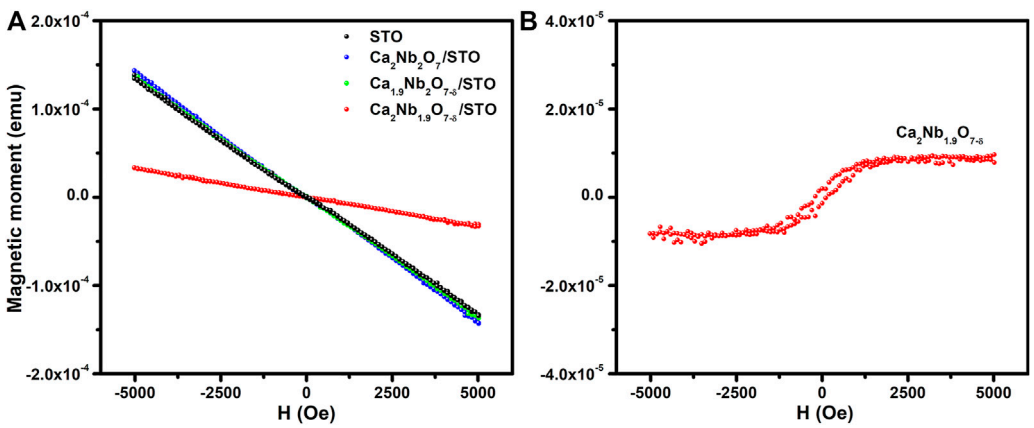

FIGURE 3 | Original MH curves for the STO substrate, $Ca_2Nb_2O_7$, $Ca_{1.9}Nb_2O_{7-\delta}$ and $Ca_2Nb_{1.9}O_{7-\delta}$ films on STO measured at room temperature **(A)**, and the MH curve for the $Ca_2Nb_{1.9}O_{7-\delta}$ film after subtraction of the diamagnetic signal from the substrate **(B)**.

corrected according to the C-C peak at the binding energy (BE) of 284.8 *e*V. In **Figure 2A**, the C-C and C-O-C peaks come from the adventitious carbon contamination, while the small amount of O-C=O peaks originate from the carbonate formed on the surface. From the Ca 2*p* and Nb 3*d* XPS in **Figures 2B,C**, Ca and Nb ions were in the valence states of +2 and +5 respectively. Since there is no other valence states present for Ca and Nb, the existence of Ca or Nb vacancy in the $Ca_2Nb_2O_7$ lattice can only induce oxygen vacancies to maintain the charge neutrality, hence the complex vacancy of V_{Ca+O} and V_{Nb+O} should be present in $Ca_{1.9}Nb_2O_{7-\delta}$ and $Ca_2Nb_{1.9}O_{7-\delta}$ films, respectively. With respect to the stoichiometric $Ca_2Nb_2O_7$ film, the $Ca_{1.9}Nb_2O_{7-\delta}$ film exhibited 0.17 *e*V lower BE for the Ca $2p_{3/2}$ peak but 0.51 *e*V higher BE for the Nb $3d_{5/2}$ peak, while the $Ca_2Nb_{1.9}O_{7-\delta}$ film exhibited 0.63 *e*V lower BE for the Ca $2p_{3/2}$ peak but 0.05 *e*V lower BE for the Nb $3d_{5/2}$ peaks. As for the O 1s XPS, lattice oxygen (O_L) and adsorbed oxygen (O_{ads}) were present in all samples, but the relative content of O_{ads} for the $Ca_2Nb_{1.9}O_{7-\delta}$ film

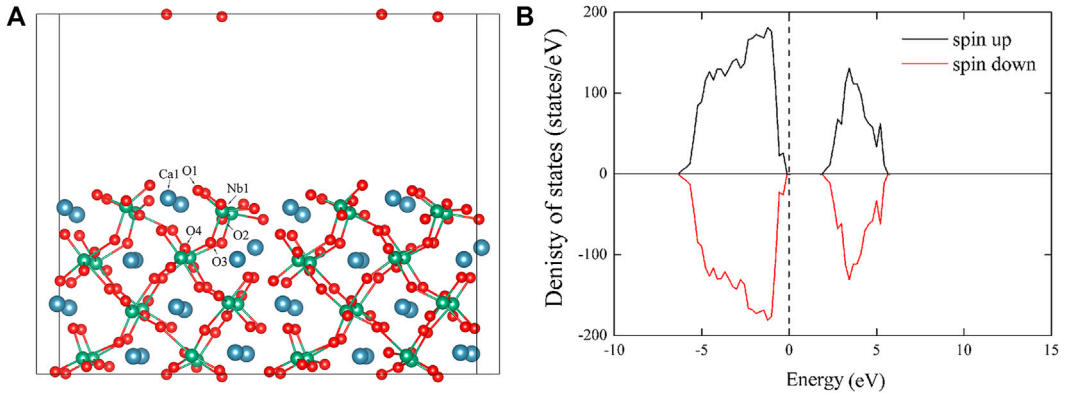

FIGURE 4 | Stable configuration of $Ca_2Nb_2O_7$ (010) surface with labeled Ca, Nb and O atoms to be removed for vacancy study **(A)**, and the total DOS of stoichiometric $Ca_2Nb_2O_7$ (010) surface **(B)**.

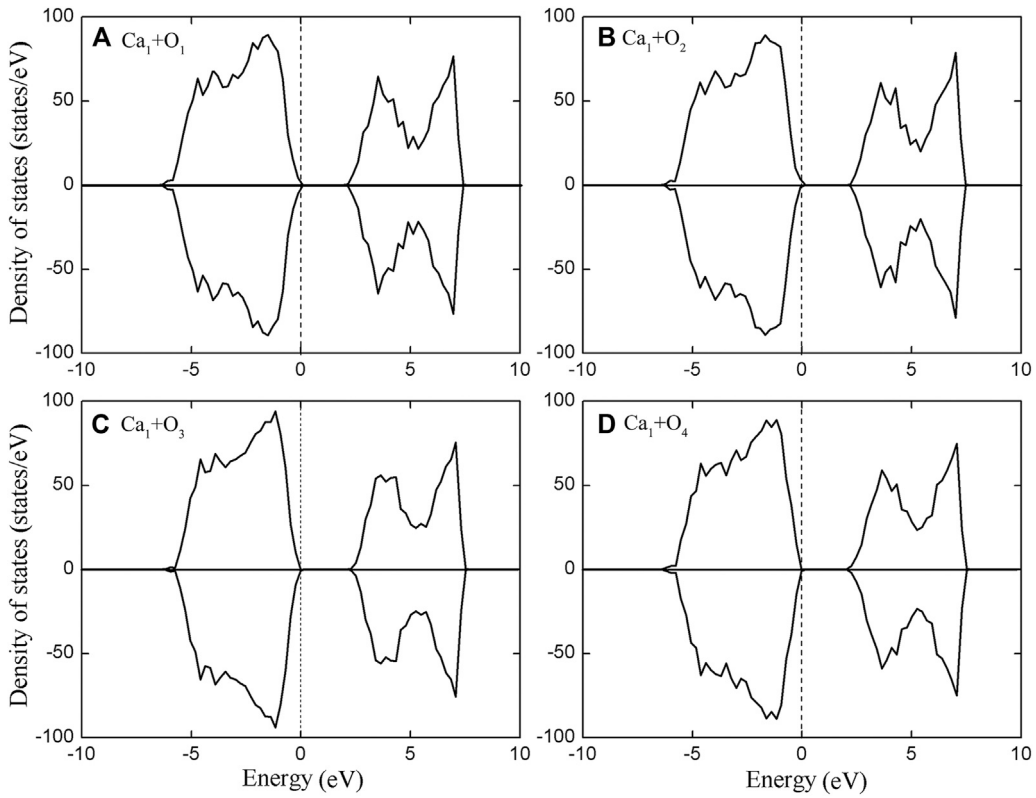

FIGURE 5 | DOSs of $Ca_2Nb_2O_7$ (010) surface with the complex vacancy of VCa+O in the distributions of Ca_1+O_1 **(A)**, Ca_1+O_2 **(B)**, Ca_1+O_3 **(C)**, and Ca_1+O_4 **(D)**.

was 58.8% which was much higher the 40.53 and 40.01% for the $Ca_2Nb_2O_7$ and $Ca_{1.9}Nb_2O_{7-\delta}$ films, respectively.

Magnetic Measurement

Figure 3 displays the MH curves for the STO substrate, $Ca_2Nb_2O_7$, $Ca_{1.9}Nb_2O_{7-\delta}$ and $Ca_2Nb_{1.9}O_{7-\delta}$ films on STO measured at room temperature. Compared with the diamagnetic behavior of the STO substrate, the stronger diamagnetic signals in the $Ca_2Nb_2O_7$ and $Ca_{1.9}Nb_2O_{7-\delta}$ films on STO suggest the presence of diamagnetism in the obtained films. However, the $Ca_2Nb_{1.9}O_{7-\delta}$ film on STO showed much weaker diamagnetic signal. As shown in **Figure 3B**, MH hysteresis loop was observed for the $Ca_2Nb_{1.9}O_{7-\delta}$ film after subtraction of the diamagnetic signal from the substrate, meaning that the $Ca_2Nb_{1.9}O_{7-\delta}$ film exhibited weak ferromagnetic behavior. Given the film thickness of 100 nm, the saturated magnetic moment of 9×10^{-6} emu corresponds to the magnetization of 3.6 emu/g for the $Ca_2Nb_{1.9}O_{7-\delta}$ film.

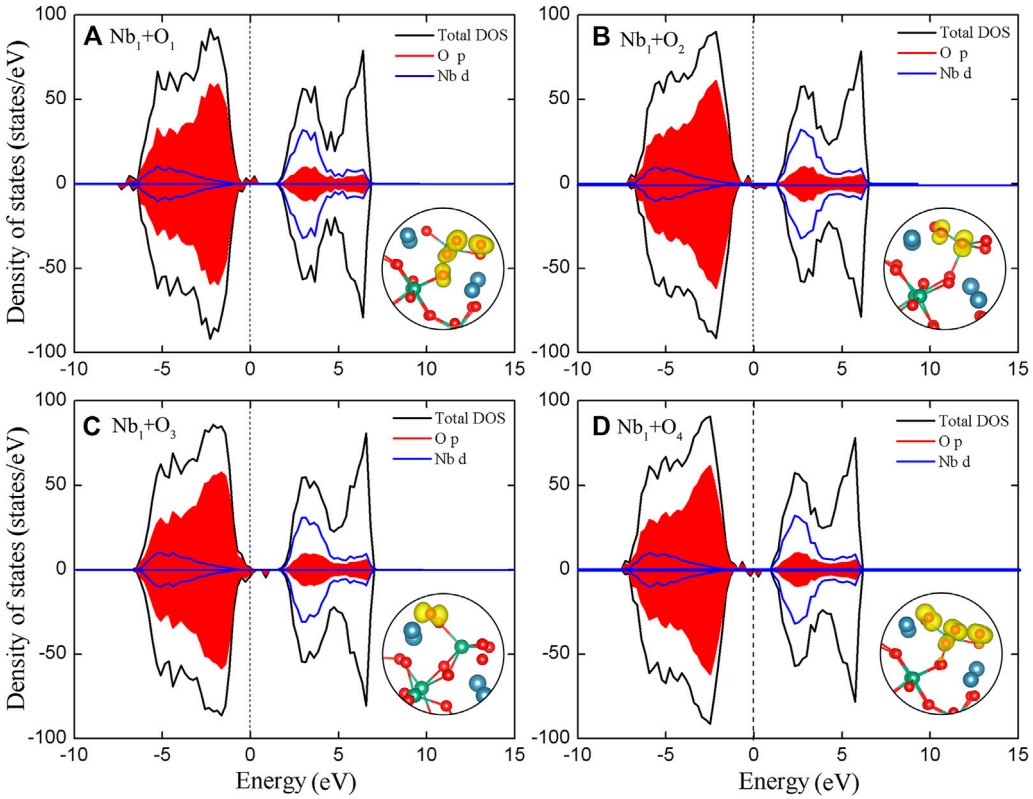

FIGURE 6 | Total and partial DOSs of $Ca_2Nb_2O_7$ (010) surface with the complex vacancy of VNb+O in the distributions of Nb_1+O_1 **(A)**, Nb_1+O_2 **(B)**, Nb_1+O_3 **(C)**, and Nb_1+O_4 **(D)**. The insets show the corresponding three-dimensional iso-surfaces of magnetization density.

Theoretical Calculation

In order to explore the origin of FM in the $Ca_2Nb_{1.9}O_{7-\delta}$ film, the density functional theory (DFT) calculations were performed using the plane-wave pseudopotential method in the Vienna Ab initio Simulation Package (VASP) (Kresse and Hafner, 1993a; Kresse and Joubert, 1999). The Projector Augmented Wave (PAW) (Kresse and Hafner, 1993b; Blöchl, 1994) potentials were employed, and General Gradient Approximate (GGA) was used to describe the exchange correlation energy. According to the XRD result, an orthorhombic $Ca_2Nb_2O_7$ $1 \times 2 \times 1$ supercell containing 176 atoms was first relaxed to get the most stable structure (see **Supplementary Figure S2A**) until the total energy in the optimized structure was converged to 1.0×10^{-4} *e*V/atom and the Hellman-Feynman force was smaller than 0.01 *e*V/Å. Then four different (010) planes were cleaved along the *b* axis, and a 10Å vacuum layer which was thick enough to isolate the atom layers was added above the supercell for further optimization. Among the four (010) surfaces, the configuration in the **Supplementary Figure S2B** showed the lowest energy, on which further calculations were performed.

The stable configuration of $Ca_2Nb_2O_7$ (010) surface with labeled Ca, Nb, and O atoms to be removed for vacancy study is displayed in **Figure 4A**, among which O1 is connected only to one Nb atom, O2 is coordinated between two neighbored Nb atoms, O3 connects one Nb atom in the outermost layer with another Nb atom in the second layer, while O4 denote the one between two Nb atoms in the second layer. Stoichiometric $Ca_2Nb_2O_7$ (010) surface was firstly studied and the total DOS was showed in **Figure 4B**. No spin polarization could be observed around the Fermi level, meaning that the stoichiometric $Ca_2Nb_2O_7$ (010) surface is nonmagnetic.

The complex vacancy of V_{Ca+O} in four different distributions, i.e., Ca1+O1, Ca1+O2, Ca1+O3, and Ca1+O4, was then studied. The relative stability (ΔE) of the $Ca_2Nb_2O_7$ (010) surface with these four types of complex vacancy was 3.51, 4.18, 0, and 2.21 *e*V respectively, meaning that the system with V_{Ca1+O3} was most stable. However, no spin polarization could be observed in the DOSs around the Fermi level in **Figure 5**, indicating that the complex vacancy of V_{Ca+O} cannot induce magnetism in the $Ca_2Nb_2O_7$ (010) surface. On the other side, the complex vacancy of V_{Nb+O} in four different distributions all induced spin polarization around the Fermi level and impurity bands in the forbidden gap (see **Figure 6**), which were contributed mainly by the O 2*p* electrons. The three-dimensional iso-surfaces of magnetization density in the inset of **Figure 6** show that the complex vacancies of V_{Nb+O} mainly induced spin polarization on the residual O atoms around the Nb vacancies. The total net magnetic moment (M_{tot}) of the system with V_{Nb1+O1}, V_{Nb1+O2}, V_{Nb1+O3}, and V_{Nb1+O4} was 1.0, 0.99, 0.96, and 1.0 μ_B, respectively. Among which, the system with V_{Nb1+O4} was the most stable one with the lowest energy, and the ΔE of the system with V_{Nb1+O1}, V_{Nb1+O2} and V_{Nb1+O3} was 1.04, 27.46, and 27.90 *e*V,

respectively. More importantly, FM coupling was energetically more favorable than AFM coupling in the cases of V_{Nb1+O1} and V_{Nb1+O4}, with the relative energy between FM and AFM as 7 and 45 m*e*V, respectively.

CONCLUSION

Nonstoichiometric $Ca_2Nb_2O_7$ single phase films with the complex vacancy of V_{Ca+O} or V_{Nb+O} were deposited on STO (110) substrate under appropriate deposition conditions using nonstoichiometric ceramic targets. The V_{Ca+O} cannot induce magnetism in the diamagnetic stoichiometric $Ca_2Nb_2O_7$ (020) single phase film, while V_{Nb+O} can induce spin polarization on the residual O atoms around the Nb vacancies, and make the $Ca_2Nb_2O_7$ film exhibit FM behavior at RT. Our work demonstrated experimentally and theoretically that the introduction of intrinsic complex vacancy during deposition should be a feasible way to induce ferromagnetism in the ferroelectric $Ca_2Nb_2O_7$ film, and this method might be applicable to other $A_2Nb_2O_7$-type niobate ferroelectric films as well.

DATA AVAILABILITY STATEMENT

The original contributions presented in the study are included in the article/**Supplementary Material**, further inquiries can be directed to the corresponding author.

AUTHOR CONTRIBUTIONS

EC contributed to conception and design of the study. LW, YZ and ZN contributed to the acquisition, analysis and interpretation of data. All authors contributed to manuscript revision, read, and approved the submitted version.

FUNDING

This work was supported by National Natural Science Foundation of China (11404236, 11604236, and 11974258), Natural Science Foundation of Shanxi Province (201901D111117 and 201901D111126).

ACKNOWLEDGMENTS

Part of this study has been performed using facilities at IBS Center for Correlated Electron Systems, Seoul National University.

SUPPLEMENTARY MATERIAL

The Supplementary Material for this article can be found online at: https://www.frontiersin.org/articles/10.3389/fmats.2021.736011/full#supplementary-material

REFERENCES

Blöchl, P. E. (1994). Projector Augmented-Wave Method. *Phys. Rev. B* 50, 17953–17979. doi:10.1103/physrevb.50.17953

Cao, D., Cai, M.-Q., Hu, W.-Y., Yu, P., and Huang, H.-T. (2011). Vacancy-induced Magnetism in BaTiO3(001) Thin Films Based on Density Functional Theory. *Phys. Chem. Chem. Phys.* 13, 4738–4745. doi:10.1039/c0cp02424d

Cao, D., Cai, M. Q., Zheng, Y., and Hu, W. Y. (2009). First-principles Study for Vacancy-Induced Magnetism in Nonmagnetic Ferroelectric BaTiO3. *Phys. Chem. Chem. Phys.* 11, 10934–10938. doi:10.1039/b908058a

Cao, E., Hu, J., Qin, H., Ji, F., Zhao, M., and Jiang, M. (2011). Room Temperature Ferromagnetism and Magnetoelectric Coupling in (K0.5Na0.5)NbO3 PLD Nanocrystalline Films. *J. Alloys Comp.* 509, 2914–2918. doi:10.1016/j.jallcom.2010.11.155

Cao, E., Zhang, Y., Ju, L., Sun, L., Qin, H., and Hu, J. (2012). The Investigation of Room Temperature Ferromagnetism in (100) Oriented BaNb2O6 PLD Films on LaAlO3 (100) Substrate. *Appl. Surf. Sci.* 258, 3795–3799. doi:10.1016/j.apsusc.2011.12.031

Cao, E., Zhang, Y., Qin, H., Zhang, L., and Hu, J. (2013). Vacancy-induced Magnetism in Ferroelectric LiNbO3 and LiTaO3. *Physica. B. Condens. Matter* 410, 68–73. doi:10.1016/j.physb.2012.10.030

Chand Verma, K., Kaur, J., Negi, N. S., and Kotnala, R. K. (2014). Multiferroic and Magnetoelectric Properties of Nanostructured BaFe0.01Ti0.99O3 Thin Films Obtained under Polyethylene Glycol Conditions. *Solid State. Commun.* 178, 11–15. doi:10.1016/j.ssc.2013.10.020

Chun, S. H., Chai, Y. S., Jeon, B. G., Kim, H. J., Oh, Y. S., Kim, I., et al. (2012). Electric Field Control of Nonvolatile Four-State Magnetization at Room Temperature. *Phys. Rev. Lett.* 108, 177201. doi:10.1103/physrevlett.108.177201

Díaz-Moreno, C. A., Farías-Mancilla, R., Matutes-Aquino, J. A., Elizalde-Galindo, J., Espinosa-Magaña, F., González-Hernández, J., et al. (2014). Magnetic Behavior in LiNbO3 Nanocrystallites Caused by Oxygen Vacancies. *J. Magnetism Magn. Mater.* 356, 82–86. doi:10.1016/j.jmmm.2013.12.029

Fiebig, M. (2005). Revival of the Magnetoelectric Effect. *J. Phys. D. Appl. Phys.* 38, R123–R152. doi:10.1088/0022-3727/38/8/r01

Hill, N. A. (2000). Why Are There So Few Magnetic Ferroelectrics? *J. Phys. Chem. B* 104, 6694–6709. doi:10.1021/jp000114x

Kresse, G., and Hafner, J. (1993). Ab Initiomolecular Dynamics for Liquid Metals. *Phys. Rev. B* 47, 558–561. doi:10.1103/physrevb.47.558

Kresse, G., and Hafner, J. (1993). Ab Initiomolecular Dynamics for Open-Shell Transition Metals. *Phys. Rev. B* 48, 13115–13118. doi:10.1103/physrevb.48.13115

Kresse, G., and Joubert, D. (1999). From Ultrasoft Pseudopotentials to the Projector Augmented-Wave Method. *Phys. Rev. B* 59, 1758–1775. doi:10.1103/physrevb.59.1758

Li, Y. D., Wang, C. C., Cheng, R. L., Lu, Q. L., Huang, S. G., and Liu, C. S. (2014). Vacancy-driven Magnetism in Nonmagnetic Double Perovskite Sr2AlNbO6: A First-Principles Study. *J. Alloys Comp.* 598, 1–5. doi:10.1016/j.jallcom.2014.01.176

Lichtenberg, F., Herrnberger, A., Wiedenmann, K., and Mannhart, J. (2001). Synthesis of Perovskite-Related Layered AnBnO3n+2 = ABOX Type Niobates and Titanates and Study of Their Structural, Electric and Magnetic Properties. *Prog. Solid State. Chem.* 29, 1–70. doi:10.1016/s0079-6786(01)00002-4

Liu, L., Shi, D., Fan, L., Chen, J., Li, G., Fang, L., et al. (2015). Ferroic Properties of Fe-Doped and Cu-Doped K0.45Na0.49Li0.06NbO3 Ceramics. *J. Mater. Sci. Mater. Electron.* 26, 6592–6598. doi:10.1007/s10854-015-3257-z

Mangalam, R. V. K., Ray, N., Waghmare, U. V., Sundaresan, A., and Rao, C. N. R. (2009). Multiferroic Properties of Nanocrystalline BaTiO3. *Solid State. Commun.* 149, 1–5. doi:10.1016/j.ssc.2008.10.023

Ramana, E. V., Yang, S. M., Jung, R., Jung, M. H., Lee, B. W., and Jung, C. U. (2013). Ferroelectric and Magnetic Properties of Fe-Doped $BaTiO_3$ Thin Films Grown by the Pulsed Laser Deposition. *J. Appl. Phys.* 113, 187219. doi:10.1063/1.4801965

Shimada, T., Uratani, Y., and Kitamura, T. (2012). Vacancy-driven Ferromagnetism in Ferroelectric PbTiO3. *Appl. Phys. Lett.* 100, 162901. doi:10.1063/1.4704362

Song, Y.-J., Zhang, Q.-H., Shen, X., Ni, X.-D., Yao, Y., and Yu, R.-C. (2014). Room-Temperature Magnetism Realized by Doping Fe into Ferroelectric $LiTaO_3$. *Chin. Phys. Lett.* 31, 017501. doi:10.1088/0256-307x/31/1/017501

Topkaya, R., Boyraz, C., and Ekmekçi, M. K. (2017). Structural and Magnetic Properties of Eu^{3+}-Doped $CdNb_2O_6$ Powders. *J. Low Temp. Phys.* 190, 244–255. doi:10.1007/s10909-017-1835-6

Yang, F., Jin, K., Lu, H., He, M., Wang, C., Wen, J., et al. (2010). Oxygen Vacancy Induced Magnetism in BaTiO3−δ and Nb:BaTiO3−δ Thin Films. *Sci. China Phys. Mech. Astron.* 53, 852–855. doi:10.1007/s11433-010-0187-x

Conflict of Interest: The authors declare that the research was conducted in the absence of any commercial or financial relationships that could be construed as a potential conflict of interest.

The handling Editor declared a past co-authorship with one of the authors NZ.

Publisher's Note: All claims expressed in this article are solely those of the authors and do not necessarily represent those of their affiliated organizations, or those of the publisher, the editors and the reviewers. Any product that may be evaluated in this article, or claim that may be made by its manufacturer, is not guaranteed or endorsed by the publisher.

frontiers in Materials

ORIGINAL RESEARCH
published: 25 August 2021
doi: 10.3389/fmats.2021.739449

Holographic Near-Eye 3D Display Method Based on Large-Size Hologram

Su-Juan Liu[1,2], *Ning-Tao Ma*[1], *Ping-Ping Li*[1] *and Di Wang*[3]*

[1]School of Physics and Electronic Engineering, Zhengzhou University of Light Industry, Zhengzhou, China, [2]Henan Key Laboratory of Magnetoelectronic Information Functional Materials, Zhengzhou University of Light Industry, Zhengzhou, China, [3]School of Instrumentation and Optoelectronic Engineering, Beihang University, Beijing, China

In this paper, we propose a holographic near-eye 3D display method based on large-size computer-generated hologram (CGH). The reconstructed image with a large viewing angle is obtained by using a time multiplexing and spatial tiling system. The large-size CGHs are generated and they record the information of the 3D object from different angles. The CGHs are reproduced at different moments. For a certain reconstructed moment, three spatial light modulators (SLMs) spatially spliced into a linear structure are used to load a single CGH. The diffraction boundary angle of the reconstructed light forming each image point is equal to the maximum diffraction angle of the SLM, so the viewing angle of the image generated by the CGH is enlarged. For different CGHs, the incident angle of reconstructed light is changed. Through time multiplexing, the reconstructed images of the CGHs are combined into a reconstructed image whose viewing angle is further enlarged. Due to the large viewing angle of the reconstructed image, the proposed method has unique advantages in near-eye display. The feasibility of the proposed method is proved by experimental results.

Keywords: holographic display, viewing angle, time multiplexing, spatial tiling, 3D display

OPEN ACCESS

Edited by:
Zhongquan Nie,
Taiyuan University of Technology, China

Reviewed by:
Luo Chenggao,
National University of Defense Technology, China
Zi Wang,
Hefei University of Technology, China

***Correspondence:**
Di Wang
diwang18@buaa.edu.cn

Specialty section:
This article was submitted to Quantum Materials, a section of the journal Frontiers in Materials

Received: *11 July 2021*
Accepted: *10 August 2021*
Published: *25 August 2021*

Citation:
Liu S-J, Ma N-T, Li P-P and Wang D (2021) Holographic Near-Eye 3D Display Method Based on Large-Size Hologram. Front. Mater. 8:739449. doi: 10.3389/fmats.2021.739449

INTRODUCTION

Holographic near-eye display technology is based on the user's observation of the real world, and can continuously provide virtual holographic image information for the user, to realize the function of real-time interaction between the real and the virtual environment (Azuma, 1997; Chen and Chu, 2015; Lee et al., 2019). It is widely used in many fields such as military, medical, education and entertainment (Choi et al., 2021; Wang et al., 2021). Recently, due to the realistic effect of the computer-generated holographic near-eye display, a series of researches on this technology have been implemented. However, this technology has some problems hindering its further development. Among them, the maximum diffraction angle of the reproduced light is only a few degrees (Senoh et al., 2011; Li et al., 2020; Liu et al., 2020; Wang et al., 2020). This is because the pixel size of currently available spatial light modulators (SLMs) is on the micron level, which is an order of magnitude larger than the light wavelength. Accordingly, the viewing angle of the holographic image is narrow and not suited for binocular observation. Therefore, in order to increase the practicality of the holographic display, some methods to improve this problem have been proposed. For example, the viewing angle is expanded through time multiplexing to combine the high-order reconstructed beams temporally (Mishina et al., 2002). In the equivalent-curved-SLM-array method, the viewing angle can be increased to 13.5° by superimposing different linear phase factors on one phase SLM

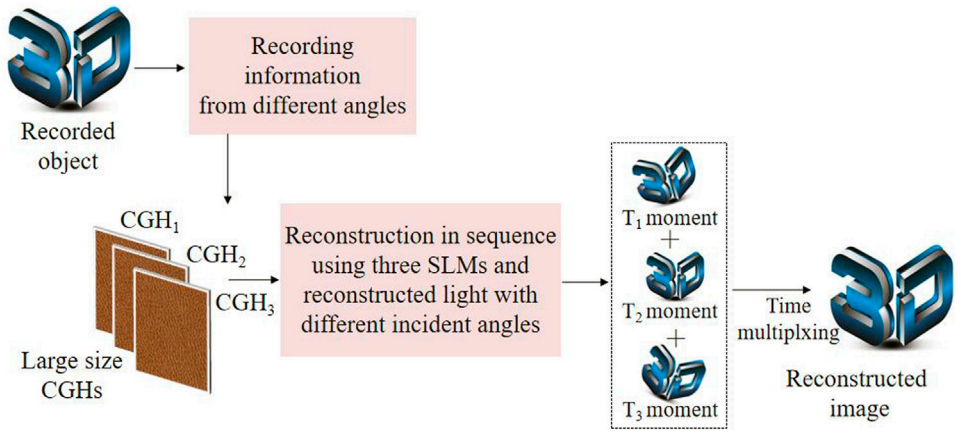

FIGURE 1 | Schematic diagram of the proposed method.

sequentially (Liu et al., 2013). In the resolution redistribution method, the horizontal resolution of the SLM is increased several times through a 4f imaging system (Takaki and Hayashi, 2008; Takaki and Tanemoto, 2010; Takaki and Nakamura, 2011). The multi-channel scanning method uses multiple projection systems and a planar scanner to obtain a large size and large viewing angle reconstruction (Takaki et al., 2015; Takaki and Nakaoka, 2016). The convex parabolic mirror method obtains a reconstructed image with a horizontal viewing angle of 180° (Sando et al., 2018). The reconstructed system of the above methods is relatively simple, and a single SLM is used to load the computer-generated hologram (CGH). However, in order to expand the viewing angle, they may put a higher demand on the refresh rate of the SLM, or reduce other performance of the reconstructed image. In addition, some methods of using multiple SLMs to expand the viewing angle of the image are proposed. In the curved-SLM-array method, some SLMs with a curved arrangement structure are used to increase the numerical aperture of the optical system, thereby expanding the viewing angle (Hahn et al., 2008; Yaras et al., 2011; Kozacki et al., 2012a; Zeng et al., 2017). Through the analysis of the Wigner distribution function, the viewing angle is increased using six SLMs (Kozacki et al., 2012b). The viewing angle of the reconstructed image can be increased to 12.8° by using a 4f concave mirror system and two SLMs (Zeng et al., 2017). These methods can obtain reconstructed images with large viewing angles, but the optical systems are relatively complex. Therefore, they are difficult to operate and high cost, which are not conducive to practical applications.

In this paper, we propose a method to enlarge the viewing angle of the holographic image. The information of different angles of the object is recorded as CGHs. The size of each CGH is increased. In the process of holographic reconstruction, three SLMs arranged in a linear structure are used to load the CGHs. After the spatial splicing effect of the SLMs and the time multiplexing of the reconstructed images in different directions, the viewer finally obtains a large viewing angle holographic reconstructed image. The method is simple and easy to operate, and can be applied to near-eye display technology.

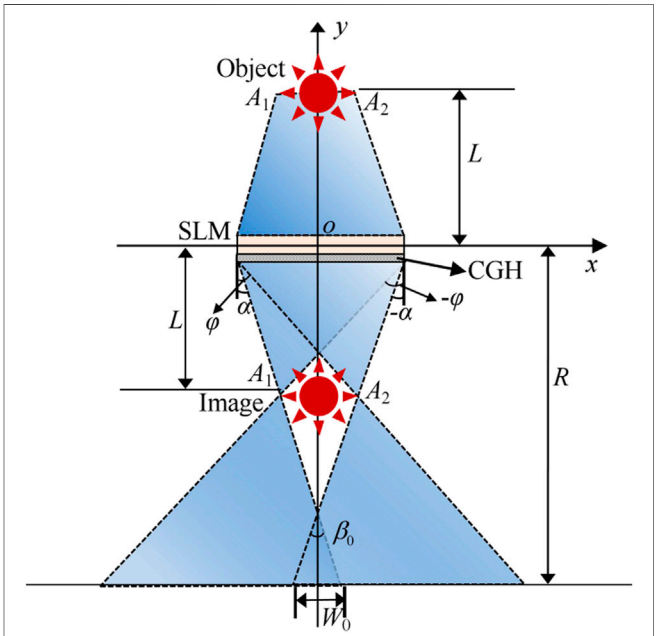

FIGURE 2 | Light distribution of the reconstructed image.

PRINCIPLE

The schematic diagram of the proposed method is shown in **Figure 1**. The viewing angle of the reconstructed image is enlarged based on the large-size CGHs. The CGHs record the information of the 3D object from different angles. In the holographic reconstruction, three SLMs in a linear configuration are used to load the CGHs. Moreover, it ensures that the incident angle of the reproduced light varies with the

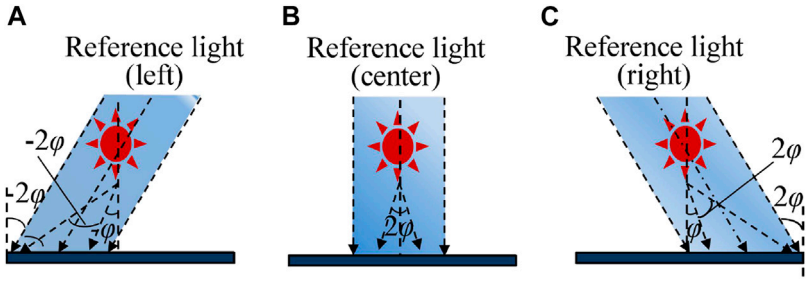

FIGURE 3 | Generation of the CGHs at different angles of the proposed method. **(A)** Reference light **(left)**. **(B)** Reference light **(center)**. **(C)** Reference light **(right)**.

CGH. Finally, the reconstructed image is obtained through time multiplexing. Next, we will introduce the theory of the proposed method in detail.

First of all, the information of three different angles of the object is recorded as a large-size CGH. We assume that the origin of the coordinate is at the center of the CGH. The size of the recorded object is D. The distance between the object and the CGH is L. The size of the SLM is H and its pixel size is p. For any object point $I(x_0, L)$, its information is recorded as an interferogram. The size of the interferogram in the traditional method is equal to the size of the SLM. The CGH is generated by superimposing all the interferograms. During reproduction, a single SLM is used to load the CGH. The light distribution of the reconstructed image can be seen in **Figure 2**. Based on the property of the field of view (FOV), the FOV is the overlapping area of the light distribution of the leftmost image point A_1 and the rightmost image point A_2, and the corresponding angle is the viewing angle. The light with the diffraction angle range of $[-\alpha, \varphi]$ reconstructs the image point A_1, and the light with the diffraction angle range of $[-\varphi, \alpha]$ reconstructs the image point A_2. According to the geometric relationship, α and φ can be calculated as follows:

$$\alpha = \arctan\left[\left(H/2 - D/2\right)/L\right], \tag{1}$$

$$\varphi = \arctan\left[\left(H/2 + D/2\right)/L\right], \tag{2}$$

where φ is the allowable maximum diffraction angle of the CGH. If the wavelength of the reconstructed light is denoted as λ, the diffraction angle φ is expressed as follows:

$$\varphi = \sin^{-1}\left(\lambda/2p\right). \tag{3}$$

It can be seen from **Figure 2** and **Eqs 1**, **2** that the diffraction boundary angle forming any image point cannot reach φ at the same time. Therefore, the viewing angle of the phenomenon is relatively small, which satisfies **Eq. 4**:

$$\beta_0 = 2\alpha \approx (H - D)/L. \tag{4}$$

The width of the FOV at the viewing distance R can be calculated according to **Eq. 5**:

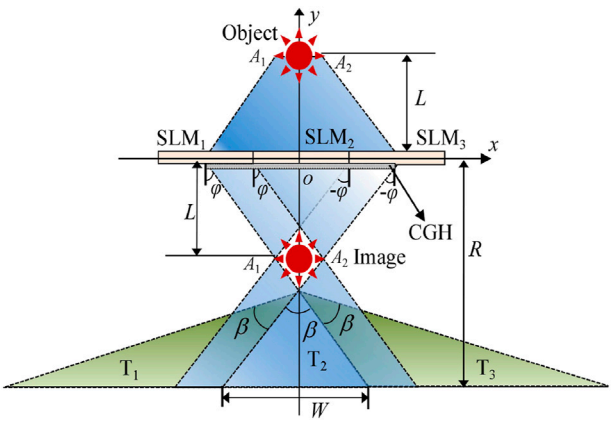

FIGURE 4 | Light distribution of the reconstructed image by the proposed method.

$$W_0 = \left[H(R - L) - DR\right]/L. \tag{5}$$

The three recording angles of the object are denoted as left, center, and right angles in the proposed method. In the process of CGHs generation with different angles, the incident angle of the reference light will also change accordingly, as shown in **Figure 3**. For the sake of simplicity, we take the center recording angle as an example to introduce. The size of the interferogram of any object point is increased. The horizontal coordinates of the image points A_1 and A_2 are denoted as x_1 and x_2 , respectively, which satisfy the following equations:

$$x_1 = x_0 + L\tan\varphi = x_0 + H/2 + D/2, \tag{6}$$

$$x_2 = x_0 - L\tan\varphi = x_0 - (H/2 + D/2). \tag{7}$$

The size of the interferogram H_1 satisfies **Eq. 8**:

$$H_1 = x_1 - x_2 = H + D. \tag{8}$$

Then, we add up all the interferograms to generate the CGH. The size of the CGH H_{CGH} is calculated according to **Eq. 9**:

$$H_{CGH} = H + 2D. \tag{9}$$

It can be seen from **Eq. 9** that the size of the CGH is increased, which is larger than that of a single SLM and less than the sum

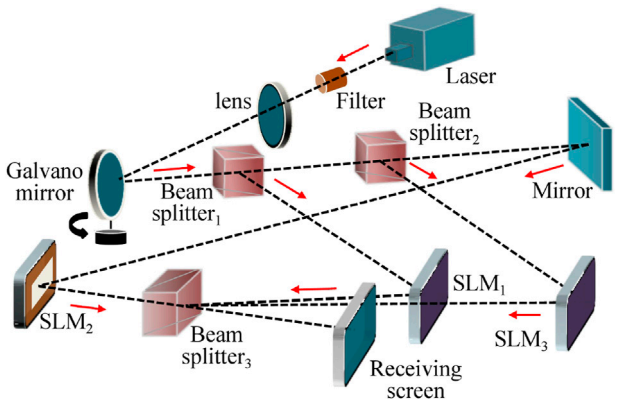

FIGURE 5 | Structure of the reconstructed system.

size of three SLMs. Therefore, a total of three large-size CGHs are generated from three different recording angles, denoted as the left CGH, the center CGH and the right CGH.

Next, the holographic reconstruction is implemented. In the optical system, three SLMs are arranged in a linear configuration. They are used to load the large-size CGHs. In order to accurately load the CGH onto the SLM, the zero padding is performed on both sides of each CGH. It ensures that the size of the CGH is equal to that of the three SLMs. The CGHs are loaded sequentially for reconstruction. Based on the principle of holographic technology, the direction of reconstructed light is consistent with that of reference light in the CGH. In **Figure 4**, the light distribution of the reconstructed image is shown. The generation and reproduction of the center CGH are shown in the blue area. According to **Eqs 6, 7** and the geometric relationship in the reconstructed system, the angle range of the diffraction light generated by any interferogram is $[-\varphi, \varphi]$. Therefore, the light distribution size of each image point is increased accordingly. At the viewing distance R, the viewing angle and the FOV of the image are calculated according to **Eqs 10**, **11**, respectively:

$$\beta = 2\varphi \approx (H + D)\Big/L, \tag{10}$$

$$W = [R(D + H) - L(H + 2D)]\Big/L. \tag{11}$$

Compared with **Eqs 4**, **5**, it shows that the viewing angle and the FOV of the proposed method are obviously enlarged.

In order to ensure the continuity of the FOV of the reconstructed image at different moments, the inclination angles of the reconstructed light of the left CGH and the right CGH are -2φ and 2φ, respectively. In the process of generating the left and right CGHs as shown in **Figure 3**, the inclination angles of the reference light are also -2φ and 2φ respectively. In **Figure 4**, the viewing zones generated by the CGHs reconstructed at three different moments are denoted as T_1, T_2, and T_3. After time multiplexing, the viewer can obtain a reconstructed image with continuously distributed viewing angle, where the viewing angle ψ satisfies:

$$\psi = 3\beta = 6\varphi \approx 3(H + D)\Big/L. \tag{12}$$

Therefore, we expands the viewing angle of the reconstructed image in one direction by generating the large-size CGH and using the spatial multiplexing of three SLMs. In addition, through time multiplexing, the reconstructed images in three directions are combined into the image with continuous viewing angle, and finally the viewing angle is further expanded to three times.

EXPERIMENTS AND RESULTS

The feasibility of the proposed method is proved by conducting a series of experiments. The optical reconstructed system is shown in **Figure 5**. The green laser is used as the reconstructed light, and its wavelength is 532 nm. A collimating system consisting of the laser, filter and lens generates the uniform plane wave. The galvano mirror generates multiple reproduced lights with different incident angles by changing the tilt angle of the mirror. Beam splitter$_1$ divides the reconstructed light into two beams. Among them, the reflected light illuminates SLM$_1$ as the reconstructed light, and the transmitted light continues to propagate forward through beam splitter$_2$ and is also divided into two beams. They are used as the reconstructed light of SLM$_2$ and SLM$_3$ respectively. The three diffracted beams modulated by the SLMs are seamlessly spliced after passing through beam splitter$_3$. Finally, the reconstructed image is obtained on the receiving screen. Three reflective phase-only SLMs provided by Xi'an Institute of Optics and Precision Mechanics have the same parameters. The resolution and size of the SLM are 1,920 × 1,080 and 6.4 μm, respectively. The frame rate is 60 Hz. The phase modulation range is $[0, 2\pi]$. In the horizontal direction, the size of the object D and the active area size of the SLM H are 6 and 12.23 mm. Based on **Eq. 3**, the maximum diffraction angle of the SLM is 2.4°. We record the object's information into the CGH from the left, center, and right angles respectively. The recorded distance L is set to 220 mm. In order to achieve the continuity of the viewing angle of the reconstructed image, the corresponding incident angles of the reference light are −4.8°, 0° and 4.8°. In each recording direction, according to **Eqs 6**, **9**, the size of the interferogram and the CGH are 18.23 and 24.23 mm, respectively.

First, we study the reconstructed image of the CGH in one direction. Taking the reproduction of the right CGH as an example, In order to load the CGH accurately, the zero padding and division operations are carried out. In the first step, we perform zero padding operation with the same resolution on the left and right sides of the CGH to make its size equal to the total size of three SLMs. In the second step, the CGH is divided into three parts in the horizontal direction, and the resolution of each part is 1,920 × 1,080. In the third step, according to the arrangement sequence, the three parts of the CGH are respectively loaded onto the SLM for reconstruction. The galvano mirror in the reconstructed system is kept stationary, ensuring that the inclination angle of the mirror is 2.4°, and the incident angle of the reconstructed light is 4.8°. The reconstructed images obtained from two different viewpoints can be seen in

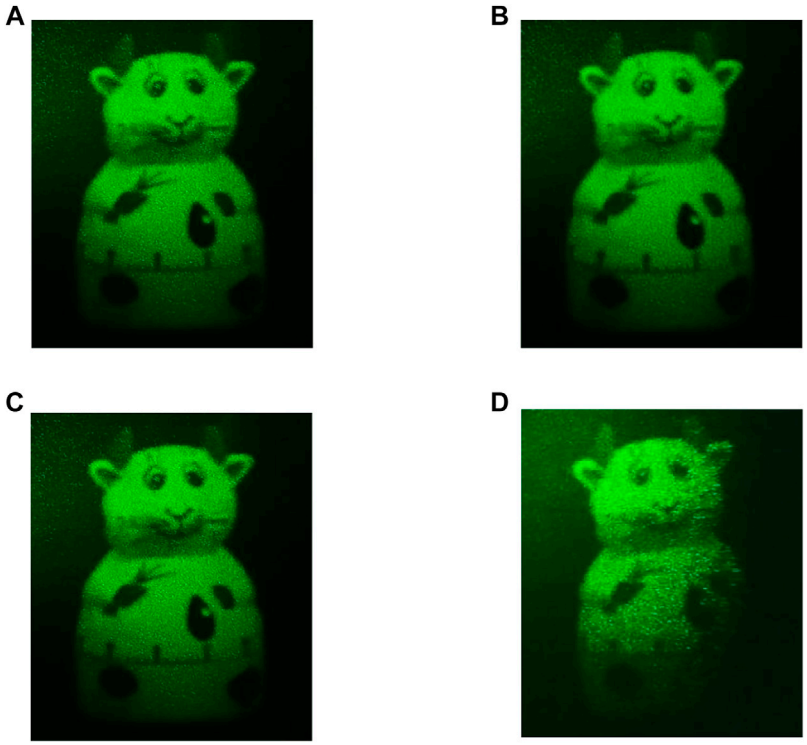

FIGURE 6 | Optical reconstructed images obtained from **(A–B)** the left and right viewpoint of the proposed method, respectively, **(C–D)** the left and right viewpoint of the traditional method, respectively.

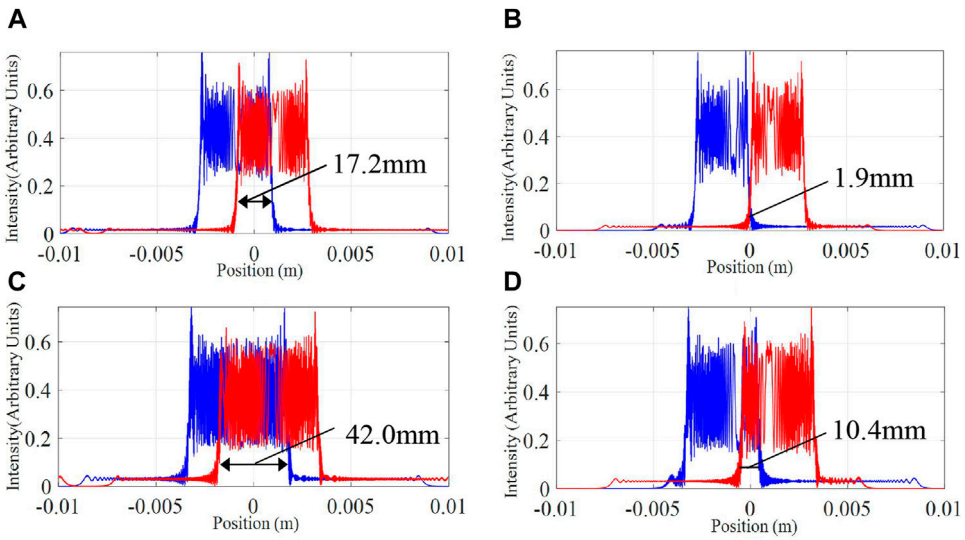

FIGURE 7 | Light intensity distribution of the leftmost and rightmost image points of **(A)** the proposed method at R = 500 mm, **(B)** the traditional method at R = 500 mm, **(C)** the proposed method at R = 800 mm and **(D)** the traditional method at R = 800 mm.

Figures 6A,B, respectively. The viewing angle interval between the left and right viewpoints is about 3°. Moreover, in order to conduct comparative analysis of the experiment, the traditional method using a single SLM is implemented. The reconstructed images obtained from the left and right viewpoints are shown in **Figures 6C,D**, respectively. The experimental results show that the complete images with parallax can be obtained at different viewpoints in the proposed method. However, in the traditional method, only a part of the reconstructed image is obtained from the right viewpoint. These results indicate that the viewing angle

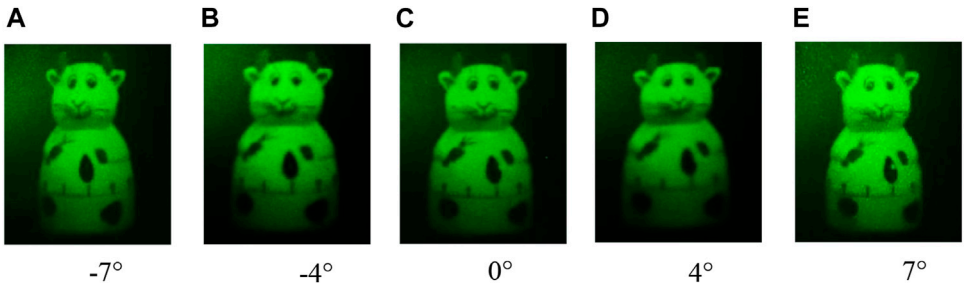

FIGURE 8 | Reconstructed images are obtained from **(A)** left −7° direction, **(B)** left −4° direction, **(C)** center 0° direction, **(D)** right 4° direction and **(E)** right 7° direction.

of the reconstructed image in one direction is expanded through the generation of the large-size CGH and the spatial splicing of the SLMs.

Furthermore, we implement simulation experiments with MATLAB software to record the light distribution of the image points, so as to analyze the FOV of the reconstructed image in one direction, as shown in **Figure 7**. The light distribution of the leftmost and rightmost image points are represented by the blue and red lines, respectively. In the proposed method, the width of the FOV is 17.2 mm at the viewing distance of R = 500 mm(**Figure 7A**). The width of the FOV is 1.9 mm in the traditional method (**Figure 7B**). In contrast, the FOV of the proposed method is enlarged by 8 times. At the viewing distance R= 800 mm, the light distribution are shown in **Figure 7C** and **Figure 7D**. Using the proposed method, the width of the FOV is increased by 3 times. The experimental results verify the theoretical values within the allowable error range (**Eqs 5**, **11**). It proves that the proposed method significantly expands the FOV, and as the viewing distance increases, the increase rate of the FOV slows down.

Then, the left, center and right CGHs are reconstructed in time sequence. The incident angle of the reconstructed light is changed by the reflection of the galvano mirror. In the experiment, when the tilt angle of the galvano mirror is set to −2.4°, 0° and 2.4° at different moments, three reconstructed lights with different incident angles are generated correspondingly, which are −4.8°, 0° and 4.8°, respectively. The changing frequency of the CGH and the galvano mirror is kept synchronized to ensure that the incident angle of the reconstructed light is the same as the angle of the reference light in the CGH. The images in the left, middle and right directions are reconstructed at different moments. Within the persistence effect of the human eye, the reconstructed image with a continuous viewing angle is obtained. Viewed from different angles, the reconstructed images can be seen in **Figure 8**. The complete images from the directions of −7°, −4°, 0°, 4°, and 7° are obtained. Therefore, through time multiplexing of the images in different directions, the reconstructed image with a continuous viewing angle of about 14° is obtained. Compared with the reproduced image in one direction, the viewing angle has been enlarged three times.

The proposed method obtains the reconstructed image with a large viewing angle through a simple optical system, so it can be applied to near-eye display technology. The following experiment is implemented for verification. In the holographic near-eye display system, a beam splitter is used to replace the receiving screen. The reconstructed image is reflected when it passes through the beam splitter. In addition, a little toy is placed aside as a real reference. The distance between the toy and the beam splitter is 500 mm. The beam splitter realizes the fusion of the real object and holographic image. The reconstructed images captured by the camera from different angles are shown in **Figure 9**. In the left direction (**Figure 9A**), the left surface of the toy and the reconstructed image has a larger size. In the center viewpoint (**Figure 9B**), the left and right surfaces have a similar size. In the right viewpoint (**Figure 9C**), the right surface becomes has a larger size. These results indicate the holographic near-eye display realize a good reproduction effect due to the viewing angle enlargement by using the proposed method.

FIGURE 9 | Reconstructed images in the holographic near-eye display obtained from **(A)** left −7° direction, **(B)** center 0° direction and **(C)** right 7° direction.

The above experiments confirm that the advantages of the proposed method are outstanding. Based on the generation of the large-size CGHs, combined with the use of time multiplexing and spatial tiling system, the viewing angle of the reconstructed image in the holographic near-eye display has been significantly increased. The optical system of the proposed method is simple and easy to operate, so it has practical application value. However, the proposed method still has some unsolved issues. For example, there is speckle noise caused by laser coherence in the reconstructed image. The denoising algorithms will be studied to improve the image quality without increasing the system's complexity. In addition, the proposed method only generates reconstructed images with monochrome information. We will use time multiplexing method to obtain the color image. In addition, we record the information of the object in three different directions. The viewing angle of the reconstructed image is increased to about 14°, which is not enough for the free viewing of multiple people. In the proposed method, the viewing angle increases as the number of CGHs increases. So, in the following work, we can increase the recording direction of the object to ensure that the number of generated CGHs is less than the refresh frequency of the SLM. During the reproduction process, within the persistence effect of human eyes, the reconstructed images of different CGHs are combined into one image, and the viewing angle of the image is further increased.

CONCLUSION

In this paper, we propose a holographic near-eye display method in which the viewing angle is enlarged. The viewing angle of the reconstructed image in one direction is expanded through the generation of the large-size CGH and the spatial splicing of the SLMs. At the viewing distance of $R = 500$ mm, the FOV is increased by 8 times compared with the traditional method. Then, using time multiplexing of the images in different directions, the reconstructed image with continuous viewing angle of about 14° is obtained. The optical system of the proposed method is relatively simple and easy to operate. Experimental results verify the feasibility of the proposed method.

DATA AVAILABILITY STATEMENT

The original contributions presented in the study are included in the article/supplementary material, further inquiries can be directed to the corresponding author.

AUTHOR CONTRIBUTIONS

S-JL conceived the initial idea and performed the experiments. N-TM, P-PL analyzed the data. DW discussed the results and supervised the project. All authors have read and approved the final manuscript.

FUNDING

National Science Foundation of China (NSFC) (61905221); Science and technology research project of Henan Province (212102310902).

REFERENCES

Azuma, R. T. (1997). A Survey of Augmented Reality. *Presence: Teleoperators & Virtual Environments* 6 (4), 355–385. doi:10.1162/pres.1997.6.4.355

Chen, J.-S., and Chu, D. P. (2015). Improved Layer-Based Method for Rapid Hologram Generation and Real-Time Interactive Holographic Display Applications. *Opt. Express* 23 (14), 18143–18155. doi:10.1364/oe.23.018143

Choi, S., Kim, J., Peng, Y., and Wetzstein, G. (2021). Optimizing Image Quality for Holographic Near-Eye Displays with Michelson Holography. *Optica* 8 (2), 143–146. doi:10.1364/optica.410622

Hahn, J., Kim, H., Lim, Y., Park, G., and Lee, B. (2008). Wide Viewing Angle Dynamic Holographic Stereogram with a Curved Array of Spatial Light Modulators. *Opt. Express* 16 (16), 12372–12386. doi:10.1364/oe.16.012372

Kozacki, T., Kujawinska, M., Finke, G., Zaperty, W., and Hennelly, B. (2012). Holographic Capture and Display Systems in Circular Configurations. *J. Display Technol.* 8 (4), 225–232. doi:10.1109/jdt.2011.2167955

Kozacki, T., Kujawińska, M., Finke, G., Hennelly, B., and Pandey, N. (2012). Extended Viewing Angle Holographic Display System with Tilted SLMs in a Circular Configuration. *Appl. Opt.* 51 (11), 1771–1780. doi:10.1364/ao.51.001771

Lee, J. S., Kim, Y. K., Lee, M. Y., and Won, Y. H. (2019). Enhanced See-Through Near-Eye Display Using Time-Division Multiplexing of a Maxwellian-View and Holographic Display. *Opt. Express* 27 (2), 689–701. doi:10.1364/oe.27.000689

Li, N.-N., Wang, D., Li, Y.-L., and Wang, Q.-H. (2020). Method of Curved Composite Hologram Generation with Suppressed Speckle Noise. *Opt. Express* 28 (23), 34378–34389. doi:10.1364/oe.406265

Liu, S.-J., Wang, D., Zhai, F.-X., Liu, N.-N., and Hao, Q.-Y. (2020). Holographic Display Method with a Large Field of View Based on a Holographic Functional Screen. *Appl. Opt.* 59 (20), 5983–5988. doi:10.1364/ao.394352

Liu, Y. Z., Pang, X. N., Jiang, S., and Dong, J. W. (2013). Viewing-angle Enlargement in Holographic Augmented Reality Using Time Division and Spatial Tiling. *Opt. Express* 21 (10), 12068–12076. doi:10.1364/OE.21.012068

Mishina, T., Okui, M., and Okano, F. (2002). Viewing-zone Enlargement Method for Sampled Hologram that Uses High-Order Diffraction. *Appl. Opt.* 41 (8), 1489–1499. doi:10.1364/ao.41.001489

Sando, Y., Satoh, K., Kitagawa, T., Kawamura, M., Barada, D., and Yatagai, T. (2018). Super-wide Viewing-Zone Holographic 3D Display Using a Convex Parabolic Mirror. *Sci. Rep.* 8, 11333. doi:10.1038/s41598-018-29798-5

Senoh, T., Mishina, T., Yamamoto, K., Oi, R., and Kurita, T. (2011). Viewing-zone-angle-expanded Color Electronic Holography System Using Ultra-high-definition Liquid crystal Displays with Undesirable Light Elimination. *J. Display Technol.* 7 (7), 382–390. doi:10.1109/jdt.2011.2114327

Takaki, Y., and Hayashi, Y. (2008). Increased Horizontal Viewing Zone Angle of a Hologram by Resolution Redistribution of a Spatial Light Modulator. *Appl. Opt.* 47 (19), D6–D11. doi:10.1364/ao.47.0000d6

Takaki, Y., Matsumoto, Y., and Nakajima, T. (2015). Color Image Generation for Screen-Scanning Holographic Display. *Opt. Express* 23 (21), 26986–26998. doi:10.1364/oe.23.026986

Takaki, Y., and Nakamura, J. (2011). Zone Plate Method for Electronic Holographic Display Using Resolution Redistribution Technique. *Opt. Express* 19 (15), 14707–14719. doi:10.1364/oe.19.014707

Takaki, Y., and Nakaoka, M. (2016). Scalable Screen-Size Enlargement by Multi-Channel Viewing-Zone Scanning Holography. *Opt. Express* 24 (16), 18772–18781. doi:10.1364/oe.24.018772

Takaki, Y., and Tanemoto, Y. (2010). Modified Resolution Redistribution System for Frameless Hologram Display Module. *Opt. Express* 18 (10), 10294–10300. doi:10.1364/oe.18.010294

Wang, D., Liu, C., Shen, C., Xing, Y., and Wang, Q. H. (2020). Holographic Capture and Projection Systemof Real Object Based on Tunable Zoom Lens. *PhotoniX* 1 (6). doi:10.1186/s43074-020-0004-3

Wang, Z., Zhang, X., Lv, G., Feng, Q., Ming, H., and Wang, A. (2021). Hybrid Holographic Maxwellian Near-Eye Display Based on Spherical Wave and Plane Wave Reconstruction for Augmented Reality Display. *Opt. Express* 29 (4), 4927–4935. doi:10.1364/oe.418329

Yaras, F., Kang, H., and Onural, L. (2011). Circular Holographic Video Display System. *Opt. Express* 19 (10), 9147–9156.

Zeng, Z., Zheng, H., Yu, Y., Asundi, A. K., and Valyukh, S. (2017). Full-color Holographic Display with Increased-Viewing-Angle [Invited]. *Appl. Opt.* 56 (13), F112–F120. doi:10.1364/ao.56.00f112

Conflict of Interest: The authors declare that the research was conducted in the absence of any commercial or financial relationships that could be construed as a potential conflict of interest.

frontiers in Materials

ORIGINAL RESEARCH
published: 13 September 2021
doi: 10.3389/fmats.2021.739448

Broadband Nonlinear Optical Response of Nitrogen-Doped Diamond

*Zhengguo Xiao[1], Yu Fang[2], Yinglin Song[3], Yanchao She[1], Changhai Tian[1], Jie Zhang[1], Liqin Cui[1] and Yong Li[1]**

[1]Department of Physics and Electronic Engineering, Tongren University, Tongren, China, [2]Jiangsu Key Laboratory of Micro and Nano Heat Fluid Flow Technology and Energy Application, School of Mathematics and Physics, Suzhou University of Science and Technology, Suzhou, China, [3]Department of Physics, Harbin Institute of Technology, Harbin, China

A nitrogen-doped diamond crystal with (111) orientation was synthesized with an NaN_3 additive in the FeNi-C system at a pressure of 6.5 GPa and a temperature of 1,310°C, using the temperature gradient growth (TGG) method. Spectroscopic properties such as the absorption spectrum and the Raman spectrum as well as the Fourier transform infrared (FTIR) spectrum were studied. FTIR spectroscopy of the C-N vibrational modes at 1,344 and 1,130 cm^{-1} suggested a nitrogen content of 310 ppm. Its nonlinear optical (NLO) response was investigated using the Z-scan technique under the femtosecond regime. Due to the presence of nitrogen defects, the synthesized crystal performed large nonlinear absorption under both 800- and 532-nm wavelength excitations. However, intrinsic diamond only experiences nonlinear refraction under these two wavelength excitations. Its broadband NLO properties indicated that nitrogen-doped diamond crystals were suitable for the application of ultrafast optical devices.

Keywords: nitrogen-doped diamond, broadband NLO response, Z-scan technique, ultrafast optical devices, TGG method

OPEN ACCESS

Edited by:
Zhongquan Nie,
Taiyuan University of Technology, China

Reviewed by:
Zhongguo Li,
Changshu Institute of Technology, China
Xiao Jin,
Lingnan Normal University, China

****Correspondence:***
Yong Li
likaiyong6@163.com

Specialty section:
This article was submitted to Quantum Materials, a section of the journal Frontiers in Materials

Received: *11 July 2021*
Accepted: *20 August 2021*
Published: *13 September 2021*

Citation:
Xiao Z, Fang Y, Song Y, She Y, Tian C, Zhang J, Cui L and Li Y (2021) Broadband Nonlinear Optical Response of Nitrogen-Doped Diamond. Front. Mater. 8:739448. doi: 10.3389/fmats.2021.739448

INTRODUCTION

Owing to low thermal expansion, high breakdown voltage, high carrier mobility, high NLO coefficients, and stable color centers, diamond attracts much attention as a promising material for many applications that include quantum optical and information processing (Maurer et al., 2012; Yang et al., 2016), nonlinear all-optical switching (Aharonovich et al., 2011; Hausmann et al., 2014), and magnetic sensing (Balasubramanian et al., 2008; Rondin et al., 2014). So far, a lot of efforts have been devoted to optical nonlinearity of intrinsic diamond (type-IIa) (Dadap et al., 1991; Sheik-Bahae et al., 1994; Preuss and Stuke, 1995; Roth and Laenen, 2001; Gagarskiĭ and Prikhod'ko, 2008; Zhang et al., 2017). Due to the broadband gap (5.5 eV), type-IIa diamond just experiences nonlinear refraction attributed to the optical Kerr effect (OKE) under the visible and infrared wavelength excitation (>390 nm). In these cases, no nonlinear absorption is observed. While using ultraviolet and blue region excitation (<390 nm), both nonlinear absorption that originated from two-photon absorption and nonlinear refraction that originated from the OKE should be taken into consideration. Almeida et al. reported third-order optical nonlinearities in type-IIa diamond at the femtosecond regime (Almeida et al., 2017), performed over a broad spectral range, from 0.83 to 4.77 eV (1,500–260 nm). Low absorption losses within its large transmission window make diamond an attractive platform for on-chip photonics. Specially, intrinsic diamond also suffered multi-photon absorption under extremely high light intensity (Kozák et al., 2012; Kononenko et al., 2014; Wang et al., 2018; Kozak et al., 2019; Zukerstein et al., 2019). In addition,

nanocrystalline diamond also shows strong NLO properties for the presence of grain boundaries (Preclíková et al., 2010; Trojánek et al., 2010).

The photo-physical properties that include electronic, optical, and thermal properties of diamond can be significantly changed by doping other elements into its structure. For example, insulated intrinsic diamond becomes a p-type semiconductor when doped with boron. When doped with nitrogen, spectroscopic properties such as absorption and emission spectra are easily influenced by the nitrogen vacancy (NV) center formed in the diamond (Wee et al., 2007; Subedi et al., 2019). As for optical nonlinearity, the negatively charged nitrogen vacancy defect center, NV-, in diamond has been investigated theoretically for one- and two-photon absorption properties involving the first excited state with the $^3A_2$-to-^3E transition (Lin et al., 2008). Recently, Motojima et al. reported that the effect of NV centers in single-crystal diamond on NLO effects under 800-nm, 40-fs laser pulses. Their results demonstrated that the OKE signal was strongly enhanced for the heavily implanted type-IIa diamond, and the NLO coefficient of the diamond crystal increased with the increase in nitrogen concentration (Motojima et al., 2019). It is worth noting that the enhanced NLO effect existed only near the surface region of diamond for the implanted depth of NV centers was about 30–40 nm in this case.

The nonlinear optical responses of materials are easily affected by synthetic methods, excitation conditions, and so on. Until now, fundamental studies on the third-order optical nonlinearities of nitrogen-doped diamond are still scarce. In order to clarify the modulation mechanism of NV centers on the optical nonlinearities of nitrogen-doped diamond, it is necessary to further illustrate the relationship of NLO properties and the structure of matter for diamond. Herein, we have synthesized a nitrogen-doped diamond crystal with (111) orientation under high-pressure high-temperature (HPHT). The NLO absorption responses of the synthesized diamond crystal were estimated using the Z-scan technique with two excitation wavelengths (532 and 800 nm) under the femtosecond regime. Our results have shown that nitrogen-doped diamond performed strong NLO absorption under 532- and 800-nm wavelengths, respectively. Its broadband NLO responses indicate that nitrogen-doped diamond can be a good candidate for ultrafast NLO devices such as optical limiters.

MATERIALS AND METHODS

Sample Preparation and Spectroscopic Characterization

A nitrogen-doped diamond crystal with (111) orientation was synthesized with an NaN_3 additive in the FeNi-C system at a pressure of 6.5 GPa and a temperature of 1,310°C, using the temperature gradient growth (TGG) method. The detailed synthetic scheme can be found in the literature (Li et al., 2018). It was a 2.05-mm-thick sample cut with its face perpendicular to the crystallographic [111] axis. Two faces of the diamond crystal were polished. The ground state absorption spectrum of the nitrogen-doped diamond crystal was recorded using a Shimadzu UV1800 spectrophotometer. The Raman spectrum and FTIR spectrum of the synthetic crystal were recorded in order to investigate crystallization quality and impurities in diamond structures. All the experiments were measured at room temperature.

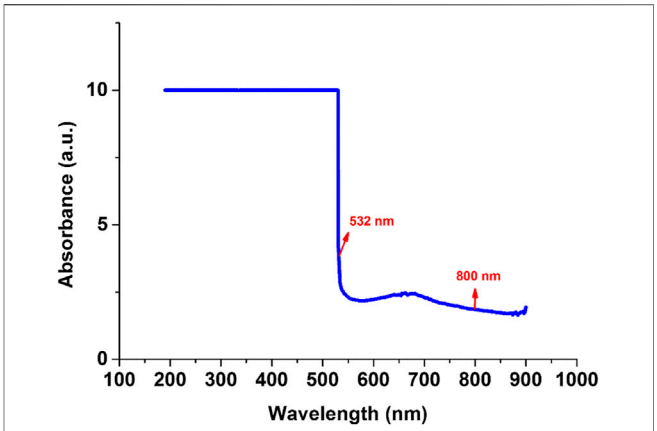

FIGURE 1 | Ground state absorption of the obtained nitrogen-doped diamond crystal.

Nonlinear Optical Measurements

Due to simple and single-beam measurement, the Z-scan technique is considered as a common method for measuring nonlinear optical coefficients of materials. In our Z-scan technique, the light source was a regeneratively amplified Yb:KGW fiber laser system (Light Conversion, PHAROS-SP) which produced 1-mJ pulses centered at 1,030 nm with a repetition rate of 6 kHz and 190 fs (FWHM). The optical parametric amplifier (OPA, ORPHEUS, Light Conversion) output was tuned to the wavelengths 532 and 800 nm as the test beams with 20-Hz, 190-fs laser pulses in the Z-scan technique. The spatial and temporal distribution of the pulse was nearly a Gaussian profile. The experimental setup was similar to the one in the study by Sheik-Bahae et al. (1990). The thickness of the synthetic diamond crystal is 2.05 mm, satisfying thin sample approximation in nonlinear optical experiments. The diamond crystal placed on the mobile platform was moved along the z-axis with respect to the focal point of a 200-mm focal lens. All beams were measured by using energy detectors (Rjp-765 energy probe) linked to an energy meter (Rj-7620 ENERGY RATIOMETER, laser probe). The experimental data were collected through a GPIB interface. The experimental system was calibrated using benchmark Kerr liquid CS_2.

RESULTS AND DISCUSSION

Spectroscopic Characterization

The ground state absorption spectrum of the nitrogen-doped diamond crystal is shown in **Figure 1**. It is well known that the intrinsic diamond exhibits the wide optical transparency range (from the ultraviolet to the far-infrared) for the broadband gap (5.5 eV) (Gagarskiĭ and Prikhod'ko, 2008). From **Figure 1**, the synthetic diamond crystal performs linear absorption in visible

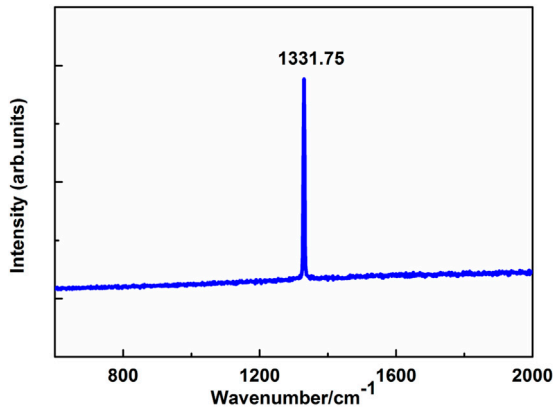

FIGURE 2 | Raman spectrum of the obtained nitrogen-doped diamond crystal.

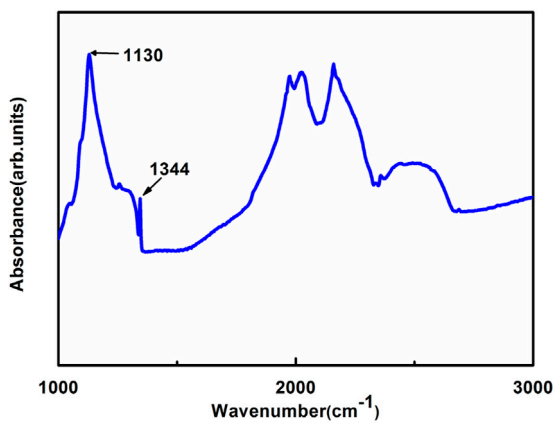

FIGURE 3 | FTIR spectrum of the obtained nitrogen-doped diamond crystal.

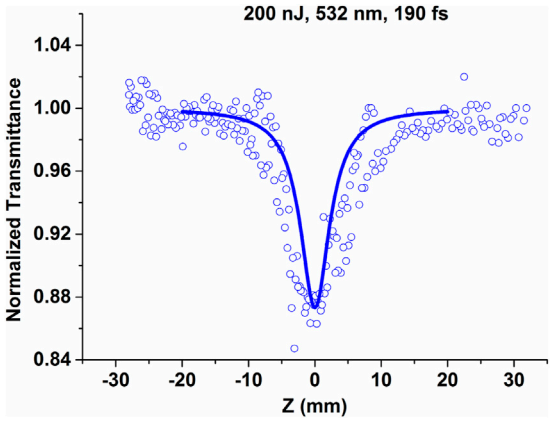

FIGURE 4 | Open-aperture Z-scan curves under 532 nm with 200 nJ for the synthetic nitrogen-doped diamond crystal. The circles are the experimental data, and the solid lines are the theoretical fitting.

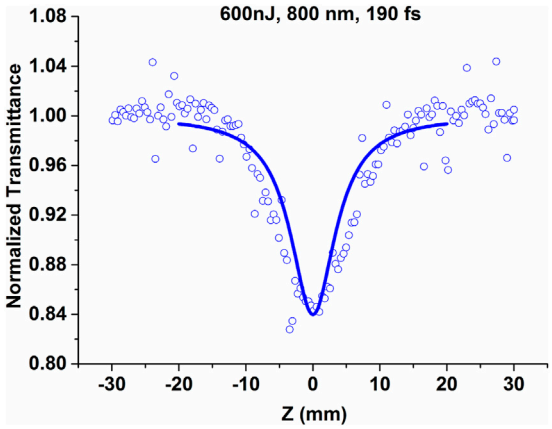

FIGURE 5 | Open-aperture Z-scan curves under 800 nm with 600 nJ for the synthetic nitrogen-doped diamond crystal. The circles are the experimental data, and the solid lines are the theoretical fitting.

regions due to the presence of nitrogen. Apparently, the linear absorption of the 532-nm wavelength was larger than that of the 800-nm wavelength in the synthetic diamond. Considering the electronic levels of NV centers (Lin et al., 2008), the electrons can be promoted from the ground state $^3A_2$ to excited states ^3E through absorbing one photon when using 532-nm wavelength excitation. However, under 800-nm wavelength excitation, the electrons in NV centers could not be promoted from $^3A_2$ to ^3E just through absorbing one photon, consistent with its ground state absorption spectrum. The Raman spectrum of the synthesized diamond crystal is presented in **Figure 2**. In intrinsic diamond (IIa type), its characteristic peaks were located at 1,332.02 cm^{-1} (Li et al., 2018). As shown in **Figure 2**, the characteristic peaks of nitrogen-doped diamond are located at 1,331.75 cm^{-1}, and there was a slight shift compared with the IIa-type diamond. Moreover, the bottom areas of the Raman spectrum were very flat, and the peak was sharp, indicating that the synthesized diamond performed at a high quality. The typical FTIR spectrum of the synthesized diamond crystal is presented in **Figure 3**. Compared with nitrogen-doped diamond, there were no absorption peaks located at 1,130 and 1,344 cm^{-1} in the FTIR spectrum of intrinsic diamond (Li et al., 2018). For the nitrogen-doped diamond crystal, the absorption peaks located at 1,130 and 1,344 cm^{-1} in the FTIR spectrum could be assigned to substitutional N impurity. Furthermore, the concentration of N impurity was approximately 310 ppm, which was estimated according to the following formula (Liang et al., 2005):

$$N_C = [\mu(1130cm^{-1})/\mu(2120cm^{-1})] \times 5.5 \times 2.5$$

Open-Aperture Z-Scan

To evaluate the ultrafast NLO properties of the synthesized nitrogen-doped diamond crystal, an open-aperture Z-scan was performed under 190-fs laser pulses with 532- and 800-nm

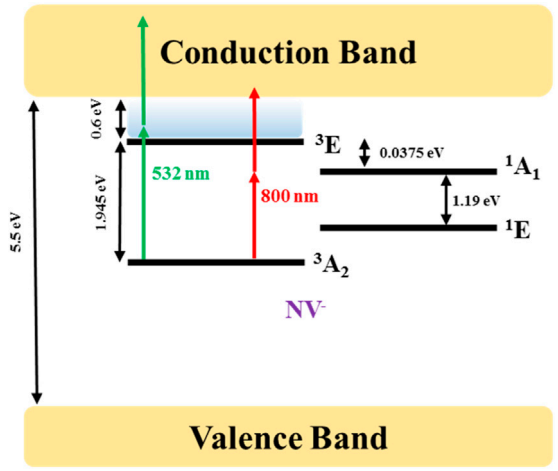

FIGURE 6 | Energy levels of NV centers in the bandgap of diamond. The green and red arrow lines represent the possible transition using 532-nm excitation and 800-nm excitation, respectively.

wavelengths, respectively. The energy used in the 532-nm Z-scan measurement was 200 nJ, and the beam waist was nearly 20 um, corresponding to a light intensity of 150 GW/cm^2. The energy used in the 800-nm Z-scan measurement was 600 nJ, and the beam waist was nearly 30 um, corresponding to a light intensity of 207 GW/cm^2. Due to the short pulse duration (190 fs) and low repetition speed (20 Hz) of our laser, the thermal effect has a negligible contribution to nonlinear absorption because the built-up time for thermal effect is rather long compared to the pulse duration (Yang and Song, 2009; Kovsh et al., 1999). It is well known that open-aperture Z-scan curves represent the NLO absorption property of materials. The open-aperture Z-scan experimental results under 532 and 800 nm are shown in **Figures 4**, **5**, respectively. The occurrence of a valley in open-aperture Z-scan curves indicated that the synthesized nitrogen-doped diamond crystal experienced reverse saturable absorption (RSA) under both 532- and 800-nm wavelengths. It is well known that no NLO absorption is observed in intrinsic diamond under 532- and 800-nm wavelength excitation. In order to generate NLO absorption, intrinsic diamond must absorb multiple photons promoting electrons from the valence band (VB) to the conduction band (CB) under these two wavelengths for its broadband gap (5.5 eV). In these cases, extremely high light intensity is needed. In our experiments, the light intensity was controlled to a low level, and the transition of electrons from the VB to the CB could be ruled out. As a result, the NLO absorption of the synthetic diamond crystal should originate from the presence of nitrogen defects under these two wavelength excitations. When doped with nitrogen, there are many NV centers formed in the synthetic diamond crystal. Each NV center consists of a substitutional nitrogen atom and adjacent lattice vacancy. The ground and excited states are spin triplets (S = 1) with a principle zero-phonon line (ZPL) at 637 nm (1.945 eV) associated with the radiative transition from ^{3}E to ^{3}A$_2$ (Ashfold et al., 2020; Ulbricht and Loh, 2018; Rogers et al., 2015). The energy levels of NV centers in the bandgap of diamond are illustrated in **Figure 6**. As **Figure 6** shows, with the absorption of photons, electrons of the ground state ^{3}A$_2$ are sent to the excited state ^{3}E. From the excited state ^{3}E, electrons can radiatively decay to the ground state with the photon emission in the visible region or non-radiatively decay to the singlet state ^{1}A$_1$, followed by the radiative transition to the metastable single ^{1}E leading to the emission band in the infrared region with the ZPL at 1042 nm (Bourgeois et al., 2005). It is noted that the excited-state energy level of the NV$^-$ is about 0.6 eV below that of the conduction band (CB). After absorbing the second photon, instead of decaying back to the ground state (radiatively or non-radiatively), the excited electron can be promoted to the CB. The time scale of the excited state ^{3}E decaying to the ground state ^{3}A$_2$ or the singlet state ^{1}A$_1$ is nearly 10 nanoseconds (Ulbricht and Loh, 2018). In our open-aperture Z-scan measurements, a 190-fs laser pulse is too short compared to the decaying time of the ^{3}E to the ^{3}A$_2$ and the ^{3}E to the ^{1}A$_1$. As a result, the energy levels of the NV$^-$ can simply be two states: ^{3}A$_2$ and ^{3}E. Considering the optical nonlinearity of the synthesized diamond crystal, there is a difference in the original mechanism of NLO absorption between the two wavelength (532 and 800 nm) excitations, although a strong RSA effect was observed under two experimental conditions. When using 800-nm wavelength excitation, the electrons of NV centers will be promoted from the ^{3}A$_2$ state to the conduction band after absorbing two photons. This absorption process is called two-photon absorption, with the participation of virtual-level states. However, when using 532-nm wavelength excitation, first, the electrons of NV centers will be promoted from the ^{3}A$_2$ state to the ^{3}E state after absorbing one photon. Then the electrons of the ^{3}E state will be promoted from the ^{3}E state to the conduction band after absorbing another photon. The third-order nonlinearity of the synthetic diamond crystal is deduced by stepwise one-photon absorption in this case, as in a cascade absorption using a long-lived free carrier located in the excited state ^{3}E. According to the Z-scan theory (Sheik-Bahae et al., 1990), we extracted the effective nonlinear absorption coefficient β_{eff} through numerical simulation. The values of the effective third-order nonlinear absorption coefficient β_{eff} under 532- and 800-nm wavelengths are summarized in **Table 1**. Compared with previous reports (Kononenko et al., 2014; Almeida et al., 2017; Motojima et al., 2019), NLO coefficients of the synthetic diamond crystal were comparable to those of nitrogen-implanted chemical vapor deposition (CVD) diamond and high-purity diamond. Our results showed that the nitrogen-doped diamond crystal performed broadband NLO responses, indicating that it can be used for the application of ultrafast nonlinear devices in the future.

CONCLUSION

In summary, a nitrogen-doped diamond crystal with (111) orientation was synthesized with an NaN_3 additive in the

TABLE 1 | NLO absorption coefficients of diamonds under different experimental conditions from open-aperture Z-scan measurements.

Sample	Experimental condition	NLO absorption coefficients
Nitrogen-doped diamond (this work)	190 fs, 532 nm	$\beta_{eff} = 3.35 \times 10^{-13}$ m/W
Nitrogen-doped diamond (this work)	190 fs, 800 nm	$\beta_{eff} = 2.14 \times 10^{-13}$ m/W
Nitrogen-implanted diamond Motojima et al. (2019)	40 fs, 800 nm	$\beta = 1.61 \times 10^{-13}$ m/W
Type-IIa diamond Kononenko et al. (2014)	120 fs, 400 nm	$\beta = 3.7 \times 10^{-13}$ m/W
Type-IIa diamond Almeida et al. (2017)	fs, 3.18–4.77 eV (390–260 nm)	0.07–0.23 cm/GW

FeNi-C system at a pressure of 6.5 GPa and a temperature of 1,310°C, using the temperature gradient growth (TGG) method. The FTIR and Raman spectroscopy characterized that the obtained diamond was high quality. FTIR spectroscopy of the C-N vibrational modes at 1,344 and 1,130 cm^{-1} suggested a nitrogen content of 310 ppm. Its NLO response was investigated using the Z-scan technique under two different wavelengths (532 and 800 nm) at the femtosecond regime. It was found that nonlinear optical absorption originated from the introduction of NV centers, which provided unique optical transitions by electronic structures in the bandgap of diamond. Our results showed that the nitrogen-doped diamond crystal performed broadband NLO responses, indicating its potential applications in future NLO devices, such as ultrafast optical power limiters.

DATA AVAILABILITY STATEMENT

The original contributions presented in the study are included in the article/Supplementary Material; further inquiries can be directed to the corresponding author.

AUTHOR CONTRIBUTIONS

ZX, YF, and YS contributed to the conception and design of the study. ZX, YL, and LC contributed to the synthesis and testing of samples. YS and CT organized the database and performed the numerical simulation. ZX wrote the first draft of the manuscript. YL and JZ wrote sections of the manuscript. All authors contributed to manuscript revision and read and approved the submitted version.

ACKNOWLEDGMENTS

The authors gratefully acknowledge the support of the National Natural Science Foundation of China (grant no. 12064038), the Science and Technology Foundation of Guizhou Province, China (grant nos. ZK[2021]031 and ZK[2021]019), the Natural Science Foundation of the Guizhou Province Education Department (grant nos. KY[2018]343 and KY[2019]179), the Science and Technology Foundation of Tongren City (grant no. (2017) 47-37), the Startup Foundation for Doctoral Research (trxyDH1622), and the Open Project of the Inner Mongolia Key Lab of High-Pressure Phase Functional Materials (cfxygy202004).

REFERENCES

Aharonovich, I., Greentree, A. D., and Prawer, S. (2011). Diamond Photonics. *Nat. Photon* 5 (7), 397–405. doi:10.1038/nphoton.2011.54

Almeida, J. M. P., Oncebay, C., Siqueira, J. P., Muniz, S. R., De Boni, L., and Mendonça, C. R. (2017). Nonlinear Optical Spectrum of diamond at Femtosecond Regime. *Sci. Rep.* 7, 14320. doi:10.1038/s41598-017-14748-4

Ashfold, M. N. R., Goss, J. P., Green, B. L., May, P. W., Newton, M. E., and Peaker, C. V. (2020). Nitrogen in Diamond. *Chem. Rev.* 120 (12), 5745–5794. doi:10.1021/acs.chemrev.9b00518

Balasubramanian, G., Chan, I. Y., Kolesov, R., Al-Hmoud, M., Tisler, J., Shin, C., et al. (2008). Nanoscale Imaging Magnetometry with diamond Spins under Ambient Conditions. *Nature* 455 (7213), 648–651. doi:10.1038/nature07278

Bourgeois, E., Jarmola, A., Siyushev, P., Gulka, M., Hruby, J., Jelezko, F., et al. (2005). Photoelectric Detection of Electron Spin Resonance of Nitrogen-Vacancy Centres in diamond. *Nat. Commun.* 6, 8577. doi:10.1038/ncomms9577

Dadap, J. I., Focht, G. B., Reitze, D. H., and Downer, M. C. (1991). Two-photon Absorption in diamond and its Application to Ultraviolet Femtosecond Pulse-Width Measurement. *Opt. Lett.* 16 (7), 499–501. doi:10.1364/ol.16.000499

Gagarskiĭ, S., and Prikhod'ko, K. (2008). Measuring the Parameters of Femtosecond Pulses in a Wide Spectral Range on the Basis of the Multiphoton-Absorption Effect in a Natural diamond crystal. *J. Opt. Techn.* 75 (3), 139–143.

Hausmann, B. J. M., Bulu, I., Venkataraman, V., Deotare, P., and Lončar, M. (2014). Diamond Nonlinear Photonics. *Nat. Photon* 8 (5), 369–374. doi:10.1038/nphoton.2014.72

Kononenko, V. V., Konov, V. I., Gololobov, V. M., and Zavedeev, E. V. (2014). Propagation and Absorption of High-Intensity Femtosecond Laser Radiation in diamond. *Quan. Electron.* 44 (12), 1099–1103. doi:10.1070/qe2014v044n12abeh015459

Kovsh, D. I., Hagan, D. J., and Stryland, E. W. V. (1999). Numerical Modeling of thermal Refraction in Liquids in the Transient Regime. *Opt. Express* 4 (8), 315–327. doi:10.1364/oe.4.000315

Kozak, M., Otobe, T., Zukerstein, M., Trojanek, F., and Maly, P. (2019). Anisotropy and Polarization Dependence of Multiphoton Charge Carrier Generation Rate in diamond. *Phys. Rev. B* 99 (10), 104305. doi:10.1103/physrevb.99.104305

Kozák, M., Trojánek, F., Dzurňák, B., and Malý, P. (2012). Two- and Three-Photon Absorption in Chemical Vapor Deposition diamond. *J. Opt. Soc. Am. B* 29 (5), 1141–1145. doi:10.1364/josab.29.001141

Li, Y., Li, Y., Wang, Y., Zhang, J., Song, M., She, Y., et al. (2018). Synthesis of Large diamond Single Crystals under High Pressure and High Temperature through Effective Utilization of the Synthesis Cavity. *CrystEngComm* 20 (29), 4127–4132. doi:10.1039/c8ce00786a

Liang, Z., Jia, X., Ma, H., Zang, C., Zhu, P., Guan, Q., et al. (2005). Synthesis of HPHT diamond Containing High Concentrations of Nitrogen Impurities Using NaN3 as Dopant in Metal-Carbon System. *Diamond Relat. Mater.* 14 (11-12), 1932–1935. doi:10.1016/j.diamond.2005.06.041

Lin, C.-K., Wang, Y.-H., Chang, H.-C., Hayashi, M., and Lin, S. H. (2008). One- and Two-Photon Absorption Properties of diamond Nitrogen-Vacancy Defect

Centers: A Theoretical Study. *J. Chem. Phys.* 129 (12), 124714. doi:10.1063/1.2987717

Maurer, P. C., Kucsko, G., Latta, C., Jiang, L., Yao, N. Y., Bennett, S. D., et al. (2012). Room-temperature Quantum Bit Memory Exceeding One Second. *Science* 336 (6086), 1283–1286. doi:10.1126/science.1220513

Motojima, M., Suzuki, T., Shigekawa, H., Kainuma, Y., An, T., and Hase, M. (2019). Giant Nonlinear Optical Effects Induced by Nitrogen-Vacancy Centers in diamond Crystals. *Opt. Express* 27 (22), 32217–32227. doi:10.1364/oe.27.032217

Preclíková, J., Kromka, A., Rezek, B., and Malý, P. (2010). Laser-induced Refractive index Changes in Nanocrystalline diamond Membranes. *Opt. Lett.* 35 (4), 577–579. doi:10.1364/ol.35.000577

Preuss, S., and Stuke, M. (1995). Subpicosecond Ultraviolet Laser Ablation of diamond: Nonlinear Properties at 248 Nm and Time-resolved Characterization of Ablation Dynamics. *Appl. Phys. Lett.* 67 (3), 338–340. doi:10.1063/1.115437

Rogers, L. J., Doherty, M. W., Barson, M. S. J., Onoda, S., Ohshima, T., and Manson, N. B. (2015). Singlet Levels of the NV−centre in diamond. *New J. Phys.* 17 (1), 013048. doi:10.1088/1367-2630/17/1/013048

Rondin, L., Tetienne, J.-P., Hingant, T., Roch, J.-F., Maletinsky, P., and Jacques, V. (2014). Magnetometry with Nitrogen-Vacancy Defects in diamond. *Rep. Prog. Phys.* 77 (5), 056503. doi:10.1088/0034-4885/77/5/056503

Roth, T., and Laenen, R. (2001). Absorption of Free Carriers in diamond Determined from the Visible to the Mid-infrared by Femtosecond Two-Photon Absorption Spectroscopy. *Opt. Commun.* 189 (4), 289–296. doi:10.1016/s0030-4018(01)01037-9

Sheik-Bahae, M., DeSalvo, R. J., Said, A. A., Hagan, D. J., Soileau, M., and Van Stryland, E. W. (1994). *Optical Nonlinearities in diamond Proc Laser-Induced Damage in Optical Materials*. Albuquerque: International Society for Optics and Photonics, 605–609.

Sheik-Bahae, M., Said, A. A., Wei, T.-H., Hagan, D. J., and Van Stryland, E. W. (1990). Sensitive Measurement of Optical Nonlinearities Using a Single Beam. *IEEE J. Quan. Electron.* 26 (4), 760–769. doi:10.1109/3.53394

Subedi, S. D., Fedorov, V. V., Peppers, J., Martyshkin, D. V., Mirov, S. B., Shao, L., et al. (2019). Laser Spectroscopic Characterization of Negatively Charged Nitrogen-Vacancy (NV−) Centers in diamond. *Opt. Mater. Express* 9 (5), 2076–2087. doi:10.1364/ome.9.002076

Trojánek, F., Žídek, K., Dzurňák, B., Kozák, M., and Malý, P. (2010). Nonlinear Optical Properties of Nanocrystalline diamond. *Opt. Express* 18 (2), 1349–1357. doi:10.1364/oe.18.001349

Ulbricht, R., and Loh, Z. H. (2018). Excited-state Lifetime of the NV- Infrared Transition in diamond. *Phys. Rev. B* 98 (9), 094309. doi:10.1103/physrevb.98.094309

Wang, Y., Zhang, W., Lin, C.-N., Ren, P., Lu, Y.-J., Shan, C., et al. (2018). Multiphoton Upconversion Emission from Diamond Single Crystals. *ACS Appl. Mater. Inter.* 10 (22), 18935–18941. doi:10.1021/acsami.8b07288

Wee, T.-L., Tzeng, Y.-K., Han, C.-C., Chang, H.-C., Fann, W., Hsu, J.-H., et al. (2007). Two-photon Excited Fluorescence of Nitrogen-Vacancy Centers in Proton-Irradiated Type Ib Diamond†. *J. Phys. Chem. A.* 111 (38), 9379–9386. doi:10.1021/jp073938o

Yang, J., and Song, Y. (2009). Direct Observation of the Transient thermal-lensing Effect Using the Phase-Object Z-Scan Technique. *Opt. Lett.* 34 (2), 157–159. doi:10.1364/ol.34.000157

Yang, S., Wang, Y., Rao, D. D. B., Hien Tran, T., Momenzadeh, A. S., Markham, M., et al. (2016). High-fidelity Transfer and Storage of Photon States in a Single Nuclear Spin. *Nat. Photon* 10 (8), 507–511. doi:10.1038/nphoton.2016.103

Zhang, B., Liu, S., Wu, X., Yi, T., Fang, Y., Zhang, J., et al. (2017). Ultrafast Dynamics of Carriers and Nonlinear Refractive index in Bulk Polycrystalline diamond. *Optik* 130, 1073–1079. doi:10.1016/j.ijleo.2016.11.107

Zukerstein, M., Trojanek, F., Rezek, B., Soban, Z., Kozak, M., and Maly, P. (2019). Coherent Phonon Dynamics in diamond Detected via Multiphoton Absorption. *Appl. Phys. Lett.* 115 (16), 161104. doi:10.1063/1.5119056

Conflict of Interest: The authors declare that the research was conducted in the absence of any commercial or financial relationships that could be construed as a potential conflict of interest.

Publisher's Note: All claims expressed in this article are solely those of the authors and do not necessarily represent those of their affiliated organizations, or those of the publisher, the editors, and the reviewers. Any product that may be evaluated in this article, or claim that may be made by its manufacturer, is not guaranteed or endorsed by the publisher.

frontiers in Materials

ORIGINAL RESEARCH
published: 13 September 2021
doi: 10.3389/fmats.2021.721101

Ultrafast Broadband Nonlinear Optical Response in Co-Doped Sb_2Se_3 Nanofilms at Near-Infrared

Di Sun[1], Yu Fang[2], Xiaoyan Yan[3], Wen Shan[1], Wenjun Sun[4] and Qingyu Meng[4]*

[1]School of Physics and Electrical Engineering, Harbin Normal University, Harbin, China, [2]School of Mathematics and Physics, Suzhou University of Science and Technology, Suzhou, China, [3]Department of Physics, Harbin Institute of Technology, Harbin, China, [4]Key Laboratory of Photonic and Electric Bandgap Materials, Ministry of Education, School of Physics and Electronic Engineering, Harbin Normal University, Harbin, China

Transition metal-doped Sb_2Se_3 has become a heated topic caused by the strong nonlinear optical response and the ultrafast response time at high laser excitation. In this paper, the Co-doped Sb_2Se_3 with different doping amount (0.5, 1.0, and 1.5 W) nanofilms were prepared by magnetron sputtering technology, and the nonlinear behavior of Co-doped Sb_2Se_3 nanofilms at near infrared were systematically studied. The results of the femtosecond Z-Scan experiment indicate that the Co-doped Sb_2Se_3 nanofilms exhibit broadband nonlinear response properties owing to the free carrier absorption, the Kerr refraction, the two-photon absorption, and the free carrier refraction. The nonlinear absorption coefficients of Co-doped Sb_2Se_3 nanofilms are from 3.0×10^{-9} to 2.03×10^{-8} m/ W under excitation at 800, 980, and 1,030 nm, and the nonlinear refractive index of the Co-doped Sb_2Se_3 nanofilms is from 4.0×10^{-16} to -3.89×10^{-15} m^2/ W at 800, 980, and 1,030 nm. More importantly, Co-doped Sb_2Se_3 (1.5 W) nanofilm exhibits ultrafast carrier absorption (<1 ps) and a stronger transient absorption intensity of ΔOD > 6.3. The Co-doping content can controllably tune the crystalline degree, the ultrafast carrier absorption, the intensity of the reverse saturation absorption, the broadband nonlinear optical response, and the carrier relaxation time of Co-doped Sb_2Se_3 nanofilms. These results are sufficient to support their applications in broadband nonlinear photonic devices.

Keywords: Co-doped Sb_2Se_3 nanofilms, ultrafast broadband response, near-infrared, ultrafast carrier absorption, reverse saturation absorption

OPEN ACCESS

Edited by:
Zhongquan Nie,
Taiyuan University of Technology, China

Reviewed by:
Zhongguo Li,
Changshu Institute of Technology, China
Junyi Yang,
Soochow University, China

****Correspondence:***
Wenjun Sun
swjgood0139@139.com

Specialty section:
This article was submitted to Quantum Materials, a section of the journal Frontiers in Materials

Received: *06 June 2021*
Accepted: *09 August 2021*
Published: *13 September 2021*

Citation:
Sun D, Fang Y, Yan X, Shan W, Sun W and Meng Q (2021) Ultrafast Broadband Nonlinear Optical Response in Co-Doped Sb_2Se_3 Nanofilms at Near-Infrared. Front. Mater. 8:721101. doi: 10.3389/fmats.2021.721101

INTRODUCTION

The special interactions between light and matter in selenide materials are ideal applications for interferometers, electrocatalysis, ultrathin transistors, sensors, and optoelectronic devices (Radisavljevic and Kis, 2013; Medina et al., 2017; Ai et al., 2018; Jiang et al., 2019). In nonlinear optics, the selenides, due to their unique reverse saturation absorption (RSA), which decreases transmittance with the incident laser increase, have attracted much attention (Wang et al., 2012; Lin et al., 2013). The RSA behavior occurs because the absorption cross-section of the excited state in the substance is larger than the ground state, which leads to the ground state absorption being less than that of the excited state (Henari and Dakhel, 2011; Tuhl et al., 2012). The RSA properties of selenides can be widely used in optical information, nonlinear optoelectronic components, optical sensing, and integrated optics (Djordjevic and Arabaci, 2010; Volz et al., 2012; Jia et al., 2018). For example, WSe_2 in selenides exhibits RSA and optical limiting properties that can be applied to nonlinear

optoelectronic components (Major et al., 2004; Andreev et al., 2011). However, the selenides with RSA properties still face the solution of the ultrafast broadband nonlinear optical response, higher carrier absorption intensity, long carrier relaxation time, and other problems.

In past decades, researchers have focused on Sb_2Se_3 (V–VI group), which is widely used in optical devices due to its excellent optical nonlinear properties (Molli et al., 2016; Liu et al., 2019). To further improve the photoelectric properties of Sb_2Se_3, the group IV, VII, and VI elements are frequently doped on Sb_2Se_3 (Choi et al., 2006; Lee et al., 2019; Ren et al., 2020). A variety of metal elements have been selected for doping with Sb_2Se_3 due to their excellent photoelectric properties (Cao et al., 2014; Ning et al., 2021). In many metal elements, Co was selected to dope the Sb_2Se_3 because it can effectively capture the photogenerated carrier and promote free-carrier absorption (FCA) at near infrared. The success of Co doping can effectively adjust the optical bandgap and accelerate the FCA and two-photon absorption (TPA) of Sb_2Se_3, making the nonlinear response transfer to the broadband. It is of great significance for the selection of a greater metal dopant to doped Sb_2Se_3 for nonlinear optical devices and electronic devices due to understanding the doping effect and nonlinear properties of Co-doped Sb_2Se_3.

In this paper, the pure and Co-doped Sb_2Se_3 nanofilms with different contents of Co dopant (0.5, 1.0, and 1.5 W) nanofilms were successfully prepared by using magnetron sputtering technology. The Co-doped Sb_2Se_3 (1.5 W) nanofilm exhibits an excellent ultrafast broadband nonlinear response at the near infrared, higher nonlinear absorption coefficients, higher transient absorption intensity, ultrafast carrier absorption, and high linear transmittance. By the precise control of magnetron sputtering conditions (such as the temperature, deposition time of the nanofilms, radio frequency, and direct current power), smooth and uniform Co-doped Sb_2Se_3 nanofilms were successfully prepared. The results of the transient absorption experiment suggest that the ultrafast broadband nonlinear optical response of Co-doped Sb_2Se_3 nanofilms is caused by FCA and TPA, and the special nonlinear optical properties in Co-doped Sb_2Se_3 nanofilms depend on the amount of Co dopant. We also obtained the close-aperture (CA) Z-scan signals of the Co-doped Sb_2Se_3 nanofilms by the CA Z-scan experiment. The composition of nonlinear refraction of the Co-doped Sb_2Se_3 nanofilms can be attributed to the free carrier refraction (FCR) and Kerr refraction. In addition, the Co-doped Sb_2Se_3 nanofilms also exhibit ultrafast carrier absorption, higher transient absorption intensity, and longer carrier relaxation time. It has a new reference value for the preparation of near-infrared broadband photonic devices.

EXPERIMENT

Materials

The magnetron sputtering target of Sb_2Se_3, with a purity of 99.99%, a diameter of 6.0 cm, a thickness of 0.3 cm, and a 0.2 cm thickness Cu back target, was purchased from Yitong Technology Co., Ltd. The sputtering target of Co with a thickness of 0.5 cm, a diameter of 6.0 cm, and a purity of 99.999% was purchased from Beijing JHCC Vacuum Equipment Co., Ltd.

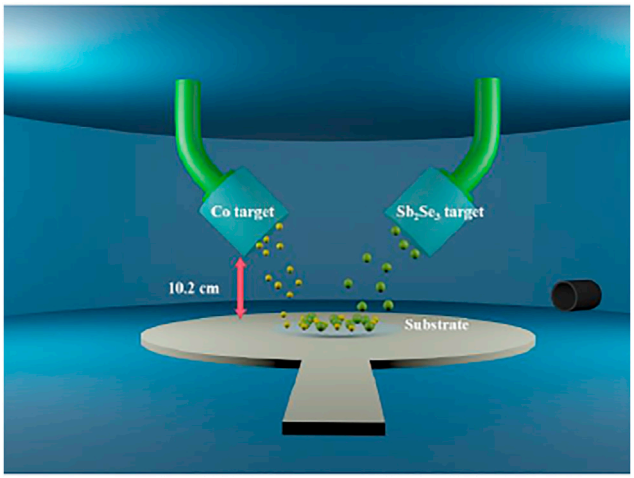

FIGURE 1 | The process of preparing Co-doped Sb_2Se_3 by using magnetron sputtering technology.

Sample Preparation

The pure Sb_2Se_3 and Co-doped Sb_2Se_3 nanofilms were prepared by using magnetron sputtering technology. The sapphire substrate was washed by anhydrous ethanol, deionized water, and acetone for 30 min until the substrate was clean completely and dried at room temperature. **Figure 1** shows the diagram of the process of the Co-doped Sb_2Se_3 nanofilms. To obtain the best thickness uniformity of the film, the distance between the target and the substrate was fixed at 10.2 cm. The sputtering power of the radio frequency target in the deposition process was 50 W, and the sputtering powers of the direct current target were 0.5, 1.0, and 1.5 W. The vacuum of the sputtering room was 4.5×10^{-5} Pa, the sputtering pressure was 3.0 Pa, Argon was employed as a working gas with a gas flow rate of 20 sccm, the substrate temperature **was** set to 150°C, and the sputtering time **was** 1 h to prepare the pure and Co-doped Sb_2Se_3 nanofilms.

Instruments

The morphology and thickness of pure and Co-doped Sb_2Se_3 nanofilms were obtained by field-scanning electron microscope (SU70, Hitachi, Japan), the X-ray diffraction analysis of pure and Co-doped Sb_2Se_3 nanofilms was carried out by using an X-ray diffractometer (XRD; D8, Bruker, Germany). The elemental analysis of Co-doped Sb_2Se_3 nanofilms was tested by energy dispersive spectroscopy (EDS; XM260S, AmetekGenesis, United States). The transmittance and linear absorption spectra of the pure and Co-doped Sb_2Se_3 nanofilms were characterized by the spectrophotometer (Uv-Vis; Uv-3600i PLUS, SHIMADZU, Japan).

In the transient absorption experiment, by changing the optical path difference between the detecting and pumping light, a variation of the white supercontinuum spectrum with different delay times can be obtained. Thus, the frequency-doubled

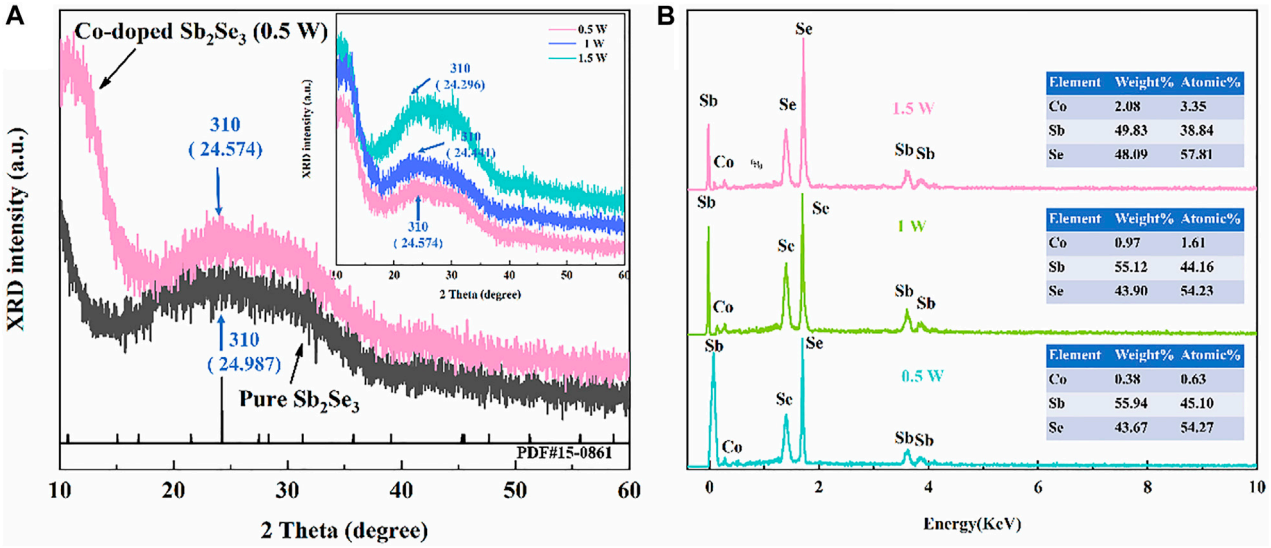

FIGURE 2 | (A) The XRD patterns of Co-doped and pure Sb_2Se_3 nanofilms. **(B)** The EDS of Co-doped Sb_2Se_3.

Yb:KGW laser was selected for the transient absorption experiment, and the laser can provide 190 femtosecond (fs) laser pulses at 450 nm. In the fs transient absorption experiment, the repetition rate, probe pulses, and specific pump fluence were set at 137 Hz, 800–1,050 nm, and 82 μJ/ cm^2, respectively (Fang et al., 2015; Fang et al., 2016). The nonlinear optical characteristics of the pure and Co-doped Sb_2Se_3 nanofilms were tested by fs Z-Scan experiments. The light source used an optical parameter amplifier (OPA, Light Conversion ORPHEUS), which was pumped by a mode-locked Yb:KGW fiber laser. The measurement parameters were set at 190 fs pulse and 20 Hz, and the waist radius of the laser was 33 μm. The energies of the laser excitation were set at 300, 400, and 500 nJ, respectively.

RESULTS AND DISCUSSION

Structural and Compositional Analysis

Figure 2 shows the XRD patterns of the Sb_2Se_3 and the Co-doped Sb_2Se_3 nanofilms. It can be seen from the XRD patterns that Co-doped Sb_2Se_3 nanofilms were successfully prepared and exhibited a polycrystalline structure. According to the XRD pattern, compared with the Sb_2Se_3 nanofilm (PDF#15-0816) (Zhou et al., 2015; Liu et al., 2019), the diffraction characteristic peak (310) of Co-doped Sb_2Se_3 nanofilms increased, and the lattice spacing of the (310) is 3.669 nm. In addition, the diffraction characteristic peaks of the Co-doped Sb_2Se_3 films exhibit an increasing trend with the increase of Co dopant. It can be clearly seen from the XRD patterns that the diffraction characteristic peaks of the Co-doped Sb_2Se_3 nanofilms are located at 24.575 (0.5 W), 24.441 (1.0 W), and 24.296 (1.5 W), respectively, which are all offset compared with the diffraction characteristic peaks of the pure Sb_2Se_3 nanofilm (24.987). In addition, the lattice constants of the Co-doped Sb_2Se_3 nanofilms are also calculated as 11.839 (0.5 W), 11.853 (1 W), and 11.891 (1.5 W), respectively, which are all smaller than the lattice constant of pure Sb_2Se_3 (11.902). In past reports, Co dopants in the Sb_2Se_3 system can be used as a substitute site of Sb or Se as well as interstitial atoms (Li et al., 2016; Mahani and El-Sayad, 2019). Under the premise that Se and Sb are abundant enough, Co can effectively replace Sb to form the most favorable structure. If the Sb position in Sb_2Se_3 is successfully replaced by some dopant, the homologous diffraction characteristic peaks are shifted and exhibited in the XRD pattern. The shift of the characteristic diffraction peaks was observed in the Co-doped Sb_2Se_3 nanofilms, confirming that the Co doping is at the grain boundary of Sb_2Se_3 rather than entering its lattice and that the Co dopant may also enter the substitution site of Sb. The supercell of Co-doped Sb_2Se_3 was shown in **Figure 3**.

The elemental composition of the Co-doped Sb_2Se_3 nanofilms was detected by EDS. The results of the EDS show that, with the increase of DC sputtering power in the Co target, the Co content of the Co-doped Sb_2Se_3 nanofilms increases, but the peak positions of the Se and Sb in the film have not shifted, and the content of Co in the Co-doped Sb_2Se_3 nanofilms was 0.63% (0.5 W), 1.61% (1.0 W), and 3.35% (1.5 W), respectively. The results of the EDS provide strong evidence for Co successfully doping at grain boundaries of Sb_2Se_3. Although the Co doping amount increases, the resistance of the Sb_2Se_3 grain boundary gradually decreases, which leads to the formation of a space charge region near the grain boundary.

Morphological and Optical Analysis

To study the morphology and thickness of pure and Co-doped Sb_2Se_3 nanofilms, the nanofilms were characterized by SEM, and the results are shown in **Figure 4**. The nanofilms that were prepared by magnetron sputtering are smooth uniform and free of cracks. In addition, we also characterize the thickness

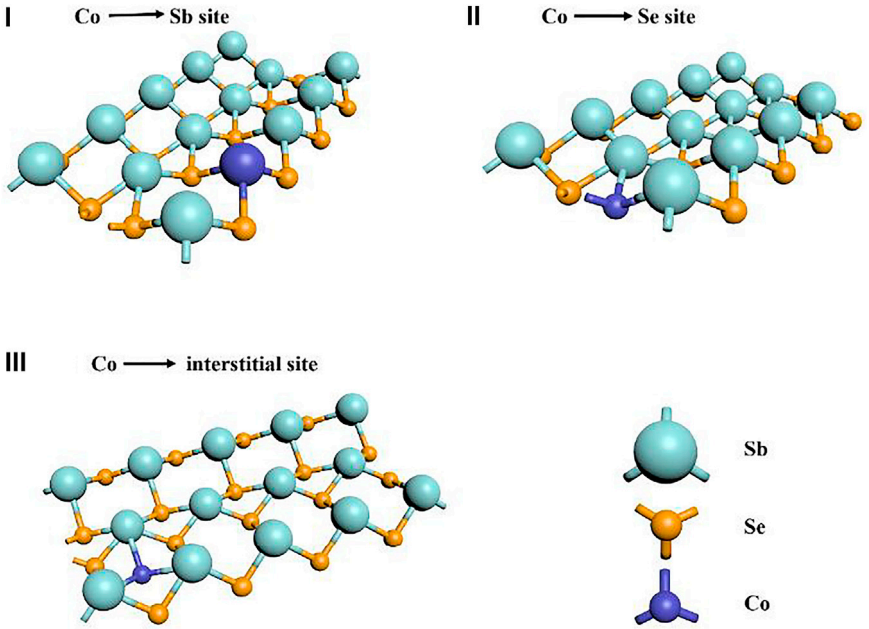

FIGURE 3 | The structures of Sb_2Se_3 with Co on (I) Sb (II) Se, and (III) interstitial site.

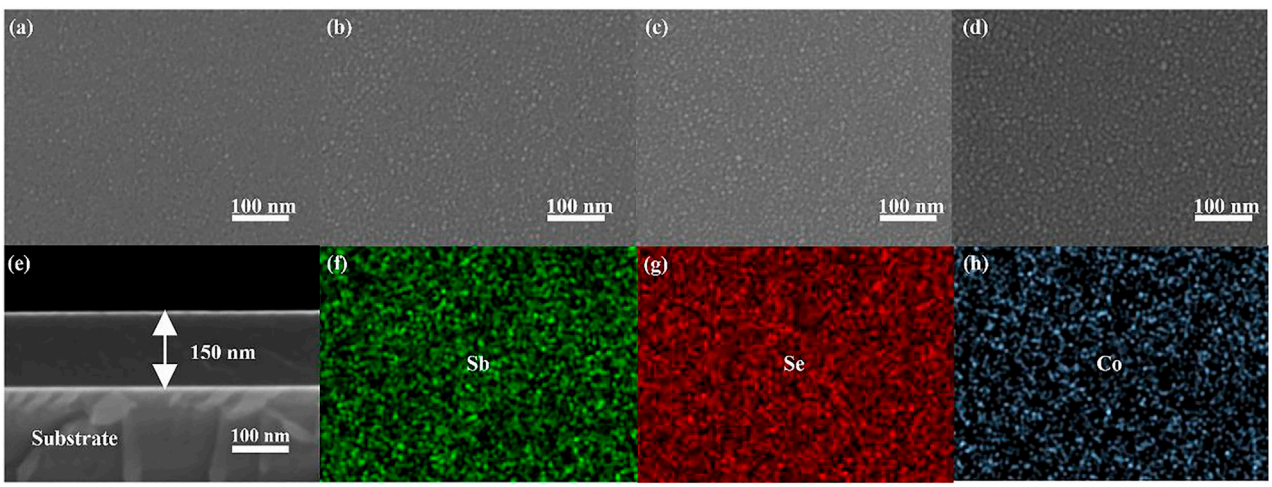

FIGURE 4 | (A–D) The SEM of pure and Co-doped Sb_2Se_3 nanofilms. **(E)** The thickness of pure and Co-doped Sb_2Se_3 nanofilms. **(F–H)** The elemental mapping of Co-doped Sb_2Se_3 (1.5 W) nanofilms.

of the pure and Co-doped Sb_2Se_3 nanofilms. The thicknesses of the pure and Co-doped Sb_2Se_3 nanofilms are both 150 nm. According to previous reports (Cattaruzza et al., 2009; Wu et al., 2015; Hymavathi et al., 2017), the morphology of doped films is determined by the deposition conditions, particularly the power of direct current magnetron sputtering. In accordance with the result of the elemental mapping (**Figure 4**(f ~ h)), the elements of Sb, Se, and Co are uniformly dispersed in the entire Co-doped Sb_2Se_3 nanofilms.

Figure 5 shows that the transmittance and absorption spectrum of pure and Co-doped Sb_2Se_3 nanofilms were obtained by spectrophotometer. The linear absorption edge of the optical bandwidths of the pure and Co-doped Sb_2Se_3 nanofilms at near infrared can be found. Compared with the pure Sb_2Se_3 nanofilms, the red shift of the linear absorption edge of the Co-doped Sb_2Se_3 nanofilms can be attributed to the different ionic radius of Co than that of Sb, which changes the bond length with Se at replacement Sb, thus leading to a change in

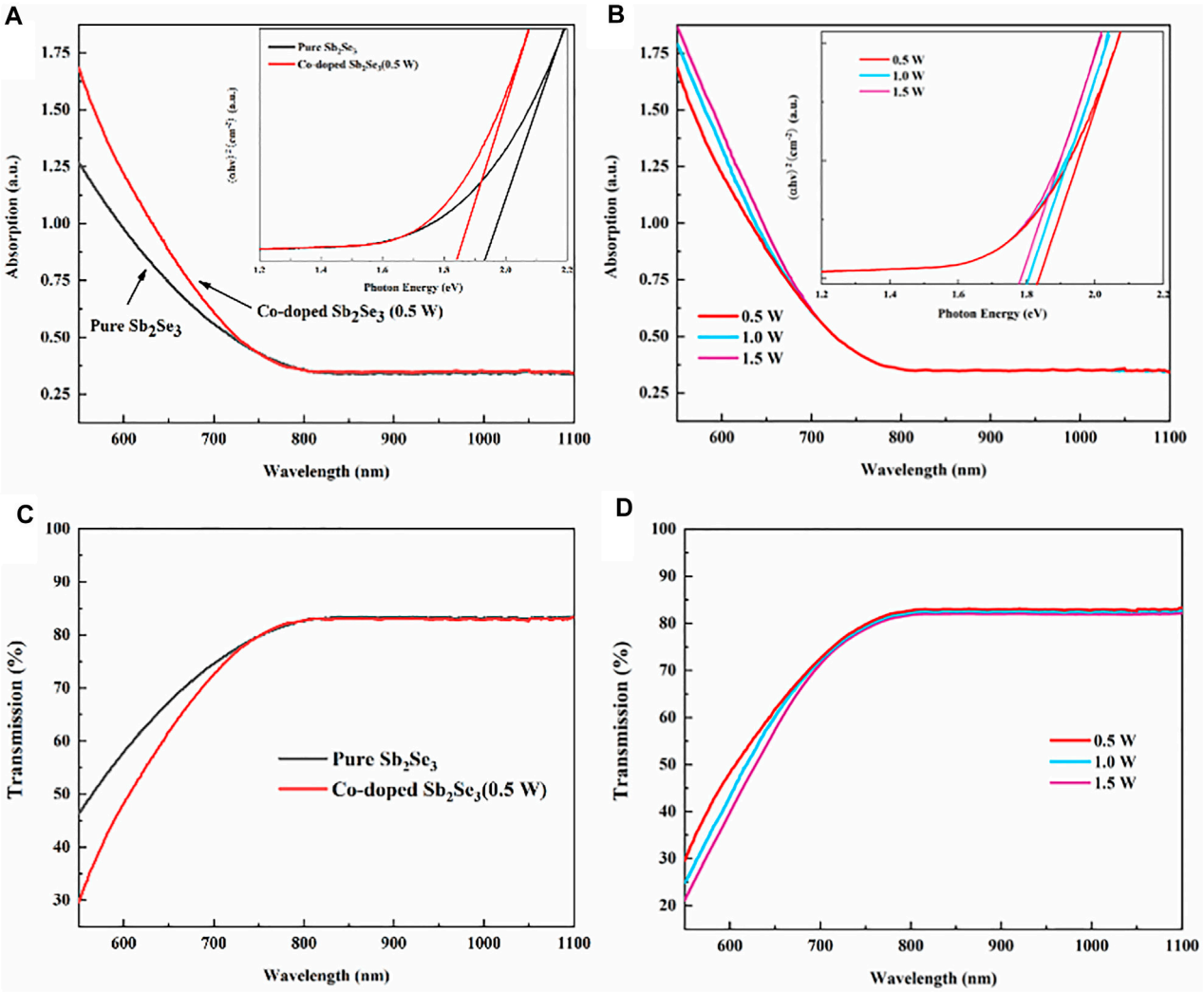

FIGURE 5 | (A, B) The linear absorption spectrum of pure and Co-doped Sb_2Se_3 nanofilms. The inset shows the relationship between the incident photon energy and absorbance. **(C)** and **(D)** exhibit the transmittance spectrum of pure and Co-doped Sb_2Se_3 nanofilms.

the eigenfrequency. The change of the eigenfrequency moves the linear absorption edge of the Co-doped Sb_2Se_3 nanofilms and, hence, the red shift (Tian and Liu, 2006). Furthermore, the increase in Co dopant content leads to increasing the deficiency, which leads to an increase in the average atomic distance, thus leading to a decrease in the energy level spacing. For linear absorption, we have Tacu's formulation, which is given as follows (Filipchenko and Naurizbaev, 1976):

$$\alpha = \frac{A}{h\nu}\left(h\nu - E_g\right)^n \quad (1)$$

where the coefficient of linear absorption is denoted by α, A represents a constant, Eg represents the optical band gap, n represents an index (n = 1, 2, 3), and the incident photon energy is denoted by $h\nu$. The optical band gap (E_g) values of the pure and Co-doped Sb_2Se_3 nanofilms (0.5, 1.0, and 1.5 W) are, respectively, calculated as 1.93, 1.83, 1.80, and 1.77 eV. **Figures 5C,D** exhibit the transmission spectrum of the pure and Co-doped Sb_2Se_3 nanofilms. It can be clearly seen that the A and B thin films both exhibit more than 80% transmission in the range of 800–1,100 nm, and the dopant of Co has no effect on the transmittance at near infrared.

Nonlinear Optical Properties

The nonlinear signals of the pure and Co-doped Sb_2Se_3 nanofilms, which were obtained by fs Z-scan experiment at 800, 980, and 1,030 nm, are used to understand the mechanism of the nonlinear response and regulation. The open-aperture (OA) Z-scan results of the pure and Co-doped Sb_2Se_3 nanofilms are shown in **Figure 6**(a~c). For the pure and Co-doped Sb_2Se_3 nanofilms, the RSA phenomenon was observed at 800 nm, and no signals were obtained at 980 and 1,030 nm for

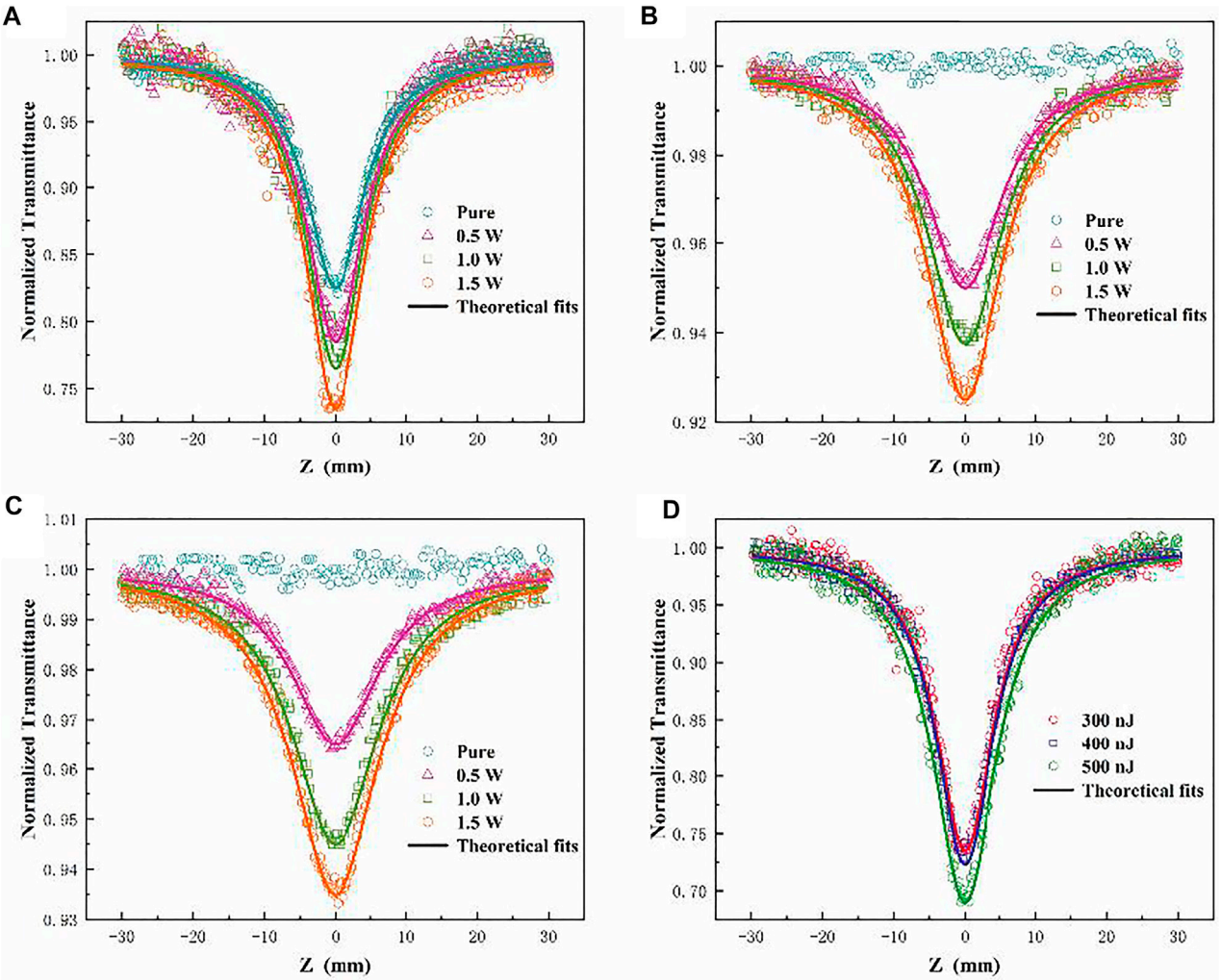

FIGURE 6 | The OA Z-scan signals of pure and Co-doped Sb_2Se_3 nanofilms at 800 **(A)**, 980, **(B)**, and 1,030 nm **(C)**. The OA Z-scan signal of Co-doped Sb_2Se_3 nanofilm (1.5 W) thin films at 800 nm under different excitation conditions **(D)**.

TABLE 1 | Nonlinear absorption parameters of the Co-doped and pure Sb_2Se_3 nanofilms under different excitation conditions.

	Pure Sb_2Se_3 nanofilm	**Co-doped Sb_2Se_3 nanofilms**									
		0.5 W		**1.0 W**		**1.5 W (300 nJ)**		**1.5 W (400 nJ)**		**1.5 W (500 nJ)**	
Wavelength (nm)	β (× 10^{-9} m/ W)	β (× 10^{-9} m/ W)	γ (× 10^{-16} cm^3/ W^2)	β (× 10^{-9} m/ W)	γ (× 10^{-16} cm^3/ W^2)	β (× 10^{-9} m/ W)	γ (× 10^{-16} cm^3/ W^2)	β (× 10^{-9} m/ W)	γ (× 10^{-16} cm^3/ W^2)	β (× 10^{-9} m/ W)	γ (× 10^{-16} cm^3/ W^2)
800	10.2	11.6	27.6	16.9	31.3	19.4	57.4	19.9	58.5	20.3	58.7
980		2.3	13.4	3.0	15.6	3.9	18.1				
1,030		1.5	4.2	2.6	8.7	3.0	11.9				

the pure Sb_2Se_3 nanofilm. Through the linear absorption spectroscopy of the pure and Co-doped Sb_2Se_3 nanofilms, it can be seen that the E_g of the pure and Co-doped Sb_2Se_3 nanofilms are greater than $h\nu$ but less than $2h\nu$, which indicates that the pure and Co-doped Sb_2Se_3 nanofilms both exhibit a TPA. For the Co-doped Sb_2Se_3 nanofilms, the OA Z-scan signals were exhibited at 980 and 1,030 nm, and it also shows that, with the increase of the doping concentration, the amplitude of the OA Z-scan signals exhibited the corresponding increase. In addition, we also obtained the OA Z-scan signals of the pure and Co-doped Sb_2Se_3 nanofilms (1.5 W) under different excitation energy at

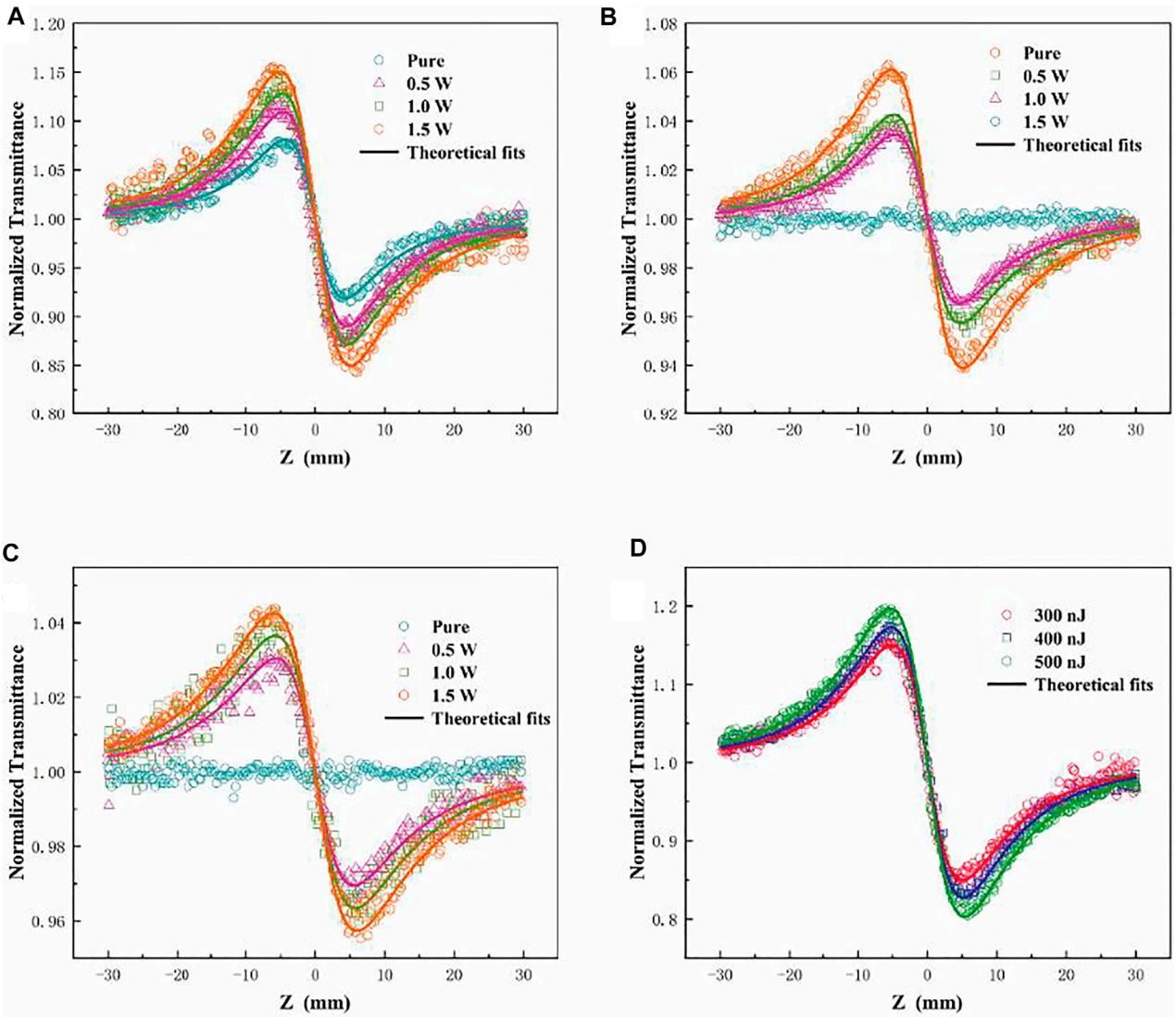

FIGURE 7 | The CA Z-scan signals of the Co-doped Sb_2Se_3 nanofilms at 800 **(A)**, 980 **(B)**, and 1,030 nm **(C)**. **(D)** The CA Z-scan signals of Co-doped Sb_2Se_3 nanofilms (1.5 W) at 800 nm under different excitation conditions (300, 400, and 500 nJ).

TABLE 2 | Nonlinear refractive index of pure and Co-doped Sb_2Se_3 nanofilms under different excitation conditions.

Sample	Pure Sb_2Se_3 nanofilm	Co-doped Sb_2Se_3 nanofilms				
		0.5 W	1.0 W	1.5 W (300 nJ)	1.5 W (400 nJ)	1.5 W (500 nJ)
Wavelength (nm)	n_2 ($\times 10^{-16}$ m^2/ W)	n_2 ($\times 10^{-16}$ m^2/ W)	n_2 ($\times 10^{-16}$ m^2/ W)	n_2 ($\times 10^{-16}$ m^2/ W)	n_2 ($\times 10^{-16}$ m^2/ W)	n_2 ($\times 10^{-16}$ m^2/ W)
800	−6.3	−13.1	−20.4	−24.4	−36.6	−38.9
980		−4.1	−6.0	−8.0		
1,030		−4.0	−4.7	−6.4		

800 nm. For the pure Sb_2Se_3 nanofilm, with the increase of the excitation energy, the OA Z-scan signals did not change; therefore, it can be inferred that the pure Sb_2Se_3 is a pure third-order nonlinear effect, and the OA Z-scan signal amplitude of the Co-doped Sb_2Se_3 nanofilms (1.5 W) increased with the increase of the excitation energy. Therefore, we infer that the Co-doped Sb_2Se_3 nanofilms have a higher-order nonlinear absorption phenomenon, that is, FCA. For the higher-order nonlinear absorption phenomenon, we have (Lakhwani et al., 2010)

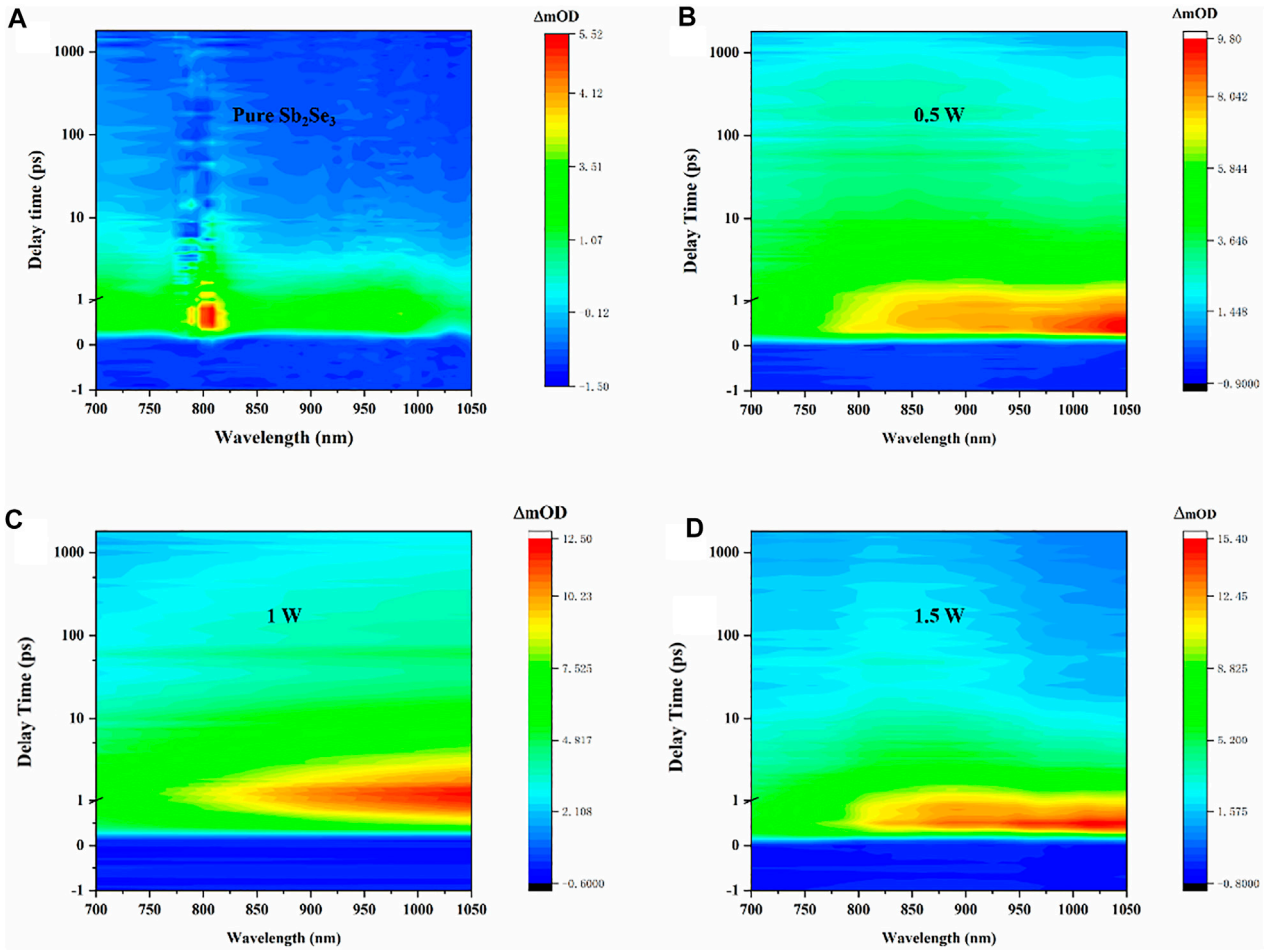

FIGURE 8 | (A) The results of the transient absorption experiment of the pure Sb_2Se_3 nanofilm at near infrared. **(C–D)** The results of the transient absorption experiment of Co-doped Sb_2Se_3 (0.5, 1, and 1.5 W) nanofilms at near infrared.

$$\alpha(I) = \alpha_0 + \beta I + \gamma I^2 \tag{2}$$

$$T(z) = \sum_{m=0}^{\infty} \frac{\left(\frac{-\alpha I L_{eff}}{1+z^2/z_0^2}\right)}{m+1} \tag{3}$$

Here, α represents the global absorption coefficient, γ stands for the fifth-order nonlinear absorption coefficient, $T(z)$ stands for the normalized transmittance, β represents the third nonlinear absorption coefficient of the thin films, and I_0 stands for the light intensity at the focus. The effective thickness of the nanofilms is denoted by L_{eff}, and $L_{eff} = 1 - e^{-\alpha_0 L}/\alpha_0$, where α_0 is the linear absorption coefficient of the thin film, L represents the thickness of the samples, z is the distance between the sample and the focal point, and z_0 is the derived length of the beam. The β and the γ of the pure and Co-doped Sb_2Se_3 nanofilms are exhibited in **Table 1**.

The calculated results show that, with the increase of excitation energy, the values of β and γ of the Co-doped Sb_2Se_3 nanofilms increase correspondingly, thus confirming that there is FCA in the Co-doped Sb_2Se_3 nanofilms. As is known to all, the interaction between matter and light can be effectively increased by Co nanoparticles, which can also illustrate the high carrier mobility (Han et al., 2006; Ahlam et al., 2012). In addition, Co nanoparticles can effectively capture photogenerated carriers and can also inhibit the combination of carriers and holes in the local electric field (Li et al., 2017; Nasir et al., 2017). The formation of the space charge region formed by the Co dopant leads to a larger electron base, so the probability of transition becomes larger during the absorption of photon energy and the increase of the Co dopant content can provide more free carriers; thus, the increment of the free carriers leads to the enhancement of the nonlinear effect. Owing to the increase of excited state absorption and high carrier mobility brought by Co nanoparticles, FCA and TPA are successfully set up in the Co-doped Sb_2Se_3 nanofilms with the successful doping of Co into Sb_2Se_3. Therefore, the RSA behavior of the Co-doped Sb_2Se_3 nanofilms was observed at 980 and 1,030 nm. As the content of the Co dopant increases, the intensity of RSA behavior exhibits a corresponding increase. This phenomenon is because the increase of the content of Co dopant can provide more Co nanoparticles, thus providing more free carriers, which can further promote faster and stronger absorption in the excited state.

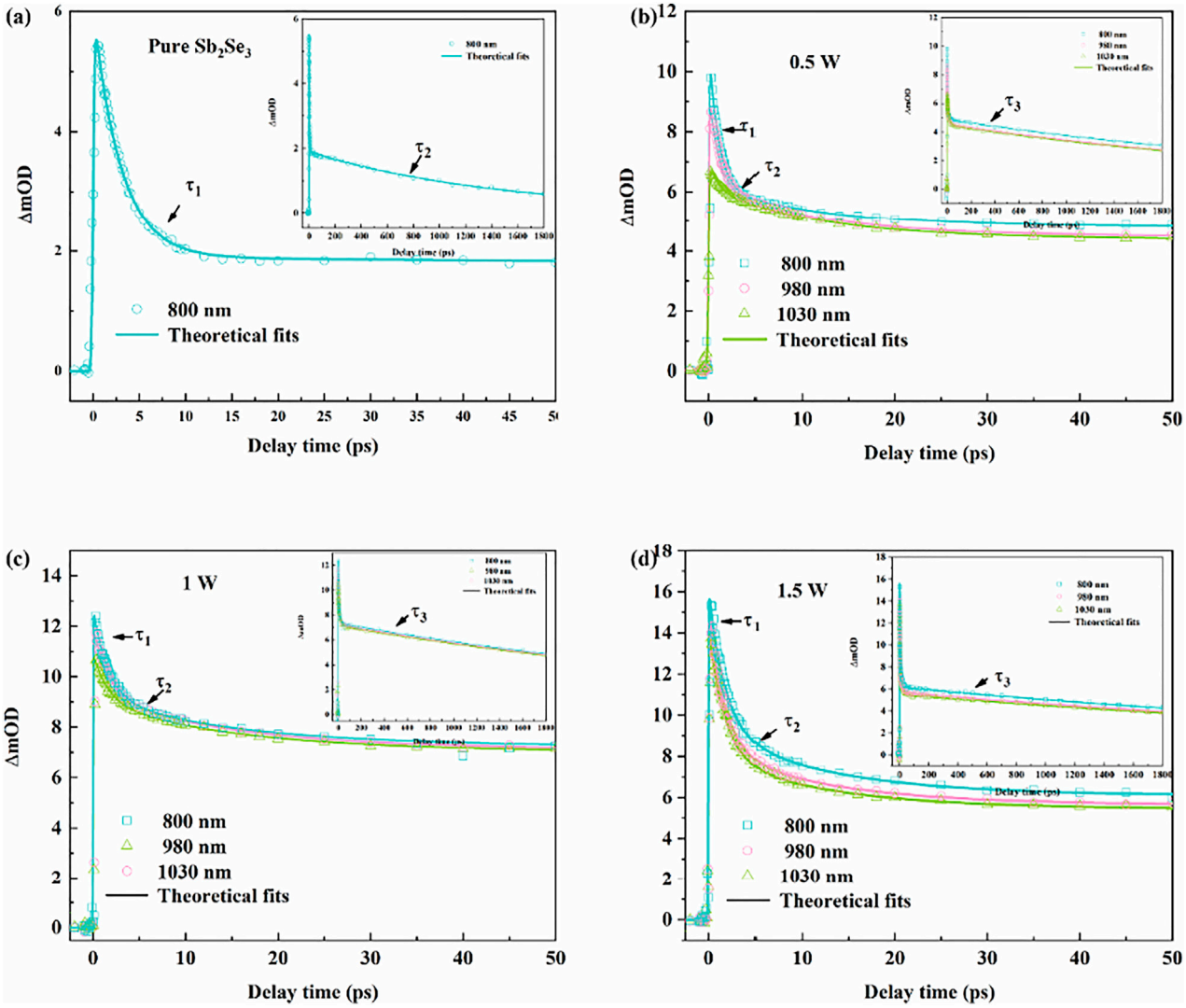

FIGURE 9 | (A) The transient nonlinear curve of pure Sb_2Se_3 nanofilm at different time scales. **(B–D)** The transient nonlinear curve of Co-doped Sb_2Se_3 (0.5, 1.0, and 1.5 W) thin films at different time scales.

The CA Z-scan signals (800, 980, and 1,030 nm) of the pure and Co-doped Sb_2Se_3 nanofilms were obtained by using the CA fs Z-scan experiment as shown in **Figure 7**. For the pure Sb_2Se_3 nanofilm, the CA Z-scan signal was observed at 800 nm, which can be attributed to Kerr refraction caused by the nonlinear systematic dispersion of bound electrons appearing near the intrinsic absorption edge although there was no CA Z-scan signal observed at 980 and 1,030 nm, and it can be caused by the weak Kerr refraction. For the Co-doped Sb_2Se_3 nanofilms, the CA Z-scan signals were observed at 800, 980, and 1,030 nm, which indicates the existence of high-order nonlinear refraction (FCR). In addition, with the increase of the Co dopant content, the amplitude of the CA Z-scan signals increased correspondingly. According to the results of the OA Z-scan signals of the Co-doped Sb_2Se_3 nanofilms, with the increase of the Co dopant content, more Co nanoparticles can be provided, which led to the increase of photogenerated carriers. Therefore, it can be concluded that the content of photogenerated carriers in the Co-doped Sb_2Se_3 nanofilms is relatively high, and the excess carriers can participate in the refraction of free carriers. Thus, it can be concluded that there are FCR at 980 and 1,030 nm, and the FCR is dominant. According to the plasma dispersion effect of carriers, the refraction effect of free carriers increases with the increase of incident wavelength (Soref and Bennett, 1987; Gao et al., 2005). Therefore, the Co-doped Sb_2Se_3 nanofilms exhibit a self-defocusing behavior at 980 and 1,030 nm, which are constructed by the FCR and Kerr refraction. In addition, we also obtained the CA Z-scan signals of the Co-doped Sb_2Se_3 nanofilm (1.5 W) and pure Sb_2Se_3 nanofilm, which were excited under different excitation energy at 800 nm as shown in **Figure 7D**. For the pure Sb_2Se_3 nanofilm, there was no change in CA

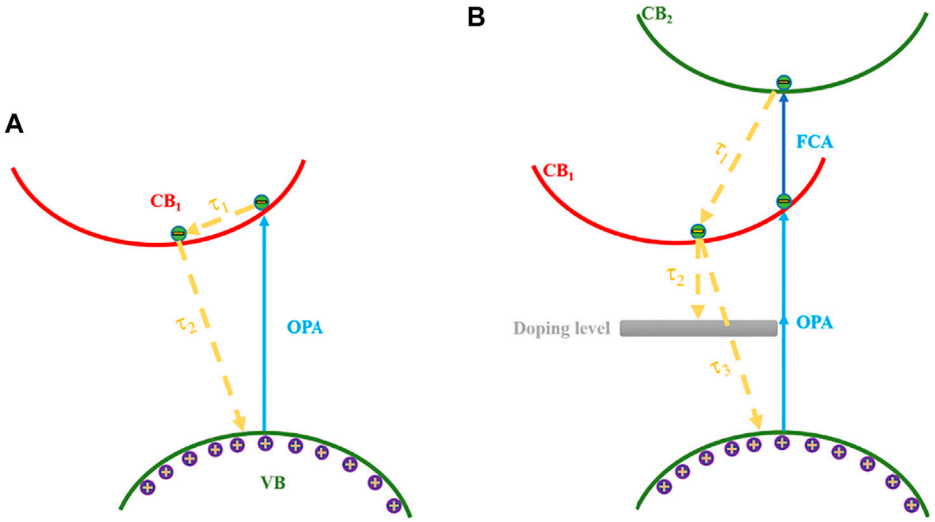

FIGURE 10 | (A) The process of pure Sb_2Se_3 nanofilm carrier relaxation time, OPA, and band. **(B)** The illustration of Co-doped Sb_2Se_3 nanofilm carrier relaxation time, OPA, and band.

Z-scan signals. For the Co-doped Sb_2Se_3 nanofilm (1.5 W), the signals of the CA Z-scan indicate that the amplitude of the nonlinear signal increases with the increase of the excitation energy. The reason for the phenomenon is that, with the increase of the excitation energy, excess carriers, which can participate in the refraction of the free carriers, are generated, thus leading to the enhancement of the refraction of the free carriers (Fang et al., 2013).

For nonlinear refraction, we assume that the incident laser has a Gaussian distribution, and then the sample transmittance on the far-field axis is proportional to the phase shift (Gao et al., 2005).

$$\Delta\varnothing = \frac{2\pi}{\lambda} L_{eff} n_2 I_0 \tag{4}$$

The effective thickness of the samples is denoted by L_{eff}, and $L_{eff} = 1 - e^{-\alpha_0 L}/\alpha_0$, where n_2 represents the nonlinear refractive index, L stands for the thickness of the samples, I_0 represents the light intensity at the focus, λ stands for the excitation wavelength, and α_0 represents the linear absorption coefficient of the thin film. For the Kerr system, the peak intensity of the incident laser and the nonlinear refractive index have the same radial profile. The interpolation formulas for the normalized peak-valley transmittance (ΔT_{p-v}) and peak-valley separation in z (ΔZ_{p-v}) are shown in **Eqs 5**, **6**; (Gao et al., 2005).

$$\Delta T_{P-V} = 0.406\Delta\varnothing \tag{5}$$

$$\Delta Z_{P-V} = 1.7 z_0 \tag{6}$$

The values of n_2 can be calculated by using **Eqs 4–6** and are shown in **Table 2**.

Transient Absorption Analysis

The nonlinear optical properties of pure and Co-doped Sb_2Se_3 nanofilms were **stu**died by transient absorption experiment. To ensure the excitation efficiency, the pumping light was set at 450 nm. The change of absorption intensity at a specific wavelength can be represented as the variation of the optical density (ΔOD), which is obtained by transient absorption spectroscopy. For the transient absorption experiment, ΔOD can be calculated as (Li et al., 2014)

$$\Delta OD\left(\lambda_p, t\right) = -\log_{10}\left(T_{on}/T_{off}\right) \tag{7}$$

where λ_p represents the wavelength of probing light, T_{on} represents the light of the probe, t stands for the delay time and the total transmittance of pumping, and the transmittance of probing light is denoted by T_{off}.

For the pure Sb_2Se_3 nanofilms, the RSA phenomenon was observed at 780–830 nm (ΔOD>0), but no nonlinear signal was detected in other probe regions (**Figures 8A,B**), which is in synchrony with the result of the fs Z-scan signal of the pure Sb_2Se_3 nanofilms. According to the results of linear absorption of the pure Sb_2Se_3 nanofilm, TPA occurs when the optical bandgap (Eg) is greater than $h\nu$ and less than $2h\nu$. With the successful doping of Co into Sb_2Se_3, TPA and FCA are successfully established in the Co-doped Sb_2Se_3 nanofilms, which is due to the increase of carrier mobility and excited-state absorption brought by Co nanoparticles. Co-doped Sb_2Se_3 nanofilms exhibit the RSA phenomenon with high transient absorption (ΔOD > 6.5), broadband nonlinear response (800–1,030 nm), and ultrafast carrier absorption (<1 picoseconds) at near infrared at **Figures 8C,D** compared with Sb_2Se_3 nanofilms.

Although the content of Co dopant increases, the carrier absorption rate and intensity of RSA of the Co-doped Sb_2Se_3 nanofilms exhibit a corresponding increase. In addition, the increase in the doping amount of Co can provide more Co nanoparticles, which can further promote the absorption of the excited state faster and stronger. When the DC sputtering power was increased to 1.5 W, the Co-doped Sb_2Se_3 nanofilm exhibited the strongest transient absorption (ΔOD > 15) and

ultrafast carrier absorption (<1 picoseconds) as shown in **Figure 8D**. Through the analysis of the transient spectrum, it can be seen that the transient absorption intensity of all Co-doped Sb_2Se_3 nanofilm is 800 < 980 < 1,030 nm; according to the plasma dispersion effect of carriers, the absorption and refraction effects of free carriers increase with the increase of incident wavelength. It is further confirmed that FCA and FCR play a dominant role in the nonlinear response at 980 and 1,030 nm. In all the transient absorption spectra, it can be found that the signal has no obvious movement during the whole delay time, which suggests that the TPA and FCA may be from the uniform energy level during the whole delay time (He et al., 2010). In addition, the sapphire substrate has no influence on the transient absorption experiment of the Co-doped and pure Sb_2Se_3 nanofilms. Moreover, the differences between Co-doped and pure Sb_2Se_3 nanofilms were measured by the Gaussian beam focal plane, which proves that the Co-doped and pure Sb_2Se_3 nanofilms do not suffer optical damage in the transient absorption experiment. **Figure 10** exhibits the schematic diagram of the energy levels of the Co-doped and pure Sb_2Se_3 nanofilms, one-photon absorption, and FCR.

Figure 9 shows the transient absorption fitting curves of pure and Co-doped Sb_2Se_3 (0.5, 1, and 1.5 W) nanofilms at different time scales under 450 nm laser excitation. For the pure and Co-doped Sb_2Se_3 nanofilms, there was no influence between the pump light and the carrier relaxation, which proves that the transient absorption experiment was carried out under steady conditions. Multiple exponential functions are selected to fit the transient absorption curve of the pure and Co-doped Sb_2Se_3 nanofilms, and the formula is as follows (Fang et al., 2017):

$$\frac{\Delta T}{T} = C_1 \exp(-t/\tau_1) + C_2 \exp(-t/\tau_2) \quad (8)$$

$$\frac{\Delta T}{T} = C_1 \exp(-t/\tau_1) + C_2 \exp(-t/\tau_2) + C_3 \exp(-t/\tau_3) \quad (9)$$

where C_3, C_2, and C_1 represent the amplitudes of the third, second, and first components, respectively. For the pure Sb_2Se_3 nanofilm, which was excited by 450 nm, the carrier relaxation time values (τ_1 and τ_2) were calculated as 1.74 ± 0.74 ps and 3.89 ± 0.73 ns. The values of transient absorption (τ_1, τ_2, and τ_3) of the Co-doped Sb_2Se_3 nanofilms under the same laser excitation were calculated as 1.58 ± 0.9 ps, 12.39 ± 0.21 ps, and 4.42 ± 0.82 ns (0.5 W); 1.32 ± 0.49 ps, 13.35 ± 0.4 ps, and 4.63 ± 0.81 ns (1.0 W); and 1.73 ± 0.99 ps, 12.03 ± 0.26 ps, and 4.89 ± 0.79 ns (1.5 W), respectively. The calculated results show that the doping amount of Co can adjust the carrier relaxation time of the Sb_2Se_3 nanofilms. In addition, the results also confirm that Co nanoparticles can effectively inhibit the composite process of carrier and hole, thus improving the FCA efficiency. The carrier relaxation processes for the pure and Co-doped Sb_2Se_3 nanofilms **are** shown in **Figure 10**. In the whole relaxation process of pure and Co-doped Sb_2Se_3 nanofilms, the different relaxation mechanisms determine the relaxation time of carriers at different steps. For the pure Sb_2Se_3 nanofilms, the τ_1 is caused by the cooling of thermal carriers, and the τ_2 is caused by the relaxation of nonradiative transition of carriers in the optical bandgap. Although for the Co-doped Sb_2Se_3 nanofilms, τ_3 is caused by the relaxation of nonradiative transition of carriers from CB to VB, the τ_2 is caused by the relaxation of nonradiative transition of carriers from CB to doping level, and the τ_1 is caused by the electron-phonon scattering.

CONCLUSION

In conclusion, this study confirms that the enhancement of excited state absorption at near infrared caused by FCA, FCR, TPA, and Kerr refraction is the main mechanism of the broadband nonlinear response of Co-doped Sb_2Se_3 films, which were prepared by magnetron sputtering. Compared with the pure Sb_2Se_3 nanofilm, the Co-doped Sb_2Se_3 nanofilms exhibit the following superior nonlinear optical properties. (I) Co-doped Sb_2Se_3 nanofilms exhibit ultrafast carrier absorption (ps) at near infrared and excellent broadband nonlinear response (800–1,030 nm). (II) High nonlinear absorption coefficients, high nonlinear refraction index, long carrier relaxation time, and the ultrafast carrier absorption of Co-doped Sb_2Se_3 nanofilms are determined by the content of the Co dopant. (III) The transient absorption intensity of Co-doped Sb_2Se_3 nanofilms (1.5 W) is achieved ΔOD>15. Finally, the Co-doped Sb_2Se_3 nanofilms provide more reference value for selecting more suitable elements as the dopants of Sb_2Se_3 to prepare the broadband nonlinear optical devices.

DATA AVAILABILITY STATEMENT

The original contributions presented in the study are included in the article/supplementary material, further inquiries can be directed to the corresponding author.

AUTHOR CONTRIBUTIONS

DS contributed to conception and design of the study. WHS organized the database. DS wrote the first draft of the manuscript. YF, WUS, QM, and XY contributed to manuscript revision, read, and approved the submitted version.

FUNDING

This work is supported by the National Natural Science Foundation of China (Grant No. 11504072), Natural Science Foundation of Heilongjiang Province (Grant No. LH 2020F032) and (Grant LH 2019A018); Key Laboratory for Photonic and Electronic Bandgap Material (Ministry of Education) and School of Physics and Electronic Engineering of Harbin Normal University of China, National Natural Science Foundation of China (No. 11704273), and Natural Science Foundation of Jiangsu Province, China (Grant No. BK20170375).

REFERENCES

Ahlam, M. A., Ravishankar, M. N., Vijayan, N., Govindaraj, G., Upadhyaya, V., and Prakash, A. P. G. (2012). The Effect of Co-60 Gamma Irradiation on Optical Properties of Some Nonlinear Optical (NLO) Single Crystals. *J. Opt.* 41, 158–166. doi:10.1007/s12596-012-0079-8

Ai, Y., Hsu, T. H., Wu, D. C., Lee, L., Chen, J.-H., Chen, Y.-Z., et al. (2018). An Ultrasensitive Flexible Pressure Sensor for Multimodal Wearable Electronic Skins Based on Large-Scale Polystyrene ball@reduced Graphene-Oxide Core-Shell Nanoparticles. *J. Mater. Chem. C* 6, 5514–5520. doi:10.1039/C8TC01153B

Andreev, Y. M., Kokh, K. A., Lanskii, G. V., and Morozov, A. N. (2011). Structural Characterization of Pure and Doped GaSe by Nonlinear Optical Method. *J. Cryst. Growth* 318, 1164–1166. doi:10.1016/j.jcrysgro.2010.10.194

Cao, X. Y., Xin, J. B., Wang, Y. Y., Hu, J. M., and Qu, X. R. (2014). Preparation of Er-Doped (Bi2Te3)0.90(Sb2Te3)0.05(Sb2Se3)0.05 by Mechanical Alloying and its Thermoelectric Properties. *Mater. Sci. Eng. B Solid State. Mater. Adv. Technol.* 188, 54–58. doi:10.1016/j.mseb.2014.06.007

Cattaruzza, E., Battaglin, G., Visentin, F., and Trave, E. (2009). Er-doped SiO2 Films by Rf Magnetron Co-sputtering. *J. Non-Crystalline Sol.* 355, 1128–1131. doi:10.1016/j.jnoncrysol.2008.11.031

Choi, J., Lee, H.-W., Kim, B.-S., Park, H., Choi, S., Hong, S. C., et al. (2006). Magnetic and Transport Properties of Mn-Doped Bi2Se3 and Sb2Se3. *J. Magnetism Magn. Mater.* 304, e164–e166. doi:10.1016/j.jmmm.2006.02.041

Djordjevic, I. B., and Arabaci, M. (2010). LDPC-coded Orbital Angular Momentum (OAM) Modulation for Free-Space Optical Communication. *Opt. Express* 18, 24722–24728. doi:10.1364/OE.18.024722

Fang, Y., Wu, X.-Z., Ye, F., Chu, X.-Y., Li, Z.-G., Yang, J.-Y., et al. (2013). Dynamics of Optical Nonlinearities in GaN. *J. Appl. Phys.* 114, 103507. doi:10.1063/1.4820929

Fang, Y., Xiao, Z., Wu, X., Zhou, F., Yang, J., Yang, Y., et al. (2015). Optical Nonlinearities and Ultrafast All-Optical Switching of M-Plane GaN in the Near-Infrared. *Appl. Phys. Lett.* 106, 251903. doi:10.1063/1.4923184

Fang, Y., Yang, J., Xiao, Z., Zhang, J., Chen, Y., Wu, Q., et al. (2017). Ultrafast All-Optical Modulation in Fe-Doped GaN at 1.31 and 1.55 μm with High Contrast and Ultralow Power. *Appl. Phys. Lett.* 110, 161902. doi:10.1063/1.4980090

Fang, Y., Yang, J., Yang, Y., Wu, X., Xiao, Z., Zhou, F., et al. (2016). Ultrafast Carrier Dynamics in Ap-type GaN Wafer under Different Carrier Distributions. *J. Phys. D: Appl. Phys.* 49, 045105. doi:10.1088/0022-3727/49/4/045105

Filipchenko, A. S., and Naurizbaev, A. (1976). Moss-burstein Effect in N-type Crystals of Indium Antimonide. *Phys. Stat. Sol. (A)* 37, K139–K142. doi:10.1002/pssa.2210370252

Gao, Y., Zhang, X., Li, Y., Liu, H., Wang, Y., Chang, Q., et al. (2005). Saturable Absorption and Reverse Saturable Absorption in Platinum Nanoparticles. *Opt. Commun.* 251, 429–433. doi:10.1016/j.optcom.2005.03.003

Han, H., Song, Y., Hou, H., Fan, Y., and Zhu, Y. (2006). A Series of Metal-Organic Polymers Assembled from MCl2(M = Zn, Cd, Co, Cu): Structures, Third-Order Nonlinear Optical and Fluorescent Properties. *Dalton Trans.* 16, 1972–1980. doi:10.1039/b514431k

He, X., Wang, Y., Yang, Z., Ma, Y., and Yang, Y. (2010). Cooperative Enhancement of TPA in Cruciform Double-Chain DSB Derivation: a Femtosecond Transient Absorption Spectra Study. *Appl. Phys. B* 100, 773–777. doi:10.1007/s00340-010-4161-0

Henari, F. Z., and Dakhel, A. A. (2011). Observation of Simultaneous Reverse Saturation Absorption and Saturation Absorption in Silver Nanoparticles Incorporated into Europium Oxide Thin Film. *Opt. Commun.* 284, 651–655. doi:10.1016/j.optcom.2010.09.090

Hymavathi, B., Rajesh Kumar, B., and Subba Rao, T. (2017). Thickness Dependent Optical Dispersion Parameters and Nonlinear Optical Properties of Nanostructured Cr Doped CdO Thin Films. *Opt. Quant Electron.* 49, 86. doi:10.1007/s11082-017-0935-5

Jia, J., Wu, X., Fang, Y., Yang, J., Guo, X., Xu, Q., et al. (2018). Ultrafast Broad-Band Optical Limiting in Simple Hydrazone Derivatives with a Π-Conjugated System: Effect of Two-Photon-Induced Singlet-State Absorption. *J. Phys. Chem. C* 122, 16234–16241. doi:10.1021/acs.jpcc.8b02149

Jiang, J., Hu, W., Xie, D., Yang, J., He, J., Gao, Y., et al. (2019). 2D Electric-Double-Layer Phototransistor for Photoelectronic and Spatiotemporal Hybrid Neuromorphic Integration. *Nanoscale* 11, 1360–1369. doi:10.1039/C8NR07133K

Lakhwani, G., Roijmans, R. F. H., Kronemeijer, A. J., Gilot, J., Janssen, R. A. J., and Meskers, S. C. J. (2010). Probing Charge Carrier Density in a Layer of Photodoped ZnO Nanoparticles by Spectroscopic Ellipsometry. *J. Phys. Chem. C* 114, 14804–14810. doi:10.1021/jp104846h

Lee, H., Yang, W., Tan, J., Oh, Y., Park, J., and Moon, J. (2019). Cu-Doped NiOx as an Effective Hole-Selective Layer for a High-Performance Sb2Se3 Photocathode for Photoelectrochemical Water Splitting. *ACS Energ. Lett.* 4, 995–1003. doi:10.1021/acsenergylett.9b00414

Li, H. B., Qiao, Y. F., Li, J., Fang, H. L., Fan, D. H., and Wang, W. (2017). A Sensitive and Label-free Photoelectrochemical Aptasensor Using Co-doped ZnO Diluted Magnetic Semiconductor Nanoparticles. *Biosens. Bioelectron.* 94, 554–565. doi:10.1016/j.bios.2015.09.066

Li, Y., Zhou, Y., Zhu, Y., Chen, C., Luo, J., Ma, J., et al. (2016). Characterization of Mg and Fe Doped Sb2Se3 Thin Films for Photovoltaic Application. *Appl. Phys. Lett.* 109, 232104. doi:10.1063/1.4971388

Li, Z.-g., Zhao, R., Li, W., Wang, H., Yang, H., and Song, Y.-l. (2014). Strain Dependent Ultrafast Carrier Dynamics in EuTiO3 Films. *Appl. Phys. Lett.* 105, 162904. doi:10.1063/1.489878710.1063/1.4898787

Lin, H., Chen, L., Zhou, L.-J., and Wu, L.-M. (2013). Functionalization Based on the Substitutional Flexibility: Strong Middle IR Nonlinear Optical Selenides AXII4XIII5Se12. *J. Am. Chem. Soc.* 135, 12914–12921. doi:10.1021/ja4074084

Liu, C., Yuan, Y., Cheng, L., Su, J., Zhang, X., Li, X., et al. (2019). Tunable Nonlinear Optical Absorption in Amorphous and Crystalline Sb2Se3 Thin Films. *J. Alloys Comp.* 791, 753–760. doi:10.1016/j.jallcom.2019.03.295

Mahani, R., and El-Sayad, E. A. (2019). Effect of Sulfur Doping on the Dielectric Properties of Sb2Se3 System. *J. Adv. Dielect.* 09, 1950001. doi:10.1142/S2010135X19500012

Major, A., Yoshino, F., Aitchison, J. S., Smith, P. W. E., Sorokin, E., and Sorokina, I. T. (2004). Ultrafast Nonresonant Third-Order Optical Nonlinearities in ZnSe for Photonic Switching at Telecom Wavelengths. *Appl. Phys. Lett.* 85, 4606–4608. doi:10.1063/1.1823599

Medina, H., Li, J.-G., Su, T.-Y., Lan, Y.-W., Lee, S.-H., Chen, C.-W., et al. (2017). Wafer-Scale Growth of WSe2 Monolayers toward Phase-Engineered Hybrid WOx/WSe2 Films with Sub-ppb NOx Gas Sensing by a Low-Temperature Plasma-Assisted Selenization Process. *Chem. Mater.* 29, 1587–1598. doi:10.1021/acs.chemmater.6b04467

Molli, M., Pradhan, P., Dutta, D., Jayaraman, A., Bhat Kademane, A., Muthukumar, V. S., et al. (2016). Study of Nonlinear Optical Absorption Properties of Sb2Se3 Nanoparticles in the Nanosecond and Femtosecond Excitation Regime. *Appl. Phys. A.* 122, 549. doi:10.1007/s00339-015-9568-3

Nasir, Z., Shakir, M., Wahab, R., Shoeb, M., Alam, P., Khan, R. H., et al. (2017). Co-precipitation Synthesis and Characterization of Co Doped SnO 2 NPs, HSA Interaction via Various Spectroscopic Techniques and Their Antimicrobial and Photocatalytic Activities. *Int. J. Biol. Macromolecules* 94, 554–565. doi:10.1016/j.ijbiomac.2016.10.057

Ning, H., Guo, H., Zhang, J., Wang, X., Jia, X., Qiu, J., et al. (2021). Enhancing the Efficiency of Sb2S3 Solar Cells Using Dual-Functional Potassium Doping. *Solar Energ. Mater. Solar Cell* 221, 110816. doi:10.1016/j.solmat.2020.110816

Radisavljevic, B., and Kis, A. (2013). Mobility Engineering and a Metal-Insulator Transition in Monolayer MoS2. *Nat. Mater* 12, 815–820. doi:10.1038/NMAT3687

Ren, D., Luo, X., Chen, S., Zheng, Z., Cathelinaud, M., Liang, G., et al. (2020). Structure, Morphology, and Photoelectric Performances of Te-Sb2Se3 Thin Film Prepared via Magnetron Sputtering. *Nanomaterials* 10, 1358–1371. doi:10.3390/nano10071358

Soref, R., and Bennett, B. (1987). Electrooptical Effects in Silicon. *IEEE J. Quan. Electron.* 23, 123–129. doi:10.1109/JQE.1987.1073206

Tian, F. H., and Liu, C. B. (2006). DFT Description on Electronic Structure and Optical Absorption Properties of Anionic S-Doped Anatase TiO2. *J. Phys. Chem. B* 110, 17866–17871. doi:10.1021/jp0635462

Tuhl, A., Manaa, H., Makhseed, S., Al-Awadi, N., Mathew, J., Ibrahim, H. M., et al. (2012). Reverse Saturation Absorption Spectra and Optical Limiting Properties of Chlorinated Tetrasubstituted Phthalocyanines Containing Different Metals. *Opt. Mater.* 34, 1869–1877. doi:10.1016/j.optmat.2012.05.018

Volz, T., Reinhard, A., Winger, M., Badolato, A., Hennessy, K. J., Hu, E. L., et al. (2012). Ultrafast All-Optical Switching by Single Photons. *Nat. Photon* 6, 605–609. doi:10.1038/nphoton.2012.181

Wang, J., Yang, C., Huang, Z., Humphrey, M. G., Jia, D., You, T., et al. (2012). Seed-catalyzed Heteroepitaxial Growth and Nonlinear Optical Properties of Zinc Selenide Nanowires. *J. Mater. Chem.* 22, 10009–10014. doi:10.1039/c2jm00091a

Wu, M., Yu, S., Chen, G., He, L., Yang, L., and Zhang, W. (2015). Structural, Optical, and Electrical Properties of Mo-Doped ZnO Thin Films Prepared by Magnetron Sputtering. *Appl. Surf. Sci.* 324, 791–796. doi:10.1016/j.apsusc.2014.11.039

Zhou, Y., Wang, L., Chen, S., Qin, S., Liu, X., Chen, J., et al. (2015). Thin-film Sb2Se3 Photovoltaics with Oriented One-Dimensional Ribbons and Benign Grain Boundaries. *Nat. Photon* 9, 409–415. doi:10.1038/nphoton.2015.78

Conflict of Interest: The authors declare that the research was conducted in the absence of any commercial or financial relationships that could be construed as a potential conflict of interest.

Publisher's Note: All claims expressed in this article are solely those of the authors and do not necessarily represent those of their affiliated organizations, or those of the publisher, the editors and the reviewers. Any product that may be evaluated in this article, or claim that may be made by its manufacturer, is not guaranteed or endorsed by the publisher.

frontiers in Materials

ORIGINAL RESEARCH
published: 13 September 2021
doi: 10.3389/fmats.2021.717760

The Broadband Nonlinear Optical Response in Graphene/MoS_2/Ag Thin Films at Near Infrared

Di Sun[1], Yu Fang[2], Xiaoyan Yan[3], Wen Shan[1], Wenjun Sun[4] and Qingyu Meng[4]*

[1]School of Physics and Electrical Engineering, Harbin Normal University, Harbin, China, [2]Jiangsu Key Laboratory of Micro and Nano Heat Fluid Flow Technology and Energy Application, School of Physical Science and Technology, Suzhou University of Science and Technology, Suzhou, China, [3]Department of Physics, Harbin Institute of Technology, Harbin, China, [4]Key Laboratory of Photonic and Electric Bandgap Materials, Ministry of Education, School of Physics and Electronic Engineering, Harbin Normal University, Harbin, China

Graphene/MoS_2/Ag thin films were successfully prepared by the magnetron sputtering technique and liquid phase exfoliation. Structure, morphology, optical properties, and nonlinear optical characteristics of the graphene/MoS_2/Ag and graphene/MoS_2 thin films were studied by X-ray diffractometer, spectrophotometer, field-scanning electron microscope, and femtosecond (fs) Z-scan technique. The results of the fs Z-scan experiment indicate that the graphene/MoS_2/Ag thin films exhibit reverse saturable absorption properties due to the free carrier absorption and two-photon absorption. More importantly, with the increase of DC magnetron sputtering power (from 5 to 15 W), the local surface plasmon resonance effect of the Ag thin films increases, which leads to the enhancement of nonlinear optical properties of the graphene/MoS_2/Ag thin films. The nonlinear absorption coefficients of the graphene/MoS_2/Ag thin films are increased from 1.14×10^{-10} to 1.8×10^{-10} m/W at 800 nm and from 4.79×10^{-11} to 6.79×10^{-11} m/W at 1,030 nm, and the nonlinear refraction index of the graphene/MoS_2/Ag thin films is -4.37 × 10^{-17}~–4.18 × 10^{-16} m^2/W under the excitation of 800 and 1,030 nm, respectively. Moreover, when the graphene/MoS_2/Ag thin films were excited at 800 and 1,030 nm, respectively, the nonlinear figure of merit values of the graphene/MoS_2/Ag thin films are increased from 1.23 to 2.91 and from 1.30 to 1.47, which are enough to support the application of the graphene/MoS_2/Ag thin films in the field of all-optical switching applications.

Keywords: nonlinear FOM, graphene/MoS_2/Ag thin films, broadband response, Z-scan, nonlinear optical response

OPEN ACCESS

Edited by:
Zhongquan Nie,
Taiyuan University of Technology, China

Reviewed by:
Atul Thakre,
Hanyang University, South Korea
Junyi Yang,
Soochow University, China

****Correspondence:***
Wenjun Sun
swjgood0139@139.com

Specialty section:
This article was submitted to Quantum Materials, a section of the journal Frontiers in Materials

Received: *31 May 2021*
Accepted: *04 August 2021*
Published: *13 September 2021*

Citation:
Sun D, Fang Y, Yan X, Shan W, Sun W and Meng Q (2021) The Broadband Nonlinear Optical Response in Graphene/MoS_2/Ag Thin Films at Near Infrared. Front. Mater. 8:717760. doi: 10.3389/fmats.2021.717760

INTRODUCTION

In recent years, graphene is widely studied due to **its** large carrier mobility and high optical absorption property (Katsnelson et al., 2009; Gao et al., 2019). However, the zero band gap property limits the research and application of graphene in the optoelectronics field. As the research develops in depth, it can be found that the emergence of graphene composite systems can solve this issue. Among these, they exhibit superior optical, electrical, and chemical properties to graphene; thus, the graphene/MoS_2 nanocomposites have been extensively studied (Fu et al., 2014; Yu et al., 2014; Kwon and Kim, 2018). Compared with graphene, the graphene/MoS_2 nanocomposites exhibit higher photoresponse (Zhang et al., 2014), higher dielectric constant,

and higher linear absorption (Jiang et al., 2015; He et al., 2017; Qiu et al., 2018; Sun et al., 2018; Xu et al., 2020) due to the excellent properties of the graphene/MoS_2; the graphene/MoS_2 nanocomposites can be widely used in the manufacture of dye-sensitized solar cells, electrical sensors, and transistors (Liu et al., 2012; Huang et al., 2013; He et al., 2014). In the field of nonlinear optics, the reverse saturable absorption (RSA) property, which is shown by graphene/MoS_2 thin film, shows that the light transmittance decreases with the increase of incident light (Ouyang et al., 2013), and it can be widely used in all optical switches, optical sensors, and other fields (Vabbina et al., 2015; Chen et al., 2016; Iqbal et al., 2019). Nevertheless, graphene/MoS_2 thin films still face many challenges, such as nonlinear response and high nonlinear figure of merit (FOM) values.

To further raise the nonlinear broadband optical response of graphene/MoS_2 thin film and increase the wide application in all optical devices, a novel structure was designed here, and it uses the noble metal to composite the graphene/MoS_2 thin films. Among the numerous noble metals, silver was chosen to composite the graphene/MoS_2 thin films due to its localized surface plasmon resonance (LSPR) effect, which can effectively capture photogenerated carriers and restrain the recombination between carriers and holes (Li et al., 2007; Zheng et al., 2007; Akhavan, 2009; Charles et al., 2009; Jiang et al., 2012). In addition, the LSPR effect of Ag can provide more free carriers to construct free carrier absorption (FCA) in the graphene/MoS_2/Ag thin films, and the FCA can effectively promote the excited state absorption at near infrared, thus leading to the nonlinear optical response move to broadband. Moreover, the addition of Ag has a good composite significance, because of which it can effectively regulate the optical band gap of the graphene/MoS_2/Ag thin films and promote the FCA and TPA (Shahriari et al., 2017). Therefore, the closed-aperture (CA) Z-scan signals of the graphene/MoS_2/Ag thin films were obtained at near infrared due to the free carrier refraction (FCR), which is constructed by the free carriers provided by the LSPR effect of Ag. Moreover, the nonlinear absorption coefficient and nonlinear refractive index of the graphene/MoS_2/Ag thin films were obtained from the broadband nonlinear signals of the graphene/MoS_2/Ag thin films, which is of great significance for evaluating the nonlinear FOM value and the application of all-optical switches. With the composite of Ag, the nonlinear FOM values of graphene/MoS_2/Ag thin films can be improved successfully and can be widely used in all-optical switching devices.

In this work, graphene/MoS_2/Ag thin films with different magnetron sputtering power in the Ag target (5, 10, and 15 W), and graphene/MoS_2 thin films were successfully prepared by using magnetron sputtering technology and liquid phase exfoliation. The graphene/MoS_2/Ag thin films show a broadband nonlinear optical response, larger nonlinear absorption coefficient, and higher nonlinear refractive index at near infrared, and the nonlinear absorption coefficient and nonlinear refractive index of the graphene/MoS_2/Ag thin films can be determined by the content of the Ag thin films. The nonlinear absorption coefficients of graphene/MoS_2/Ag thin films (from 5 to 15 W) are from 1.14×10^{-10} to 1.8×10^{-10} m/W at 800 nm and from 4.79×10^{-11} to 6.79×10^{-11} m/W at 1,030 nm, respectively. The nonlinear refractive index of the graphene/MoS_2/Ag thin films (from 5 to 15 W) are from -1.12×10^{-16} to -4.18×10^{-16} m^2/W at 800 nm and from -4.37×10^{-17} to -8.00×10^{-17} m^2/W at 1,030 nm, respectively. Moreover, the nonlinear FOM values of graphene/MoS_2/Ag thin films (from 5 to 15 W) are from 1.23 to 2.91 at 800 nm and from 1.30 to 1.47 at 1,030 nm. Surprisingly, compared with the graphene/MoS_2 thin film, the FOM values of the graphene/MoS_2/Ag thin films are successfully improved under the same excitation conditions, which can be widely used in all-optical switching devices.

EXPERIMENT

Materials

The sputtering target of Ag (99.99% purity, 6.0 cm diameter, 0.6 cm thickness) was purchased from Hebei Qinbang New Material Technology Co. The filter membranes (220 nm diameter) that were used to deposit graphene/MoS_2 thin films were purchased from Tianjin Jinteng Co. Ltd. The flake graphite used for the liquid phase exfoliation technique was purchased from Sinopharm Chemical Reagent Co. Ltd. The MoS_2 used for the liquid phase exfoliation technique was purchased from Shanghai Acmec Biochemical Co. Ltd. The N-methyl-2-pyrrolidone solvent (NMP) used for the dispersant of graphene/MoS_2 was purchased from Tian in Fuyu Fing Chemical Co. Ltd.

Sample Preparation

The Ag thin films were precisely deposited on the sapphire substrate by direct current (DC) magnetron sputtering. The sapphire substrate was, respectively, washed by anhydrous ethanol, deionized water, and acetone for 15 min until the substrate was completely clean and then dried at room temperature. The precise sputtering power of 5, 10, and 15 W in the Ag target can be achieved by regulating the magnetron sputtering conditions (current and voltage). During the deposition, high-purity argon was employed as a working gas (purity 99.999 vol%) with a gas flow rate of 20 sccm, and the working pressure was 1.0 Pa, the sputtering time was 35 s, the sputtering temperature was 25°C, and the vacuum of the sputtering room was 5.5×10^{-4} Pa.

The graphene/MoS_2 thin films were prepared by the liquid phase exfoliation technology. The NMP **is** widely used as the dispersing agent for the graphene and MoS_2 in the report; thus, the NMP was selected as the dispersing agent for the graphene/MoS_2 (Kim et al., 2015; Hua et al., 2017; Qi et al., 2017). The graphite and MoS_2 powders at a weight ratio of 1:1 were dispersed in NMP to fabricate dispersion. The concentration of the dispersion was 0.2 mg/ml. Then, the dispersion was sonicated for 1–2 h at a high power of 600 W, which can produce such a result that the graphite and the MoS_2 are well exfoliated. The obtained suspension was centrifuged at 6,000 rpm/min for 1 h,

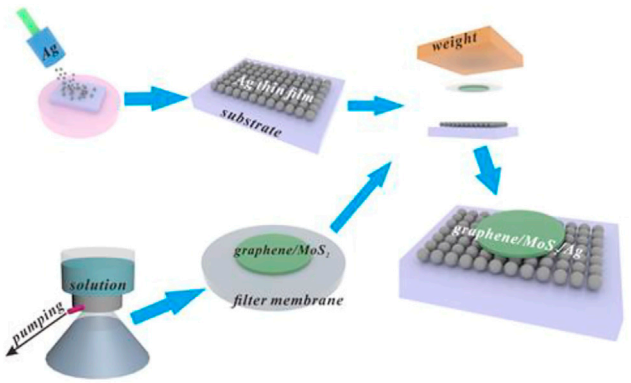

FIGURE 1 | Graphene/MoS_2/Ag thin film preparation process and structure diagram.

and half of the supernatant was extracted. The formation of the graphene/MoS_2 thin films were made by using 40 ml supernatant to be deposited on the 220 nm pore size membranes by a vacuum filtration technique and then naturally dried at room temperature.

Then, the dried films were put upside down on the prepared Ag thin films and pressure applied with a 2 kg weight to make the graphene/MoS_2 thin films better fit on the Ag thin films. The weight was removed after 2 h, and then the graphene/MoS_2/Ag thin films (with the filter membranes) were washed with the acetone, which was used to remove the filter membranes. After washing, the graphene/MoS_2/Ag thin films were placed at room temperature and then dried naturally for 1 h, and finally, the graphene/MoS_2/Ag thin films were successfully prepared. The schematic diagram of the graphene/MoS_2/Ag thin film preparation process is shown in **Figure 1**. To make the expression more concise, A and B are used to represent the graphene/MoS_2 and the graphene/MoS_2/Ag thin films, where B_1, B_2, and B_3 are, respectively, used to represent the graphene/MoS_2/Ag (5, 10, and 15 W) thin films.

Instruments

The morphology and thickness of A and B thin films were observed by field-scanning electron microscope (FE-SEM) (SU70, Hitachi, Japan), the X-ray diffractometer (XRD) pattern was characterized by XRD (D8, Bruker, Germany), and the linear absorption spectrum of A and B thin films was characterized by spectrophotometer (Uv-Vis) (Uv-3600i PLUS, SHIMADZU, Japan).

The nonlinear optical characteristics of A and B thin films were tested by femtosecond (fs) Z-Scan experiments. The light source used an optical parameter amplifier (Light Conversion ORPHEUS), which was pumped by a mode-locked Yb:KGW fiber laser. The measurement parameters were set at 190 fs pulse and 20 Hz, and the waist radius of the laser was 33 μm. The energies of the laser excitation were set at 400, 500, and 600 nJ, respectively. The fs Z-scan experiment was carried out with the device described in the report (Wang et al., 2001; Yao et al., 2013).

RESULTS AND DISCUSSION

Structure Analysis

Figure 2 shows the XRD patterns of A and B thin films. The XRD patterns show that A and B thin films both present the polycrystalline structure. For the A thin film, compared with the XRD standard card (PDF#17-0744), the diffraction characteristic peak of MoS_2 (003) **was** detected at 14.53° (2θ) with the lattice spacing of 6.09 nm. The diffraction characteristic peak of graphene (002) **was** detected at 26.6° (2θ) with the lattice spacing of 3.69 nm (PDF#41-1,487), which is consistent with reports in the literature; it can be confirmed that the graphene is successfully prepared by liquid phase exfoliation (Wang et al., 2017). For the B thin films with the successful composite of the Ag thin films, the diffraction characteristic peaks of graphene (002) and MoS_2 (003) were enhanced; the diffraction characteristic peak of Ag (200) was detected at 44.27° (2θ) with the lattice spacing of 2.038 nm (PDF#04–0783). Compared with the XRD standard card (PDF#17-0744), the diffraction characteristic peak of MoS_2 (006) was also detected at 29.35° (2θ) with the lattice spacing of 3.04 nm. In addition, the increase of magnetron sputtering power in the Ag target induces the enhancement of the diffraction characteristic peaks of Ag (200), and the highest XRD intensity **was** obtained at the B thin film (15 W). Moreover, we also calculated the lattice constants of graphene, MoS_2, and Ag in the B thin film, which are 6.64, 3.16, and 4.08 nm, respectively, in which the lattice constant of MoS_2 is consistent with the few layers MoS_2 in the report (Ghadiyali and Chacko, 2019; Qi et al., 2019; Cior et al., 2020). The obtained results are consistent with the literature. The results of the XRD pattern show that the B thin films are successfully prepared.

Morphology and Optical Properties Analysis

The morphologies and thicknesses of the Ag thin films under different DC magnetron sputtering powers were obtained by SEM as shown in **Figures 3A–C**. The distribution of Ag nanoparticles in the Ag thin films are uniform, and with the increase of magnetron sputtering power, the size of the Ag particles increases accordingly. In addition, the average Ag particle size of the Ag thin films under different DC magnetron sputtering power was also calculated as 18 (5 W), 24 (10 W), and 30 nm (15 W), respectively. **Figures 3D–F** exhibit the thickness of the Ag films. With the increase of the magnetron sputtering power, the thickness of the Ag thin films increases from 50 to 90 nm.

The morphology and thickness of the B thin films were characterized by SEM as shown in **Figure 4**. To observe the morphology of the B thin films more intuitively, the edge of the A thin film was selected for shooting so as to distinguish between the Ag thin film and the graphene/MoS_2 thin film as shown in **Figure 4A**. In addition, the thickness of the B thin films (from 5 to 15 W) was characterized by SEM and is shown in **Figure 4B–D**. The thickness of the B thin films is 350, 370, and 390 nm, respectively, which corresponds to the B thin films with the different magnetron sputtering power of 5, 10, and 15 W, respectively. It can be seen from the SEM that the successful composite of Ag thin films improves the thickness of the B thin films. It can be inferred that the thickness of graphene/MoS_2 thin

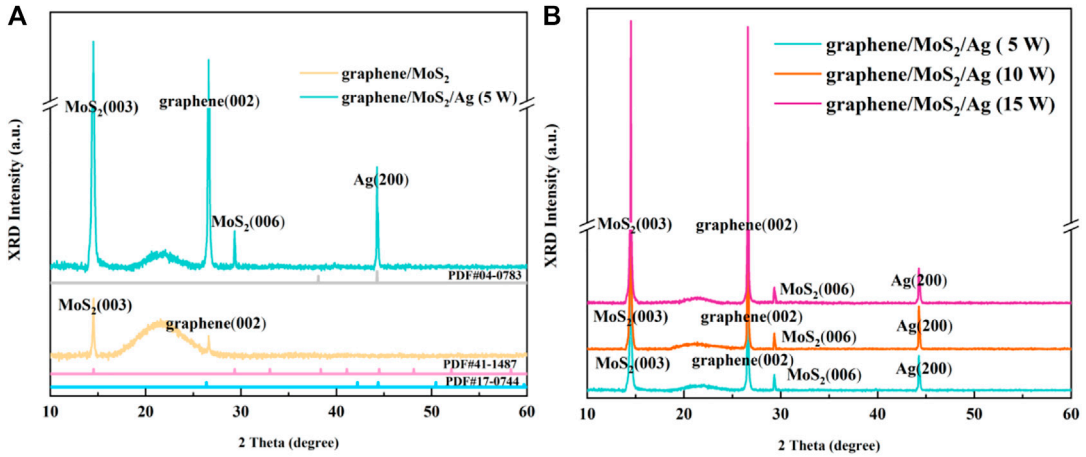

FIGURE 2 | (A) The XRD patterns of the A and B thin films (5 W). **(B)** The XRD patterns of the B thin films (from 5 to 15 W).

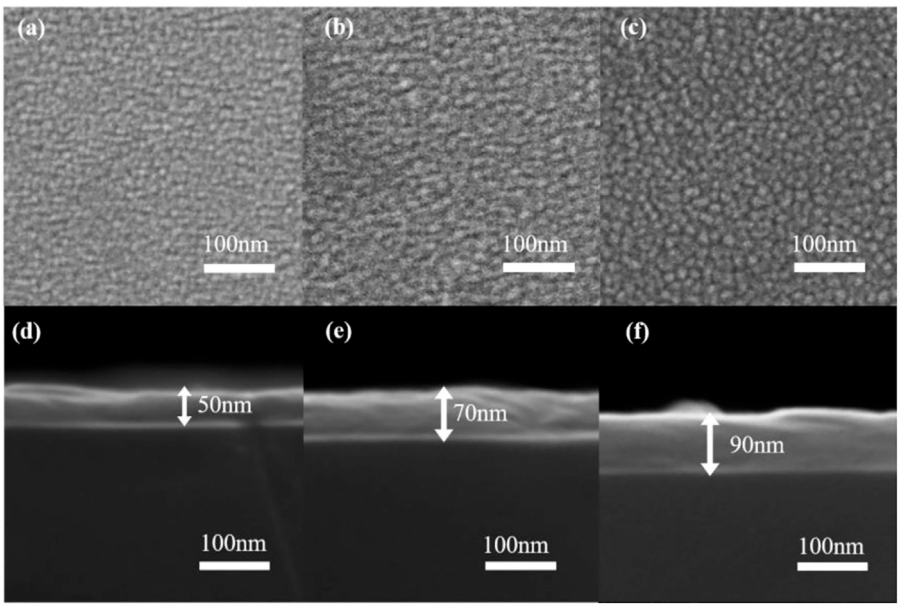

FIGURE 3 | (A) The morphology of the Ag thin film under 5 **(A)**, 10 **(B)**, and 15 W **(C)** DC magnetron sputtering power. **(D)** The thickness of the Ag thin film under 5 **(D)**, 10 **(E)**, and 15 W **(F)** DC magnetron sputtering power.

film **is** 300 nm. In past reports, the absorption of the composite films **is** enhanced with the increase of the content of Ag films; thus, we preliminarily infer that the absorption of the graphene/MoS_2/Ag thin films is enhanced with the increase of the thickness of the Ag thin films.

The linear absorption and transmission spectrums of the A and the B thin films were tested by spectrophotometer as shown in **Figure 5**. It can be seen from **Figure 5A** that A and B thin films exhibit two obvious absorption peaks, which are caused by the two exciton transition absorption peaks A and B at the Brillouin K/K′ point due to the direct band gap transition of MoS_2 (Yin et al., 2019). In addition, with the increase of the magnetron sputtering power in the Ag target, the absorption peak of the B thin films exhibits a tendency of red shift that is consistent with the report by Yang et al., and it can be seen from the report that the light absorption of metal nanoparticles is affected by the size of the metal nanoparticles, and the conclusion is that the size of the Ag nanoparticles in Ag thin films can be affected by the increase of the magnetron sputtering power in the Ag target, which was given in SEM. With the increase of the magnetron sputtering power in the Ag target, the size of the Ag nanoparticles increases. The increase of the size of the Ag nanoparticles can lead to the lattice contraction of the nanoparticles, which leads to the decrease of the resonance

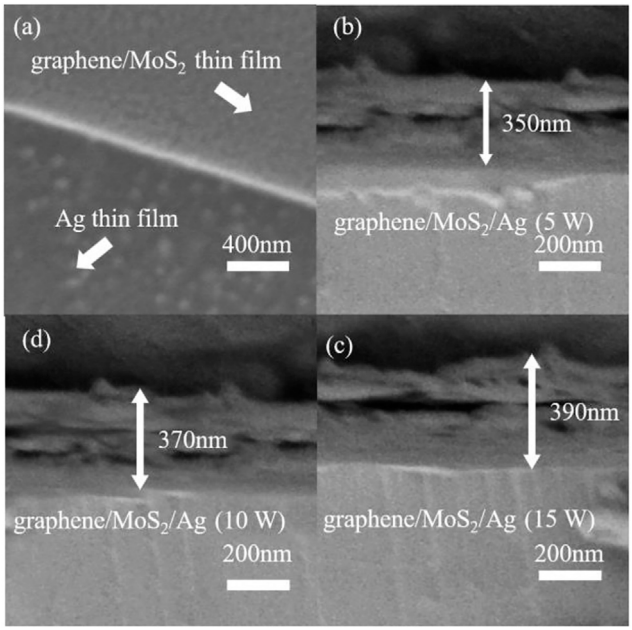

FIGURE 4 | (A) The morphology of the B thin film and the thickness of the B_1 **(B)**, B_2 **(C)**, and B_3 **(D)** thin films.

frequency of the surface plasmons. Thus, the absorption peak of the B thin films is red shifted. In addition, with the composite of the Ag thin films, the LSPR effect of the Ag nanoparticles can lead to the electron filling of graphene/MoS_2 bang; thus, the overall bang gap of the B thin films decreases, leading to an increased absorption of the B thin films. This result confirms the correct inference that the absorption of the B thin films increases as the thickness of the Ag thin films increases. For the linear absorption, we have that Tacu's formulation is given as follows (Qian et al., 2014):

$$\alpha = \frac{A}{h\nu}\left(h\nu - E_g\right)^n \quad (1)$$

where α is the coefficient of linear absorption, A is a constant, n is an index (n = 1, 2, 3), $h\nu$ is the energy of the incident photon, and E_g is the optical bandwidth. The optical band width of A and B thin films **were** calculated as 1.77 eV, 1.73 eV (5 W), 1.70 eV (10 W), and 1.62 eV (15 W), respectively. **Figure 5B** exhibits the transmission spectrum of the A and B thin films. It can be clearly seen that the A and B thin films both exhibit more than 65% transmission in the range of 800–1,050 nm, and the composite of Ag thin films has no effect for the transmittance at near infrared.

Nonlinear Optical Properties Analysis

To further understand the mechanism of nonlinear response and regulation, the nonlinear signals of the A and B thin films were obtained by using the fs Z-scan technique at 800 and 1,030 nm. The Z-scan curve shows a smooth valley shape, and it **is** symmetric to the focal point (Z = 0), which confirms that the main nonlinear absorption characteristics of the A and B thin films are the RSA characteristic. The open-aperture (OA) Z-scan results of the A and B thin films are shown in **Figures 6A,B**. The A thin film exhibited RSA properties at 800 nm although no signal was observed at 1,030 nm. It can be seen from the linear spectrum that the E_g of the A and B thin films is greater than $h\nu$ but less than $2h\nu$; thus, the A and B thin films all exhibit a TPA characteristic (Honda et al., 2011). The OA Z-scan signals of the B thin films were observed at 1,030 nm. Moreover, with the increment of the DC magnetron sputtering power in the Ag target (from 5 to 15 W), the amplitude of the OA Z-scan signals of the films exhibited a corresponding increase. In addition, to study the relationship between the laser intensity and the nonlinear signal of the A and B thin films, the A and B_3 thin films were excited at 800 and 1,030 nm with different laser energy, as

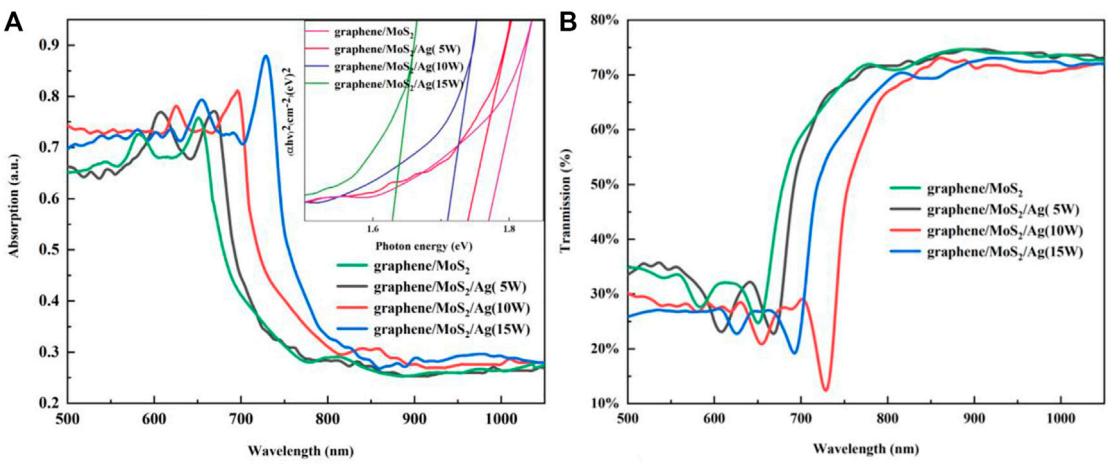

FIGURE 5 | The linear absorption **(A)** and transmission **(B)** of the A and B thin films.

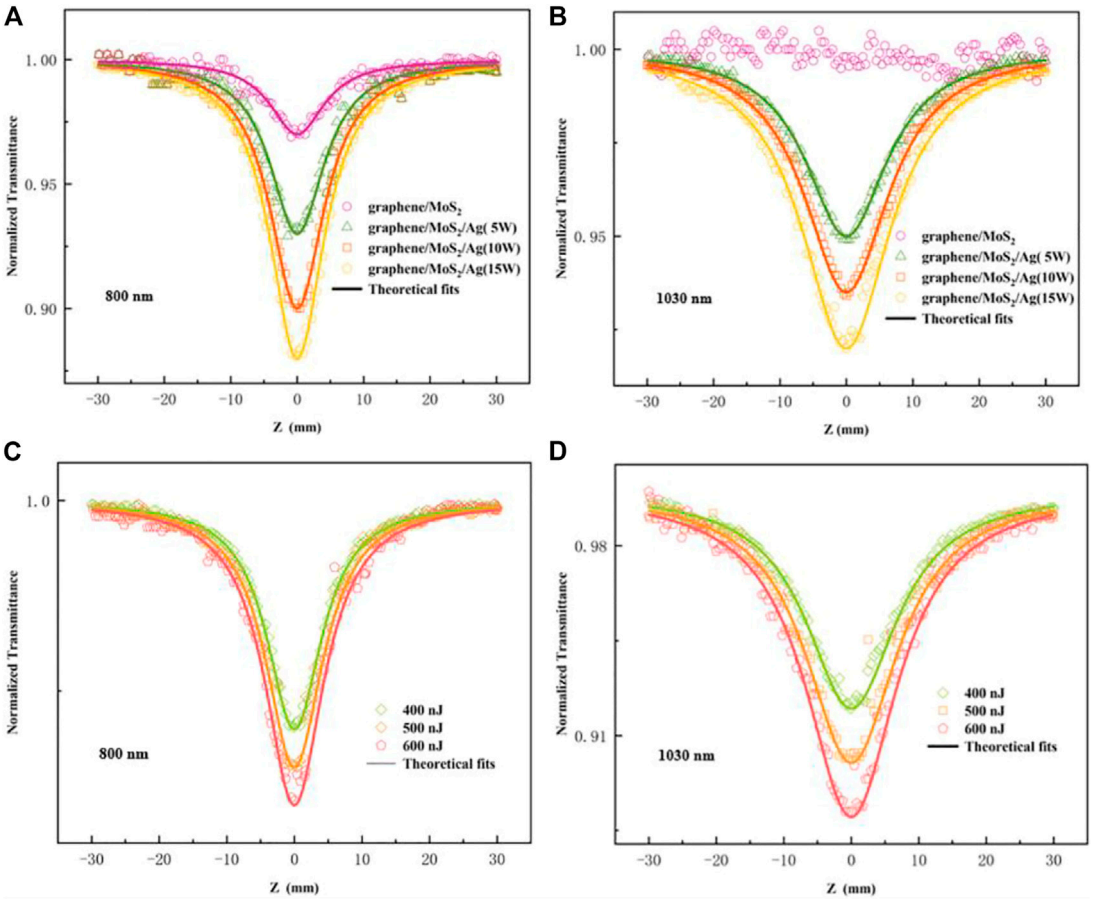

FIGURE 6 | The OA Z-scan signals of A and B thin films at 800 **(A)** and 1,030 nm **(B)**. The OA Z-scan signals of B_3 thin film at 800 **(C)** and 1,030 nm **(D)** under different excitation conditions.

is shown in **Figures 6C,D**. For the A thin film, with the increase of the excitation laser energy, the OA Z-scan signal of the A thin film had no change; thus, it is confirmed that the A thin film exhibits a pure third-order nonlinear effect, which is caused by the absorption of the excited state induced by the TPA. For the B_3 thin film, with the increase of the laser energy, the amplitude of the OA Z-scan signal increased. In combination with the OA Z-scan signals of the B thin films, which were obtained by changing the DC magnetron sputtering power in the Ag target (5–15 W), thus, we infer that there is a high-order nonlinear absorption effect in the nonlinear absorption phenomenon of the B thin films. For the high-order nonlinear absorption phenomenon, we have (Chen and Zhao, 2018)

$$\alpha(I) = \alpha_0 + \beta I + \gamma I^2 \tag{2}$$

$$T(z) = \sum_{m=0}^{\infty} \frac{\left(\frac{-\alpha I L_{eff}}{1+z^2/z_0^2}\right)}{m+1} \tag{3}$$

Here, α is the global absorption coefficient, γ is the fifth-order nonlinear absorption coefficient, $T(z)$ stands for the normalized transmittance, β is the nonlinear absorption coefficient of the thin films, and I_0 is the light intensity at the focus. The effective thickness of the thin films is denoted by L_{eff}, and the L_{eff} can be calculated by $L_{eff} = 1 - e^{-\alpha_0 L}/\alpha_0$, where α_0 is the linear absorption coefficient of the thin film, L is the thickness of the thin films, z is the distance from the sample to the focal point, and z_0 is the derived length of the beam. The β and the γ of the A and B thin films are exhibited in **Table 1**.

It can be seen from the calculation results of the nonlinear absorption coefficient of the B thin films that, with the increase of the laser energy, the nonlinear absorption coefficients of the B thin films exhibit the corresponding increase; thus, our inference is confirmed. The reason for the high-order nonlinear absorption effect can be attributed to the FCA, which is caused by the composite of the Ag thin films.

For Ag nanoparticles, the LSPR effect on their surface can effectively increase the interaction between light and matter, promote the separation of photogenerated carriers and holes, and can effectively capture photogenerated carriers (Xiang et al., 2012; Xi et al., 2014; Agrawal et al., 2018; Ye et al., 2019). When the Ag thin films are successfully composited with

TABLE 1 | Nonlinear absorption parameters of the A and B thin films under different excitation conditions.

Sample	A_1	B_1		B_2		B_3 (400 nJ)		B_3 (500 nJ)		B_3 (600 nJ)	
Wavelength (nm)	β (m/W × 10^{-11})	β (m/W × 10^{-11})	γ (cm^3/W^2 × 10^{-19})	β (m/W × 10^{-11})	γ (cm^3/W^2 × 10^{-19})	β (m/W × 10^{-11})	γ (cm^3/W^2 × 10^{-19})	β (m/W × 10^{-11})	γ (cm^3/W^2 × 10^{-19})	β (m/W\ × 10^{-11})	γ (cm^3/W^2 × 10^{-19})
800	9.7	11.4	34.2	14.2	47.1	17.0	61.3	17.2	63.2	18.0	69.4
1,030	—	4.79	4.32	5.44	4.93	6.47	6.14	6.52	6.58	6.79	7.13

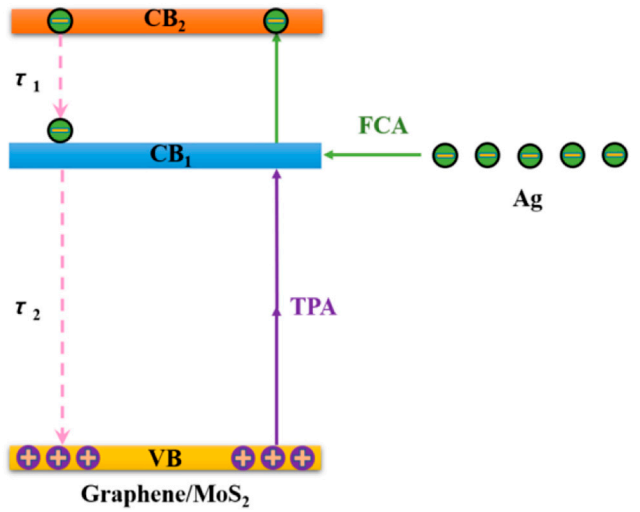

FIGURE 7 | The energy level diagram of the graphene/MoS_2/Ag thin film.

the graphene/MoS_2 thin film, it can provide more carriers for the B thin film; thus, the FCA is constructed in the excited state, so a combination of FCA and TPA is successfully presented, and thus, the nonlinear absorption effect of the B thin films is enhanced. In addition, with the increment of DC magnetron sputtering in the Ag target, Ag thin films that were prepared by different DC magnetron sputtering power can provide more Ag nanoparticles and then provide more photogenerated carriers to enhance the FCA effect; thus, the excited state absorption and RSA behavior of B thin films are enhanced. The energy level diagram of B thin film is shown in **Figure 7**. The τ_1 can be attributed to the radiative relaxation of carriers from the conduction band to the valence band. The τ_2 can be attributed to the cooling of the carriers in the conduction band.

Figures 8A,B show the CA Z-scan signals that were obtained by the A and B thin films at 800 and 1,030 nm. For the A thin film, the CA Z-scan signal was only observed at 800 nm, which can be attributed to Kerr refraction caused by the nonlinear systematic dispersion of bound electrons appearing near the intrinsic absorption edge, and there was no CA Z-scan signal observed at 1,030 nm, which can be caused by the weak Kerr refraction. For the B thin films, the CA Z-scan signals were both observed at 800 and 1,030 nm, which exhibits the existence of high-order nonlinear refraction. In addition, the amplitude of the CA Z-scan signals increases with the increase of the DC magnetron sputtering power in the Ag target at 800 and 1,030 nm. According to the results of the OA Z-scan signals, with the increase of the DC magnetron sputtering power in the Ag target, more Ag nanoparticles can be provided by Ag thin films, which leads to the increase of the photogenerated carriers. Therefore, it can be summarized that the content of the photogenerated carriers in the B thin films is relatively high, and the excess photogenerated carriers can participate in the refraction effect of free carriers. Thus, it can be inferred that the FCR effect at 1,030 nm is the dominant effect. According to the plasma dispersion effect of carriers, the refraction effect of free carriers increase with the increase of incident wavelength (Sameshima et al., 2009; Soref and Bennett, 1987). Therefore, the B thin films exhibit a self-defocusing behavior at 1,030 nm, which is constructed by the free carrier reflection and Kerr refraction. In addition, we also obtained the CA Z-scan signals of the A and B_3 thin films, which were excited at different laser energy as shown in **Figures 8C,D**. For the A thin film, there **was** no CA signal change. For the B_3 thin film, the signals of the CA Z-scan indicate that the amplitude of the nonlinear signal increases with the increase of the laser energy. The reason for the phenomenon is that, with the increase of the laser energy, excess carriers are generated, and they can participate in the refraction of the free carriers, thus leading to the enhancement of the FCR (Fang et al., 2015). For nonlinear refraction, we assume that the incident laser has a Gaussian distribution, and then, the sample transmittance on the far-field axis is proportional to the phase shift (Gao et al., 2005).

$$\Delta\varnothing = \frac{2\pi}{\lambda} L_{eff} n_2 I_0 \tag{4}$$

The effective thickness of the samples is denoted by L_{eff} and $L_{eff} = 1 - e^{-\alpha_0 L}/\alpha_0$, where α_0 is the linear absorption coefficient of the thin film, L is the thickness of the samples, I_0 is the light intensity at the focus, λ is the excitation wavelength, and n_2 is the nonlinear refractive index. For the Kerr system, the nonlinear refractive index and the peak intensity of the incident laser have the same radial profile. The interpolation formulas for the normalized peak-valley transmittance (ΔT_{p-v}) and peak-valley separation in z (ΔZ_{p-v}) are shown in **Eqs 5**, **6** (Gao et al., 2005).

$$\Delta T_{P-V} = 0.406\Delta\varnothing \tag{5}$$

$$\Delta Z_{P-V} = 1.7 z_0 \tag{6}$$

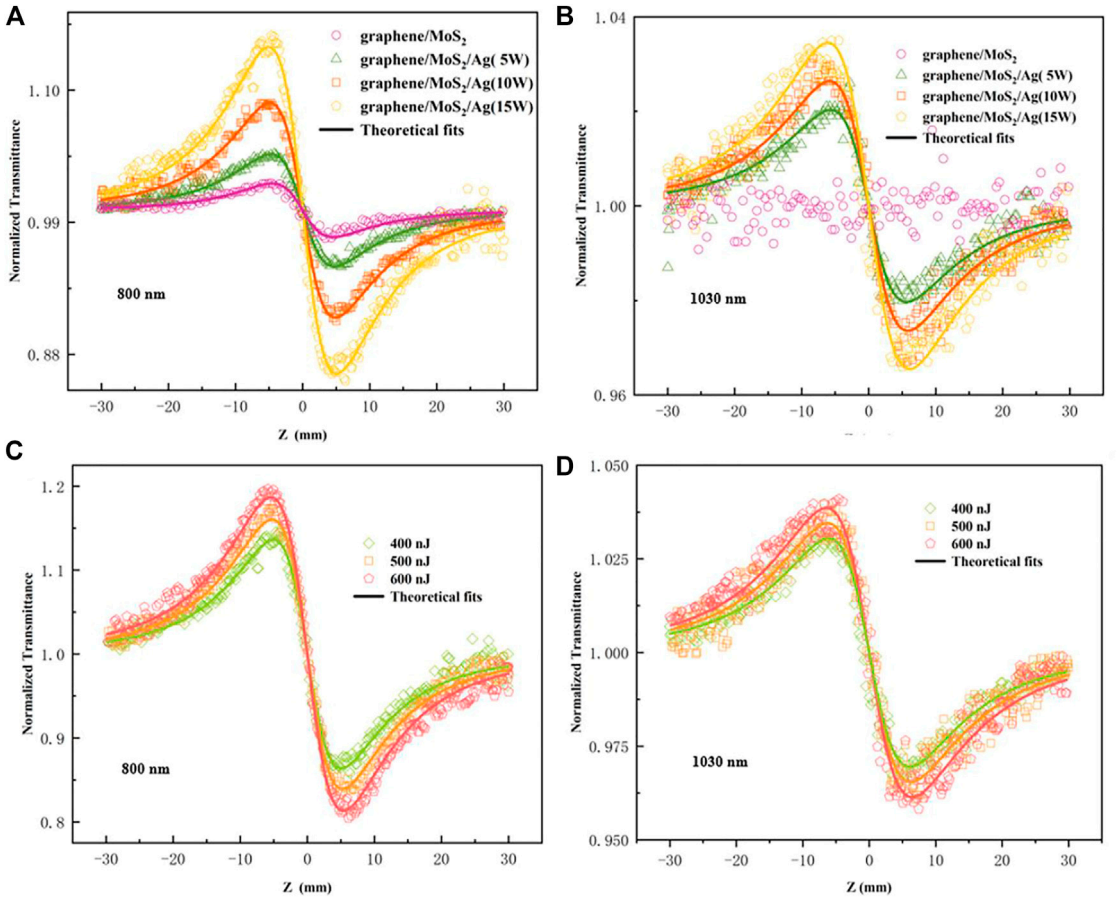

FIGURE 8 | The CA Z-scan signal of A and B thin films at 800 **(A)** and 1,030 nm **(B)**. The CA Z-scan signals of B_3 thin film at 800 **(C)** and 1,030 nm **(D)** under different excitation conditions.

TABLE 2 | Nonlinear refraction index of the A and the B thin films under different excitation conditions.

Sample	A_1	B_1	B_2	B_3 (400 nJ)	B_3 (500 nJ)	B_3 (600 nJ)
Wavelength (nm)	n_2 ($m^2/W \times 10^{-17}$)	n_2 ($m^2/W \times 10^{-17}$)	n_2 ($m^2/W \times 10^{-17}$)	n_2 ($m^2/W \times 10^{-17}$)	n_2 ($m^2/W \times 10^{-17}$)	n_2 ($m^2/W \times 10^{-17}$)
800	−1.42	−11.2	−21.4	−32.6	−39.3	−41.8
1,030	—	−4.37	−5.89	−7.31	−7.58	−8.00

The values of n_2 can be calculated by using **Eq. 4–6**. The calculated results of n_2 are shown in **Table 2**. The calculated results agree with our inference and confirm our point.

According to the analysis of the signals of the OA and CA Z-scans, the B thin films have the potential to be applied in the fields of nonlinear all-optical switching and optical limiters. Therefore, for nonlinear all-optical switches, one of the core criteria is the nonlinear FOM. Here, the FOM values of A and B thin films under different energy excitation at 800 and 1,030 nm are calculated to judge their advantages and disadvantages in the application of all-optical switches. For the nonlinear FOM value, we have (7) (Sheik-Bahae et al., 1990)

$$F = n_2/(\beta\lambda) \tag{7}$$

where n_2 is the nonlinear refractive index, β is the nonlinear absorption coefficient, and λ is the excitation wavelength. Compared with the FOM value of the A thin film (0.15) at 800 nm, the FOM values of the B_1, B_2, and B_3 thin films are successfully improved at 800 nm, and the nonlinear FOM value were calculated as 1.23, 1.88, and 2.39, respectively. In addition, the nonlinear FOM values of the B_1, B_2, and B_3 thin films at 1,030 nm are also calculated as 1.30, 1.35, and 1.42, respectively. With the increase of magnetron sputtering power in the Ag target, the values of nonlinear FOM of the B thin films exhibit a corresponding increase at 800 and 1,030 nm. In addition, with the increase of the laser intensity, the values of nonlinear FOM of the B_3 thin film also exhibit a corresponding increase up to the maximum numbers of 2.91 and 1.47 at 800 and 1,030 nm.

TABLE 3 | The nonlinear figure of merit (FOM) of different materials.

Wavelength (nm)	Pulse	Sample	FOM	References
800	190 fs	B_3 (400 nJ)	2.39	This work
	190 fs	B_3 (500 nJ)	2.85	This work
	190 fs	B_3 (600 nJ)	2.91	This work
1,030	190 fs	B_3 (400 nJ)	1.42	This work
	190 fs	B_3 (500 nJ)	1.45	This work
	190 fs	B_3 (600 nJ)	1.47	This work
840	120 fs	MEH-PPV/PMMA	0.6	Lin et al. (2002)
1,560	67 fs	GO	0.5	Xu et al. (2017)
700	190 fs	Trithiophene Chalcone (6")	1.0	Niu et al. (2021)
532	190 fs	Bi_2S_2Se/PMMA	0.3	Shubar et al. (2020)
535	150 fs	Au/Ag_2Se	0.58	Liu et al. (2020)
635	120 fs	Anthocyanin	0.67	Jeyaram and Geethakrishnan, (2020)
532	150 ps	lanthanum oxide	0.26	Faznny et al. (2020)

Compared with other materials, the B_3 thin film exhibits an excellent value of the nonlinear FOM. The results of the value of nonlinear FOM are shown in **Table 3**.

CONCLUSION

In summary, the study confirms that, with the composite of the Ag thin films, the nonlinear response of the graphene/MoS_2/Ag thin films is successfully constructed at near infrared. In addition, we also confirm that FCA and TPA are the main reasons for the nonlinear absorption enhancement of the graphene/MoS_2/Ag thin films, and the Kerr refraction and the FCR are the main reasons for the formation of nonlinear refraction of graphene/MoS_2/Ag thin films at near infrared. Compared with graphene/MoS_2 thin films, the graphene/MoS_2/Ag thin films exhibit a significant broadband nonlinear response at near infrared and the higher nonlinear absorption coefficients that are from 4.79×10^{-11} to 1.8×10^{-10} m/W at 800 and 1,030 nm and the higher nonlinear refraction index, which is from -4.37×10^{-17} to -4.18×10^{-16} m^2/W at 800 and 1,030 nm. More importantly, the broadband nonlinear response, nonlinear absorption coefficients, and nonlinear refraction index can be determined by the amount of the composite of the Ag thin films. Moreover, the graphene/MoS_2/Ag thin films exhibit the superior value of the nonlinear FOM and the maximum value of nonlinear FOM is 2.85. The result provides the possibility for the fabrication of all-optical switch at near infrared.

DATA AVAILABILITY STATEMENT

The original contributions presented in the study are included in the article/Supplementary Material, further inquiries can be directed to the corresponding author.

AUTHOR CONTRIBUTIONS

DS contributed to conception and design of the study. WS organized the database. DS wrote the first draft of the manuscript. DS, YF, XY, WJS, and QM wrote sections of the manuscript. All authors contributed to manuscript revision, read, and approved the submitted version.

FUNDING

This work is supported by the National Natural Science Foundation of China (Grant No. 11504072), Natural Science Foundation of Heilongjiang Province (Grant No. LH 2020F032) and (Grant LH 2019A018); Key Laboratory for Photonic and Electronic Bandgap Material (Ministry of Education) and School of Physics and Electronic Engineering of Harbin Normal University of China, National Natural Science Foundation of China (No. 11704273) and Natural Science Foundation of Jiangsu Province, China (Grant No. BK20170375)

REFERENCES

Agrawal, A., Cho, S. H., Zandi, O., Ghosh, S., Johns, R. W., and Milliron, D. J. (2018). Localized Surface Plasmon Resonance in Semiconductor Nanocrystals. *Chem. Rev.* 118, 3121–3207. doi:10.1021/acs.chemrev.7b00613

Akhavan, O. (2009). Lasting Antibacterial Activities of Ag-TiO2/Ag/a-TiO2 Nanocomposite Thin Film Photocatalysts under Solar Light Irradiation. *J. Colloid Interf. Sci.* 336, 117–124. doi:10.1016/j.jcis.2009.03.018

Charles, D. E., Aherne, D., Gara, M., Ledwith, D. M., Gun'ko, Y. K., Kelly, J. M., et al. (2009). Versatile Solution Phase Triangular Silver Nanoplates for Highly Sensitive Plasmon Resonance Sensing. *ACS Nano* 4, 55–64. doi:10.1021/nn9016235

Chen, H., and Zhao, Y. (2018). Applications of Light-Responsive Systems for Cancer Theranostics. *ACS Appl. Mater. Inter.* 10, 21021–21034. doi:10.1021/acsami.8b01114

Chen, H., Zhang, Y., Zhang, B., and Gao, L. (2016). Optical Bistability in a Nonlinear-Shell-Coated Metallic Nanoparticle. *Sci. Rep.* 6, 21741. doi:10.1038/srep21741

Cior, A., Suciu, M., Macavei, S., Kacso, I., Lung, I., Soran, M. L., et al. (2020). Green Synthesis of Ag-MnO_2 Nanoparticles using Chelidonium majus and Vinca minor Extracts and their in Vitro Cytotoxicity. *Molecules* 25, 819. doi:10.3390/molecules25040819

Fang, Y., Wu, X., Yang, J., Xiao, Z., Yang, Y., Zhou, F., et al. (2015). Effect of Fe-Doping on Nonlinear Optical Responses and Carrier Trapping Dynamics in GaN Single Crystals. *Appl. Phys. Lett.* 107, 051901. doi:10.1063/1.4928125

Faznny, M. F., Halimah, M. K., Eevon, C., Latif, A. A., Muhammad, F. D., Asyikin, A. S., et al. (2020). Comprehensive Study on the Nonlinear Optical Properties of Lanthanum Nanoparticles and Lanthanum Oxide Doped Zinc Borotellurite Glasses. *Opt. Laser Technol.* 127, 106161. doi:10.1016/j.optlastec.2020.106161

Fu, W., Du, F.-H., Su, J., Li, X.-H., Wei, X., Ye, T.-N., et al. (2014). *In Situ* catalytic Growth of Large-Area Multilayered graphene/MoS2 Heterostructures. *Sci. Rep.* 4, 4673. doi:10.1038/srep04673

Gao, Y., Zhang, X., Li, Y., Liu, H., Wang, Y., Chang, Q., et al. (2005). Saturable Absorption and Reverse Saturable Absorption in Platinum Nanoparticles. *Opt. Commun.* 251, 429–433. doi:10.1016/j.optcom.2005.03.003

Gao, Y.-Y., Han, B., Zhao, W.-Y., Ma, Z.-C., Yu, Y.-S., and Sun, H.-B. (2019). Light-Responsive Actuators Based on Graphene. *Front. Chem.* 7, 506. doi:10.3389/fchem.2019.00506

Ghadiyali, M., and Chacko, S. (2019). Hydrogenated-Graphene-Encapsulated Graphene: A Versatile Material for Device Applications. *ACS Omega* 4, 17494–17503. doi:10.1021/acsomega.9b02329

He, T., Zhen, T., Wu, C., Wang, X., Mohammad, M. A., Xie, D., et al. (2014), Novel Field-Effect Schottky Barrier Transistors Based on Graphene-MoS_2 Heterojunctions. *Ren. Sci. Rep*. 4, 5951. doi:10.1038/srep05951

He, M., Quan, C., He, C., Huang, Y., Zhu, L., Yao, Z., et al. (2017). Enhanced Nonlinear Saturable Absorption of MoS2/Graphene Nanocomposite Films. *J. Phys. Chem. C* 121, 27147–27153. doi:10.1021/acs.jpcc.7b08850

Honda, S., Yokoya, S., Ohkita, H., Benten, H., and Ito, S. (2011). Light-Harvesting Mechanism in Polymer/Fullerene/Dye Ternary Blends Studied by Transient Absorption Spectroscopy. *J. Phys. Chem. C* 115, 11306–11317. doi:10.1002/cssc.20140011110.1021/jp201742v

Hua, W., Yang, Z., Nie, H., Li, Z., Yang, J., Guo, Z., et al. (2017). Polysulfide-Scission Reagents for the Suppression of the Shuttle Effect in Lithium-Sulfur Batteries. *ACS Nano* 11, 2209–2218. doi:10.1021/acsnano.6b08627

Huang, K.-J., Wang, L., Li, J., and Liu, Y.-M. (2013). Electrochemical Sensing Based on Layered MoS2-Graphene Composites. *Sensors Actuators B: Chem.* 178, 671–677. doi:10.1016/j.snb.2013.01.028

Iqbal, A., Asif, H. M., Zhou, Y., Zhang, L., Wang, T., Khurum Shehzad, F., et al. (2019). From Simplicity to Complexity in Grafting Dawson-Type Polyoxometalates on Porphyrin, Leading to the Formation of New Organic-Inorganic Hybrids for the Investigation of Third-Order Optical Nonlinearities. *Inorg. Chem.* 58, 8763–8774. doi:10.1021/acs.inorgchem.9b01163

Jeyaram, S., and Geethakrishnan, T. (2020). Vibrational Spectroscopic, Linear and Nonlinear Optical Characteristics of Anthocyanin Extracted from Blueberry. *Results Opt.* 1, 100010. doi:10.1016/j.rio.2020.100010

Jiang, L., Zhou, G., Mi, J., and Wu, Z. (2012). Fabrication of Visible-Light-Driven One-Dimensional Anatase TiO2/Ag Heterojunction Plasmonic Photocatalyst. *Catal. Commun.* 24, 48–51. doi:10.1016/j.catcom.2012.03.017

Jiang, Y., Miao, L., Jiang, G., Chen, Y., Qi, X., Jiang, X.-f., et al. (2015). Broadband and Enhanced Nonlinear Optical Response of MoS2/graphene Nanocomposites for Ultrafast Photonics Applications. *Sci. Rep.* 5, 16372. doi:10.1038/srep16372

Katsnelson, M. I., Guinea, F., and Geim, A. K. (2009). Scattering of Electrons in Graphene by Clusters of Impurities. *Phys. Rev. B* 79, 195426.1–195426.5. doi:10.1103/PhysRevB.79.195426

Kim, H. H., Kang, B., Suk, J. W., Li, N., Kim, K. S., Ruoff, R. S., et al. (2015). Clean Transfer of Wafer-Scale Graphene via Liquid Phase Removal of Polycyclic Aromatic Hydrocarbons. *Acs Nano* 9, 4726–4733. doi:10.1021/nn5066556

Kwon, J., and Kim, J. (2018). Fabrication and Properties of Pn Diodes with Hybrid 2D Layers: Graphene/MoS2. *mat express* 8, 299–303. doi:10.1166/mex.2018.1430

Li, H., Bian, Z., Zhu, J., Huo, Y., Li, H., and Lu, Y. (2007). Mesoporous Au/TiO2Nanocomposites with Enhanced Photocatalytic Activity. *J. Am. Chem. Soc.* 129, 4538–4539. doi:10.1021/ja069113u

Lin, Y., Zhang, J., Brzozowski, L., Sargent, E. H., and Kumacheva, E. (2002). Nonlinear Optical Figures of merit of Processible Composite of Poly(2-Methoxy,5-(2′-(ethyl)hexyloxy)-P-Phenylene Vinylene) and Poly(methyl Methacrylate). *J. Appl. Phys.* 91, 522–524. doi:10.1063/1.1420760

Liu, C.-J., Tai, S.-Y., Chou, S.-W., Yu, Y.-C., Chang, K.-D., Wang, S., et al. (2012). Facile Synthesis of MoS2/graphene Nanocomposite with High Catalytic Activity toward Triiodide Reduction in Dye-Sensitized Solar Cells. *J. Mater. Chem.* 22, 21057–21064. doi:10.1039/c2jm33679k

Liu, X.-L., Han, S., and Sun, G.-L. (2020). Good Nonlinear Figures of Merit of Au/Ag2Se Core/Shell Nanostructures with Small Size. *Acta Phys. Pol. A.* 138, 364–367. doi:10.12693/aphyspola.138.364

Niu, R. P., Chen, S., Zhou, W. F., Wu, X., Yang, J., Wang, Y., et al. (2021). Modulation of Trithiophene-Based Chalcone Positional Isomers by Twist Angle Variation: Ultrafast Nonlinear Optical Properties and Excited-State Dynamics. *J. Photochem. Photobiol.* 411, 33–38. doi:10.1016/j.jphotochem.2021.113210

Ouyang, Q., Yu, H., Wu, H., Lei, Z., Qi, L., and Chen, Y. (2013). Graphene/MoS2 Organic Glasses: Fabrication and Enhanced Reverse Saturable Absorption Properties. *Opt. Mater.* 35, 2352–2356. doi:10.1016/j.optmat.2013.06.033

Qi, X., Zhang, H.-B., Xu, J., Wu, X., Yang, D., Qu, J., et al. (2017). Highly Efficient High-Pressure Homogenization Approach for Scalable Production of High-Quality Graphene Sheets and Sandwich-Structured α-Fe2O3/Graphene Hybrids for High-Performance Lithium-Ion Batteries. *ACS Appl. Mater. Inter.* 9, 11025–11034. doi:10.1021/acsami.7b00808

Qi, K., Cui, X., Gu, L., Yu, S., Fan, X., Luo, M., et al. (2019). Single-atom Cobalt Array Bound to Distorted 1T MoS2 with Ensemble Effect for Hydrogen Evolution Catalysis. *Nat. Commun.* 10, 5231. doi:10.1038/s41467-019-12997-7

Qian, X., Fuku, K., Kuwahara, Y., Kamegawa, T., Mori, K., and Yamashita, H. (2014). Design and Functionalization of Photocatalytic Systems within Mesoporous Silica. *ChemSusChem* 7, 1528–1536. doi:10.1002/cssc.201400111

Qiu, B., Zhao, X., Hu, G., Yue, W., Ren, J., and Yuan, X. (2018). Optical Properties of Graphene/MoS2 Heterostructure: First Principles Calculations. *Nanomaterials* 8, 962. doi:10.3390/nano8110962

Sameshima, T., Hayasaka, H., and Haba, T. (2009). Analysis of Microwave Absorption Caused by Free Carriers in Silicon. *Jpn. J. Appl. Phys.* 48, 021204–021237. doi:10.1143/JJAP.48.021204

Shahriari, E., Farsani, Z. M., Varnamkhasti, M. G., and Zamiri, R. (2017). Linear and Non-linear Optical Properties of Ag Doped ZnS Thin Film. *Opt. Quant Electron.* 49, 151. doi:10.1007/s11082-017-0991-x

Sheik-Bahae, M., Said, A. A., Wei, T.-H., Hagan, D. J., and Van Stryland, E. W. (1990). Sensitive Measurement of Optical Nonlinearities Using a Single Beam. *IEEE J. Quan. Electron.* 26, 760–769. doi:10.1109/3.53394

Shubar, M. Y., Saadon, H. L., and Abbas, S. J. (2020). Nonlinear Optical Switching and All-Figures of merit in Bi2S3-xSex/PMMA Nanocomposite Films Investigated by Z Scan under Visible CW Laser. *Chin. Opt. Lett.* 18, 011902. doi:10.3788/COL202018.011902

Soref, R., and Bennett, B. (1987). Electrooptical Effects in Silicon. *IEEE J. Quan. Electron.* 23, 123–129. doi:10.1109/JQE.1987.1073206

Sun, X., Zhang, B., Li, Y., Luo, X., Li, G., Chen, Y., et al. (2018). Tunable Ultrafast Nonlinear Optical Properties of Graphene/MoS2 van der Waals Heterostructures and Their Application in Solid-State Bulk Lasers. *ACS Nano* 12, 11376–11385. doi:10.1021/acsnano.8b06236

Vabbina, P., Choudhary, N., Chowdhury, A.-A., Sinha, R., Karabiyik, M., Das, S., et al. (2015). Highly Sensitive Wide Bandwidth Photodetector Based on Internal Photoemission in CVD Grown P-type MoS2/Graphene Schottky Junction. *ACS Appl. Mater. Inter.* 7, 15206–15213. doi:10.1021/acsami.5b00887

Wang, P., Zhang, S., Wu, P., Ye, C., Liu, H., and Xi, F. (2001). Optical Limiting Properties of Optically Active Phthalocyanine Derivatives. *Chem. Phys. Lett.* 340, 261–266. doi:10.1016/S0009-2614(01)00429-8

Wang, H., Wei, C., Zhu, K., Zhang, Y., Gong, C., Guo, J., et al. (2017). Preparation of Graphene Sheets by Electrochemical Exfoliation of Graphite in Confined Space and Their Application in Transparent Conductive Films. *ACS Appl. Mater. Inter.* 9, 34456–34466. doi:10.1021/acsami.7b09891

Xi, M., Zhao, Q., Duan, R., Yuan, J., Quan, Y., and Yang, H. (2014). A Reusable Localized Surface Plasmon Resonance Biosensor for Quantitative Detection of Serum Squamous Cell Carcinoma Antigen in Cervical Cancer Patients Based on Silver Nanoparticles Array. *Ijn*, 1097–1104. doi:10.2147/IJN.S58499

Xiang, Q., Yu, J., and Jaroniec, M. (2012). Synergetic Effect of MoS2 and Graphene as Cocatalysts for Enhanced Photocatalytic H2 Production Activity of TiO2 Nanoparticles. *J. Am. Chem. Soc.* 134, 6575–6578. doi:10.1021/ja302846n

Xu, X., Zheng, X., He, F., Wang, Z., Subbaraman, H., Wang, Y., et al. (2017). Observation of Third-Order Nonlinearities in Graphene Oxide Film at Telecommunication Wavelengths. *Sci. Rep.* 7, 9646. doi:10.1038/s41598-017-09583-6

Xu, Y., Yan, L., Si, J., Li, M., Ma, Y., Li, J., et al. (2020). Nonlinear absorption Properties and Carrier Dynamics in MoS2/Graphene van der Waals Heterostructures. *Carbon* 165 (2020), 421–427. doi:10.1016/j.carbon.2020.04.092

Yao, C.-B., Zhang, Y.-d., Chen, D.-T., Yin, H.-T., Yu, C.-Q., Li, J., et al. (2013). Study of All-Optical Switching and Optical Limiting Properties in Phenoxy-

Phthalocyanines Liquid. *Opt. Laser Technol.* 47, 228–231. doi:10.1016/j.optlastec.2012.08.039

Ye, Y., Loh, J. Y. Y., Flood, A., Fang, C. Y., Chang, J., Zhao, R., et al. (2019). Plasmonics of Diffused Silver Nanoparticles in Silver/Nitride Optical Thin Films. *Sci. Rep.* 9, 20227. doi:10.1038/s41598-019-56719-x

Yin, X., Tang, C. S., Wu, D., Kong, W., Li, C., Cao, Q. L., et al. (2019). Unraveling High-Yield Phase-Transition Dynamics in Transition Metal Dichalcogenides on Metallic Substrates. *Adv. Sci.* 6, 1802093. doi:10.1002/advs.201802093

Yu, L., Lee, Y.-H., Ling, X., Santos, E. J. G., Shin, Y. C., Lin, Y., et al. (2014). Graphene/MoS2 Hybrid Technology for Large-Scale Two-Dimensional Electronics. *Nano Lett.* 14, 3055–3063. doi:10.1021/nl404795z

Zhang, W., Chuu, C.-P., Huang, J.-K., Chen, C.-H., Tsai, M.-L., Chang, Y.-H., et al. (2014). Ultrahigh-Gain Photodetectors Based on Atomically Thin Graphene-MoS2 Heterostructures. *Sci. Rep.* 4, 3826. doi:10.1038/srep03826

Zheng, Y., Zheng, L., Zhan, Y., Lin, X., Zheng, Q., and Wei, K. (2007). Ag/ZnO Heterostructure Nanocrystals: Synthesis, Characterization, and Photocatalysis. *Inorg. Chem.* 46, 6980–6986. doi:10.1021/ic700688f

Conflict of Interest: The authors declare that the research was conducted in the absence of any commercial or financial relationships that could be construed as a potential conflict of interest.

Publisher's Note: All claims expressed in this article are solely those of the authors and do not necessarily represent those of their affiliated organizations, or those of the publisher, the editors and the reviewers. Any product that may be evaluated in this article, or claim that may be made by its manufacturer, is not guaranteed or endorsed by the publisher.

frontiers in Physics

ORIGINAL RESEARCH
published: 24 September 2021
doi: 10.3389/fphy.2021.749880

Tailorable Stimulated Brillouin Scattering Laser Based on Silicon Ring Waveguides

Yulei Wang[1,2], Kai Li[1,2], Yu Yu[1,2,3], Sensen Li[3], Yunfei Li[1,2], Wuyue Wang[1,2], Changyu Song[1,2], Zhiyong Wang[1,2], Gong Wang[1,2], Yong Zhang[2,4], Zhiwei Lu[1,2], Yuhai Li[3], Tongyu Liu[3] and Xiusheng Yan[3]*

[1]Center for Advanced Laser Technology, Hebei University of Technology, Tianjin, China, [2]Hebei Key Laboratory of Advanced Laser Technology and Equipment, Tianjin, China, [3]Science and Technology on Electro-Optical Information Security Control Laboratory, Tianjin, China, [4]School of Science, Hebei University of Technology, Tianjin, China

Stimulated Brillouin scattering (SBS) lasers based on silicon waveguides with large SBS gain, have been widely used in frequency tunable laser emission, mode-locked pulse laser, low-noise oscillator, optical gyroscope, and other fields. However, current SBS lasers still need long waveguide lengths to realize Brillouin laser output, which increases the waveguide losses and is not conductive to be integrated. In this paper, we propose a silicon ring waveguide, in order to tune the frequency of the phonon field of SBS laser based on the silicon substrate of the ring cavity. The simulation results exhibit that the tailorable forward SBS effect is realized in the silicon-based optical waveguide with a large SBS gain up to 1.90 $W^{-1}m^{-1}$. Particularly, with the mutual restraint between photoelastic and moving boundary effects, the tunable phonon frequencies emitting from 1 to 15 GHz are realized through the conversion among higher order modes by modifying the widths of the ring cavity. Therefore, this silicon waveguide based on ring cavity will provide a new technical scheme for designing tunable SBS lasers by tuning the ring widths. In addition, this enhanced and broadband acoustic radiation will pave the way for hybrid integration in silicon-based optical waveguide, micro-electromechanical system, and CMOS signal processing technology.

Keywords: fiber optics, optical communications, optical solitons, nonlinear optics, optical waveguide

OPEN ACCESS

Edited by:
Zhongquan Nie,
Taiyuan University of Technology, China

Reviewed by:
Yi Liu,
Taiyuan University of Technology, China
Xuehua Zhu,
Anhui Polytechnic University, China

****Correspondence:***
Yu Yu
yuyu1990@hebut.edu.cn

Specialty section:
This article was submitted to Optics and Photonics, a section of the journal Frontiers in Physics

Received: *30 July 2021*
Accepted: *06 September 2021*
Published: *24 September 2021*

Citation:
Wang Y, Li K, Yu Y, Li S, Li Y, Wang W, Song C, Wang Z, Wang G, Zhang Y, Lu Z, Li Y, Liu T and Yan X (2021) Tailorable Stimulated Brillouin Scattering Laser Based on Silicon Ring Waveguides. Front. Phys. 9:749880. doi: 10.3389/fphy.2021.749880

INTRODUCTION

Stimulated Brillouin scattering (SBS) effect is a third-order nonlinear effect, which is produced by the interaction of photons with phonons in the medium [1–3]. The SBS effect can be exploited to realize the conversion from optical waves (with higher frequency) to acoustic waves. Various applications based on the SBS effect, such as distributed sensing [4,5], slow light and fast light [6,22], microwave photonics [7–9], and narrow line width Brillouin lasers [10,11], have gained tractions and developped rapidly for decades. However, the realization of the SBS effect based on traditional waveguides such as optical fiber requires length of several kilometers, which makes the entire experimental device more complex and is not conducive to miniaturization and integration. The SBS effect can be realized by using microstructures; while the main reported platforms are micro resonant cavity, sulfur waveguide, and silicon-based waveguide, respectively.

If the optical gain generated by SBS exceeds the round-trip loss, SBS lasing will occur. Particularly, as a kind of nonlinear photo-acoustic coupling, the SBS effect is significant and can surpass Kerr and

Raman interaction effects in most transparent media [12]. Due to the phonon dissipation induced by the substrate, the integrated silicon waveguide with enhanced Raman and Kerr nonlinearity tends to produce tiny SBS coupling. However, it is difficult for acoustic waves to be guided in a pure silicon on insulator (SOI) waveguide on account of the high intensity in silicon, i.e., the high speed of phonons. This will greatly inhibit the interaction between photons and phonons, which leads to a decrease of SBS effect in SOI. In order to excite the strong photon-phonon interaction in SOI, different structures of silicon-based optical waveguides were further proposed, including silicon ridge [13], suspended silicon waveguide membrane [14,15], silicon disk [16], silicon ring [17], and silicon bullseye [18]. Independent control of acoustic and optical characteristics is allowed, since optical and acoustic modes are limited by different physical mechanisms. SOI provides a stable platform for on chip nonlinear optical processing, which makes it effective in integrated system. Several structures have been fabricated in order to enhance the nonlinear effect, such as suspended waveguide, photonic crystal waveguide, ring waveguide, disk waveguide, and so on, so that the laser output based on forward stimulated Brillouin scattering (FSBS) can be realized in a smaller device size. However, the length of ridged waveguide is always several centimeters [19], which is not easy to be integrated and makes the processing of the target center and disk waveguide more complex. Therefore, there is still a need for a more local method to obtain enhanced SBS gain and high Q value in a limited area, especially for the forward Brillouin scattering in a compact-designed on-chip waveguide system.

In this paper, we demonstrate a Brillouin laser in silicon by using a ring guided wave forward Brillouin scattering (called stimulated multimode Brillouin scattering), in which the coupled light field is coupled in different optical spatial modes. By adjusting the ring width, the acoustic frequency is tuned and the SBS gain is increased. This work represents an imperative step in the field of designing SBS laser and paves the way for hybrid integration in silicon-based optical waveguide, micro-electromechanical system, and CMOS signal processing technology [6].

THEORY MODEL

In the process of SBS effect, the pump light with frequency w_p interferes with the Stokes light with frequency w_s ($w_s < w_p$), resulting in a light force distribution that varies with time and space; while the beat frequency produces the phonon signal with frequency Ω. In SBS process, the phase matching condition should be satisfied, that is, the conservation of momentum and energy should be satisfied as follows [18],

$$\Omega = \omega_p - \omega_s \tag{1}$$

$$\boldsymbol{q} = \boldsymbol{k_p} - \boldsymbol{k_s} \tag{2}$$

where, q , k_p and k_s is phonon frequency, pump frequency, and Stokes wave frequency, respectively. Given the propagation direction of Stokes wave, SBS can be divided into backward stimulated Brillouin scattering (BSBS), and FSBS. During the progress of FSBS, pump wave and Stokes wave are transmitted in the same direction; while in the BSBS, they are transmitted in the reverse direction. Light waves can have an initial optical mode (in mode coupling) or different optical modes (inter mode coupling). In this paper, we only focus on the coupling between modules in forward SBS.

It is assumed that the electric field distribution of the pump pulse and Stokes pulses satisfies the following relationships:

$$E_p(r,t) = E_p(x,y) \cdot e^{i\left(k_p z - \omega_p t\right)} \tag{3}$$

$$E_s(r,t) = E_s(x,y) \cdot e^{i\left(k_p z - \omega_p t\right)} \tag{4}$$

Using the small signal approximation, assuming that the pump power in the waveguide is greater than the Stokes signal power, the coupling between the pump light and the Stokes signal light should meet the following requirements:

$$\frac{dP_p}{dz} = -\left(\alpha + \beta P_p + \gamma P_p^2\right) P_p \tag{5}$$

$$\frac{dP_s}{dz} = \left(\alpha - gP_p + 2\beta P_p + \gamma P_p^2\right) P_s \tag{6}$$

where, p_p and p_s are the power of pump light and Stokes light, α is the linear loss of light wave, β and γ are the nonlinear loss coefficient caused by two-photon absorption and the nonlinear loss coefficient caused by free carrier absorption, respectively. In **Eq. 6**, g is the SBS gain coefficient, which can be expressed by Lorentz model as follows:

$$g(\Omega) = \sum_m G_m \frac{(\Gamma_m/2)^2}{(\Omega - \Omega_m) + (\Gamma_m/2)^2} \tag{7}$$

where, Ω_m is the eigenfrequency satisfied by the u_m eigenequation of the acoustic mode without considering the acoustic loss. Γ_m is the loss coefficient of acoustic mode considering the acoustic loss, which depends on the mechanical quality factor Q_m, and shall meet the following relationship:

$$Q_m = \Omega_m / \Gamma_m \tag{8}$$

where the subscript m is the m-order acoustic mode (m = 1,2,3...).

Considering the acoustic loss, the peak value of SBS gain spectrum can be simplified as follows:

$$G_m = \frac{2\omega Q_m}{\Omega_m^2 \nu_{gp} \nu_{gs}} \frac{\left|\langle f, u_m \rangle\right|^2}{\langle E_p, \varepsilon E_p \rangle \langle E_s, \varepsilon E_s \rangle \langle u_m, \rho u_m \rangle} \tag{9}$$

where, ν_{gs}, ε and ρ are light group velocity, conductivity, and density, respectively. f is the sum of the optical forces of pump light and Stokes light. It is assumed that, $\omega_m \approx \omega_s = \omega$ and $\langle A, B \rangle = \int A^* \cdot B ds$ integrally covers the entire waveguide cross-sectional area. It is the overlap integral between the total optical force and the single m-order optical eigenmode, which represents the optical mechanical coupling strength in the silicon-based waveguide on the silicon substrate.

The acoustic displacement field is caused by the total optical force and should meet the phase matching conditions of **Eq. 1** and **Eq. 2**. In order to calculate u_m, the elastic loss can be

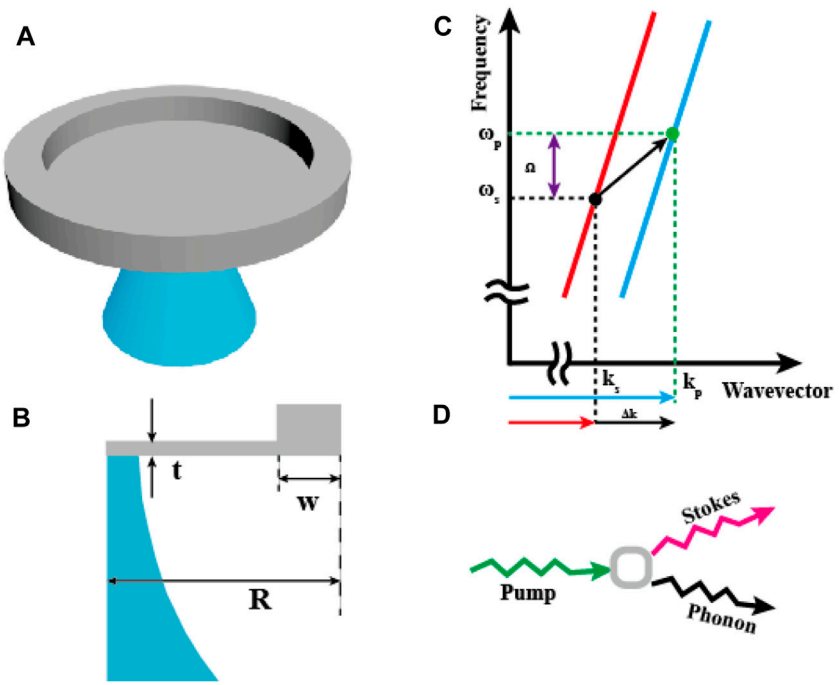

FIGURE 1 | (A) Structural diagram of micro ring cavity system. **(B)** Design drawing of ring cavity: t = 250 nm, w = 100 nm, Si radius corresponding to R = 5 μm. **(C)** Schematic diagram of the optical dispersion diagram. The optical resonance is represented by discrete points (black and blue) along the overall dispersion curve. The lower arrow indicates the resonance optical transition from pump light (k_p) to Stokes light mode (k_s) due to SBS. **(D)** When the optical frequency matches the mechanical acoustic mode, the phase matching and energy conservation of Stokes process are described by the photon density of state (PDOS) and the acoustic frequency Ω.

neglected in isotropic medium, and the ideal acoustic equation should satisfy as follows:

$$-\rho\partial_t^2 u_i + \sum_{jkl} \partial_j c_{ijkl}\partial_k u_l = -f_i \tag{10}$$

where, C_{ijkl} represents photoelastic tensor, u_i and f_i are displacement component and total light force of phonon field, respectively. The equation is the derivative along the j-th space direction of j, in which $j \in \{x, y, z\}$. When there is no driving force f_i in **Eq. 10**, the displacement component u_{mi} of phonon field in different modes can be obtained. Hybrid acoustic wave (HAW), including shear wave and longitudinal displacement component excited in waveguide structure.

To further clarify **Eq. 9**, **Eq. 9** can be rewritten as:

$$G_m = C_{OT_m}|Q_{Cm}|^2 \tag{11}$$

where, $Q_{Cm} = \langle f, u_m \rangle$ represents the influence of optomechanical coupling on GM; while $C_{OT_m} = C_{FV_m}C_{EF_m}$ is the influence of other factors (including light group velocity, material quality factor, light energy flow, and phonon energy flow) on G_m, where, $C_{FV_m} = \frac{2\omega Q_m}{\Omega_m^2 v_{gp} v_{gs}}$, $C_{EF_m} = \frac{1}{\langle E_p, \varepsilon E_p\rangle \langle E_s, \varepsilon E_s\rangle \langle u_m, \rho u_m\rangle}$. From the two parameters in the above expression, we can see that in the waveguide structure, the angular frequency, the speed of group light wave, the energy flow of light wave and phonon wave, and the factors of waveguide material are all related to C_{OTm}.

SIMULATION RESULTS

As shown in **Figure 1A**, the Brillouin silicon laser system is made of a silicon wafer on a single crystal insulator, which is composed of a ring-shaped silicon runway resonance cavity. In the whole device, the light is fully reflected in the ring-shaped waveguide cavity. The design diagram of the ring cavity Brillouin laser is shown in **Figure 1B**. The silicon thickness is t = 250 nm, and the ring width is w = 500–2000 nm. The displacement field related to each phase matched Brillouin active waveguide mode is shown in **Figure 1C**. In the forward mode Brillouin scattering on the ring cavity, the phase matching condition satisfying $m = 0$ is shown in **Eqs 1**, **2**. This multimode waveguide provides low loss guidance for different types of spatial modes [with their own propagation constants k_1 (red line) and k_2 (blue line)], resulting in different high quality factor (Q_m) cavity modes with slightly different free spectral range (FSR). The phase matching condition shall meet the matching of energy and frequency as shown in **Figure 1C**. Under the condition of $k_s > 0$ and $k_p > 0$, since the same propagation direction of the pump and Stokes pulses, these two values are very close. Therefore, the wave vector size of the phonon wave will be quite small, which causes the axial displacement of the phonon field to be extremely weak and the lateral displacement to dominate. In order to allow the phonon field to interact with the photon field long enough, the transverse phonon mode must be well confined to the waveguide medium. Therefore, the ring structure has been fabricated in **Figure 1A**. Most of the silicon is exposed to the air with a small part

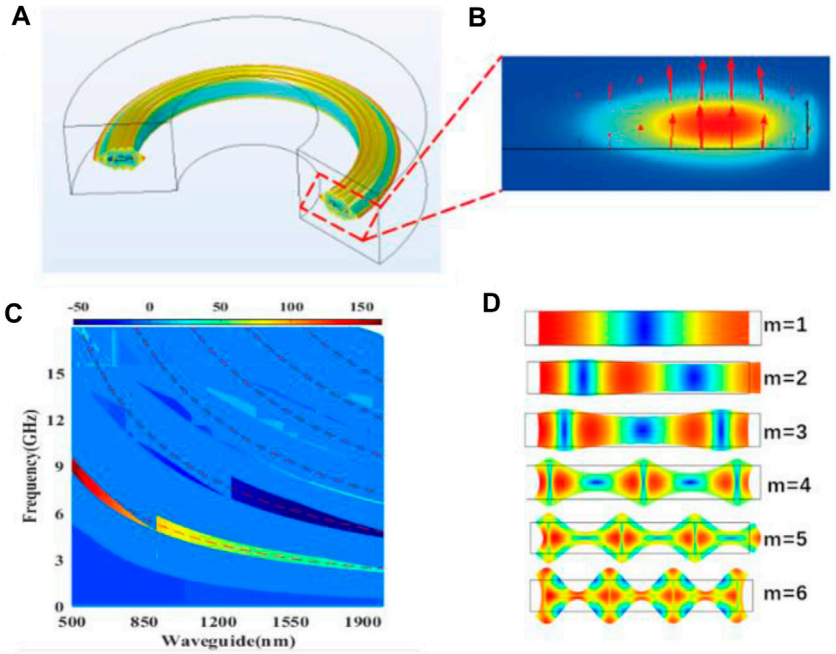

FIGURE 2 | (A) A model of photo-acoustic interaction in an annular cavity, in which the thickness of the silicon layer is 250 nm and the radius of the annular cavity is 10 μm. **(B)** The electric field distribution of the pump light when the width is w = 1,750 nm. **(C)** The finite element simulation of the change of the photo-acoustic coupling rate with the section width in the annular cavity structure, and the red dotted line is the frequency calculated according to the multi-order mode of Fabry Perot. **(D)** When the width is 1,750 nm, the pattern distribution of each sub mode (red dot) that satisfies the phase matching determined in c is shown. Each mode (m = 1, 2, ..., 6) is marked according to the pattern index c.

connected to the silicon dioxide. Since the refractive index of silicon differ widely with that of air, the light field has been restricted effectively. At the same time, owing to the higher speed of sound in silicon than that in air, the leakage of phonons is also effectually prevented. Besides, traditional waveguide media, such as optical fibers, have a long limitation on the transverse phonon field. This is why only BSBS can be observed in ordinary fiber waveguides. Meanwhile, the mutual conversion of electric field distribution with different modes can generate multi-mode transmission spectrum with multiple characteristic frequencies. As shown in **Figure 1D**, when the pump light excites the silicon ring waveguide, the Stokes signal light and the acoustic signal with beat frequency signal will be generated. The frequency detuning of the pump wave and Stokes wave results in the mismatch of the wave vector k, caused by the dispersion of the waveguide mode.

Due to the two edge constraint mechanisms of electrostriction effect and moving boundary effect, circular waveguide resonators with different width can be analyzed, as shown in **Figure 2A**. Because the refractive index of silicon at 1,550 nm is particularly high, the transverse size and thickness of floating ring structure can reach several hundred nanometers. The distribution of the pump electric field is shown in **Figure 2B**. In the process of forward SBS effect, the strong constraint on photon wave and elastic phonon wave also increases the disturbance of photoelastic effect (PE) and moving boundary effect (MB). **Figure 2C** shows the dispersion curves of all acoustic modes satisfying the phase matching condition of forward scattering between modes of **Eqs 1**, **2**. As shown in **Figure 2C**, a red color indicates a larger photo mechanical coupling (dark blue indicates zero photo mechanical coupling). It is worthy to note that the existence of quasi band gap (the frequency range of phonon waves with high reflectivity) not only limits the acoustic mode to the position towards the edge of the disk, but also increases the optical mechanical coupling and optical mode due to the large overlap between $\delta\varepsilon$rr. In **Figure 2C**, we also show the spatial profile of the main photoelastic and moving boundary components of the radial breathing sample mechanical mode in the whole circular cavity structure. Although there is a symmetrical fracture in the z-direction (the grating strut is along the bottom of the disk), which results in a radial u_r and a vertical u_z displacement coupling, there is no significant difference in the origin of the optomechanical coupling. These analyses can be easily applied to other crystals and composites to form a target cavity. All mechanical modes coupled to TE optical mode by PE and MB perturbations are calculated using **Eq. 3**. The corresponding spectrum is normalized such that its peak height is proportional to the total optomechanical coupling rate. Clearly only one mode family, namely the breathing mode, is dominant in this case. Assuming that the phonon wave is limited by the width of the ring and the velocity of the longitudinal wave V_1 in the silicon disk, the frequencies of different modes of phonon waves can be estimated. Multiple orders of the acoustic modes are given by $\Omega_p = pV_l/(2w)$, where V_l = 9,660 m/s, and p is the integer representing the order of the mode. The red dotted lines in **Figure 2C** represent these estimated frequency dispersion curves as a function of the ring width of the order p in each mode. The

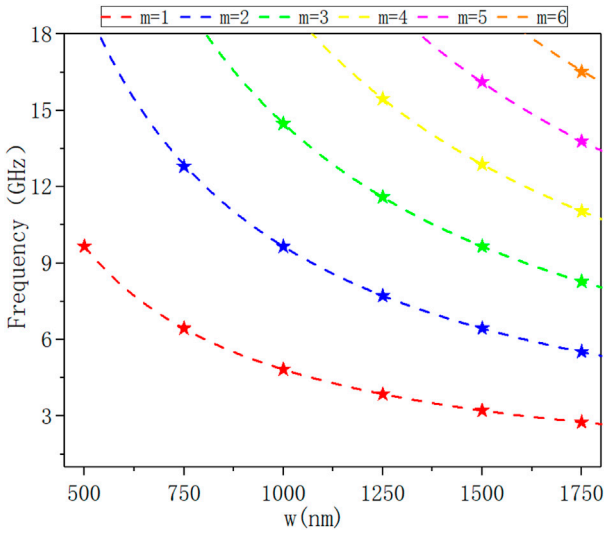

FIGURE 3 | The relationship between the coupling efficiency and the frequency in the Brillouin ring laser with the variation of waveguide width *w*.

correct design of ring and acoustic mode sequence can be used to enhance photo-acoustic coupling or automatically cancel photo-acoustic coupling. As shown in **Figure 2D**, when the waveguide width is 1,750 nm, there are six acoustic modes ($m = 6$) in the ring cavity under the photoelastic effect and moving boundary effect. In particular, the efficiency of optomechanical coupling between the first-order acoustic breathing mode and the optical mode is improved. In this case, because the maximum strain component almost completely overlaps with the optical mode, a large coupling efficiency can be achieved.

On the other hand, for the coupling between the third-order breathing mode and the surrounding TE mode, there is a competition between photoelastic effect and moving boundary effect. The product of boundary and volume has the opposite phase to the geometry, which leads to the self-cancellation effect. In addition, in the mode forward scattering state, a simple ring cavity is not enough to limit the elastic phonon wave to the edge of the ring [20]. discussed a method of using the target core structure to limit the phonon wave to the edge of the disk [20].

By finite element simulation, the curve of the nonlinear Brillouin optical acoustic coupling efficiency with frequency of the ring waveguide with different width is obtained. The resonant Brillouin generated by multiple ring waveguides as shown in **Figure 3**, is $w = 0.5$, 0.75, 1.0, 1.25, 1.5 and 1.75 μm, respectively. The characteristic frequency of each Brillouin active phonon mode (pentagram star) can be calculated with the change of waveguide size *w*, and each trace satisfying the characteristic frequency can be obtained. Each waveguide has a resonant mode marked with mode index *m*.

As can be seen from **Figure 3**, each waveguide will generate a series of regular interval Brillouin resonance, clear signal can be observed, showing nonlinear Brillouin response. As shown in **Figure 2C**, only the phonon mode with uniform displacement symmetry relative to the waveguide core can produce effective Brillouin coupling due to the spatial symmetry of optical force distribution. When the Brillouin spectrum changes with the waveguide size, different resonance features are color coded (red, blue, green, etc.) to indicate the mode order of each phonon resonance (first, second, third, etc.). As shown in **Figure 4**, the change in cavity size allows for precise brucellian resonance at almost any frequency from 1 to 15 GHz, enabling unprecedented nonlinear tunability. For example, when the cavity size *w* changes from 1,750 to 500 nm, the first-order acoustic mode ($m = 1$) resonates (red). In this case, because the maximum strain component overlaps the optical mode to almost the same degree, a large coupling efficiency can be achieved. The acoustic frequency changes from 3.2 to 9.3 GHz, at which a strong Brillouin resonance occurs.

In order to accurately determine the Brillouin nonlinear coefficient G_{SBS} with respect to the intrinsic Kerr nonlinear coefficient G_K and the nonlinear free carrier dispersion coefficient G_{FC}, the nonlinear coupled amplitude equation is formulated as: the power forms of Stokes and anti-Stokes line shapes are derived. Because SBS is a kind of resonance effect, its nonlinear coefficient presents a Lorentz shape centered on each Brillouin active phonon mode. In contrast, the electron Kerr nonlinearity is non resonant at the wavelength of 1,550 nm, resulting in a frequency independent nonlinear coefficient. As Wang et al. did in the fiber-based study [21], the frequency-dependent interference between Kerr and Brillouin effects produced an asymmetric (Fano like) alignment. It should be noted that our simulations are quite different, resulting in a different set of coupled amplitude equations. In addition, under our simulated conditions, the nonlinear free carriers in silicon are the reason for the different order of Stokes and anti-Stokes, and the influence of the nonlinear background is greater for frequencies below 2 GHz. When the free carrier effect decays at high frequency, the 16 GHz Kerr response is used as a reference

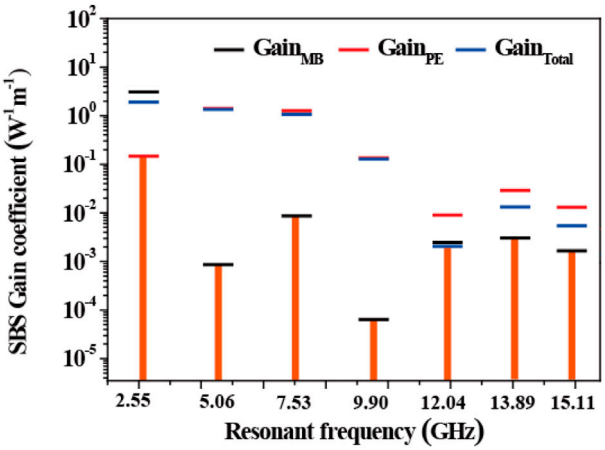

FIGURE 4 | The contribution of different effects to SBS gain coefficient in the process of stimulated Brillouin scattering when waveguide width w = 1,750 nm, including the contribution of moving boundary effect (black short line), radiation pressure effect (red short line), and the whole Brillouin gain (blue short line).

to determine the amplitude of Brillouin nonlinear coefficient. Using the resonance characteristics in **Figure 3**, the size of the Brillouin nonlinear coefficient G_{SBS} can be obtained. According to the electron Kerr nonlinear effect, the interference at Stokes and anti-Stokes frequencies is caused by the cross phase modulation between the pump beam and the probe beam in the silicon waveguide core.

In the optical waveguide structure on silicon substrate, the linear sum of all the overlapping integrals between a single optical force (f^n) and a single m-order acoustic eigenmode in the process of optical mechanical coupling can be expressed as follows:

$$Q_{C_m} = \sum_n \langle f^n, u_m \rangle \tag{12}$$

It is worth noting that the contribution of a single overlapping integral depends on the light force, and their relative phases are directly affected by the interference effect. In order to calculate **Eq. 9** and obtain the SBS gain coefficient in the nanometer optical waveguide, we need to consider two main factors: the electrostrictive force and the radiation pressure, namely $F_{Total} = F_{PE} + F_{MB}$. Electrostriction is the secondary response of mechanical strain excited by external electric field. The i-th component of the electrostrictive force is defined as:

$$f_i^{es} = -\sum_{ij} \frac{\partial}{\partial j} \sigma_{ij} \tag{13}$$

where, σ_{ij} is the electrostrictive tensor, which can be expressed as:

$$\sigma_{ij} = -\frac{1}{4}\varepsilon_0 \varepsilon_r^2 p_{ijkl}\left(E_{pk}E_{sl}^* + E_{pl}E_{sk}^*\right) \tag{14}$$

where, p_{ijkl} is the element of photoelastic tensor, ε_r and ε_0 are the relative permittivity and vacuum permittivity, respectively. Since common materials used in integrated photonics have either cubic crystalline lattice (e.g., silicon) or are isotropic (e.g., silica glass), and most waveguide structures are fabricated to be aligned with the principal axes of the material, we consider the crystal structure of the waveguide material to be symmetric with respect to plane $x = 0$, plane $y = 0$, and plane $z = 0$, Therefore, p_{ijkl} is zero if it contains odd number of a certain component. In the contracted notation, **Eq. 15** can be written as:

$$\begin{bmatrix} \sigma_{xx} \\ \sigma_{yy} \\ \sigma_{zz} \\ \sigma_{yz} \\ \sigma_{xz} \\ \sigma_{xy} \end{bmatrix} = -\frac{1}{2}\varepsilon_0 n^4 \begin{bmatrix} p_{11} & p_{12} & p_{13} & & & \\ p_{21} & p_{22} & p_{23} & & & \\ p_{31} & p_{32} & p_{33} & & & \\ & & & p_{44} & & \\ & & & & p_{55} & \\ & & & & & p_{66} \end{bmatrix} \times \begin{bmatrix} E_{px}E_{sx}^* \\ E_{py}E_{sy}^* \\ E_{pz}E_{sz}^* \\ E_{py}E_{sz}^* + E_{pz}E_{sy}^* \\ E_{px}E_{sz}^* + E_{pz}E_{sx}^* \\ E_{px}E_{sy}^* + E_{py}E_{sx}^* \end{bmatrix} \tag{15}$$

The electrostrictive force is given by the divergence of electrostrictive tensor. In a system consisting of domains of homogeneous materials, electrostrictive forces can exist inside each material (producing an electrostriction body force), and at interfaces where discontinuous stresses are present (yielding an electrostrictive pressure). From the divergence of **Eq. 16**, the electrostrictive body force become $F^{PE}e^{i(qx-\Omega t)}$, with vector components:

$$\begin{aligned} F_x^{PE} &= -iq\sigma_{xx} - \partial_y\sigma_{xy} - \partial_z\sigma_{xz} \\ F_y^{PE} &= -iq\sigma_{xy} - \partial_y\sigma_{yy} - \partial_z\sigma_{yz} \\ F_z^{PE} &= -iq\sigma_{xz} - \partial_y\sigma_{zy} - \partial_z\sigma_{zz} \end{aligned} \tag{16}$$

The gradient of ε_r radiation pressure is not equal to the boundary of zero. It can be derived from the Maxwell stress tensor (MST) between materials 1 and 2, which can be expressed as:

$$T_{ij} = \varepsilon_0 \varepsilon_r \left(E_i E_j - \frac{1}{2}\sigma_{ij}E^2\right) \tag{17}$$

For the waveguide with constant horizontal direction, only the transverse component of the force can contribute to the SBS gain coefficient.

This strong photon phonon coupling is produced by a constructive combination of PE force and nanometer radiation pressure. Large radiation pressure induced coupling represents new forms of boundary induced Brillouin nonlinearity and boundary mediated Brillouin coupling in subwave length structure. This novel waveguide geometry can independently control the phonon mode and the driving force of the opto mechanical system, thus creating a customizable Brillouin coupling over a wide bandwidth. The simulation results show that the tunable forward SBS effect is realized in the silicon-based optical waveguide with a larger SBS gain of 1.90 $W^{-1}m^{-1}$, The higher SBS gain excites high-power phonons, as a result, the tunable phonon frequency from 1 to 15 GHz is realized.

CONCLUSION

In this contribution, we have developed a waveguide system on silicon substrate, and proposed a Brillouin laser with ring cavity waveguide structure. By using the larger refractive index and better photoelastic component of silicon material, the tuning of SBS acoustic field signal frequency were realized by adjusting the ring section width and enhancing the forward SBS effect of main drive. Multi physical field simulation demonstrates that the strong photon phonon coupling is produced by the constructive combination of PE force and nanometer radiation pressure. The emergence of large radiation pressure induced coupling represents new forms of boundary induced Brillouin nonlinearity and boundary mediated Brillouin coupling in subwavelength structure. This novel waveguide geometry can independently control the phonon mode and the driving force of the optomechanical system, thus creating a customizable Brillouin coupling over a wide bandwidth. According to the radiation pressure effect and the boundary moving effect, the SBS laser with the ring cavity structure shows a larger SBS gain (up to 1.90 W^{-1} m^{-1}), which is 100 times of the reported SBS gain.

Coupled to massive transverse phonon modes, a relatively flat Brillouin gain can be generated over the entire 1–15 GHz frequency range. Therefore, the photon-phonon conversion based on Brillouin nonlinear effect can be realized through guiding and manipulating the phonons emitted by Brillouin on chip. This work opens up new possibilities in the field of CMOS and MEMS by the mixing of Brillouin device physics with silicon photons [22].

DATA AVAILABILITY STATEMENT

The original contributions presented in the study are included in the article/Supplementary Files, further inquiries can be directed to the corresponding author.

AUTHOR CONTRIBUTIONS

YW and KL: Data curation, Writing- Original draft preparation, Software, and Validation; YY: Conceptualization, Methodology, and Software; SL: Visualization and Investigation; YL: Writing-Reviewing and Editing; WW, CS and ZW: Visualization and Investigation; GW, YZ and ZL: Editing.

FUNDING

This work was supported by the National Natural Science Foundation of China (Grant Nos. 62005074, No. 61927815, No. 62075056 and No. 6142107200313), and Key Laboratory Fund Project (No. 61421070302).

REFERENCES

1. Shin H, Qiu W, Jarecki R, Cox JA, Olsson RH, Starbuck A, et al. Tailorable Stimulated Brillouin Scattering in Nanoscale Silicon Waveguides. *Nat Commun* (2013) 4:1944. doi:10.1038/ncomms2943
2. Clarke JT, Gérard J-C, Grodent D, Wannawichian S, Gustin J, Connerney J, et al. Morphological Differences between Saturn's Ultraviolet Aurorae and Those of Earth and Jupiter. *Nature* (2005) 433:717–9. doi:10.1038/nature03331
3. Zhu Z, Gauthier DJ, and Boyd RW. Stored Light in an Optical Fiber via Stimulated Brillouin Scattering. *Science* (2007) 318:1748–50. doi:10.1126/science.1149066
4. Stiller B, Foaleng SM, Beugnot J-C, Lee MW, Delqué M, Bouwmans G, et al. Photonic crystal Fiber Mapping Using Brillouin Echoes Distributed Sensing. *Opt Express* (2010) 18:20136–42. doi:10.1364/OE.18.020136
5. Sanghoon Chin S, Primerov N, and Thevenaz L. Sub-Centimeter Spatial Resolution in Distributed Fiber Sensing Based on Dynamic Brillouin Grating in Optical Fibers. *IEEE Sensors J* (2012) 12:189–94. doi:10.1109/JSEN.2011.2126568
6. Boyd RW, and Gauthier DJ. Controlling the Velocity of Light Pulses. *Science* (2009) 326:1074–7. doi:10.1126/science.1170885
7. Chin S, Thévenaz L, Sancho J, Sales S, Capmany J, Berger P, et al. Broadband True Time Delay for Microwave Signal Processing, Using Slow Light Based on Stimulated Brillouin Scattering in Optical Fibers. *Opt Express* (2010) 18:22599–613. doi:10.1364/OE.18.022599
8. Sancho J, Sanghoon Chin S, Sagues M, Loayssa A, Lloret J, Gasulla I, et al. Dynamic Microwave Photonic Filter Using Separate Carrier Tuning Based on Stimulated Brillouin Scattering in Fibers. *IEEE Photon Technol Lett* (2010) 22:1753–5. doi:10.1109/LPT.2010.2082514
9. Sancho J, Primerov N, Chin S, Antman Y, Zadok A, Sales S, et al. Tunable and Reconfigurable Multi-Tap Microwave Photonic Filter Based on Dynamic Brillouin Gratings in Fibers. *Opt Express* (2012) 20:6157–62. doi:10.1364/OE.20.006157
10. Gundavarapu S, Brodnik GM, Puckett M, Huffman T, Bose D, Behunin R, et al. Sub-hertz Fundamental Linewidth Photonic Integrated Brillouin Laser. *Nat Photon* (2019) 13:60–7. doi:10.1038/s41566-018-0313-2
11. Tow KH, Léguillon Y, Besnard P, Brilland L, Troles J, Toupin P, et al. Relative Intensity Noise and Frequency Noise of a Compact Brillouin Laser Made of As_38Se_62 Suspended-Core Chalcogenide Fiber. *Opt Lett* (2012) 37:1157–9. doi:10.1364/OL.37.001157
12. Pettit RM, Ge W, Kumar P, Luntz-Martin DR, Schultz JT, Neukirch LP, et al. An Optical Tweezer Phonon Laser. *Nat Photon* (2019) 13:402–5. doi:10.1038/s41566-019-0395-5
13. Yang KY, Oh DY, Lee SH, Yang Q-F, Yi X, Shen B, et al. Bridging Ultrahigh-Q Devices and Photonic Circuits. *Nat Photon* (2018) 12:297–302. doi:10.1038/s41566-018-0132-5
14. Schmidt MK, Poulton CG, Mashanovich GZ, Reed GT, Eggleton BJ, and Steel MJ. Suspended Mid-infrared Waveguides for Stimulated Brillouin Scattering. *Opt Express* (2019) 27:4976–89. doi:10.1364/OE.27.004976
15. Otterstrom NT, Behunin RO, Kittlaus EA, Wang Z, and Rakich PT. A Silicon Brillouin Laser. *Science* (2018) 360:1113–6. doi:10.1126/science.aar6113
16. Espinel YAV, Santos FGS, Luiz GO, Alegre TPM, and Wiederhecker GS. Brillouin Optomechanics in Coupled Silicon Microcavities. *Sci Rep* (2017) 7:43423. doi:10.1038/srep43423
17. Mirnaziry SR, Wolff C, Steel MJ, Morrison B, Eggleton BJ, and Poulton CG. Lasing in Ring Resonators by Stimulated Brillouin Scattering in the Presence of Nonlinear Loss. *Opt Express* (2017) 25:23619–33. doi:10.1364/OE.25.023619
18. Wiederhecker GS, Dainese P, and Mayer Alegre TP. Brillouin Optomechanics in Nanophotonic Structures. *APL Photon* (2019) 4:071101. doi:10.1063/1.5088169
19. Otterstrom NT, Behunin RO, Kittlaus EA, and Rakich PT. Optomechanical Cooling in a Continuous System. *Phys Rev X* (2018) 8:041034. doi:10.1103/PhysRevX.8.041034
20. Santos FGS, Espinel YAV, Luiz GO, Benevides RS, Wiederhecker GS, and Mayer Alegre TP. Hybrid Confinement of Optical and Mechanical Modes in a Bullseye Optomechanical Resonator. *Opt Express* (2017) 25:508–29. doi:10.1364/OE.25.000508
21. Wang J, Zhu Y, Zhang R, and Gauthier DJ. FSBS Resonances Observed in a Standard Highly Nonlinear Fiber. *Opt Express* (2011) 19:5339–49. doi:10.1364/OE.19.005339
22. Chin S, Gonzalez-Herraez M, and Thévenaz L. Zero-gain Slow & Fast Light Propagation in an Optical Fiber. *Opt Express* (2006) 14:10684–92. doi:10.1364/OE.14.010684

Conflict of Interest: The authors declare that the research was conducted in the absence of any commercial or financial relationships that could be construed as a potential conflict of interest.

Publisher's Note: All claims expressed in this article are solely those of the authors and do not necessarily represent those of their affiliated organizations, or those of the publisher, the editors and the reviewers. Any product that may be evaluated in this article, or claim that may be made by its manufacturer, is not guaranteed or endorsed by the publisher.

frontiers in Materials

ORIGINAL RESEARCH
published: 08 October 2021
doi: 10.3389/fmats.2021.726270

Construction of Hierarchical Porous Architecture on Ni Foam for Efficient Oxygen Evolution Reaction Electrode

Guang-Hong Ao[1], Pei-Zhi Zhao[1], Zhi-Gang Peng[1], Shuo Wang[2], Ying-Shuang Guo[2], Chun-Tian Chen[2] and Zhi-Hong Wang[2]**

[1]School of Science, Harbin University of Science and Technology, Harbin, China, [2]School of Physics, Harbin Institute of Technology, Harbin, China

Nickel foam (NF) with a three-dimensional porous structure plays an important role in a wide variety of applications such as energy storage and conversion, catalysis, and sensor due to its high porosity, low density, and excellent conductivity. However, the main drawback of NF is that its ligaments are very smooth, and thus the surface area is relatively low. In this work, we propose a novel strategy, oxidization and reduction process, *in situ* to construct micron/nano pores on the ligaments of commercial NF to fabricate a typical hierarchical porous architecture. This process is simple and green, avoiding the use of sacrificial materials. Furthermore, MnO_2 is coated on the micron/nano-porous Ni foam (MPNF) to construct an oxygen evolution reaction (OER) electrode through pulse electrodeposition. The designed MPNF-MnO_2 electrode presents enhanced OER electrocatalysis activity with a low overpotential of 363.5 mV at the current density of 10 mA cm^{-2} in an alkaline solution, which is 66.4 mV lower than that of the NF-MnO_2 electrode in the same operating conditions. Furthermore, the porous and wrinkled structures of the MPNF also improve the mechanical integrity of the electrode, resulting in super-long stability.

Keywords: oxidation-reduction, micron/nano-structure, oxygen evolution reaction, current collector, nickel foam

OPEN ACCESS

Edited by:
Keng-Te Lin,
Swinburne University of Technology, Australia

Reviewed by:
Jialiang Wang,
University of Wisconsin-Madison, United States
Xifeng Ding,
Nanjing University of Science and Technology, China
Kongfa Chen,
Fuzhou University, China

****Correspondence:***
Guang-Hong Ao
aghoptics@163.com
Zhi-Hong Wang
wangzhihong@hit.edu.cn

Specialty section:
This article was submitted to Energy Materials, a section of the journal Frontiers in Materials

Received: *17 June 2021*
Accepted: *27 August 2021*
Published: *08 October 2021*

Citation:
Ao G-H, Zhao P-Z, Peng Z-G, Wang S, Guo Y-S, Chen C-T and Wang Z-H (2021) Construction of Hierarchical Porous Architecture on Ni Foam for Efficient Oxygen Evolution Reaction Electrode. Front. Mater. 8:726270. doi: 10.3389/fmats.2021.726270

INTRODUCTION

Nickel foam (NF) is a three-dimensional (3D) porous metal composed of pores and ligament skeleton with the advantages of high porosity, good conductivity, and mechanical performance, which has very important applications in many fields such as energy storage and conversion, catalysis, and sensing (Yuan et al., 2012; Zhou et al., 2013; Huang et al., 2015; Tong et al., 2019; Zeng et al., 2020). With the rapid development of the new energy technology, NF was demonstrated to be promising excellent electrodes/catalysts or their supports, which has attracted considerable attention. However, as the commercial NF was prepared for diverse applications, its natural architecture could not always meet the demand of the electrochemical electrode/support. For example, the pore diameter of NF was in the range of hundreds of microns and the porosity could be as high as 90%, whereas the proportion of the ligament was relatively small and its diameter was ~50 μm. Taking electrochemical electrode in solution as an example, the large pore structure in NF was indeed conducive to liquid infiltration and ion transmission (Xu et al., 2015). However, the lower active surface of ligaments became a major obstacle, limiting the electrochemical performance. Furthermore, when NF was applied as an electrode/catalyst support, the surface of the ligament was smooth, which was not beneficial for the adhesion of active materials on its surface. The shedding

of active materials on NF support was indeed a serious issue for the long-term stability of the electrode/catalyst (Yu et al., 2014).

To overcome these problems, acid–base corrosion and dealloying have been developed for the treatment of NF. However, it is a certain technical challenge to carry out the elaborate process on these ligaments with such small diameters to increase their coarseness uniformly. Yu et al. (Yu et al., 2014) developed a porous Ni@NiO core-shell electrode obtained by activated commercial Ni foam (NF) in a 3M HCl solution at 90 °C. The asymmetric supercapacitor based on the electrode exhibited an ultrahigh areal capacitance and super-long cycling stability. Xu Guorong et al. (Xu et al., 2015) created a porous structure with 1–15 μm cracks on the ligaments of NF by the alloying and dealloying approach. In this process, nickel–zinc alloy was first prepared by electrochemical deposition on the ligament of NF, and then the higher active Zn was removed by electrochemical dealloying. The porous Ni foam could be used as an efficient supercapacitor substrate to increase the loading capacity for the MnO_2 electrode. However, for these existing treatments for NF, a strong acid was often needed in the corrosion and dealloying treatment, which is harmful to the environment. Furthermore, the dealloying process requires time-consuming preparation of an alloy precursor and subsequent removal of active metal, which is complex and a waste of resource. Therefore, it is highly desirable to develop a simple, green, and efficient technology for treatment of NF.

This work reports a novel oxidation–reduction method for *in situ* micron/nano-porous treatment of commercial NF. The formation of pore structures on NF can be attributed to the volume expansion and shrink during the oxidation–reduction process, as well as the diffusion and spontaneous reconstruction of nickel atoms. This process is simple and green, avoiding the use of sacrificial materials. Furthermore, as a representative application, MnO_2 is coated on an MPNF to construct an OER electrode through pulse electrodeposition. The designed MPNF-MnO_2 electrode presents excellent OER electrocatalysis activity.

EXPERIMENTAL

Fabrication of MPNF

The purchased commercial NF (99.9%, LZY Battery Sales Department, China) was placed in a furnace and oxidized at 850°C for 36 h in atmospheric air. Then, oxidized NF was placed in a tube furnace and reduced at 650°C for 10 min under a hydrogen atmosphere. The MPNF samples were fabricated through simple oxidation and subsequent reduction treatment.

Preparation of the Composite Electrode

The prepared MPNF and NF were cleaned with acetone, anhydrous ethanol, and deionized water. MnO_2 was coated on the two kinds of supports through pulse electrodeposition in the three-electrode system proposed by Li et al. (Li et al., 2016). Ag/AgCl and platinum pallets were employed as reference and counter electrodes, respectively. 0.1 mol L^{-1} of $KMnO_4$ was selected as an electrolyte. Each pulse electrodeposition cycle consisted of on-time of 1 s at -0.15 V and off-time of 10 s at 0.65 V. The mass loading was tuned by the change of electrodeposition cycles (15, 25, and 35 cycles).

Material Characterization and Electrochemical Measurement

The microstructures of MPNF/NF-MnO_2 composite electrode were observed by scanning electron microscope (SEM, JEOL-2100F). The phases were characterized by X-ray diffraction (RIGAKU D/max2200, Japan) and Raman spectroscopy (Raman, nanobase, 532 nm laser).

Electrochemical tests were carried out in 1 mol L^{-1} KOH electrolyte at 25°C by CHI660e electrochemical workstation (Shanghai ch instruments, China). Hg/HgO and Pt were used as reference and counter electrodes, respectively. EIS (electrochemical impedance spectroscopy) was tested at 1.62 V potential (vs RHE) and 5 mV AC voltage. The frequency range of the test was from high frequency 10^5 Hz to low frequency 10^{-2} Hz. The long-term stability of the composite electrodes was evaluated by chronopotentiometry.

RESULTS AND DISCUSSION

Fabrication and Characterization of MPNF

Figures 1A–C shows the construction process of micron/nano-porous structure on the ligament of NF by an oxidation–reduction method. As seen in **Figure 1A**, the commercial NF exhibited a typical metallic luster. The diameter of the pores was in the range of hundreds of micrometers, and the diameter of the ligaments was in the range of tens of micrometers. As mentioned above, such "larger pores and smaller ligament" structures reduced the effective active area of the NF to a certain extent. **Figures 1D and G** show the SEM images of fresh NF. The crystalline grain in the ligaments was obvious and continuous, forming a smooth surface without pore and wrinkle structures. **Figure 1B** is an electronic image of NF after oxidation. The color of NF changed from metallic luster to dark green which indicates the formation of NiO. As shown in **Figure 1E and H**, a number of particles grew out of the surface of the Ni foam, suggesting the formation of NiO grains. These grains presented a typical "ridged" appearance, which was consistent with the microstructures of Ni/NiO after oxidation at 900°C (Haugsrud, 2003). The formation of NiO on NF was further confirmed by the XRD patterns (**Figure 1K**) and Raman spectra (**Figure 1M**).

From **Figure 1C**, after the reduction treatment, the color of NF almost recovered its metallic luster. The reflectivity seems to decrease slightly owing to the construction of micron/nano-pore structures. The SEM images in **Figures 1F,I** show that a large number of micron/nano-pores and wrinkles appeared on the surface of NF after the oxidation–reduction treatment. The amount of pores reached ~45 per 100 μm^2 with an average of ~214 nm (**Figure 1J**). The average pore size of the MPNF was smaller than that of cracks (~15 μm) prepared by dealloying (Xu et al., 2015), which is a more beneficial and effective support for

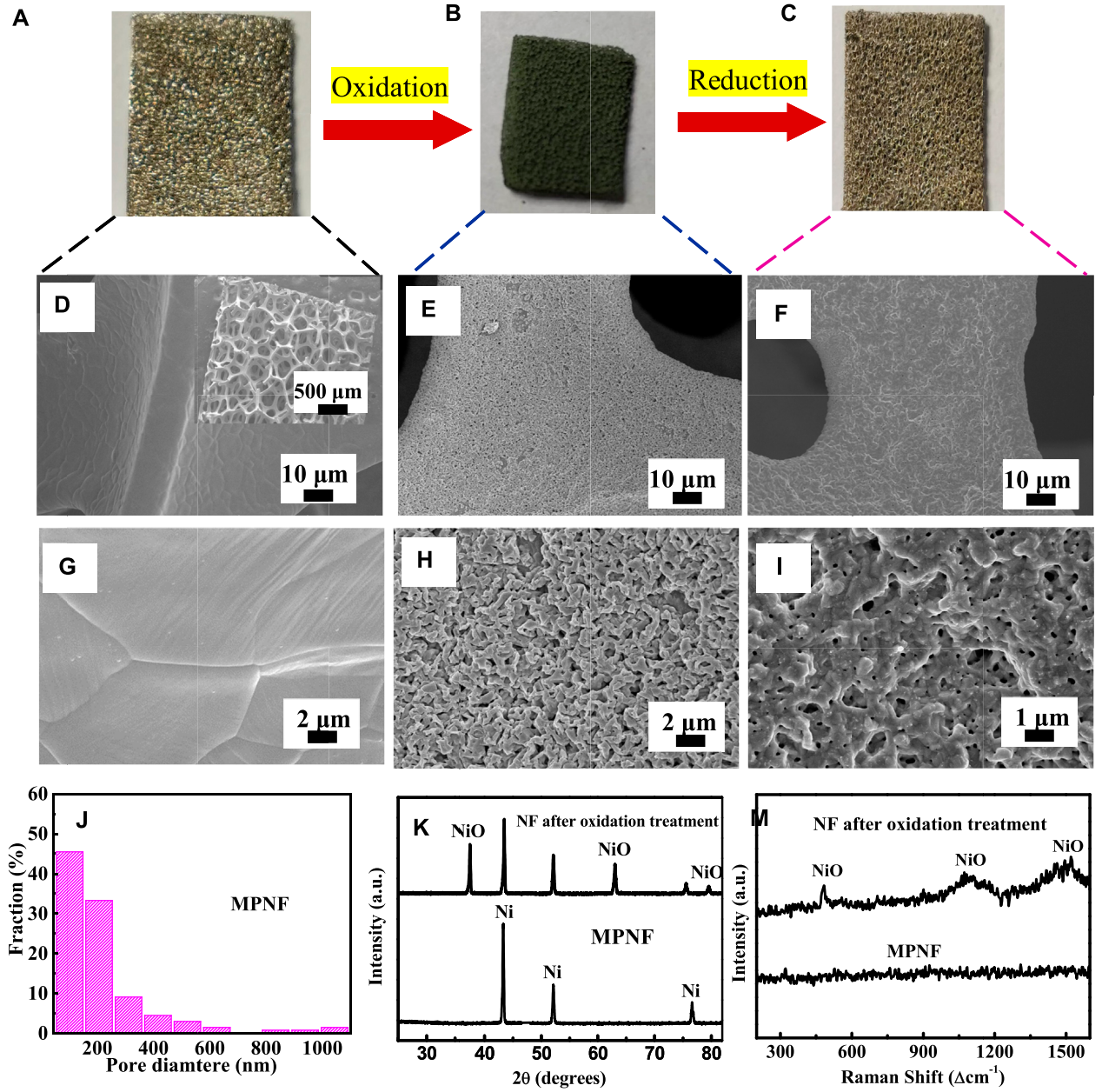

FIGURE 1 | (A–C) The scheme for the fabrication of MPNF. **(D,G)** SEM images of NF, **(E,H)** SEM images of NF after the oxidation treatment, **(F,I),** and SEM images of the fabricated MRNF. **(J)** Diameter distribution graph of the fabricated MRNF. **(K)** XRD patterns of NF after the oxidation treatment and MRNF. **(M)** Raman spectra of NF and MPNF.

nanometer catalyst materials. The formation of the micron/nano-structure is mainly due to the oxidation–reduction process. At the first stage of the oxidation process, a dense oxide layer was formed on the surface of NF. With further progress of oxidation, nickel atoms needed to diffuse outward through the oxide layer, while oxygen atoms also needed to diffuse inward through the oxide layer. However, the diffusion rate of nickel atoms in the oxide layer was much higher than that of nickel diffusion in the oxide layer. For example, at 1400°C, the diffusion rate of Ni^{2+} was 6 orders of magnitude higher than that of O^{2-} (Faes et al., 2012). Therefore, simultaneous diffusion of the two kinds of atoms will lead to the formation of internal defects (pore structures) in the inside of the ligament, which can be considered as a Kendall effect (Galinski et al., 2011). Afterward, as the oxidized NF was reduced in the H_2 atmosphere, the oxygen atoms were taken away and quick volume shrinkage took place. The volume shrinkage for the reduction of NiO was as high as 41%. Rapid reduction and volume shrinkage promoted the formation of porous structure on the surface of NF, resulting in the exposure of porous structure that was originally covered under the oxide layer (Nakamura

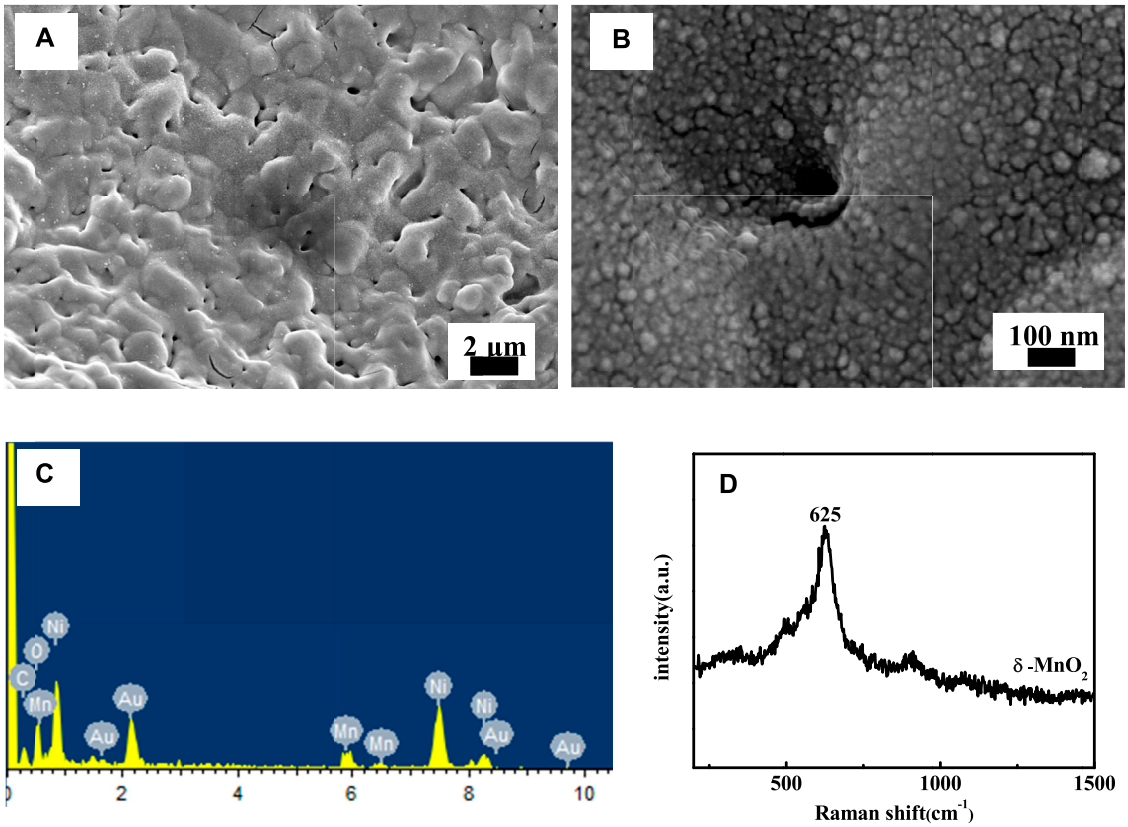

FIGURE 2 | (A) Low- and **(B)** high-magnification SEM images of MPNF-MnO_2 electrode. **(C,B)** are the EDX analysis and Raman spectra of the MPNF-MnO_2 electrode, respectively.

et al., 2008; Wang et al., 2017). In addition, the wrinkled structure observed on MPNF was mainly due to the surface reconstruction formed by the spontaneous migration of nickel atoms in the process of long-time oxidation and high-temperature thermal etching (Meulenberg et al., 2001). These wrinkle structures also significantly increased the roughness of the nickel ligament surface, which is conducive to improve the contact area between MPNF and active materials. In this approach, through this simple metal oxide–metal treatment, commercial NF was directly transformed to MPNF with hierarchical porous architecture. The large pores in the skeleton of MPNF could ensure the fast ion transport in the solution and the formed micron/nano pores and wrinkle structures in the ligaments of MPNF inevitably expands the effective area. The MPNF could be used as a promising electrode/electrode support.

XRD in **Figure 1K** exhibited that the formed MPNF was composed of pure Ni without any impurities. This was confirmed by the more sensitive Raman spectra in Figure 1M. The Raman spectrum of MPNF was a typical metal spectrum without any peaks, indicating that there was no detectable NiO after the H_2 reduction treatment under this experimental condition. In contrast, when acid etching was used to form a porous structure, oxide particles will be formed (Yu et al., 2014). While, the dealloying process could leave residual active metal components in the formed porous structure (Xu et al., 2015). Compared with the traditional acid–base corrosion and dealloying approaches, this approach avoids the involution of impurities in principle, which can prepare pure micron/nano-porous metals without the participation of acid–base solutions. Therefore, it is a green and large-scale approach.

Characterization of Phase and Microstructures of MPNF-MnO_2 Composite Electrodes

Figures 2A,B are the microstructures of MPNF-MnO_2 composite electrodes prepared through pulse electrodeposition of MnO_2 for 25 cycles. The electrodeposited MnO_2 film was uniformly covered on the surfaces of MPNF, which makes the micron/nano-porous structure of the surface fuzzy. Furthermore, many clusters of MnO_2 particles have been plated into the micron/nano-porous structure to form a unique contact interface between MPNF and MnO_2. Some researchers reported that the active materials embedded in the micro/nano-porous support can expand the contact interface between support and active materials, resulting in the improvement of the electrochemical performance stability of the electrodes (Lang et al., 2011; Meng and Ding, 2011; Wang et al., 2017). The results of EDX (**Figure 2C**) further confirmed that Mn oxides were formed on the surface of MPNF. The typical peak of 625 cm^{-1} (**Figure 2D**) in the Raman spectrum of the

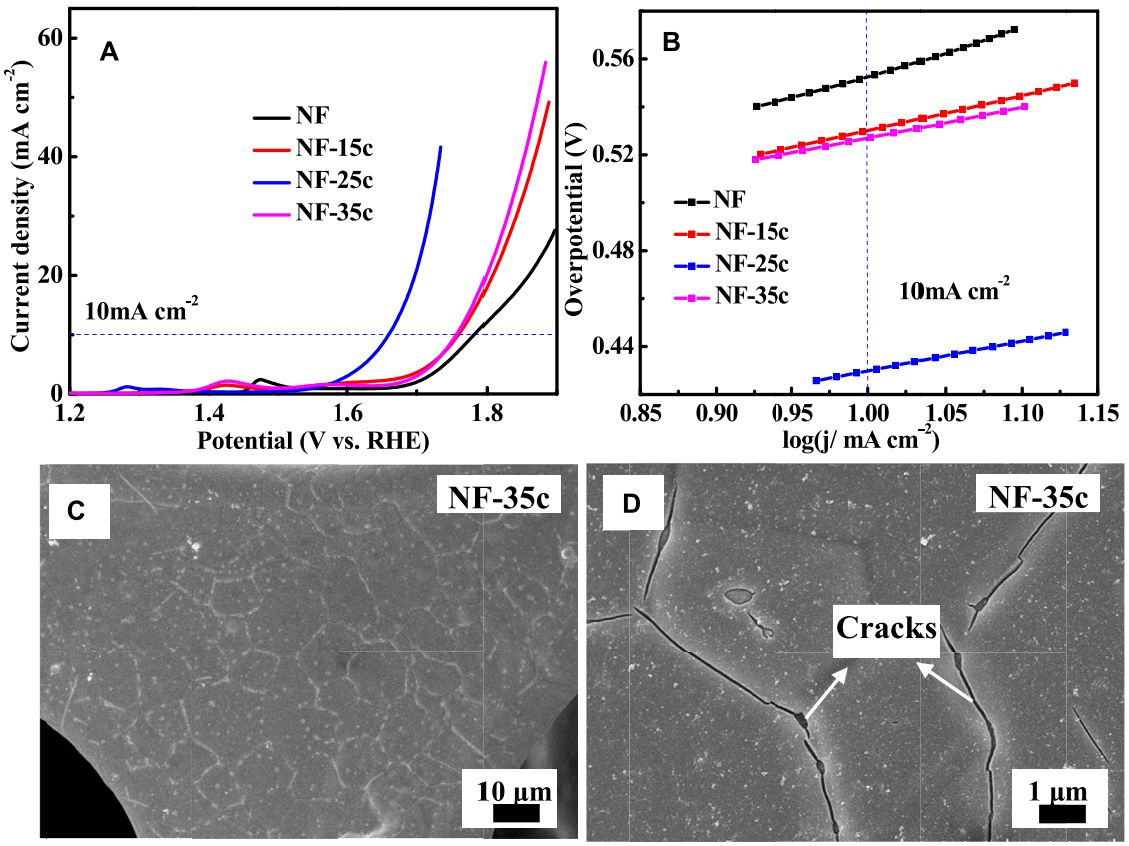

FIGURE 3 | OER measurement curves of the electrode with different cycles of electrodeposition **(A)** LSV curves and **(B)** Tafel slopes. The **(C)** low and **(D)** high magnification SEM images of NF-MnO_2 electrode with pulse electrodeposition for 35 cycles.

MnO_2 film was consistent with the report in the literature (Julien et al., 2002). It has been reported that δ type MnO_2 was formed through the pulse electrodeposition.

Electrochemical Performance

It was reported the loading mass of active material was an important parameter on the electrochemical performance of the composite electrodes (Li et al., 2016). In this study, to determine the effects of pulse electrodeposition cycles on the OER electrocatalytic performance of the composite electrodes, the number of electrodeposition cycles (15–35 cycles) was tuned. In **Figure 3** the electrode with 25 cycles shows the minimum overpotential and the minimum Tafel slope at a current density of 10 mA cm^{-2}, demonstrating the superior electrochemical activity. This was understandable because as the number of electrodeposition cycles was less, the electrochemical performance was poor mainly owing to the lack of active materials. Meanwhile, the electrochemical performance of the composite electrode could not increase monotonously with the continuous increase in electrodeposition cycles considering that obvious cracks were observed in the thick MnO_2 layer as the pulse electrodeposition cycle was increased to 35 (**Figures 3C,D**). In addition, with a continuous increase in thickness of MnO_2, the outer layer does not participate in the catalytic reaction fully due to its poor electrical conductivity (Huang et al., 2015). In general, there was an appropriate loading mass for each electrode support. Therefore, in this study, we considered the suitable cycle of electrodeposition to be 25, and thus the composite electrodes in the following were prepared under the same electrodeposition conditions.

Considering that Ni-based metals could be used as self-supporting oxygen evolution electrodes, the OER electrocatalytic properties of NF, MPNF, NF, MnO_2, and MPNF-MnO_2 were characterized through a three-electrode system (**Figure 4**). From the LSV curves of NF and MPNF in **Figure 4A**, a peak in the potential range of 1.327–1.328 V was observed, which corresponded to the oxidation peak of Ni (II)/Ni (III) (Yu et al., 2016). There was a more obvious peak in the potential range of 1.28–1.29 V for the composite electrodes of NF-MnO_2 and MPNF-MnO_2, which was ascribed to the oxidation peak of Mn (II)/Mn (III) (Devadoss et al., 2003). MPNF and MPNF-MnO_2 electrodes exhibited higher electrocatalytic activities than those of the corresponding reference electrodes (NF and NF-MnO_2). The overpotential of MPNF-MnO_2 at 10 mA cm^{-2} was 363.5 mV, which was lower than that of MPNF (370.6 mV), NF-MnO_2 (429.9 mV), and NF (444 mV). Furthermore, the overpotential was lower than those of most reported electrodes with manganese oxide as the active

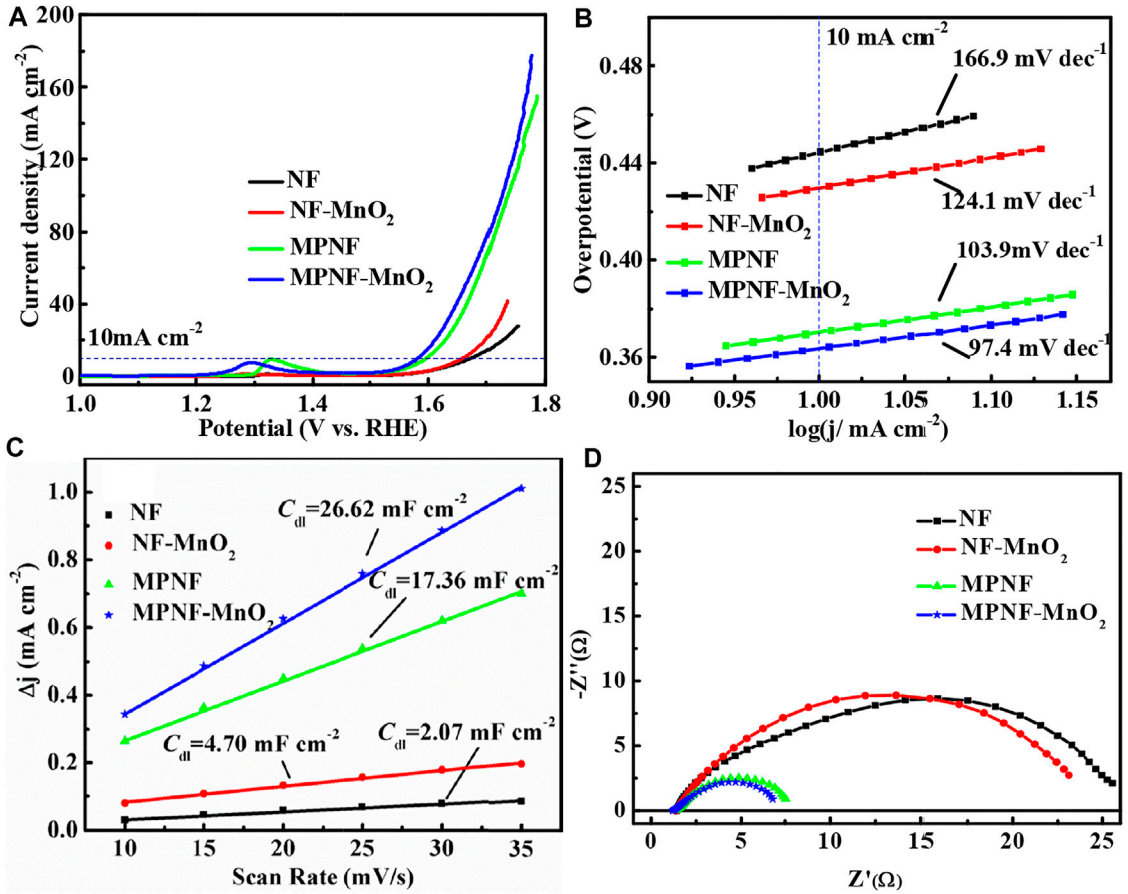

FIGURE 4 | OER curves of NF, MPNF, NF-MnO_2, and MPNF-MnO_2. **(A)** LSV at 5 mV/s of scanning rate, **(B)** Tafel slope linear, **(C)** C_{dl} linear fit by C-V curve, and **(D)** EIS curves at 1.62 V (VS RHE).

TABLE 1 | Comparisons of OER activities of electrodes based on MnO_2.

Active materials	Electrolyte	Supports	Overpotential (mV)	Current density (mA cm^{-2})	References
δ-MnO_2	1M KOH	MPNF	363.5	10	This work
MnO_2	1M NaOH	Glassy Carbon	500	N/A	Jung et al. (2016)
β-MnO_2	1M NaOH	Carbon Paper	450	10	Kim et al. (2016)
Ni^{2+}/MnO_2	1M KOH	Glassy Carbon	400	10	Thenuwara et al. (2016a)
MnNixOx	0.1M KOH	Glassy Carbon	430	10	Ledendecker et al. (2015)
δ-MnO_2	0.1M KPi	Glassy Carbon	441	10	Bergmann et al. (2013)
MnO_2	1M KOH	Carbon fiber paper	467	20	Ye et al. (2017)
Co^{2+}/MnO_2	1M KOH	Glassy Carbon	360	10	Thenuwara et al. (2016b)
α-MnO_2	1M KOH	Ni Foam	357	10	Tian et al. (2020)
MnO_2 with various structures	1 M KOH	Pyrolytic Graphite Carbon	490–740	5	Meng et al. (2014)
Ultrathin δ-MnO_2	1M KOH	Ni Foam	320	10	Zhao et al. (2017)

material (**Table 1**). The Tafel slope of the MPNF-MnO_2 electrode (97.4 mV dec^{-1}) is lower than that of MPNF (103.9 mV dec^{-1}), NF-MnO_2 (124.1 mV dec^{-1}), and NF (166.9 mV dec^{-1}) (**Figure 4B**), showing that the porous substrate obviously accelerates the dynamic process of the composite electrode.

To further investigate the enhancement mechanism of micron/nano-porous and wrinkle structures on MPNF for electrocatalytic activity toward OER, the electrochemically active areas (ECSA) of the four electrodes were extracted from CV curves (**Figure 4C**). The electric double-layer capacitance (C_{dl}) of MPNF-MnO_2 and MPNF were 26.62 and 17.36 mF, respectively, which are much higher than those of NF-MnO_2 (4.70 mF) and NF (2.07 mF). The double capacitance of MPNF is ~8 times higher than that of NF, which indicates that the specific

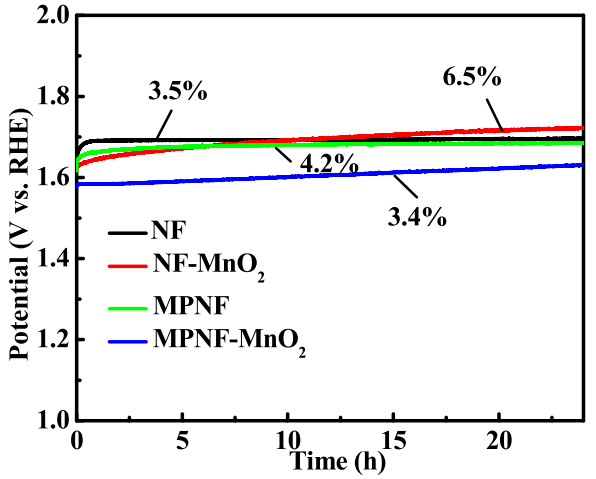

FIGURE 5 | The long-term stability of the MPNF-MnO_2 and NF-MnO_2 electrodes at a constant current density of 10 mA cm^{-2} for 24 h.

surface area of NF could be greatly expanded by the formation of a micron/nano porous and wrinkle structures. Furthermore, the deposition of nano-MnO_2 materials could increase the specific surface area of the supports. Considering these profiles of overpotential, Tafel slope, and C_{dl} of the electrodes, it can be concluded that the porous treatment of NF can significantly improve the OER electrocatalytic activity of the composite electrode. The enhancement of the performance was mainly due to the typical hierarchical porous architecture of MPNF. Larger pores in the skeleton of MPNF ensure the fast conduction of solution ions on the surface of the electrode, and the created micron/nano-porous structure on the ligament greatly increases the contact area between the MPNF and MnO_2, reducing the electrochemical reaction resistance. This can be confirmed by the impedance spectrum of the electrode at a voltage of 1.62 V (**Figure 4D**). The charge transfer resistance (R_{ct}) of the MPNF-MnO_2 electrode was 5.5 Ω, which was much lower than that of the NF-MnO_2 electrode (21.7 Ω).

Long-term stability is another key criterion to evaluate the catalytic performance of OER electrodes. The long-term stability of four electrodes at 10 mA cm^{-2} was investigated (**Figure 5**). It can be seen from the stability test curve that the overpotential of the MPNF-MnO_2 electrode increased by 54 mV within 24 h. The increased rate of the overpotential of MPNF-MnO_2 composite electrode was almost the same as that of Ni substrate. However, the increase in the overpotential of NF-MnO_2 composite electrode was as larger as 105 mV. The enhancement of the stability mainly depended on the added micron/nano porous and wrinkle structure, increasing the contact area between the Ni support and MnO_2 (**Figure 2**, **3**). This could enhance the binding force between the active material MnO_2 and the Ni collector to a certain extent, reducing the shedding of the deposited MnO_2 from the Ni collector and improving the mechanical integrity of the electrode (Xu et al., 2015; Wang et al., 2017).

CONCLUSIONS

In summary, we proposed a simple and green approach to construct *in situ* micron/nano-porous and wrinkle structures on ligaments of commercial NF based on an oxidation–reduction strategy. The formation of micron/nano-porous structure was attributed to the volume expansion and shrink of Ni metal, as well as the diffusion and reconstruction of atoms during the oxidation–reduction process. The resulting MPNF was applied to support and fabricate an efficient OER electrode of MPNF-MnO_2. The micron/nano-porous structures located on the ligaments of NF expand the contact area between the active material (MnO_2) and the Ni support, leading to enhanced OER activity and stability. The overpotential of the MPNF-MnO_2 electrode at 10 mA cm^{-2} is 363.5 mV, which is much higher than that of the NF-MnO_2 electrode (429.9 mV). Furthermore, the strategy of oxidation–reduction developed in this study may open up a new and facile route to fabricate and design hierarchical porous structures on other metal systems (such as Co., Cu, and Fe) for a wide range of structural and functional applications.

DATA AVAILABILITY STATEMENT

The original contributions presented in the study are included in the article/Supplementary Material, and further inquiries can be directed to the corresponding authors.

AUTHOR CONTRIBUTIONS

All authors listed have made a substantial, direct, and intellectual contribution to the work and approved it for publication.

FUNDING

This work was supported by Heilongjiang Natural Science Foundation (QC2018060).

REFERENCES

Bergmann, A., Zaharieva, I., Dau, H., and Strasser, P. (2013). Electrochemical Water Splitting by Layered and 3D Cross-Linked Manganese Oxides: Correlating Structural Motifs and Catalytic Activity. *Energy Environ. Sci.* 6 (9), 2745–2755. doi:10.1039/c3ee41194j

Devadoss, V., Noel, M., Jayaraman, K., and Basha, C. A. (2003). Electrochemical Behaviour of Mn^{3+}/Mn^{2+}, Co^{3+}/Co^{2+} and Ce^{4+}/Ce^{4+} Redox Mediators in Methanesulfonic Acid. *J. Appl. Electrochemistry* 33 (3-4), 319–323. doi:10.1023/A:1024136500644

Faes, A., Hessler-Wyser, A., Zryd, A., and Van herle, J. (2012). A Review of RedOx Cycling of Solid Oxide Fuel Cells Anode. *Membranes* 2 (2), 585–664. doi:10.3390/membranes2030585

Galinski, H., Bieberle-Hütter, A., Rupp, J. L. M., and Gauckler, L. J. (2011). Nonlinear Oxidation Kinetics of Nickel Cermets. *Acta Materialia* 59 (16), 6239–6245. doi:10.1016/j.actamat.2011.06.032

Haugsrud, R. (2003). On the High-Temperature Oxidation of Nickel. *Corrosion Sci.* 45 (1), 211–235. doi:10.1016/S0010-938X(02)00085-9

Huang, M., Li, F., Dong, F., Zhang, Y. X., and Zhang, L. L. (2015). MnO_2-based Nanostructures for High-Performance Supercapacitors. *J. Mater. Chem. A.* 3 (43), 21380–21423. doi:10.1039/C5TA05523G

Julien, C., Massot, M., Rangan, S., Lemal, M., and Guyomard, D. (2002). Study of Structural Defects in ?-MnO_2 by Raman Spectroscopy. *J. Raman Spectrosc.* 33 (4), 223–228. doi:10.1002/jrs.838

Jung, S., McCrory, C. C. L., Ferrer, I. M., Peters, J. C., and Jaramillo, T. F. (2016). Benchmarking Nanoparticulate Metal Oxide Electrocatalysts for the Alkaline Water Oxidation Reaction. *J. Mater. Chem. A.* 4 (8), 3068–3076. doi:10.1039/c5ta07586f

Kim, J., Kim, J. S., Baik, H., Kang, K., and Lee, K. (2016). Porous β-MnO_2 Nanoplates Derived from MnCO3 Nanoplates as Highly Efficient Electrocatalysts toward Oxygen Evolution Reaction. *RSC Adv.* 6 (32), 26535–26539. doi:10.1039/c6ra01091a

Lang, X., Hirata, A., Fujita, T., and Chen, M. (2011). Nanoporous Metal/oxide Hybrid Electrodes for Electrochemical Supercapacitors. *Nat. Nanotech* 6 (4), 232–236. doi:10.1038/nnano.2011.13

Ledendecker, M., Clavel, G., Antonietti, M., and Shalom, M. (2015). Highly Porous Materials as Tunable Electrocatalysts for the Hydrogen and Oxygen Evolution Reaction. *Adv. Funct. Mater.* 25 (3), 393–399. doi:10.1002/adfm.201402078

Li, Y.-Q., Shi, X.-M., Lang, X.-Y., Wen, Z., Li, J.-C., and Jiang, Q. (2016). Remarkable Improvements in Volumetric Energy and Power of 3D MnO_2 Microsuper capacitors by Tuning Crystallographic Structures. *Adv. Funct. Mater.* 26 (11), 1830–1839. doi:10.1002/adfm.201504886

Meng, F., and Ding, Y. (2011). Sub-Micrometer-Thick All-Solid-State Supercapacitors with High Power and Energy Densities. *Adv. Mater.* 23 (35), 4098–4102. doi:10.1002/adma.201101678

Meng, Y., Song, W., Huang, H., Ren, Z., Chen, S.-Y., and Suib, S. L. (2014). Structure-Property Relationship of Bifunctional MnO_2 Nanostructures: Highly Efficient, Ultra-stable Electrochemical Water Oxidation and Oxygen Reduction Reaction Catalysts Identified in Alkaline Media. *J. Am. Chem. Soc.* 136 (32), 11452–11464. doi:10.1021/ja505186m

Meulenberg, W. A., Teller, O., Flesch, U., Buchkremer, H. P., and Stöver, D. (2001). Improved Contacting by the Use of Silver in Solid Oxide Fuel Cells up to an Operating Temperature of 800°C. *J. Mater. Sci.* 36 (13), 3189–3195. doi:10.1023/A:1017930201907

Nakamura, R., Lee, J.-G., Mori, H., and Nakajima, H. (2008). Oxidation Behaviour of Ni Nanoparticles and Formation Process of Hollow NiO. *Phil. Mag.* 88 (2), 257–264. doi:10.1080/14786430701819203

Thenuwara, A. C., Cerkez, E. B., Shumlas, S. L., Attanayake, N. H., McKendry, I. G., Frazer, L., et al. (2016a). Nickel Confined in the Interlayer Region of Birnessite: an Active Electrocatalyst for Water Oxidation. *Angew. Chem. Int. Ed.* 55 (35), 10381–10385. doi:10.1002/anie.201601935

Thenuwara, A. C., Shumlas, S. L., Attanayake, N. H., Aulin, Y. V., McKendry, I. G., Qiao, Q., et al. (2016b). Intercalation of Cobalt into the Interlayer of Birnessite Improves Oxygen Evolution Catalysis. *ACS Catal.* 6 (11), 7739–7743. doi:10.1021/acscatal.6b01980

Tian, L., Zhai, X., Wang, X., Pang, X., Li, J., and Li, Z. (2020). Morphology and Phase Transformation of α-MnO_2/MnOOH Modulated by N-CDs for Efficient Electrocatalytic Oxygen Evolution Reaction in Alkaline Medium. *Electrochimica Acta* 337, 135823. doi:10.1016/j.electacta.2020.135823

Tong, Y.-L., Xing, L., Dai, M.-Z., and Wu, X. (2019). Hybrid Co3O4@Co9S8 Electrocatalysts for Oxygen Evolution Reaction. *Front. Mater.* 6, 233. doi:10.3389/fmats.2019.00233

Wang, Z., Yan, Y., Chen, Y., Han, W., Liu, M., Zhang, Y., et al. (2017). 3D-Hierarchical Porous Nickel Sculptured by a Simple Redox Process and its Application in High-Performance Supercapacitors. *J. Mater. Chem. A.* 5 (39), 20709–20719. doi:10.1039/C7TA04293K

Xu, G.-r., Wen, Y., Min, X.-p., Dong, W.-h., Tang, A.-p., and Song, H.-s. (2015). Construction of MnO_2/3-Dimensional Porous Crack Ni for High-Performance Supercapacitors. *Electrochimica Acta* 186, 133–141. doi:10.1016/j.electacta.2015.10.136

Ye, Z., Li, T., Ma, G., Dong, Y., and Zhou, X. (2017). Metal-Ion (Fe, V, Co, and Ni)-Doped MnO_2 Ultrathin Nanosheets Supported on Carbon Fiber Paper for the Oxygen Evolution Reaction. *Adv. Funct. Mater.* 27 (44), 1704083. doi:10.1002/adfm.201704083

Yu, M., Wang, W., Li, C., Zhai, T., Lu, X., and Tong, Y. (2014). Scalable Self-Growth of Ni@NiO Core-Shell Electrode with Ultrahigh Capacitance and Super-long Cyclic Stability for Supercapacitors. *NPG Asia Mater.* 6 (9), e129. doi:10.1038/am.2014.78

Yu, X.-Y., Feng, Y., Guan, B., Lou, X. W., and Paik, U. (2016). Carbon Coated Porous Nickel Phosphides Nanoplates for Highly Efficient Oxygen Evolution Reaction. *Energ. Environ. Sci.* 9 (4), 1246–1250. doi:10.1039/c6ee00100a

Yuan, C., Li, J., Hou, L., Zhang, X., Shen, L., and Lou, X. W. D. (2012). Ultrathin Mesoporous NiCo2O4Nanosheets Supported on Ni Foam as Advanced Electrodes for Supercapacitors. *Adv. Funct. Mater.* 22 (21), 4592–4597. doi:10.1002/adfm.201200994

Zeng, J., Zhang, S., Xue, J., Dai, H., Xia, L., Cai, W., et al. (2020). Enhanced Dielectric Loss and Magnetic Loss Properties of Copper Oxide-Nanowire-Covered Carbon Fiber Composites by Porous Nickel Film. *Front. Mater.* 7, 123. doi:10.3389/fmats.2020.00123

Zhao, Y., Chang, C., Teng, F., Zhao, Y., Chen, G., Shi, R., et al. (2017). Defect-Engineered Ultrathin δ-MnO_2 Nanosheet Arrays as Bifunctional Electrodes for Efficient Overall Water Splitting. *Adv. Energ. Mater.* 7 (18), 1700005. doi:10.1002/aenm.201700005

Zhou, W., Wu, X.-J., Cao, X., Huang, X., Tan, C., Tian, J., et al. (2013). Ni3S2 nanorods/Ni Foam Composite Electrode with Low Overpotential for Electrocatalytic Oxygen Evolution. *Energ. Environ. Sci.* 6 (10), 2921–2924. doi:10.1039/c3ee41572d

Conflict of Interest: The authors declare that the research was conducted in the absence of any commercial or financial relationships that could be construed as a potential conflict of interest.

Publisher's Note: All claims expressed in this article are solely those of the authors and do not necessarily represent those of their affiliated organizations, or those of the publisher, the editors and the reviewers. Any product that may be evaluated in this article, or claim that may be made by its manufacturer, is not guaranteed or endorsed by the publisher.

frontiers in Materials

ORIGINAL RESEARCH
published: 22 October 2021
doi: 10.3389/fmats.2021.767812

Florescence Intensity Ratio Thermometer in the First Biological Window Based on Non-Thermally Coupled Energy Levels of Tm^{3+} and Ho^{3+} Ions

*Liang Li and Haoyue Hao**

School of Physics and Optoelectronic Engineering, Shandong University of Technology, Zibo, China

In this study, the up-conversion luminescence and optical temperature sensing properties of Ho^{3+}/Tm^{3+}/Yb^{3+}-co-doped $NaLuF_4$ phosphors were investigated. The visible (475, 540, and 650 nm) and near-infrared light (692 and 800 nm) radiated from 1Ho^{3+}/4Tm^{3+}/Yb^{3+}-co-doped $NaLuF_4$ phosphors were obvious enough for subsequent detection. The slopes in the ln*I*–ln*P* plot of the emissions located in the first biological window (650, 692, and 800 nm) were both ~1.5, which mean that the power had little effect on the three fluorescence peak ratios. Based on the florescence intensity ratios (FIRs) of 650 and 692 nm, the relative sensing sensitivity reaches 0.029 K^{-1} (476 K). The relative sensing sensitivity based on the FIRs of 800 and 692 nm reaches 0.0076 K^{-1} (476 K). The results reveal that 1Ho^{3+}/4Tm^{3+}/Yb^{3+}-co-doped $NaLuF_4$ phosphors have potential applications in FIR-based temperature sensing in biological tissue for their high sensing sensitivity. In addition, the emission colors of the sample stabilize in the white light region as the temperature increased from 303 to 467 K, implying that it can also be used in white display.

Keywords: rare earth doped, up-conversion luminescent materials, fluorescence intensity ratio, temperature sensing sensitivity, first biological window

OPEN ACCESS

Edited by:
Zhongquan Nie,
Taiyuan University of Technology, China

Reviewed by:
Peng Du,
Ningbo University, China
Caixia Xu,
Chongqing Normal University, China

****Correspondence:***
Haoyue Hao
haohao_yue@163.com

Specialty section:
This article was submitted to Quantum Materials, a section of the journal Frontiers in Materials

Received: *31 August 2021*
Accepted: *16 September 2021*
Published: *22 October 2021*

Citation:
Li L and Hao H (2021) Florescence Intensity Ratio Thermometer in the First Biological Window Based on Non-Thermally Coupled Energy Levels of Tm^{3+} and Ho^{3+} Ions. Front. Mater. 8:767812. doi: 10.3389/fmats.2021.767812

INTRODUCTION

Temperature (T) is a basic physical parameter in scientific research, production, and living. Therefore, it is crucial to obtain accurate T. Traditional methods of temperature measurement are based on different thermometers, thermal resistance, thermocouples, semiconductor temperature sensor, etc. However, these methods require the physical contact with the object and cannot be used in a corrosive environment or organism. To overcome this issue, numerous types of luminescent thermometers, made up of quantum dots, polymer-based systems, organic dyes, and lanthanide ion (Ln^{3+})–doped materials, have been investigated (Feng et al., 2011; Vlaskin et al., 2010; Yan et al., 2010; Jia et al., 2020). Among these luminescent thermometers, Ln^{3+}-doped up-conversion materials have drawn extensive attention in the research of non-invasive temperature measurement due to their fast response, high resolution, low toxicity, remote detection, and so on (Labrador-Páez et al., 2018; Ximendes et al., 2016; Skripka et al., 2017; Nexha et al., 2021). In recent years, the florescence intensity ratio (FIR) from the Ln^{3+}-doped up-conversion materials has often been utilized in thermometry, rather than emission lifetime, peak position, and emission color (Runowski et al., 2019; Yuan et al., 2017; Qiu et al., 2020; Du et al., 2018). The FIR temperature sensing method is based on

the emissions, radiated from thermally coupled energy levels ($200\ cm^{-1}<\Delta E<2000\ cm^{-1}$) (Runowski et al., 2019; Yuan et al., 2017; Du et al., 2018) or non-thermally coupled energy levels ($\Delta E>2000\ cm^{-1}$ or different Ln^{3+}) (Han et al., 2019; Peng et al., 2021; Chen et al., 2015). Er^{3+} ion is promising in FIR temperature sensing for its bright green emission from $^2H_{11/2}/^4S_{3/2}$ and excellent thermal coupling property owing to the suitable energy gap ($700–800\ cm^{-1}$), whereas the sensing sensitivity is restricted by the constant energy gap (Xiang et al., 2020; Wang et al., 2018). As far as we know, the sensing sensitivity value is decided by the variation rate of FIR with the temperature. Thus, many strategies are utilized to improve sensitivity, such as choosing the suitable co-doped ions (Lu et al., 2017), changing the suitable host (Huang et al., 2015), distorting local symmetric (Xiang et al., 2020), and using stark sublevels (Suo et al., 2018), while the commonly used fluorescence peaks are located in the visible range, like 520 and 550 nm from Er^{3+}, which limit the penetration depth in biological tissues. Therefore, the selected emissions should be located in biological windows to decrease light scattering when they were used in biological tissue temperature sensing (Runowski et al., 2019; del Rosal et al., 2017).

In this study, the emissions (450–850 nm) from $Ho^{3+}/Tm^{3+}/Yb^{3+}$-co-doped $NaLuF_4$ phosphors are systemically investigated. High absolute and relative temperature sensitivity can be achieved *via* choosing suitable FIR. Moreover, the slopes in the ln*I*–ln*P* plot of emissions located in the first biological window (650, 692 and 800 nm) are both ~1.5, which means that power has little effect on the three fluorescence peak ratios. We can take the advantages of these and detect the three emissions for non-invasive temperature measure in biological tissues.

EXPERIMENTAL DETAILS

Sample Preparation

Materials

$Lu(NO_3)_3{\cdot}6H_2O$ (99.9%), $Yb(NO_3)_3{\cdot}6H_2O$ (99.9%), $Tm(NO_3)_3{\cdot}6H_2O$ (99.9%), and $Ho(NO_3)_3{\cdot}6H_2O$ (99.9%) were all purchased from Jining Zhong Kai New Type Material Science Co., Ltd. Ammonium fluoride (AR), sodium hydroxide (AR), oleic acid (AR), and cyclohexane (AR) were purchased from Tianjin Tianli Chemical reagent Co. Ltd. All the chemicals were used directly without further purification.

Preparation of $NaLuF_4$:1 mol% Ho^{3+}, 4 mol% Tm^{3+}, and 20 mol% Yb^{3+} Phosphors

The $NaLuF_4$:1 mol% Ho^{3+}, 4 mol% Tm^{3+}, and 20 mol% Yb^{3+} phosphors were prepared using a typical hydrothermal method. The preparation processes of $NaLuF_4$: Ho^{3+}, Tm^{3+}, and Yb^{3+} phosphors were as follows. First, calculated amounts of sodium hydroxide were dissolved into 2 ml deionized water. Second, 10 ml absolute ethyl alcohol and 18 ml oleic acid were added in the nitrate solution and then stirred for 5 min at room temperature to form a faint yellow solution. Third, 5 ml aqueous solution was then added, which contained a calculated amount of $Lu(NO_3)_3{\cdot}6H_2O$, $Yb(NO_3)_3{\cdot}6H_2O$, $Ho(NO_3)_3{\cdot}6H_2O$, and $Tm(NO_3)_3{\cdot}6H_2O$ $C_6H_8O_7{\cdot}H_2O$ and 5 ml ammonium fluoride aqueous solution. After stirring for 30 min at room temperature, the mixed solution was transferred into a 50-ml autoclave and heated at 180°C for 12 h in a drying oven. After cooling down to room temperature and adding ethanol and cyclohexane, the khaki suspension was centrifuged (8,000 rpm, 2 min) for collection and washed three times with ethanol and deionized water. Finally, phosphors were obtained after drying at 60°C for 10 h.

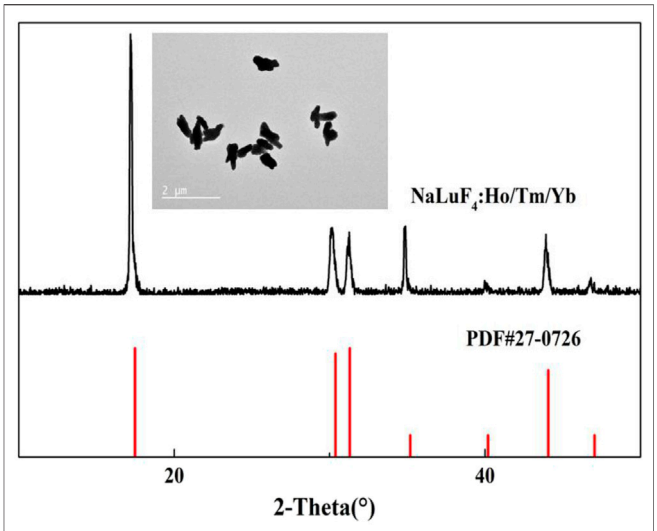

FIGURE 1 | XRD patterns of $NaLuF_4$: Ho^{3+}, Tm^{3+}, and Yb^{3+} phosphors (the inset displays the TEM image of the phosphors).

Instruments

The X-ray diffraction (XRD) pattern of the sample was tested using an X-ray diffractometer (D8-02, Bruker AXS, Germany). The morphology was tested using a transmission electron microscope (TEM: Tecnai G2F 20, FEI, America). The spectra of the samples were tested with an iHR550 grating spectrograph (iHR550, Horiba, France). The 980-nm laser, used to excite the sample, was purchased from Beijing Kipling Photoelectric technology Co., Ltd. The sample was heated by the Linkam THMS 600 heating stage. The temperature of sample was monitored by thermocouple.

RESULTS AND DISCUSSIONS

XRD Analysis

The XRD pattern of $NaLuF_4$: Ho^{3+}, Tm^{3+}, and Yb^{3+} phosphors is presented in **Figure 1**. We can find that the XRD patterns of the samples can be indexed to a hexagonal $NaLuF_4$ crystal (the JCPDS standard card no. 27-0726), indicating that the dopants (Ho^{3+}, Tm^{3+}, and Yb^{3+} ions) were successfully incorporated into the host lattice and did not cause significant changes to the crystal structure. The inset showed the TEM images of the sample and the morphology was approximately rod-like.

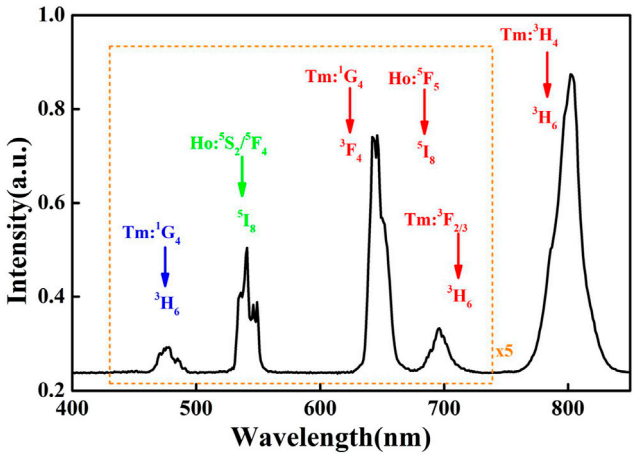

FIGURE 2 | Up-conversion spectra of the sample under the excitation of 980-nm laser (the emission intensities of 475, 540, 650, and 692 nm was magnified five times).

Power-dependent Up-Conversion Luminescence

Figure 2 showed the room temperature up-conversion luminescence of $NaLuF_4$: Ho^{3+}, Tm^{3+}, and Yb^{3+} phosphors. Under 980-nm laser excitation, the sample exhibited five obvious emission bands centered at 475, 540, 650, 692, and 800 nm. The emissions were attributed to $^1G_4 \rightarrow {}^3H_6$ (Tm^{3+}), $^5S_2/{}^5F_4 \rightarrow {}^5I_8$ (Ho^{3+}), $^1G_4 \rightarrow {}^3F_4$ (Tm^{3+})/$^5F_5 \rightarrow {}^5I_8$ (Ho^{3+}), $^3F_{2/3} \rightarrow {}^3H_6$ (Tm^{3+}), and $^3H_4 \rightarrow {}^3H_6$ (Tm^{3+}). It was obvious that the Ho^{3+}, Tm^{3+}, and Yb^{3+}-co-doped $NaLuF_4$ could provide visible light (475, 540, 650 and 692 nm), which can be used for colorful displaying. Meanwhile, the emissions (650, 692, and 800 nm) located in the first biological window can be utilized to florescent location and temperature detection in biological tissue.

The power-dependent up-conversion spectra of the sample are exhibited in **Figure 3A**, and the emission intensity increased obviously with the power rising. The relationship between laser power (P) and emission intensity (I) can be expressed as $I \propto P^n$, where n refers to the number of the required photons participated in the up-conversion process (Pollnau et al., 2000). Thus, the value of n can be calculated by the slope obtained from the double logarithmic plot between I and P, as shown in **Figure 3B**. The values of n were ~2.1, ~1.4, ~1.5, ~1.5, and ~1.5, respectively. It implied that the 475, 540, 650, 692, and 800 nm emissions were three-photon, two-photon, two-photon, two-photon, and two-photon processes, respectively. What is more, the value of n for the emissions located in the first biological window was similar to each other, which means that the power has little effect on the three fluorescence peak ratios (Jia et al., 2020). **Figure 4** showed the schematic energy levels and the possible up-conversion and energy transfer (ET) processes. Under 980-nm laser excitation, Yb^{3+} continuously absorbed 980-nm photons and transfers them to Ho^{3+}/Tm^{3+}. As described in other research, the possible ET occurred between Tm^{3+} and Ho^{3+}, inducing the enhancement of 800 nm emission (Wang et al., 2012). Therefore, the FIR of 692/800 was fitted through the cubic function rather than the exponential function.

Temperature-dependent Up-Conversion Luminescence Analysis

For FIR-based non-contact thermometry, we studied the temperature-dependent emissions (visible light and the first biological window range) of Ho^{3+}, Tm^{3+}, and Yb^{3+}-co-doped $NaLuF_4$ powder. The temperature-dependent emission spectra are shown in **Figure 5A**, and the emission intensities changed as the temperature varied from 303 to 476 K (as shown in **Figure 5B**). In the visible light range, we choose 475 and 550-nm emissions in the FIR-based non-contact thermometry. In addition, the emission colors of the sample stabilized in the white light region as the temperature increased from 303 to 467 K, implying that it can also be used in white display. The detail calculated chromaticity coordinates (x,y) at different temperature are shown in **Supplementary Table S1**.

Figure 6A showed the ratio (R) of blue to green ($R_{475/550}$) at varied temperature. The temperature dependence of FIR from the non-thermal coupled levels was commonly fitted by polynomial (Lu et al., 2017). Here, we fitted it by mean of a cubic function

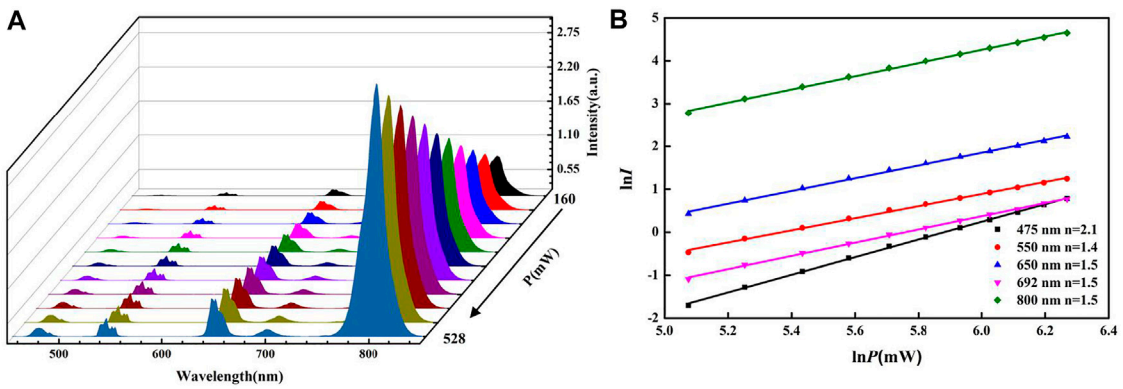

FIGURE 3 | (A) Up-conversion spectra with the increasing power of 980-nm laser; **(B)** lnI–lnP plot.

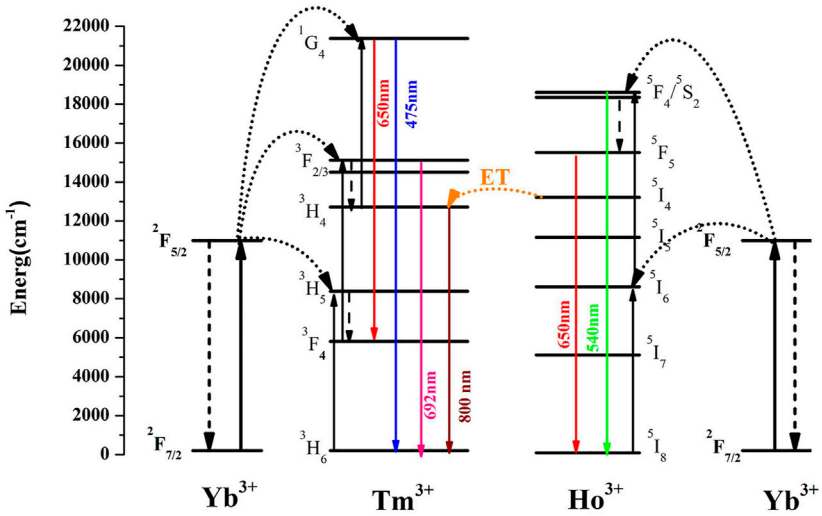

FIGURE 4 | Schematic energy levels, possible up-conversion processes, and energy transfer processes in Ho^{3+}, Tm^{3+}, and Yb^{3+}-co-doped materials.

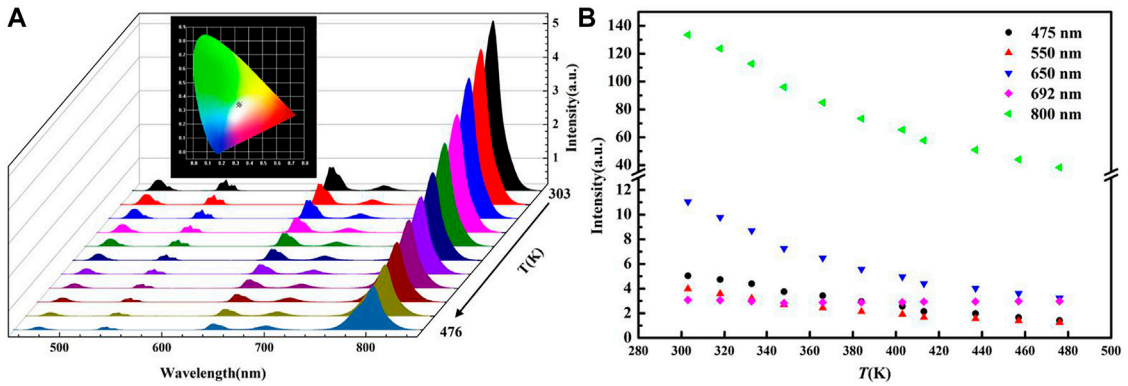

FIGURE 5 | (A) Up-conversion luminescence of the sample at different temperature, the inset shows the CIE chromaticity coordinates of the sample at different temperature; **(B)** temperature-dependent integrated intensity of the emissions located at different wavelength.

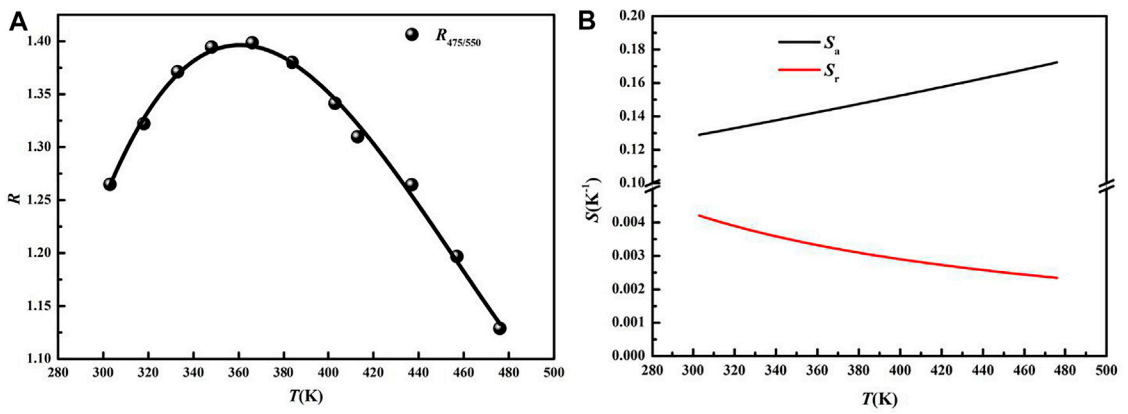

FIGURE 6 | (A) Temperature-dependent $R_{475/550}$; **(B)** S_a and S_r from 303–476 K.

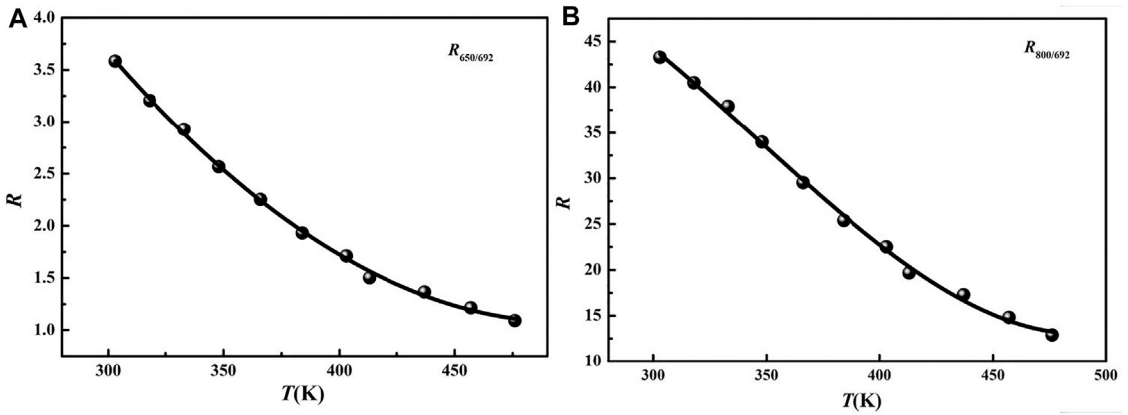

FIGURE 7 | Temperature-dependent **(A)** $R_{650/692}$ and **(B)** $R_{800/692}$.

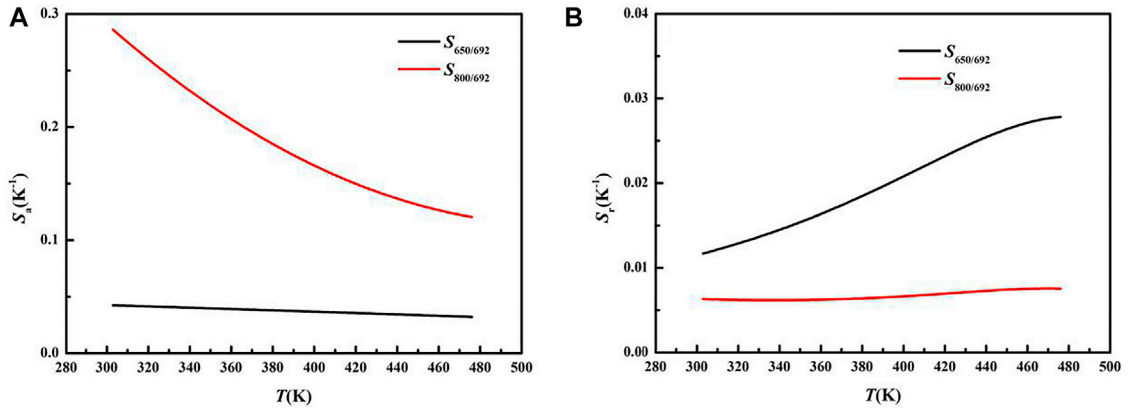

FIGURE 8 | Temperature-dependent **(A)** S_a and **(B)** S_r of I_{650}/I_{692} and I_{800}/I_{692}, respectively.

$R = B_0 + B_1T + B_2T^2 + B_2T^3$, and the fitting parameters are displayed in **Supplementary Table S2**. To evaluate the sensing capacity of different thermometry method, we calculated the absolute sensing sensitivity (S_a) and relative sensing sensitivity (S_r) through the expression $S_a = \frac{dR}{dT} = B_1 + B_2T + B_3T^2$; $S_r = \frac{1}{R}\frac{dR}{dT}$ (Jia et al., 2020; Peng et al., 2021). As shown in **Figure 6B**, the maximum value of S_a and S_r reached 0.17 K^{-1} (467 K) and 0.0043 (303 K), respectively. Therefore, the ratio of blue and green can be used for temperature measurement.

Figures 7A,B showed the values of $R_{650/692}$ and $R_{800/692}$ at different temperatures. The values were fitted *via* cubic function and the fitting parameters are displayed in **Supplementary Table S2**. The absolute sensing sensitivity and relative sensing sensitivity are displayed in **Figures 8A,B**. The maximum values of S_a reached 0.042 K^{-1} ($R_{650/692}$) and 0.29 K^{-1} ($R_{800/692}$) at 303 K, respectively. The maximum values of S_r reached 0.028 K^{-1} at 467 K ($R_{650/692}$) and 0.0076 at 303 K ($R_{800/692}$). The ratio of emissions in the first biological window showed higher relatively sensing sensitivity than in the visible range, indicating its extensive application value in temperature measurement, especially in biological temperature measurement. To compare the thermometric capacities of this sample, relevant parameters of other related research studies are listed in **Table 1**. It can be seen that the sensing sensitivities of our samples are relatively high in these studies. In addition, this method is flexible and practical in thermometry application, such as the selection of detection wavelengths, exciting powers, and detection materials.

CONCLUSION

In conclusion, up-conversion luminescence and temperature-dependent emissions of the transitions $^1G_4 \rightarrow {}^3H_6$ (475 nm), $^5S_2/{}^5F_4 \rightarrow {}^5I_8$ (550 nm), $^1G_4 \rightarrow {}^3F_4/{}^5F_5 \rightarrow {}^5I_8$ (650 nm), $^3F_{2/3} \rightarrow {}^3H_6$ (692 nm), and $^3H_4 \rightarrow {}^3H_6$ (800 nm) from $Ho^{3+}/Tm^{3+}/Yb^{3+}$-co-doped $NaLuF_4$ phosphors were studied under 980 excitation, and the slopes in the ln*I*–ln*P* plot of the emissions were ~2.1, ~1.4, ~1.5, ~1.5, and ~1.5, respectively. It implied that the 475, 540, 650, 692, and 800-nm emissions were three-photon, two-photon, two-photon, two-photon, and two-photon processes, respectively.

TABLE 1 | Comparison of sensing sensitivities in FIR thermometry.

Material	Detection wavelengths (nm)	FIR $S_r(K^{-1})$ (temperature, K)	Ref
$KLu(WO_4)_2$:Ho/Tm	696/755	0.0186 (300)	Diaz et al. (2018)
$Ba_2In_2O_5$:Ho/Yb	653/661	0.0025 (273)	Wang et al. (2018)
$Ba_3Y_4O_9$: Ho/Tm/Yb	808/668	0.0028 (380)	Liu et al. (2019)
$Ba_3Y_4O_9$: Ho/Tm/Yb	693/668	0.0111 (475)	Liu et al. (2019)
$NaYbF_4/NaYF_4$:Tm/Yb/$NaYF_4$	800/1800	0.0033 (300)	Xu et al. (2020)
NaY_2F_7:Yb/Tm	678/700	0.016 (415)	Chen et al. (2020)
$BaMoO_4$:Yb/Tm	650/691	0.013 (0.37)	Liu et al. (2019)
$NaYF_4$: Ho	961/1,183	0.008 (367)	Li et al. (2021)
Bi_5IO_7: Er	520/550	0.0136 (303)	Luo et al. (2020)
$NaLuF_4$:Eu@g-C_3N_4	575/625	0.00455 (383)	Du et al. (2021)
$NaLuF_4$:Ho/Tm/Yb	450/550	0.0043 (303)	This work
—	800/692	0.0076 (476)	This work
—	650/692	0.029 (476)	This work

More importantly, the values of *n* for the emissions located in the first biological window were similar to each other, which means that power had little effect on the three fluorescence peak ratios. Based on FIRs of 450 and 550 nm, S_r reached 0.0043 K^{-1}. Based on the emissions in the first biological window ($R_{650/692}$ and $R_{800/692}$), S_r reached 0.29 and 0.0076 K^{-1}, respectively. The result reveals that $1Ho^{3+}/4Tm^{3+}/Yb^{3+}$-co-doped $NaLuF_4$ phosphors have potential applications in FIR-based temperature sensing in biological tissue for their high sensing sensitivity. In addition, the emission colors of the sample stabilized in the white light region as the temperature increased from 303 to 467 K, implying that it can also be used in white display.

DATA AVAILABILITY STATEMENT

The original contributions presented in the study are included in the article/**Supplementary Material**; further inquiries can be directed to the corresponding author.

AUTHOR CONTRIBUTIONS

All authors listed have made a substantial, direct, and intellectual contribution to the work and approved it for publication.

FUNDING

The work was financially supported by the National Natural Science Foundation of China (Grant No. 12004217) and the Natural Science Foundation of Shandong province (Grant Nos. ZR201910230199 and ZR201910230202).

SUPPLEMENTARY MATERIAL

The Supplementary Material for this article can be found online at: https://www.frontiersin.org/articles/10.3389/fmats.2021.767812/full#supplementary-material

REFERENCES

Chen, D., Liu, S., Xu, W., and Li, X. (2017). Yb3+/Ln3+/Cr3+ (Ln = Er, Ho) Doped Transparent Glass Ceramics: Crystallization, Ln3+ Sensitized Cr3+ Upconversion Emission and Multi-Modal Temperature Sensing. *J. Mater. Chem. C* 5 (45), 11769–11780. doi:10.1039/c7tc04410k

Chen, S., Song, W., Cao, J., Hu, F., and Guo, H. (2020). Highly Sensitive Optical Thermometer Based on FIR Technique of Transparent NaY2F7:Tm3+/Yb3+ Glass Ceramic. *J. Alloys Compd.* 825, 154011. doi:10.1016/j.jallcom.2020.154011

del Rosal, B., Ximendes, E., Rocha, U., and Jaque, D. (2017). *In Vivo* luminescence Nanothermometry: from Materials to Applications. *Adv. Opt. Mater.* 5 (1), 1600508. doi:10.1002/adom.201600508

Du, P., Luo, L., Huang, X., and Yu, J. S. (2018). Ultrafast Synthesis of Bifunctional Er3+/Yb3+-Codoped NaBiF4 Upconverting Nanoparticles for Nanothermometer and Optical Heater. *J. Colloid Interf. Sci.* 514, 172–181. doi:10.1016/j.jcis.2017.12.027

Du, P., Tang, J., Li, W., and Luo, L. (2021). Exploiting the Diverse Photoluminescence Behaviors of NaLuF4:xEu3+ Nanoparticles and G-C3n4 to Realize Versatile Applications in white Light-Emitting Diode and Optical Thermometer. *Chem. Eng. J.* 406, 127165. doi:10.1016/j.cej.2020.127165

Feng, J., Tian, K., Hu, D., Wang, S., Li, S., Zeng, Y., et al. (2011). A Triarylboron-Based Fluorescent Thermometer: Sensitive over a Wide Temperature Range. *Angew. Chem.* 123 (35), 8222–8226. doi:10.1002/ange.201102390

Han, Q., Hao, H., Yang, J., Sun, Z., Sun, J., Song, Y., et al. (2019). Optical Temperature Sensing Based on thermal, Non-thermal Coupled Levels and Tunable Luminescent Emission Colors of Er3+/Tm3+/Yb3+ Tri-doped Y7O6F9 Phosphor. *J. Alloys Compd.* 786, 770–778. doi:10.1016/j.jallcom.2019.02.047

Huang, F., Gao, Y., Zhou, J., Xu, J., and Wang, Y. (2015). Yb3+/Er3+ Co-doped CaMoO4: a Promising green Upconversion Phosphor for Optical Temperature Sensing. *J. Alloys Compd.* 639, 325–329. doi:10.1016/j.jallcom.2015.02.228

Jia, M., Sun, Z., Xu, H., Jin, X., Lv, Z., Sheng, T., et al. (2020). An Ultrasensitive Luminescent Nanothermometer in the First Biological Window Based on Phonon-Assisted thermal Enhancing and thermal Quenching. *J. Mater. Chem. C* 8 (44), 15603–15608. doi:10.1039/d0tc04082g

Labrador-Páez, L., Pedroni, M., Speghini, A., García-Solé, J., Haro-González, P., and Jaque, D. (2018). Reliability of Rare-Earth-Doped Infrared Luminescent Nanothermometers. *Nanoscale* 10 (47), 22319–22328. doi:10.1039/c8nr07566b

Li, Z., Lin, L., Feng, Z., Huang, L., Wang, Z., and Zheng, Z. (2021). Wide-range Temperature Sensing of NaYF4: Ho3+ Nanoparticles by Multi-Emissions in Dual Spectral Ranges. *J. Lumin.* 232, 117873. doi:10.1016/j.jlumin.2020.117873

Liu, S., Cui, J., Jia, J., Fu, J., You, W., Zeng, Q., et al. (2019a). High Sensitive Ln3+/Tm3+/Yb3+ (Ln3+ = Ho3+, Er3+) Tri-doped Ba3Y4O9 Upconverting Optical Thermometric Materials Based on Diverse thermal Response from Non-thermally Coupled Energy Levels. *Ceramics Int.* 45 (1), 1–10. doi:10.1016/j.ceramint.2018.09.162

Liu, X., Lei, R., Li, Y., and Xu, S. (2019b). Tm^{3+}/Yb^{3+}: $BaMoO_4$ Phosphor for High-Performance Thermometry Operating in the First Biological Window. *Opt. Lett.* 44 (15), 3633–3636. doi:10.1364/ol.44.003633

Lu, H., Hao, H., Zhu, H., Shi, G., Fan, Q., Song, Y., et al. (2017). Enhancing Temperature Sensing Behavior of NaLuF4:Yb3+/Er3 via Incorporation of Mn2+ Ions Resulting in a Closed Energy Transfer. *J. Alloys Compd.* 728, 971–975. doi:10.1016/j.jallcom.2017.09.080

Luo, L., Ran, W., Du, P., Li, W., and Wang, D. (2020). Photocatalytic and Thermometric Characteristics of Er 3+ -Activated Bi 5 IO 7 Upconverting Microparticles. *Adv. Mater. Inter.* 7 (11), 1902208. doi:10.1002/admi.201902208

Nexha, A., Carvajal, J. J., Pujol, M. C., Díaz, F., and Aguiló, M. (2021). Lanthanide Doped Luminescence Nanothermometers in the Biological Windows: Strategies and Applications. *Nanoscale* 13 (17), 7913–7987. doi:10.1039/d0nr09150b

Peng, Y., Cheng, Z., Khan, W. U., Liu, T., Shen, M., Yang, S., et al. (2021). Enhancing Upconversion Emissions and Temperature Sensing Properties by Incorporating Mn2+ for KLu2F7:Yb3+/Er3+ Nanocrystals Based on Thermally and Non-thermally Coupled Levels. *New J. Chem.* 45 (8), 3876–3885. doi:10.1039/d0nj06195f

Pollnau, M., Gamelin, D. R., Lüthi, S. R., Güdel, H. U., and Hehlen, M. P. (2000). Power Dependence of Upconversion Luminescence in Lanthanide and Transition-Metal-Ion Systems. *Phys. Rev. B* 61 (5), 3337–3346. doi:10.1103/physrevb.61.3337

Qiu, X., Zhou, Q., Zhu, X., Wu, Z., Feng, W., and Li, F. (2020). Ratiometric Upconversion Nanothermometry with Dual Emission at the Same Wavelength Decoded via a Time-Resolved Technique. *Nat. Commun.* 11 (1), 4–9. doi:10.1038/s41467-019-13796-w

Runowski, M., Stopikowska, N., Szeremeta, D., Goderski, S., Skwierczyńska, M., and Lis, S. (2019). Upconverting Lanthanide Fluoride Core@Shell Nanorods for Luminescent Thermometry in the First and Second Biological Windows: β-NaYF4:Yb3+- Er3+@SiO2 Temperature Sensor. *ACS Appl. Mater. Inter.* 11 (14), 13389–13396. doi:10.1021/acsami.9b00445

Savchuk, O. A., Carvajal, J. J., Brites, C. D. S., Carlos, L. D., Aguilo, M., and Diaz, F. (2018). Upconversion Thermometry: A New Tool to Measure the thermal Resistance of Nanoparticles. *Nanoscale* 10 (14), 6602–6610. doi:10.1039/c7nr08758f

Skripka, A., Benayas, A., Marin, R., Canton, P., Hemmer, E., and Vetrone, F. (2017). Double Rare-Earth Nanothermometer in Aqueous media: Opening the Third Optical Transparency Window to Temperature Sensing. *Nanoscale* 9 (9), 3079–3085. doi:10.1039/c6nr08472a

Suo, H., Zhao, X., Zhang, Z., Shi, R., Wu, Y., Xiang, J., et al. (2018). Local Symmetric Distortion Boosted Photon Up-Conversion and Thermometric Sensitivity in Lanthanum Oxide Nanospheres. *Nanoscale* 10 (19), 9245–9251. doi:10.1039/c8nr01734d

Vlaskin, V. A., Janssen, N., van Rijssel, J., Beaulac, R., and Gamelin, D. R. (2010). Tunable Dual Emission in Doped Semiconductor Nanocrystals. *Nano Lett.* 10 (9), 3670–3674. doi:10.1021/nl102135k

Wang, D., Zhang, P., Ma, Q., Zhang, J., and Wang, Y. (2018). Synthesis, Optical Properties and Application of Y7O6F9:Er3+ for Sensing the Chip Temperature of a Light Emitting Diode. *J. Mater. Chem. C* 6 (48), 13352–13358. doi:10.1039/c8tc05307c

Wang, L., Qin, W., Liu, Z., Zhao, D., Qin, G., Di, W., et al. (2012). Improved 800 Nm Emission of Tm̈3+ Sensitized by Yb3+ and Hö3+ in β-NaYF_4 Nanocrystals under 980 Nm Excitation. *Opt. Express* 20 (7), 7602–7607. doi:10.1364/oe.20.007602

Wang, Z., Jiao, H., and Fu, Z. (2018). Investigating the Luminescence Behaviors and Temperature Sensing Properties of Rare-Earth-Doped Ba2In2O5 Phosphors. *Inorg. Chem.* 57 (15), 8841–8849. doi:10.1021/acs.inorgchem.8b00739

Xiang, G., Liu, X., Liu, W., Wang, B., Liu, Z., Jiang, S., et al. (2020b). Multifunctional Optical Thermometry Based on the Stark Sublevels of Er 3+ in CaO-Y 2 O 3 : Yb 3+/Er 3 +. *J. Am. Ceram. Soc.* 103 (4), 2540–2547. doi:10.1111/jace.16939

Xiang, G., Xia, Q., Liu, X., and Wang, X. (2020a). Optical Thermometry Based on the Thermally Coupled Energy Levels of Er3+ in Upconversion Materials. *Dalton Trans.* 49 (47), 17115–17120. doi:10.1039/d0dt03100c

Ximendes, E. C., Santos, W. Q., Rocha, U., Kagola, U. K., Sanz-Rodríguez, F., Fernández, N., et al. (2016). Unveiling *In Vivo* Subcutaneous thermal Dynamics by Infrared Luminescent Nanothermometers. *Nano Lett.* 16 (3), 1695–1703. doi:10.1021/acs.nanolett.5b04611

Xu, W., Zhao, D., Zhu, X., Zheng, L., Zhang, Z., and Cao, W. (2020). NIR to NIR Luminescence Thermometry in Core/multishells-Structured Nanoparticles Operating in the Biological Window. *J. Lumin.* 225, 117358. doi:10.1016/j.jlumin.2020.117358

Yan, Q., Yuan, J., Kang, Y., Cai, Z., Zhou, L., and Yin, Y. (2010). Dual-sensing Porphyrin-Containing Copolymer Nanosensor as Full-Spectrum Colorimeter and Ultra-sensitive Thermometer. *Chem. Commun.* 46 (16), 2781–2783. doi:10.1039/b926882k

Yuan, N., Sun, H.-X., Ju, D.-D., Liu, D.-Y., Zhang, Z.-B., Wong, W.-H., et al. (2017). A Simple, Compact, Low-Cost, Highly Efficient Thermometer Based on green Fluorescence of Er3+/Yb3+-Codoped NaYF4 Microcrystals. *Mater. Sci. Eng. C* 81, 177–181. doi:10.1016/j.msec.2017.07.055

Conflict of Interest: The authors declare that the research was conducted in the absence of any commercial or financial relationships that could be construed as a potential conflict of interest.

Publisher's Note: All claims expressed in this article are solely those of the authors and do not necessarily represent those of their affiliated organizations, or those of the publisher, the editors, and the reviewers. Any product that may be evaluated in this article, or claim that may be made by its manufacturer, is not guaranteed or endorsed by the publisher.

frontiers in Materials

ORIGINAL RESEARCH
published: 01 November 2021
doi: 10.3389/fmats.2021.754842

Ultrafast Dynamics of Optical Nonlinearities in β-Ga_2O_3

Yingfei Sun[1], Yu Fang[2], Zhongguo Li[3], Junyi Yang[1], Xingzhi Wu[2], Jidong Jia[4], Kun Liu[1], Lu Chen[1] and Yinglin Song[1,4]**

[1]School of Physical Science and Technology, Soochow University, Suzhou, China, [2]Jiangsu Key Laboratory of Micro and Nano Heat Fluid Flow Technology and Energy Application, School of Physical Science and Technology, Suzhou University of Science and Technology, Suzhou, China, [3]School of Electronic and Information Engineering, Changshu Institute of Technology, Changshu, China, [4]Department of Physics, Harbin Institute of Technology, Harbin, China*

We report the different nonlinear optical mechanisms and defect-related carrier dynamics in Sn-doped β-Ga_2O_3 crystal by utilizing time-resolved pump-probe technique based on phase object under UV excitation. The obtained nonlinear optical parameters arise from bound electron can be well explained by the theoretical calculation of two-band model and Kramers-Kronig transformation. By tuning the probe wavelength, the carrier nonlinearity can be modulated greatly due to additional absorption of defects within the bandgap. The results reveal that by choosing a proper probe wavelength that matches the defect state to the valence band, the nonlinear absorption and refraction of the carriers can be greatly enhanced, which provides an important reference for the design of gallium oxide-based waveguide materials and all-optical switching materials in the future.

Keywords: Ga2O3, nonlinear optical, defect state, pump probe technique, carrier dynamic

OPEN ACCESS

Edited by:
Zhongquan Nie,
Taiyuan University of Technology, China

Reviewed by:
Zhibo Liu,
Nankai University, China
Venugopal Rao Soma,
University of Hyderabad, India

****Correspondence:***
Yu Fang
yufang@usts.edu.cn
Yinglin Song
ylsong@hit.edu.cn

Specialty section:
This article was submitted to Quantum Materials, a section of the journal Frontiers in Materials

Received: *07 August 2021*
Accepted: *15 October 2021*
Published: *01 November 2021*

Citation:
Sun Y, Fang Y, Li Z, Yang J, Wu X, Jia J, Liu K, Chen L and Song Y (2021) Ultrafast Dynamics of Optical Nonlinearities in β-Ga_2O_3. Front. Mater. 8:754842. doi: 10.3389/fmats.2021.754842

INTRODUCTION

Beta-phase gallium oxide (β-Ga_2O_3) is a transparent conductive oxide with an ultra-wide band gap of 4.9 eV (Tippins, 1965). It is also regarded as a promising candidate for UV detectors (Ji et al., 2006; Kokubun et al., 2007) and high-temperature gas sensors (Fleischer and Meixner, 1991; Liu et al., 2008). From the perspective of optoelectronic devices, it is very necessary to understand the optical properties of this material. Recently, many studies have been carried out to explore the electrical and optical properties of β-Ga_2O_3 (Suzuki et al., 2007; Mi et al., 2014; Chikoidze et al., 2016; Bhandari et al., 2019). However, reports on the nonlinear characteristics of β-Ga_2O_3 crystals under strong light are elusive.

In 2018, Hong Chen et al. used Z-Scan to measure the two-photon absorption coefficient and Kerr refractive index of gallium oxide (Chen et al., 2018), their research focuses on ultrafast nonlinear processes caused by bound electrons, but ignores the slow nonlinear processes associated with carriers. Okan Koksal et al. presented optical pump-probe spectroscopy results on defect-assisted recombination of photoexcited carriers in β-Ga_2O_3 (Koksal et al., 2018). They used a single wavelength to probe the additional carrier absorption of polarization-related defect states, but ignored the carrier refraction. The study of gallium oxide nonlinear absorption/refraction dynamics is of great significance to the design of all-optical switches and ultrafast optoelectronic devices. In 2020, Okan Koksal et al. verified the intra- and inter-conduction band optical absorption processes of β-Ga_2O_3 through steady state and ultrafast optical spectroscopy measurements (Singh et al., 2020), but they ignored the influence of defect state at 500-650 nm on absorption, which we will be explained explicitly in this paper. Gallium oxide has many impurities or intrinsic defects, such as Si, Sn, oxygen vacancy and gallium vacancy, which promote the radiative and nonradiative

recombination of carriers (Varley et al., 2010; Dong et al., 2017; Neal et al., 2018). They can affect the photoelectric properties of materials, including conductivity, absorption, and even nonlinear optical properties (Yuksek et al., 2009; Ganesh et al., 2017; Bhandari and Zvanut, 2020; McCluskey, 2020). The reason why we choose Sn-doped β-Ga_2O_3 is that impurity Sn^{4+} instead of Ga^{3+} will generate additional free electrons (Zhang et al., 2010), so modulating the conduction band electron density by Sn doping is more conducive to measuring free carrier absorption.

In this paper, we studied the variation process of the nonlinear absorption/refraction of Sn-doped β-Ga_2O_3 with delay time by phase object pump-probe technique (POPP) at different probe wavelengths. The existence of the defect states is also proved by pump-probe spectroscopy. The bound electron-related and carriers-related nonlinear parameters as well as the defect state-related carrier dynamic processes are evaluated reasonably.

EXPERIMENTAL SECTION

The Sn-doped β-Ga_2O_3 (β-Ga_2O_3: Sn) crystal used in the experiment was a commercial single crystal material with the size of $5 \times 10 \times 0.68$ mm^3. The double-sided polished crystal had a monoclinic structure with a crystal orientation (2(_)01). The β-Ga_2O_3: Sn crystal was prepared by edge-defined film-fed growth (EFG) technique. The electron concentration is ~5×10^{18} cm^{-3}.

Q-switched and mode-locked Nd: YAG laser (355 nm, 8 ps) was employed as the degenerate POPP light sources. The laser is divided into two parts through the beam splitter: one part of the stronger energy is used as the pump light, and the other part of the weaker light after passing through the neutral density attenuator is used as the probe light. The light source of non-degenerate POPP is Yb: KGW femtosecond laser (Light Conversion, PHAROS-SP, 1,030 nm, 190 fs). The output laser beam is divided into two parts: a part of the higher energy light is used as the pump light, and the wavelength is tuned to 355 nm after passing through the optical parametric amplifier. The other part of the light with weaker energy is used as the probe light, and the wavelength becomes 515 nm after passing through the frequency doubling crystal. The schematic diagram of POPP is similar to our previous work (Sun et al., 2021). The pump light and probe light focus on the same point of the sample at a small angle (less than 5°), and the nonlinear dynamic process is explored by adjusting the delay time of the two beams. The probe light is focused on the sample after passing through the PO, and is directly received by the detector (open-aperture) after passing through the sample to obtain the nonlinear absorption response. If the aperture is closed (closed-aperture), the nonlinear refraction response of the sample can be obtained. The function of PO is to enhance the interference effect between the dielectric region and the outside region. The far-field diffraction pattern is greatly modulated after transmitting from the rear surface of the sample, so that the nonlinear phase shift signal of the sample is converted into the intensity signal. The experimental details were described explicitly in Yang et al. (2009a), Fang et al. (2013). The repetition rate was set to 10 Hz to avoid heat accumulation in the sample (Yang et al., 2009a; Yang et al., 2009b). The polarization of pump and probe beams were adjusted to be perpendicular in order to minimize the interference, where the pump beams were parallel to the (010) direction and the probe beams were parallel to the (102) direction. All measurements were performed at room temperature.

RESULTS AND DISCUSSION

The nonlinear effects caused by bound electrons (two-photon absorption, Kerr refraction) are instantaneous, while the recovery time of the nonlinear effects caused by carriers (carrier absorption and carrier refraction) is relatively long. We can distinguish different nonlinear effects of samples by time-resolved POPP, and study the dynamics of nonlinear absorption/refraction of β-Ga_2O_3: Sn. The pump light with wavelength of 355 nm (3.49 eV) we choose satisfies the condition of $E_g/2 < \hbar\omega_e < E_g$, therefore two-photon absorption (TPA) of the pump beam may occur.

Degenerate POPP Experiment (355 nm for Pump and 355 nm for Probe)

β-Ga_2O_3: Sn was pumped and probed by 355 nm, excited under a peak intensity at 11 GW/cm^2. **Figure 1** shows the open-aperture 1) and closed-aperture 2) measurements of degenerate POPP for β-Ga_2O_3: Sn. It can be seen from 1) that there is a fast absorption process at the zero-delay position, which represents the degenerate TPA, and the weak tail behind represents the weak carrier absorption. At the same time, we get the closed-aperture curve as shown in 2). there is a negative weak Kerr refraction near zero delay, the tail behind represents the carrier induced refraction, and there is almost no recovery process of the tail with the delay time, which indicates that the carrier lifetime is long.

Non-Degenerate POPP Experiment (355 nm for Pump and 515 nm for Probe)

As gallium oxide is a semiconductor with abundant energy bands, a large number of literatures have determined that the defect energy level of gallium oxide is between 2 and 3 eV above the valence band by means of luminescence spectroscopy and theoretical calculations. (Hajnal et al., 1999; Nakano, 2017; Gao et al., 2018). So we choose 515 nm (2.4 eV) to probe and observe the nonlinear absorption/refraction dynamics of β-Ga2O3: Sn. The peak intensity of pump light was set to 24 GW/cm^2 and a faster femtosecond laser was used to study its ultrafast process.

Figure 2 shows the open-aperture 1) and closed-aperture 2) measurements of non-degenerate POPP for β-Ga_2O_3: Sn. It can be seen from 1) that the peak near the zero delay is caused by the non-degenerate TPA, and the tail behind is obviously deeper than that of the degenerate POPP. We speculate that the additional absorption causes the enhancement of carrier absorption. It is reported that Sn doping is a shallow donor level (Varley et al.,

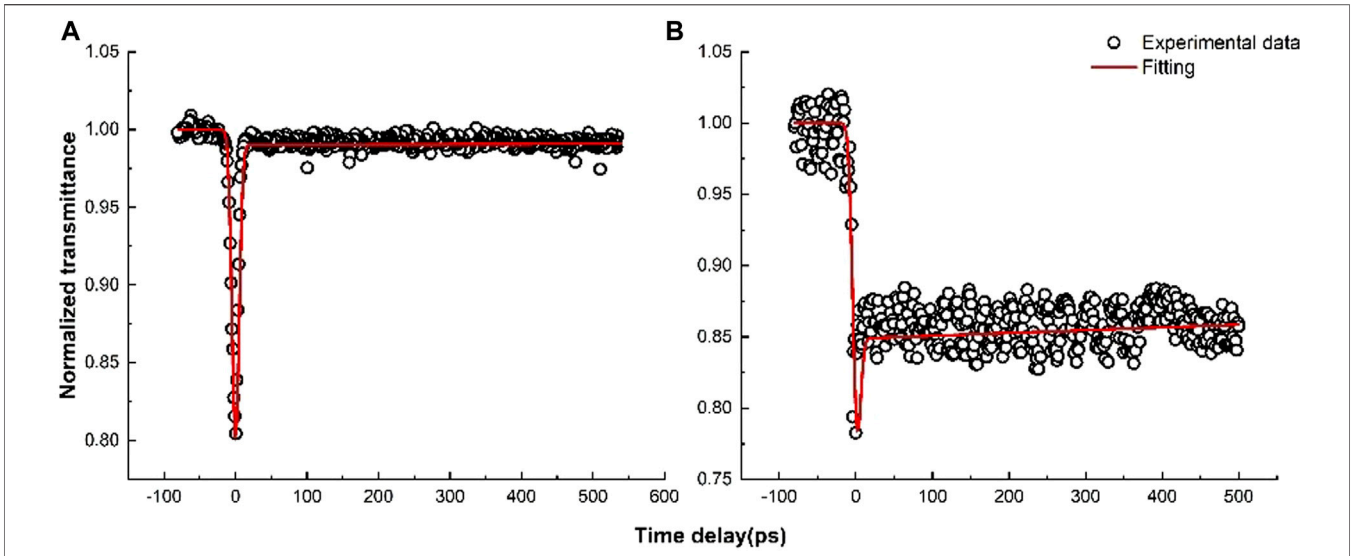

FIGURE 1 | Nonlinear absorption curves **(A)** and nonlinear refraction curves **(B)** of β-Ga_2O_3: Sn at 355 nm pump and 355 nm probe.

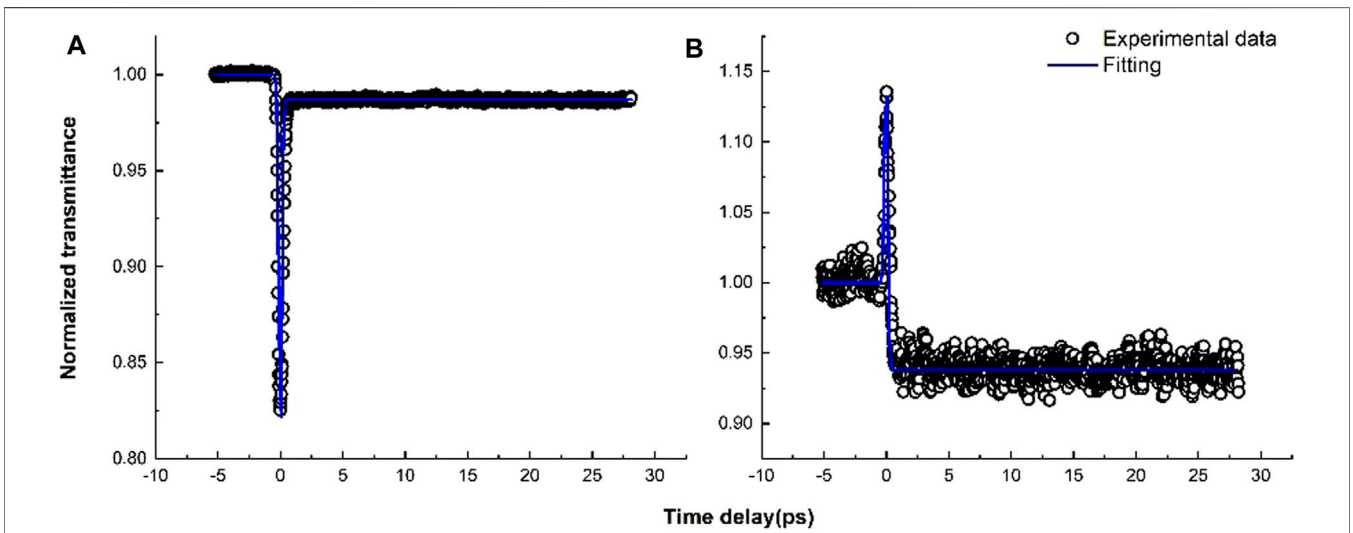

FIGURE 2 | Nonlinear absorption curves **(A)** and nonlinear refraction curves **(B)** of β-Ga_2O_3: Sn at 355 nm pump and 515 nm probe.

2010; Zhang et al., 2010), we did the same experiment on unintentionally doped (UID) gallium oxide, and found that there were similar results, proving that the additional absorption was not caused by doping, but may be caused by intrinsic defect in the growth process, as we will prove later. It can be seen from 2) that there is a weak peak caused by Kerr refraction near zero delay, which is different from the result of degenerate POPP. The tail behind represents carrier refraction. Since the non-degenerate POPP uses ultrafast laser, the recombination time is much longer than the detection window, and the recombination time is not significantly attenuated in the limited detection window, so we judge that the recombination time of the non-degenerate POPP is also very long at 515 nm (longer than 5 ns).

Bound Electrons-Related Nonlinear Optical Parameters

When the incident laser pulse is Gaussian light, the light intensity distribution of the pump light on the front surface of the sample to be measured can be described by the following formula:

$$I_e = I_{0e}\frac{\omega_{0e}^2}{\omega_e^2}\exp\left[-\frac{2r^2}{\omega_e^2}-\frac{(t-t_d)^2}{\tau^2}\right] \quad (1)$$

Where I_{0e} is the peak light intensity of the pump light, $\omega_e(z) = \omega_{0e}[1+(z/z_{0e})^2]^{1/2}$ is the spot radius of the pump light at the sample to be measured, z is the distance between the sample to be measured and the beam waist of the pump light, $z_{0e} = \pi\omega_{0e}{}^2/\lambda$ is the Rayleigh (diffraction) length of the pump light, ω_{0e} is the beam

TABLE 1 | Bound electrons-related nonlinear optical parameters. β, TPA coefficient; n2, Kerr refractive index.

Degenerate		Nondegenerate	
β (10^{-11} m/W)	n_2 (10^{-19} m^2/W)	β (10^{-11} m/W)	n_2 (10^{-19} m^2/W)
0.4	−0.1	0.23	0.2

waist radius of the pump light, τ_d is the time delay between the pump light and the detection light.

According to the standard two-band model, in the case of weak probe light, it can be considered that the carrier generation mainly comes from the TPA of the pump light. So the equation rate of carriers can be expressed as (Sun et al., 2021):

$$\frac{d\Delta n}{dt} = \frac{\beta}{2\hbar\omega} I_e^2 - \frac{n}{\tau_r} \tag{2}$$

In the formula, β is the TPA coefficient, I_e is the light intensity at the pump light sample, τ_r denote the recombination time (The overall time of direct recombination from conduction band to valence band and indirect recombination caused by defect states). The propagation formula of the probe light and pump light inside the β-Ga_2O_3: Sn crystal is (Sun et al., 2021):

$$\frac{dI_p}{dz} = -2\beta I_e I_p - \sigma n I_p \tag{3}$$

$$\frac{d\varphi_p}{dz} = \frac{\omega}{c}\left(2n_2 I_e + \eta\Delta N\right) \tag{4}$$

$$\frac{dI_e}{dz} = -\beta I_e^2 \tag{5}$$

In the formula, I_p and φ_p respectively represent the intensity and phase of the probe light, σ is absorption cross-section, n_2 is the Kerr refractive index of the bound electron, and η is carrier refractive volume. According to the above rate **Eqs 2–5**, we fit bound electrons-related nonlinear optical parameters of degenerate and non-degenerate POPP, the results are listed in **Table 1**. In the following discussion, ω_e denotes 355 nm pump beam and ω_{p1}, ω_{p2} denote 355, and 515 nm probe beams respectively. We found that after changing the probe wavelength, the Kerr refraction changes from negative to positive.

We further verify the accuracy of our TPA coefficient and Kerr refraction coefficient through the theoretical expression of the two-band model (Sheik-Bahae et al., 1991). The degenerate and nondegenerate TPA spectra predicted using:

$$\beta(\omega) = K\frac{\sqrt{E_p}}{n_0^2 E_g^3} F_2\left(\frac{\hbar\omega}{E_g}\right) \tag{6}$$

$$\beta\left(\omega_p;\omega_e\right) = K\frac{\sqrt{E_p}}{n_p n_e E_g^3} F_2\left(\frac{\hbar\omega_p}{E_g};\frac{\hbar\omega_e}{E_g}\right) \tag{7}$$

Where E_p is related to the interband momentum matrix element and for the two-parabolic-band model is defined $E_p = 2|\mathbf{P}_{vc}|^2/m_o$ (E_p is approximately 21 eV for most semiconductors) (Kane, 1980), n_p and n_e are the linear probe and pump refractive indices, respectively, F_2 is the dimensionless spectral function, in **Eq. 6**, $F_2(x) = (2x-1)^{1.5}/(2x)^5$, in **Eq. 7**, $F_2(x) = (x_1+x_2-1)^{1.5}\ (1/x_1+1/x_2)^2/2^7 \times 1 \times {}_2{}^2$ (Sheik-Bahae et al., 1991), K is ~3,100 cm GW^{-1} eV$^{5/2}$ (Hutchings and Van Stryland, 1992). According to this relationship, the calculated ratio of degenerate and non-degenerate TPA is 1.4, which is almost consistent with our experimental results. At the same time, we also measured 355 nm PS open-aperture Z-scan (as shown in **Figure 3**), and the fitted two-photon absorption coefficient ($\beta = 1.1 \times 10^{-11}$ m/W) is three times larger than the degenerate POPP result, because the pump light and probe light in POPP are vertically polarized, resulting in the decrease of polarization tensor.

The degenerate and non-degenerate n_2 (ω_p; ω_e) is calculated via the Kramers-Kronig transformation resulting in (Sheik-Bahae et al., 1994; Zhao et al., 2016):

$$n_2(\omega) = K\frac{\hbar c\sqrt{E_p}}{E_g^4 n_0^2} G_2\left(\frac{\hbar\omega}{E_g}\right) \tag{8}$$

$$n_2\left(\omega_p;\omega_e\right) = K\frac{\hbar c\sqrt{E_p}}{E_g^4 n_p n_e} G_2\left(\frac{\hbar\omega_p}{E_g};\frac{\hbar\omega_e}{E_g}\right) \tag{9}$$

G_2 is the dimensionless dispersion function (Sheik-Bahae et al., 1994). The calculated trend of the degenerate nonlinear refractive index n_2 with $\hbar\omega$, from 0 to $E_g/2$, n_2 increases to the maximum, and finally becomes negative as $\hbar\omega$ approaches the band gap E_g. So the 355 nm ($\hbar\omega/E_g$ = 0.71) Kerr refraction obtained by degenerate POPP tends to zero. The non-degenerate n_2 (ω_p; ω_e) of β-Ga_2O_3: Sn crystal is calculated as a function of probe photon energy $\hbar\omega_p$. n_2 (ω_p; ω_e) is positive at low ω_p. Due to the intermediate-state resonance enhancement, it increases to the maximum when $\hbar\omega_p = E_g - \hbar\omega_e = 0.29\ E_g$. Then n_2 (ω_p; ω_e) becomes abnormally dispersive and finally becomes negative when ω_p approaches the band gap. Therefore, the results obtained from the non-degenerate ($\hbar\omega_e/E_g$ = 0.71, $\hbar\omega_p/E_g$ = 0.49) POPP meet the trend calculated by the two-band model, which is a positive value. We found that the theory is applicable to gallium oxide, and the refraction sign changed at different probe wavelengths.

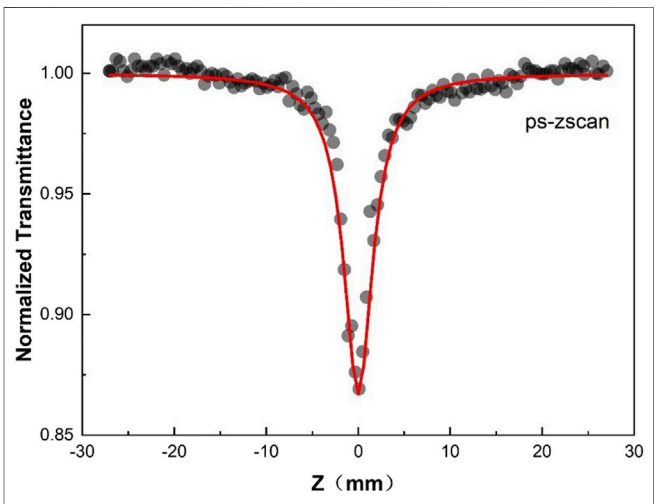

FIGURE 3 | 355 nm PS open-aperture Z-scan for Ga_2O_3: Sn bulk crystals. The solid lines are the numerical fits to the experimental data.

TABLE 2 | Free carrier -related nonlinear optical parameters. σ, FCA cross-section; η, FCR volume; τ_r, carrier lifetime.

Degenerate			Nondegenerate		
σ (10^{-22} m^2)	η (10^{-28} m^3)	τ_r (ns)	σ (10^{-22} m^2)	η (10^{-28} m^3)	τ_r (ns)
0.55	−0.32	7	36	−8	—

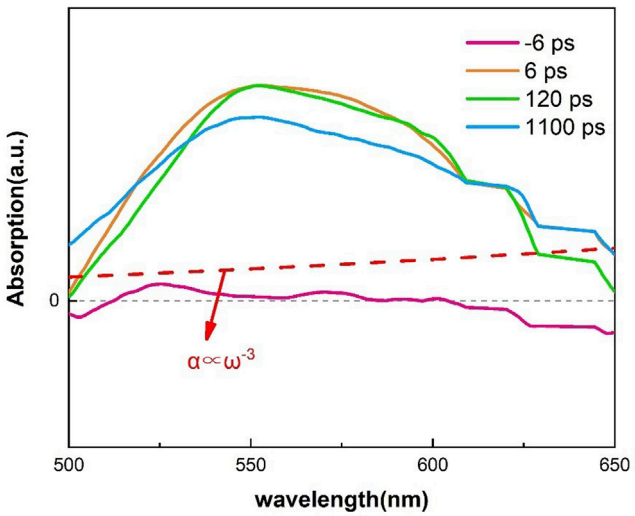

FIGURE 4 | Transient absorption spectra of β-Ga_2O_3: Sn in 500–650 nm.

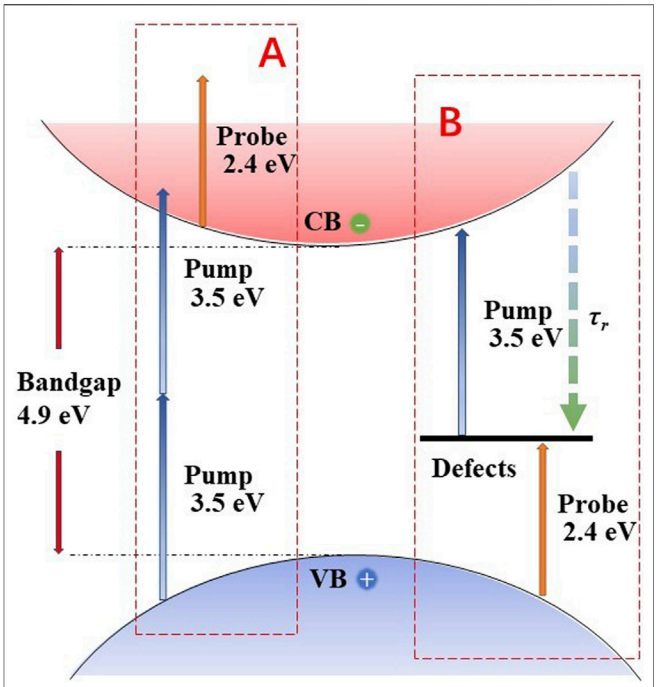

FIGURE 5 | Schematic diagram of the energy levels and carrier decay processes of β-Ga2O3: Sn. The blue up arrow represents the two-photon excitation, the green down arrow represents the recombination process related to the defect state, and the orange up arrow represents the transition from the valence band to the defect state.

Free Carrier -Related Nonlinear Optical Parameters

According to the above rate **Eqs 2–5**, we also fit free carrier-related nonlinear optical parameters of degenerate and non-degenerate POPP, the results are listed in **Table 2**. We found that after changing the probe wavelength, the responses of carrier absorption and refraction both increase by at least an order of magnitude. The increase of σ and η indicates that there indeed exists an additional absorption of defect state. We will explain in detail later.

In order to further verify the existence of the defect state, we focus the probe light on the sapphire to generate a white supercontinuum, thereby measuring the 500–650 nm transient absorption spectrum of β-Ga_2O_3: Sn crystal under two-photon excitation. The details of the experiment were described explicitly in Fang et al. (2016). The absorption results are shown in **Figure 4**. We can see that the transient absorption spectrum with different delay time shows broadband absorption, corresponding to a peak value of 550 nm (2.48 eV), and the profile and peak value of transient absorption have almost no change in the delay time of 6–1,100 ps. This is a typical defect state absorption. In Singh et al. (2020), they did the absorption spectra of different probe wavelengths (515, 600, 660, 800, 940 nm) under 450 nm excitation, and found that they were related to the transition in the conduction band (intraband free-carrier absorption) through $\alpha\propto\omega^{-3}$ fitting (Drude model, as shown by the red dotted line in **Figure 4**), while the extra absorption due to defect state between 500 and 650 nm is ignored. The difference between our experimental results and the Drude line proves the existence of defect state absorption.

Next, we discuss the carrier dynamics of β-Ga_2O_3: Sn. It is reported that the effective mass of hole is much larger than that of electron (Yeo et al., 1998). According to Drude model, it can be considered that free carrier absorption and refraction mainly come from electrons. Since gallium oxide can be considered as a direct band gap semiconductor with a large band gap and low excited carrier concentration, the probability of direct recombination (radiation transition) is very low. Almost all carriers are recombined indirectly through defect energy levels (either radiation recombination or non-radiation recombination). As mentioned earlier, what we have probed is basically the response of electrons, so the dynamic process is dominated by the indirect recombination process of electrons.

In the case of degenerate POPP (355 nm pump, 355 nm probe), the valence band electrons can transition to the conduction band through degenerate TPA. When the probe light is incident on the semiconductor, electrons in the conduction band can continue to absorb a probe photon and transition to a higher conduction band energy level, which is free carrier absorption. Subsequently, the electrons transition to the defect state through indirect recombination, which leads to a decrease in the conduction band electron concentration, so that the absorption of free carriers under 355 nm detection is reduced, thereby forming a long tail (as shown in **Figure 1**).

TABLE 3 | Photo-physical parameters of β-Ga_2O_3: Sn, GaN, ZnO and UID β-Ga_2O_3. E_g, bandgap; E_e/E_g, relative photon energy; β, TPA coefficient; σ, FCA cross-section; n_2, kerr refractive index; η, FCR volume; τ_r, carrier lifetime.

	E_g	E_e/E_g	B (10^{-11} m/W)	Σ (10^{-22} m^2)	n_2 (10^{-19} m^2/W)	H (10^{-28} m^3)	τ_r (ns)
β-Ga2O3: Sn Degenerate	4.9	0.7	0.4	0.55	−0.1	-0.32	7
β-Ga2O3: Sn Nondegenerate	4.9	0.7	0.23	36	0.2	−8	>5
GaN Fang et al. (2013)	3.39	0.7	12	2.5	−1~0	−2	12
ZnO Li et al. (2013)	3.4	0.7	2.9	47	-0.1	−1.9	8.9
UID β-Ga_2O_3 Chen et al. (2018)	4.85	0.63	0.6	—	−2.9	—	—

In the case of non-degenerate POPP (355 nm pump, 515 nm probe), the valence band electrons are also excited by degenerate TPA and absorb the probe photons in the conduction band to produce carrier absorption (Corresponding to process A in **Figure 5**). At the same time, the pump light also excites the electrons in the defect state to the conduction band, which makes the defect state partially empty and makes it possible for the valence band electrons to transition to the defect state. Moreover, the probe photon energy just meets the energy level of the defect state (~2.2 eV) extracted from transient absorption spectrum (**Figure 4**), so under non-degenerate conditions, the additional absorption of the defect state can be probed (Corresponding to process B in **Figure 5**). The increased σ and η obtained by non-degenerate POPP can be considered as a combination of free carrier effect (carrier dispersion effect) and defect state (absorption and refraction) effects, which cause the change in the real part and the imaginary part of the dielectric constant. Then the electron transitions to the defect state through indirect recombination (Corresponding to τ_r in **Figure 5**). This also leads to a decrease in the conduction band electron concentration, so that the free carrier absorption under 515 nm probe is reduced, and secondly, due to the indirect recombination of the electron transition to the defect state, causing the defect state to be partially occupied, so that the defect state's absorption of the 515 nm probe is reduced. Therefore, based on the previous experimental results, it can be judged that the indirect recombination time under non-degenerate POPP is also in the order of nanoseconds.

In **Table 3**, we list the nonlinear optical parameters of more popular semiconductor materials recently. Through comparison, we not only find that our test methods can accurately obtain more comprehensive nonlinear optical parameters, but also find that the nonlinear absorption and refraction are relatively small compared with other materials, which means that as a waveguide material, it has lower loss (Lin et al., 2007; Sierra et al., 2019), and β-Ga_2O_3 can be used as a substrate under the growth conditions of GaN-based compounds (Ohira et al., 2008), which shows that gallium oxide is expected to be used in integrated photonics applications. The transformation of refraction symbol and carrier lifetime also show the potential application value of gallium oxide in the field of ultrafast all-optical switching (Nozaki et al., 2010; Fang et al., 2015). Therefore, it is very important to understand these parameters, which provides an important reference for the design of gallium oxide optoelectronic devices in the future.

CONCLUSION

In summary, POPP technologies were utilized to discuss the optical nonlinear response of Sn-doped β-Ga_2O_3 crystal under excitation at 355 nm and the defect state dependent carrier dynamics. The corresponding parameters at different probe wavelengths were obtained through rate equation model fitting. We find that the sign of Kerr refraction changed from negative to positive, which satisfies the theoretical calculation of the two-band model under the Kramers-Kronig relationship. Moreover, when the probe photon energy satisfies the defect state transition to the valence band, the carrier absorption cross-section and the carrier refraction volume are increased by at least an order of magnitude, which indicates that the carrier absorption and refraction caused by defect states are wavelength-dependent parameters. Understanding the carrier dynamics and nonlinear optical parameters is essential for the development of β-Ga_2O_3 technology, and provides important references for future design based on all-optical switches and optical waveguide devices.

DATA AVAILABILITY STATEMENT

The original contributions presented in the study are included in the article/Supplementary Material, further inquiries can be directed to the corresponding authors.

AUTHOR CONTRIBUTIONS

YFS, YF, ZL, and YLS contributed to conception and design of the study. JY, XW, and JJ contributed to experiments and data fitting. KL and LC contributed to manuscript revision. All authors contributed to read, and approved the submitted version.

ACKNOWLEDGMENTS

We gratefully acknowledge the NSAF (Grant No. U1630103), Special Fund from State Key Laboratory of Intense Pulsed Radiation Simulation and Effect (No. SKLIPR1715), National Natural Science Foundation of China (No. 11704273, 11804244), Natural Science Foundation of Jiangsu Province, China (Grant No. BK20180965).

REFERENCES

Bhandari, S., and Zvanut, M. E. (2020). Optical Transitions for Impurities in Ga2O3 as Determined by Photo-Induced Electron Paramagnetic Resonance Spectroscopy. *J. Appl. Phys.* 127, 065704. doi:10.1063/1.5140193

Bhandari, S., Zvanut, M. E., and Varley, J. B. (2019). Optical Absorption of Fe in Doped Ga2O3. *J. Appl. Phys.* 126, 165703. doi:10.1063/1.5124825

Chen, H., Fu, H., Huang, X., Montes, J. A., Yang, T.-H., Baranowski, I., et al. (2018). Characterizations of the Nonlinear Optical Properties for (010) and (2 0 1) Beta-phase Gallium Oxide. *Opt. Express* 26, 3938–3946. doi:10.1364/oe.26.003938

Chikoidze, E., Von Bardeleben, H. J., Akaiwa, K., Shigematsu, E., Kaneko, K., Fujita, S., et al. (2016). Electrical, Optical, and Magnetic Properties of Sn Doped α-Ga2O3 Thin Films. *J. Appl. Phys.* 120, 025109. doi:10.1063/1.4958860

Dong, L., Jia, R., Xin, B., Peng, B., and Zhang, Y. (2017). Effects of Oxygen Vacancies on the Structural and Optical Properties of β-Ga2O3. *Sci. Rep.* 7, 40160. doi:10.1038/srep40160

Fang, Y., Yang, J. Y., Yang, Y., Wu, X., Xiao, Z., Zhou, F., et al. (2016). Ultrafast Carrier Dynamics in a P-type GaN Wafer under Different Carrier Distributions. *J. Phys. D Applied Phys.* 49, 045105. doi:10.1088/0022-3727/49/4/045105

Fang, Y., Wu, X.-Z., Ye, F., Chu, X.-Y., Li, Z.-G., Yang, J.-Y., et al. (2013). Dynamics of Optical Nonlinearities in GaN. *J. Appl. Phys.* 114, 103507. doi:10.1063/1.4820929

Fang, Y., Xiao, Z., Wu, X., Zhou, F., Yang, J., Yang, Y., et al. (2015). Optical Nonlinearities and Ultrafast All-Optical Switching of M-Plane GaN in the Near-Infrared. *Appl. Phys. Lett.* 106, 251903. doi:10.1063/1.4923184

Fleischer, M., and Meixner, H. (1991). Gallium Oxide Thin Films: A New Material for High-Temperature Oxygen Sensors. *Sensors Actuators B: Chem.* 4, 437–441. doi:10.1016/0925-4005(91)80148-d

Ganesh, V., Yahia, I. S., Alfaify, S., and Shkir, M. (2017). Sn-doped ZnO Nanocrystalline Thin Films with Enhanced Linear and Nonlinear Optical Properties for Optoelectronic Applications. *J. Phys. Chem. Sol.* 100, 115–125. doi:10.1016/j.jpcs.2016.09.022

Gao, H., Muralidharan, S., Pronin, N., Karim, M. R., White, S. M., Asel, T., et al. (2018). Optical Signatures of Deep Level Defects in Ga2O3. *Appl. Phys. Lett.* 112, 242102. doi:10.1063/1.5026770

Hajnal, Z., Miró, J., Kiss, G., Réti, F., Deák, P., Herndon, R. C., et al. (1999). Role of Oxygen Vacancy Defect States in Then-type Conduction of β-Ga2O3. *J. Appl. Phys.* 86, 3792–3796. doi:10.1063/1.371289

Hutchings, D. C., and Van Stryland, E. W. (1992). Nondegenerate Two-Photon Absorption in Zinc Blende Semiconductors. *J. Opt. Soc. Am. B* 9, 2065. doi:10.1364/josab.9.002065

Ji, Z., Du, J., Fan, J., and Wang, W. (2006). Gallium Oxide Films for Filter and Solar-Blind UV Detector. *Opt. Mater.* 28, 415–417. doi:10.1016/j.optmat.2005.03.006

Kane, E. (1980). "Band Structure of Narrow gap Semiconductors," in *Narrow Gap Semiconductors Physics and Applications* (Berlin: Springer), 13–31.

Koksal, O., Tanen, N., Jena, D., Xing, H., and Rana, F. (2018). Measurement of Ultrafast Dynamics of Photoexcited Carriers inβ-Ga2O3by Two-Color Optical Pump-Probe Spectroscopy. *Appl. Phys. Lett.* 113, 252102. doi:10.1063/1.5058164

Kokubun, Y., Miura, K., Endo, F., and Nakagomi, S. (2007). Sol-gel Prepared β-Ga2O3 Thin Films for Ultraviolet Photodetectors. *Appl. Phys. Lett.* 90, 031912. doi:10.1063/1.2432946

Li, Z.-g., Yang, J.-y., Wei, T.-H., and Song, Y.-l. (2013). Intensive Two-Photon Absorption Induced Decay Pathway in a ZnO crystal: Impact of Light-Induced Defect State. *Appl. Phys. Lett.* 103, 252107. doi:10.1063/1.4855375

Lin, Q., Painter, O. J., and Agrawal, G. P. (2007). Nonlinear Optical Phenomena in Silicon Waveguides: Modeling and Applications. *Opt. Express* 15, 16604–16644. doi:10.1364/oe.15.016604

Liu, Z., Yamazaki, T., Shen, Y., Kikuta, T., Nakatani, N., and Li, Y. (2008). O2 and CO Sensing of Ga2O3 Multiple Nanowire Gas Sensors. *Sensors Actuators B: Chem.* 129, 666–670. doi:10.1016/j.snb.2007.09.055

McCluskey, M. D. (2020). Point Defects in Ga2O3. *J. Appl. Phys.* 127, 101101. doi:10.1063/1.5142195

Mi, W., Du, X., Luan, C., Xiao, H., and Ma, J. (2014). Electrical and Optical Characterizations of β-Ga2O3:Sn Films Deposited on MgO (110) Substrate by MOCVD. *RSC Adv.* 4, 30579. doi:10.1039/c4ra02479f

Nakano, Y. (2017). Communication-Electrical Characterization of β-Ga2O3 Single Crystal Substrates. *ECS J. Solid State. Sci. Technol.* 6, P615–P617. doi:10.1149/2.0181709jss

Neal, A. T., Mou, S., Rafique, S., Zhao, H., Ahmadi, E., Speck, J. S., et al. (2018). Donors and Deep Acceptors in β-Ga2O3. *Appl. Phys. Lett.* 113, 062101. doi:10.1063/1.5034474

Nozaki, K., Tanabe, T., Shinya, A., Matsuo, S., Sato, T., Taniyama, H., et al. (2010). Sub-femtojoule All-Optical Switching Using a Photonic-crystal Nanocavity. *Nat. Photon.* 4, 477–483. doi:10.1038/nphoton.2010.89

Ohira, S., Suzuki, N., Arai, N., Tanaka, M., Sugawara, T., Nakajima, K., et al. (2008). Characterization of Transparent and Conducting Sn-Doped β-Ga2O3 Single crystal after Annealing. *Thin Solid Films* 516, 5763–5767. doi:10.1016/j.tsf.2007.10.083

Sheik-Bahae, M., Hutchings, D. C., Hagan, D. J., and Van Stryland, E. W. (1991). Dispersion of Bound Electron Nonlinear Refraction in Solids. *IEEE J. Quan. Electron.* 27, 1296–1309. doi:10.1109/3.89946

Sheik-Bahae, M., Wang, J., and van Stryland, E. W. (1994). Nondegenerate Optical Kerr Effect in Semiconductors. *IEEE J. Quan. Electron.* 30, 249–255. doi:10.1109/3.283767

Sierra, J. H., Rangel, R. C., Samad, R. E., Vieira, N. D., Alayo, M. I., and Carvalho, D. O. (2019). Low-loss Pedestal Ta2O5 Nonlinear Optical Waveguides. *Opt. Express* 27, 37516–37521. doi:10.1364/oe.27.037516

Singh, A., Koksal, O., Tanen, N., McCandless, J., Jena, D., Xing, H., et al. (2020). Intra- and Inter-conduction Band Optical Absorption Processes in β-Ga2O3. *Appl. Phys. Lett.* 117, 072103. doi:10.1063/5.0016341

Sun, Y., Fang, Y., Li, Z., Yang, J., Zhou, W., Liu, K., et al. (2021). Free Carrier-Induced Optical Nonlinearities in β-Ga2O3 Single Crystals at 355 Nm. *J. Phys. D: Appl. Phys.* 54, 495105. doi:10.1088/1361-6463/ac24c6

Suzuki, N., Ohira, S., Tanaka, M., Sugawara, T., Nakajima, K., and Shishido, T. (2007). Fabrication and Characterization of Transparent Conductive Sn-Doped β-Ga2O3 Single crystal. *Phys. Stat. Sol.* 4, 2310–2313. doi:10.1002/pssc.200674884

Tippins, H. H. (1965). Optical Absorption and Photoconductivity in the Band Edge ofβ–Ga2O3. *Phys. Rev.* 140, A316–A319. doi:10.1103/physrev.140.a316

Varley, J. B., Weber, J. R., Janotti, A., and Van de Walle, C. G. (2010). Oxygen Vacancies and Donor Impurities in β-Ga2O3. *Appl. Phys. Lett.* 97, 142106. doi:10.1063/1.3499306

Yang, J., Song, Y., Wang, Y., Li, C., Jin, X., and Shui, M. (2009). Time-resolved Pump-Probe Technology with Phase Object for Measurements of Optical Nonlinearities. *Opt. Express* 17, 7110–7116. doi:10.1364/oe.17.007110

Yang, J., Zhang, X., Wang, Y., Shui, M., Li, C., Jin, X., et al. (2009). Method with a Phase Object for Measurement of Optical Nonlinearities. *Opt. Lett.* 34, 2513–2515. doi:10.1364/ol.34.002513

Yeo, Y. C., Chong, T. C., and Li, M. F. (1998). Electronic Band Structures and Effective-Mass Parameters of Wurtzite GaN and InN. *J. Appl. Phys.* 83, 1429–1436. doi:10.1063/1.366847

Yuksek, M., Elmali, A., Karabulut, M., and Mamedov, G. M. (2009). Switching from Negative to Positive Nonlinear Absorption in P Type 0.5 at% Sn Doped GaSe Semiconductor crystal. *Opt. Mater.* 31, 1663–1666. doi:10.1016/j.optmat.2009.04.003

Zhang, Y., Yan, J., Zhao, G., and Xie, W. (2010). First-principles Study on Electronic Structure and Optical Properties of Sn-Doped β-Ga2O3. *Phys. B: Condens. Matter* 405, 3899–3903. doi:10.1016/j.physb.2010.06.024

Zhao, P., Reichert, M., Hagan, D. J., and Van Stryland, E. W. (2016). Dispersion of Nondegenerate Nonlinear Refraction in Semiconductors. *Opt. Express* 24, 24907. doi:10.1364/oe.24.024907

Conflict of Interest: The authors declare that the research was conducted in the absence of any commercial or financial relationships that could be construed as a potential conflict of interest.

The handling Editor declared a past co-authorship with one of the author YS.

Advantages of publishing in Frontiers

OPEN ACCESS
Articles are free to read for greatest visibility and readership

FAST PUBLICATION
Around 90 days from submission to decision

HIGH QUALITY PEER-REVIEW
Rigorous, collaborative, and constructive peer-review

TRANSPARENT PEER-REVIEW
Editors and reviewers acknowledged by name on published articles

Frontiers
Avenue du Tribunal-Fédéral 34
1005 Lausanne | Switzerland

Visit us: www.frontiersin.org
Contact us: frontiersin.org/about/contact

REPRODUCIBILITY OF RESEARCH
Support open data and methods to enhance research reproducibility

DIGITAL PUBLISHING
Articles designed for optimal readership across devices

FOLLOW US
@frontiersin

IMPACT METRICS
Advanced article metrics track visibility across digital media

EXTENSIVE PROMOTION
Marketing and promotion of impactful research

LOOP RESEARCH NETWORK
Our network increases your article's readership